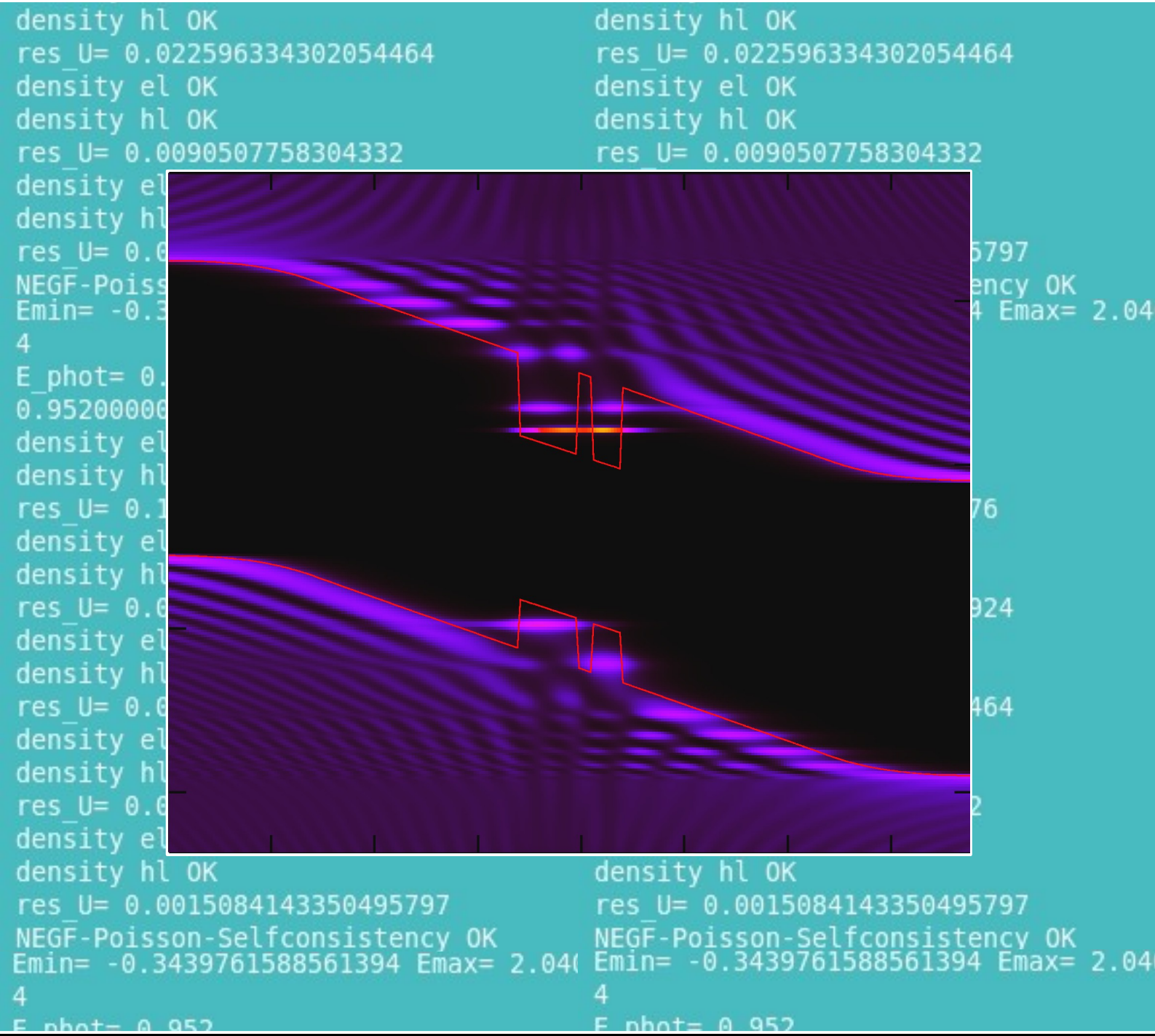


Emin= -0.3439761588561394 Emax= 2.044 E_phot= 0.952

A MICROSCOPIC THEORY OF QUANTUM WELL PHOTOVOLTAICS



Diss. ETH No. 17966

A Microscopic Theory of Quantum Well Photovoltaics

A dissertation submitted to the
SWISS FEDERAL INSTITUTE OF TECHNOLOGY
ZURICH

for the degree of
Doctor of Sciences, ETH Zürich

presented by
URS AEBERHARD
Dipl. phys., ETH Zürich
born 28.7.1978
citizen of Jegenstorf BE

accepted on the recommendation of
Prof. Dr. M. Sigrist, examiner
Dr. R.H. Morf, co-examiner
Prof. Dr. J. Faist, co-examiner

2008

Abstract

The main topic of this thesis is a theoretical investigation of the photovoltaic properties of semiconductor quantum well structures embedded in the intrinsic region of nanoscale *p-i-n* junctions. For that purpose, a microscopic theory of the dominant processes in such devices is formulated, based on the nonequilibrium Green's function formalism, and is implemented for numerical simulation.

Apart from the appealing generality and the novelty of the theoretical approach in the field of photovoltaics, the relevance of the research is given by the increasing importance of its main area of application, which is that of the quantum well solar cell as a high efficiency concept for solar energy conversion.

Quantum well solar cells are characterized by peculiarities that make it hard to assess their optoelectronic properties with conventional theories of transport and optical interband transitions in semiconductors: They are dominated by the quantum effects arising from the confined states in the quantum wells, and their operating point is far from equilibrium. A proper description of the relevant processes and the device characteristics, this combination and the unavoidable presence of carrier relaxation via scattering with phonons thus requires the use of a quantum kinetic transport theory, together with a microscopic theory of the electronic structure.

Such a theory is provided by the framework of the nonequilibrium Green's function formalism, also called Keldysh method, in combination with an empirical tight-binding basis. In this theory, physical characteristics such as density and current in systems driven out of equilibrium by the application of electrical or optical bias are determined by means of non-equilibrium quantum statistical mechanics. The central problem is the solution of Dyson's equations of motion for the steady state nonequilibrium Green's function. These Green's functions are nonequilibrium statistical ensemble averages of single-particle operators and contain all the required information about the system. Interactions among the constituents of the system are naturally included in terms of corresponding self-energies. For weak interactions, the latter can be obtained using standard many-body perturbation

theory methods, such as Wick expansions, Feynman-diagrams or functional derivative techniques.

To describe the fundamental processes in quantum well solar cells, which are photogeneration, transport, relaxation, radiative and non-radiative recombination, the Hamiltonians for the interactions of electrons and holes with photons, phonons and among each other are formulated and used to derive the corresponding self-energies. The coupling of the open quantum system to the environment represented by the emitter and collector contacts is achieved via the reduction of the semi-infinite contact regions into additional boundary self-energy terms.

The application of the theory to nanoscale *p-i-n* junctions, with plain bulk, single quantum wells or coupled double quantum wells in the intrinsic region, sheds new light on the effects of ultra-small dimensions, one-dimensional confinement and scattering on interband absorption and perpendicular transport in quantum well structures, like the joint density of states for radiative transitions between both quantized and continuum states and the availability and occupation of carrier escape channels as a function of the photon energy. Strong indications are found that the device performance can be enhanced using specific geometrical configurations of asymmetrically coupled quantum well structures.

Zusammenfassung

Hauptthema der vorliegenden Arbeit ist eine theoretische Untersuchung der photovoltaischen Eigenschaften von Halbleiter-Quantentopfstrukturen eingebettet in die intrinsische Zone eines $p-i-n$ -Kontakts. Zu diesem Zweck wird ein mikroskopisches Modell, basierend auf dem Nichtgleichgewichts-Green's-Funktionen Formalismus, erstellt und zur numerischen Simulation implementiert.

Nebst der Allgemeinheit und formalen Eleganz des theoretischen Ansatzes sowie seiner Neuartigkeit auf dem Gebiet der Photovoltaik beruht die Relevanz dieser Forschung auf der wachsenden Bedeutung ihres Hauptanwendungsgebietes, der Verwendung von Halbleiter-Quantenstrukturen in innovativen Hocheffizienz-Solarzellen.

Auf Quantentopfstrukturen basierende Solarzellen sind charakterisiert durch Eigenheiten, die den Zugang zu ihren optoelektronischen Eigenschaften mittels konventioneller Theorien für Transport und optische Übergänge in Halbleitern erschweren, wenn nicht gar verunmöglichen: Sie werden einerseits beherrscht durch die Quanteneffekte hervorgerufen von lokalisierten Zuständen in den Quantentöpfen, und andererseits befindet sich ihr Arbeitspunkt weit vom Gleichgewicht entfernt. Aufgrund dieser Kombination und der unerlässlichen Berücksichtigung von Ladungsträger-Relaxation durch Streuung an Gitterschwingungen verlangt eine geeignete Beschreibung der relevanten Prozesse und der resultierenden Bauteil-Charakteristik nach einer quanten-kinetischen Transporttheorie, zusammen mit einer mikroskopischen Theorie der elektronischen Bandstruktur.

Eine Theorie der gesuchten Art findet sich im Nichtgleichgewichts Green's-Funktionen Formalismus - auch *Keldysh*-Methode genannt - unter Verwendung einer Tight-Binding Basis. In dieser Theorie werden physikalische Größen wie Ladungsträgerdichten und -ströme in Systemen, die durch Anlegen einer elektrischen Spannung oder durch optische Anregung aus dem Gleichgewicht gebracht werden, mittels Methoden der Nichtgleichgewichts-quanten-statistischen Mechanik ermittelt. Das zentrale Problem ist das Lösen der Dyson-Gleichungen welche die Bewegungsgleichungen der Green'schen Funktionen für den stationären Nichtgleichgewichtszustand darstellen. Die Green'schen Funktionen sind dabei

Nichtgleichgewichts-statistische Erwartungswerte für Einteilchen Operatoren und enthalten die gesamte benötigte Information über das System. Wechselwirkungen zwischen den Konstituenten des Systems werden auf eine natürliche Weise durch entsprechende Selbstenergien berücksichtigt. Für schwache Wechselwirkungen können diese unter Verwendung üblicher Methoden der Vielteilchen-Störungsrechnung bestimmt werden.

Um die grundlegenden Prozesse in Quantentopf-Solarzellen zu beschreiben, nämlich die Erzeugung von Elektron-Loch Paaren durch Photonabsorption, Ladungsseparation und -transport zu den Kontakten, die Relaxation durch Streuprozesse sowie strahlende und nichtstrahlende Rekombination, werden die Terme des Hamiltonian für die Wechselwirkung von Elektronen und Löchern mit Photonen, Phononen und unter sich bestimmt und zur Herleitung der entsprechenden Selbstenergien verwendet. Die zur Beschreibung von Transportphänomenen notwendige Kopplung des offenen quantenmechanischen Systems an die Umgebung (in Form der Kontakte) wird durch zusätzliche Rand-Selbstenergieterme berücksichtigt.

Die Anwendung der Theorie auf $p-i-n$ Dioden mit Ausdehnungen unterhalb des μm -Bereichs, für homogene Strukturen, einzelne Quantentöpfe sowie gekoppelte Doppeltopf-Systeme in der intrinsischen Zone, zeigt die Effekte äusserst kleiner Dimensionen, Quantisierung und Streuung an Gitterschwingungen auf die Interband-Absorption und den Transport normal zur Schichtrichtung, wie etwa die kombinierte Zustandsdichte für optische Übergänge zwischen quantisierten sowie kontinuierlichen Zuständen oder die Verfügbarkeit und Besetzung von Transport-Kanälen zur rascheren Entleerung tiefliegender Subbänder als Funktion der Photonenergie. Dabei finden sich Anzeichen für die Möglichkeit einer Verbesserung der photovoltaischen Leistung unter Verwendung spezifischer geometrischer Konfigurationen asymmetrisch gekoppelter Quantentopfstrukturen.

Contents

Abstract	i
Zusammenfassung	iii
1 Motivation and Outline	1
1.1 Introduction	1
1.2 Outline	3
2 Quantum well solar cells	5
2.1 Principles of photovoltaic energy conversion	5
2.1.1 Crystalline bulk $p(-i)-n$ junction based solar cells	6
2.2 Quantum well solar cells	10
2.2.1 Basic principles, structure and processes	10
2.2.2 Material systems and experimental realizations	11
2.2.3 Optical and electronic properties	14
2.2.4 Current-voltage characteristics	18
2.2.5 Efficiency	21
2.2.6 Fundamental open questions	23
2.3 Theoretical models for QWSC	25
2.3.1 Thermodynamic and detailed-balance theories	26
2.3.2 Macroscopic continuum and hybrid transport models	26
2.3.3 Conclusions	28
2.3.4 Requirements for novel approaches	29

2.3.5	Quantum transport models for QWSC	32
2.3.6	Summary	38
3	Quantum transport with nonequilibrium Green's functions	41
3.1	Introduction	41
3.2	Nonequilibrium statistical averages	42
3.3	Nonequilibrium Green's functions	47
3.3.1	Equations of motion	47
3.3.2	Analytic continuation	50
3.3.3	Steady state representation	54
3.3.4	Physical quantities from NEGF	56
3.4	Application to transport in nanoscale devices	60
3.4.1	System partitioning, Hamiltonian and self-energies	60
3.4.2	Basis functions and spatial discretization	61
3.4.3	Coupling to extended contacts: boundary self-energy treatment	68
3.4.4	Physical interpretation	70
3.4.5	Self-consistent solution procedure	71
4	A NEGF model of quantum well solar cells	73
4.1	Introduction	73
4.1.1	Model Hamiltonian	75
4.2	Electron-photon interaction	76
4.2.1	Quantization of the electromagnetic field and photon Green's function	77
4.2.2	Interaction Hamiltonian for layered systems	80
4.2.3	Electron-photon self-energy	81
4.2.4	Absorption and emission from microscopic polarization	82
4.2.5	Renormalization of the photon propagator: photon self-energy	86
4.2.6	Quantum efficiency	88
4.3	Electron-phonon interaction	88
4.3.1	Interaction Hamiltonian in planar orbital basis	89

4.3.2	Scattering self-energies	91
4.3.3	Power dissipation	94
4.4	Carrier-carrier interaction	94
4.4.1	Hamiltonian in planar orbital basis	94
4.4.2	First order: Hartree and Fock terms	95
4.4.3	Second order Born approximation: direct-collision term	97
5	Numerical results	99
5.1	Introduction	99
5.2	Photovoltaic properties of nanoscale bulk $p-i-n$ diodes	101
5.2.1	Introduction	101
5.2.2	Device characterization	102
5.2.3	Numerical considerations	102
5.2.4	Equilibrium and non-equilibrium properties in the dark	104
5.2.5	Effects of relaxation due to scattering with phonons	107
5.2.6	Properties under illumination at short circuit conditions	109
5.2.7	Current-voltage characteristics	116
5.2.8	Bandstructure effects: comparison with sp^3s^* multiband model	119
5.2.9	Summary and conclusions	121
5.3	Photogeneration and transport in single quantum well $p-i-n$ diodes	122
5.3.1	Introduction	122
5.3.2	Electronic properties in the dark	124
5.3.3	Optoelectronic properties under illumination	129
5.3.4	Summary and conclusions	138
5.4	Geometry effects in coupled quantum well systems	140
5.4.1	Introduction	140
5.4.2	Device	140
5.4.3	Coupling	141
5.4.4	Asymmetry	143

5.4.5	Summary and conclusions	146
6	Summary and Outlook	147
A	Analytic continuation: Langreth's theorem and the Keldysh formalism	151
A.1	Introduction	151
A.2	Langreth's theorem	151
A.3	Keldysh formalism	154
B	The recursive Green's function formalism	155
C	Multiband formalism	161
C.1	Introduction	161
C.2	Bulk Hamiltonian and band structure	161
C.3	Optical matrix elements	162
C.4	Tight-binding model for layered semiconductors: planar orbital basis	163
C.4.1	Basis functions and representation of the Hamiltonian	163
C.4.2	Dipole-matrix elements for optical transitions	164
C.4.3	Green's functions	165
C.4.4	Density and current	166
C.4.5	Multi-atom basis	169
C.5	Single-band model	170
C.5.1	Boundary self energies	171
C.5.2	Single orbital two-band model	172
C.6	Diatomic two-band model	173
C.7	Spinless sp^3s^* model	176
D	Boundary self-energies for multiband models	183
E	Interaction self-energies	187
E.1	Introduction	187

E.2	Diagrammatic perturbation expansion	187
E.3	Interactions of carriers with phonons and photons	188
F	The electrostatic problem	195
F.1	Introduction	195
F.2	Poisson's equation for bipolar structures	195
	Bibliography	197
	List of publications	213
	Curriculum Vitae	215
	Acknowledgements	217

Chapter 1

Motivation and Outline

1.1 Introduction

Already at the end of the 20th century, the search for sustainable energy sources revealed itself as one of the major challenges that mankind will have to face in the near future. Both fossil and nuclear fuels are of limited abundance and their use poses a threat to humanity either through the effects on the climate or the inherent destructive potential. In the long run it is thus mandatory to rely on alternative, clean power sources such as hydroelectric, wind and solar energy.

Solar energy, as compared to other energy sources like fossil or nuclear has the advantage that it is abundant, providing a constant global energy current of 1.7×10^{14} kW, which is more than enough to cover the actual (2002) global energy consumption of 1.24×10^{10} kW [1]. However, as neither the illumination nor the consumption are equally distributed, the actual solar energy conversion efficiency that is required to cover the energy need in a country like Switzerland or Germany is considerably higher than the ratio of the above values.

Although the basic principles of solar energy conversion have been known for half a century by now, its use has been strongly limited by the high cost per extracted amount of power (\$/W), due to limited efficiency and expensive production processes inherent in the bulk single-junction crystalline silicon technology that had become the standard in photovoltaics, comprising over 90% of the installed power. These shortcomings motivated the definition of two complementary strategies: *low cost* production on one hand and *high efficiency* concepts on the other hand. The resulting two road maps of photovoltaic research led to the development of the so called second and third generations [2] of solar cells, respectively.

In the low cost sector, or the second generation, much progress was achieved by the development of thin film, dye sensitized and even organic solar cells. However, due to low efficiency, most of these technologies are rather suited as power supply for small electronic devices than for large scale, grid-connected electricity production. For the latter, high efficiency concepts such as multi-junction cells with additional concentration of the sunlight could soon reach competitive consumer prices in countries with favourable insolation conditions, such as Spain and Italy.

To increase the efficiency of a solar cell, detailed knowledge is required of where exactly energy is wasted in the conversion process. The major source of energy loss is found in the poor utilization of the solar spectrum by devices with a single band gap: even if the gap energy is near the optimum with respect to the spectrum, there will be a whole energy range below the band gap where photons are not absorbed, and an energy range above the band gap where the excess energy is lost via thermalization. After these generation losses, carriers are still subject to radiative and non-radiative recombination, which decrease the device efficiency further. While non-radiative recombination via trap states in the band gap is a matter of material quality, the losses due to the Auger effect are intrinsic and represent an open problem.

Much work was dedicated to improve the utilization of the solar spectrum by extension of the range of absorption, either by stacking materials with different band gaps, as in multi-junction cells or in quantum well solar cells, or by the use of fluorescent concentrators with specific absorption and emission in adjustable spectral ranges. Absorption in thin structures is enhanced by the use of back mirrors or distributed Bragg reflectors, which also solves the problem of radiative losses in terms of reabsorption. More challenging is the issue of carrier thermalization: to utilize the hot carriers, cooling by optical phonons has to be suppressed, which can in principle be achieved via phonon dispersion engineering; moreover, carriers have to be extracted in a very narrow energy range, requiring energy selective contacts, as could be provided by the discrete spectrum of quantum dots. A different approach to high efficiency solar energy conversion aims not at the losses, but the generation efficiency: in the multiple-exciton generation or carrier multiplication concept, an internal quantum efficiency $IQE > 1$ is achieved, i.e. more than one electron-hole pair is created per incoming photon.

All the above high-efficiency concepts have in common that they rely on quantum effects in low dimensional semiconductor nanostructures. To theoretically assess the photovoltaic properties of such nanostructures, the use of modern solid state theory is indicated, similar to the situation in the fields of solid state laser and quantum transport theory, which are both well developed and can now provide the required theoretical concepts and tools. This

sets the wider frame for this thesis: it is a first step towards a comprehensive microscopic theory of the photovoltaic processes in structures that are governed by quantum effects due to their dimensionality and spatial extension, and can therefore not be described by the conventional models used in macroscopic bulk photovoltaics.

In this thesis, the novel theoretical approach, based on the non-equilibrium (or Keldysh) Green's function formalism, is developed on the example of the quantum well solar cell, which by itself is of considerable interest, both from a technological point of view, since it represents a type of high efficiency concept that can be realized, and within a wide range of fundamental research, where it has been the subject of numerous experimental and theoretical investigations.

1.2 Outline

This thesis is organized as follows: in a first part, the basic principles of quantum well photovoltaics are introduced, together with an overview of existing experimental and theoretical work and the principal open questions in this area of research. The discussion is then focused on the requirements that a comprehensive microscopic theory should meet in order to accurately describe the systems under consideration, and the conclusions are used to motivate our choice of theoretical framework.

In a second part, the theoretical framework is introduced and set up, from the concept of non-equilibrium Green's functions to the corresponding formulation of quantum transport and the application to device-modelling, including the system partitioning, self-energy representation of interactions, coupling to extended contacts, basis functions and the self-consistent solution procedure.

The third part presents and discusses the application of the approach to the quantum well solar cell system. After identification of the required ingredients, i.e. the dominant interactions, these are discussed separately: the coupling of carriers to photons and phonons, responsible for absorption, photogeneration, radiative recombination and relaxation, respectively, is studied in detail, whereas non-radiative recombination is touched only briefly.

In the last part, the results of the numerical implementation for a number of specific bulk and quantum well structures are presented in order to illustrate the kind of information and insight provided by this approach. Besides an evaluation of the characteristic macroscopic and spectral quantities like, e.g. local density of states, carrier and current densities, electrostatic potential and internal field as well as entire IV-characteristics for

bulk and single-quantum well devices, the impact of geometry on absorption and transport in coupled quantum well structures is investigated.

Chapter 2

Quantum well solar cells

Abstract In this chapter, the basic principles and features of quantum well solar cells (QWSC) are reviewed. After a very short introduction to the basics of semiconductor $p(-i)-n$ junction based solar cells, the use of quantum wells to enhance conversion efficiency is motivated, and an overview over the achievements of QWSC research is given. From the open questions identified in the present status of QWSC research, the requirements for a novel and predictive QWSC theory are formulated, and a promising candidate is proposed.

2.1 Principles of photovoltaic energy conversion

The high demand for clean electricity has in last years led to a great diversity of solar energy conversion concepts. Although very different in appearance and use of materials, they are all based on the same principal mechanisms, which are: 1. *electron-hole pair (exciton) generation* via absorption of photons, and 2. *charge separation* at carrier selective contacts in order to generate a photovoltage that provides power by driving current through a load. To deal with all the specialities in the realization of these processes within the different concepts is beyond the scope of this thesis. We will therefore focus on the mechanisms in conventional crystalline semiconductor solar cells based on bipolar junctions, which form the basis of more advanced devices including quantum wells.

2.1.1 Crystalline bulk $p(-i)-n$ junction based solar cells

Fundamental processes

In this prototype of bulk semiconductor solar energy conversion device, shown in Fig. 2.1 electron-hole pairs (or, more precisely, excitons) are created by the promotion of an electron from the valence band to the conduction band via the absorption of a photon. Only photons with energy exceeding the band gap value are absorbed. Quickly ($\sim fs$) after being generated, the carriers relax to the corresponding band edge due to scattering among themselves and with lattice vibrations, the phonons. This *thermalization* process stops once the carriers have reached the band edge, since there are no lower energy states into which to relax, unless there is a channel for interband transitions, i.e. electron-hole *recombination*. There are indeed two main categories of such processes, in which the electron-hole pair is annihilated, which however are much slower than thermalization ($\sim \mu s$): *radiative* recombination, i.e. via the emission of photons, which is nothing else than the inverse process of photogeneration, and *nonradiative* recombination, via *trap* states in the bandgap (SRH: Shockley-Read-Hall [3, 4]) or the *Auger* process [5], where the energy freed by the annihilation of an electron-hole pair is used to promote an electron in the conduction band (or a hole in the valence band) to an excited state. Charge separation and carrier selective contacts are obtained by the use of diodes, i.e. $p-n$ or $p-i-n$ junctions, where in the latter, to increase the width of the depleted layer, an intrinsic region is inserted between the highly doped emitter and base, respectively. The built-in field originating in the asymmetric doping leads to a net *photocurrent* I_γ due to the drift of photogenerated carriers.

Current-voltage characteristics

From the electric circuit point of view, a solar cell is equivalent to a current generator in parallel with an asymmetric, non-linear resistive element (diode) [6]. At zero voltage, the cell under illumination produces what is called the *short circuit current* I_{sc} (zero load resistance), with the corresponding *current density* $J_{sc} = I_{sc}/\mathcal{A}$, where \mathcal{A} is the cell area. The short circuit current depends on the spectrum of the incident light via the spectral photon flux density ϕ_s and the *external quantum efficiency* $EQE(E)$ of the cell,

$$J_{sc} = q \int \phi_s(E) EQE(E) dE, \quad (2.1)$$

where q is the electron charge, $\phi_s(E)$ the number of photons in the energy range $[E, E + dE]$ incident per unit area and unit time, and $EQE(E)$ the probability that an incident

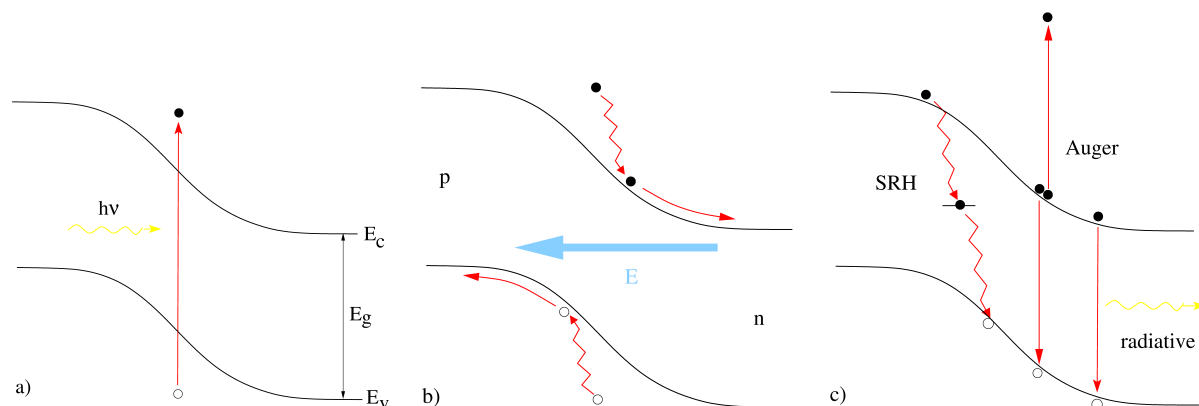


Figure 2.1: *Generation, transport and recombination processes in bulk p-n solar cell: a) The energy $h\nu$ of an incident photon is used to promote an electron from the valence band (represented by the band edge E_v) to the conduction band (with band edge E_c), thus creating an exciton, which quickly dissociates in an electron-hole pair; b) The photogenerated carriers quickly thermalize to the band edges by giving up the excess energy $h\nu - E_g$ to phonons (heat), and are swept out to the contacts by the built-in field \mathcal{E} of the junction; c) Before the carriers reach the contacts, they may recombine, either non-radiatively via trap states in the band gap (SRH) or the Auger process, where the electron-hole pair energy is used to highly excite a second electron in the conduction band (or a second hole in the valence band), or radiatively, via the emission of photons with energy $h\nu \approx E_g$.*

photon of energy E will deliver one electron to the external circuit. The external quantum efficiency depends upon the absorption coefficient, the efficiency of charge separation and the efficiency of charge collection, and is also called the *spectral response* (SR) of the cell. The latter two efficiencies are sometimes combined into an *internal quantum efficiency IQE*, which quantifies probability that a photogenerated electron (hole) will be delivered to the circuit.

In order to do work, the solar cell needs to operate at finite voltage V , since the *power density* of the cell is given by the product $P = J \cdot V$. At non-vanishing load resistance, the potential difference that develops between the terminals of the cell generates a current in the opposite direction of the photocurrent, reducing the total current. This reverse current is similar to the current which is generated in the case where the terminal voltage is not due to external illumination but to external (forward) bias, and it is therefore referred to as *dark current* I_d . In solar cells, this current also contains a contribution due to recombination which increases with voltage, and in the limit of strong external biasing, the device can even start acting as a light emitting diode [7]. The dark current density is often approximated by the non-ideal diode current, which as a function of terminal voltage

is given by

$$J_d(V) = J_0 (e^{qV/mk_B T} - 1), \quad (2.2)$$

where J_0 denotes the reverse saturation current, and m is the *ideality factor* lying typically between 1 (ideal diode) and 2 (effects of non-radiative recombination). In the superposition approximation, the net, or total current of a solar cell is obtained as the sum of the two currents, with the density

$$J(V) = J_{sc} - J_d(V). \quad (2.3)$$

Since dark current has the opposite sign of photocurrent¹, there is a voltage where the currents compensate each other, which is called the *open circuit voltage* V_{oc} , since it corresponds to the voltage that is developed when the terminals are isolated (infinite load resistance). In the ideal diode model, this voltage is given by

$$V_{oc} = \frac{k_B T}{q} \ln \left(\frac{J_{sc}}{J_0} + 1 \right). \quad (2.4)$$

More realistic estimations of V_{oc} e.g. taking into account the intrinsic Auger effect [8, 9], are of the form

$$V_{oc} \approx \frac{3k_B T}{2q} \ln \left(\frac{J_{sc}}{J_0} \right). \quad (2.5)$$

The variation of total current with terminal voltage as given by Eq. 2.3 provides the *current-voltage* or *IV-characteristics*, which corresponds to a fingerprint of the solar cell and allows a direct evaluation of the cell quality. It is shown qualitatively in Fig. 2.2 for the case of dark current given by Eq. 2.2.

The most important among the properties of a solar cell is the total energy conversion *efficiency* given by the ratio of electrical output power density P to the incoming irradiation power density P^γ . The highest efficiency is reached at the *maximum power point* (MPP) given by the set (J_m, V_m) that defines the rectangle inscribed to the *IV-curve* with the largest area. The ratio between the area of this rectangle and that of the one circumscribed to the *IV-curve*, i.e. the rectangle defined by (J_{sc}, V_{oc}) , is quantified by the *fill-factor*

$$FF \equiv \frac{J_m V_m}{J_{sc} V_{oc}} < 1. \quad (2.6)$$

A reduced fill-factor is an indicator of loss processes. Maximum efficiency is thus given by

$$\eta = \frac{J_{sc} V_{oc} FF}{P^\gamma}. \quad (2.7)$$

¹In photovoltaics, the sign convention for current and voltage is such that the photocurrent is positive. This relocates the *IV-curve* with positive output power in the first quadrant of the *IV-plane*, as shown in Fig. 2.2.

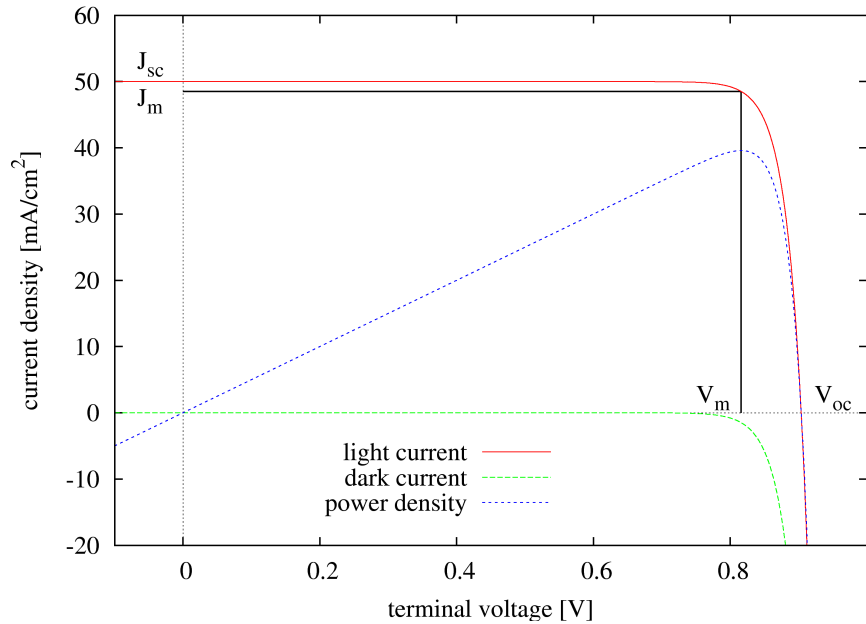


Figure 2.2: Typical current-voltage characteristics (*IV-curve*) of a bulk *p-i-n* diode, with the short circuit current J_{sc} , the open circuit voltage V_{oc} and the maximum power point *MPP* defined by the corresponding current J_m and voltage V_m .

The upper efficiency limit of such a solar cell is given by the Shockley-Queisser detailed balance limit [10], which is around 31% for a single band gap and unconcentrated sunlight. One of the main reasons why this value is so low is the fact that only the small part of the solar spectrum in the close vicinity of the energy of the band gap is fully utilized: lower energy photons are not absorbed, and higher energy photons lose their excess energy to phonons. Fig. 2.3 shows the the global air mass 1.5 solar spectrum² and its utilization by a crystalline silicon solar cell. Unfortunately, a lower band gap leads to a lower V_{oc} , which might outweigh the gain in J_{sc} due to the extended absorption range. To conceive a device that would allow higher conversion efficiencies through the possibility of separate optimization of the factors determining current and voltage was one of the main motivations behind the development of the quantum well solar cell [11].

²The air mass value describes the light attenuation due to the passage through the atmosphere at a specific solar zenith angle, 48.19°s in the case of AM 1.5.

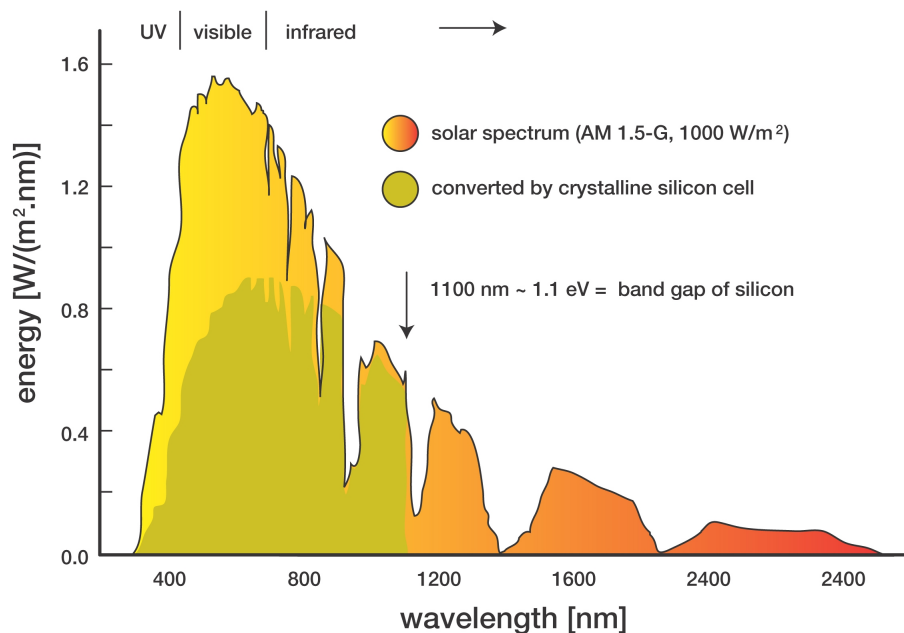


Figure 2.3: Solar global air mass 1.5 spectrum and utilization by a crystalline silicon solar cell. The terrestrial solar spectrum is highly structured due to many infrared absorption bands. From [12].

2.2 Quantum well solar cells

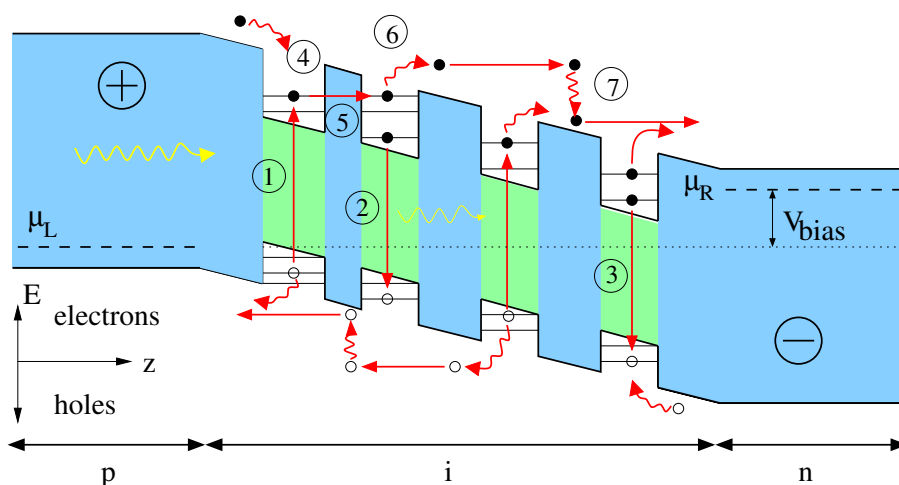
2.2.1 Basic principles, structure and processes

Quantum well solar cells were originally proposed as an alternative to multi-junction devices, with the advantage of absent current matching and lossy interconnection problems. In this device, to make better use of the solar spectrum, the absorption range is extended to longer wavelengths by the insertion of quantum wells made of low band-gap material (e.g. GaAs) in the intrinsic region of a $p-i-n$ diode made of a higher band gap material (e.g. $\text{Al}_x\text{Ga}_{1-x}\text{As}$ with $x > 0$).

A typical QWSC is shown schematically in Fig. 2.4. Valence band electrons are excited by incoming photons across the band gap, creating electron-hole pairs both in the quasi-continuum and in the discrete confined states of the quantum wells. From there, the photogenerated carriers escape via tunneling or thermionic emission and are swept out by the electric field determined by the built-in and the applied bias. On their way to the contacts, carriers relax towards lower energy states due to scattering, e.g. with polar optical phonons, and some are lost due to radiative and nonradiative recombination (SRH

and Auger).

Since these processes have a direct impact on the photovoltaic performance of the structure, many of them have been investigated in great detail. In the next section we will thus summarize the corresponding results obtained by different research groups.



Generation and recombination

1. Photogeneration of electron-hole pairs
2. Radiative recombination
3. Nonradiative recombination
(Auger, trap/SRH)

Transport

4. Carrier capture
5. Resonant and nonresonant tunneling
6. Thermal escape and sweep-out
by built-in field
7. Relaxation by inelastic scattering
(optical phonons)

Figure 2.4: *Characterizing structure and processes of a p-i-n QWSC. Under operating conditions, the terminal voltage V_{bias} corresponds to the separation of the chemical potentials μ_L and μ_R of the left and the right contacts, respectively.*

2.2.2 Material systems and experimental realizations

Since efficient absorption in the thin quantum well region is crucial, direct gap semiconductors are preferred over indirect ones. For that reason, most optoelectronic devices are made of binary III-V direct band gap semiconductors like GaAs, GaN, InAs or InP, and their ternary and quaternary alloys, e.g. $Al_xGa_{1-x}As$ or $In_xGa_{1-x}As_yP_{1-y}$. Quantum well structures are obtained as heterostructures from alloys of differing band gaps. The band offsets, which determine the depth of the wells or height of the barriers, respectively, are

controlled by the alloy fraction. The quantum wells used in QWSC are of type I, i.e. the offset has the same sign for all the bands, and the direct band gap favours optical transitions.

The first QWSCs were based on GaAs-Al_xGa_{1-x}As heterostructures, due to the vast amount of experimental and theoretical characterization data for this material owing to its widespread use in other optoelectronic device applications, such as lasers and optical modulators. As shown in Fig. 2.5, these compounds offer the advantage of perfect lattice-matching, however, the low quality of the GaAs-Al_xGa_{1-x}As interfaces turned out to be a performance-limiting factor, and the available range of band gaps is not well matched to the solar spectrum, since the optimum band gap value is exceeded already in GaAs. Better matching could be achieved by replacing the Aluminum with Indium, but at the price of introducing strain due to the lattice-mismatch, which limits the number of quantum well layers that can be grown without dislocations [13]. The problem of strain can be avoided using strain-balanced heterostructures [14, 15, 16, 17, 18]: in these materials, the tensile strain in a material grown on a substrate of larger lattice constant is compensated for by the compressive strain in a material of lattice constant exceeding that of the substrate, as in the example of the QWSC with GaAsP barriers and InGaAs wells grown on a GaAs substrate that was developed by the Imperial College group. These strain-balanced QWSC were also proposed as a replacement for GaAs in GaAsP/GaAs tandem cells, since they allow for perfect current matching at a suitable effective band gap.

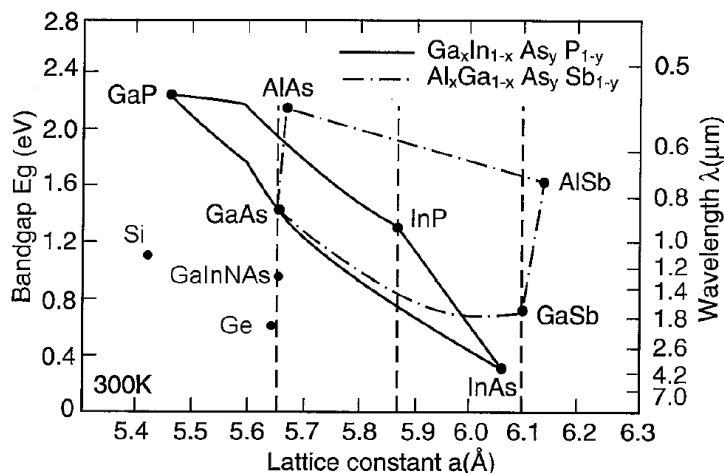


Figure 2.5: Band gap vs. lattice constants of some binary III-V compounds. From [14].

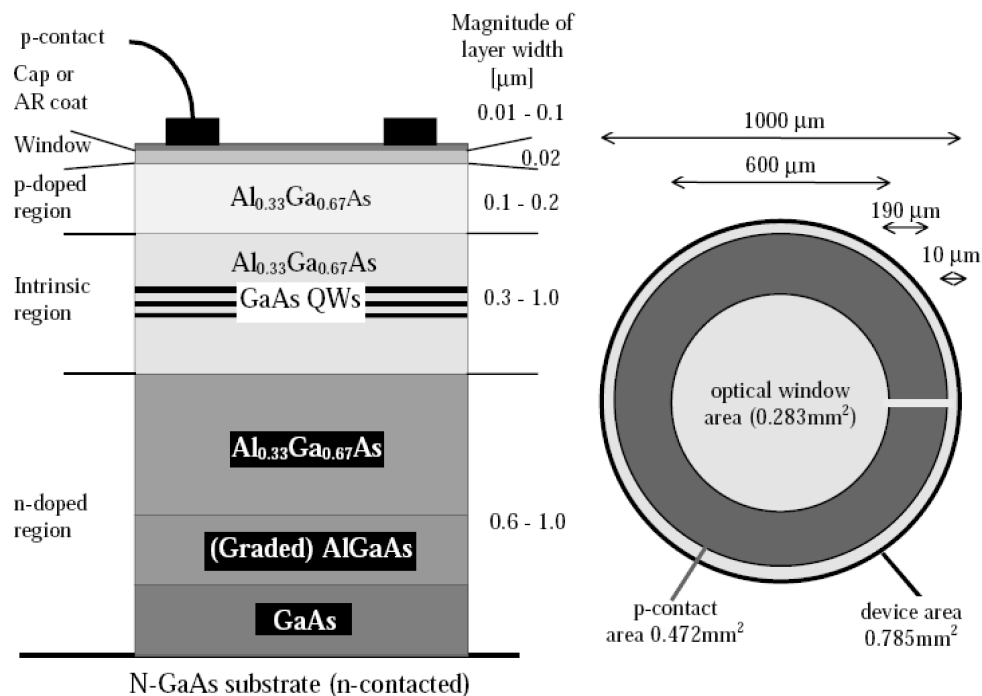


Figure 2.6: Typical device configuration of a practical QWSC. Taken from [19].

QWSC, like other thin film multilayer devices, are usually manufactured using epitaxial growth techniques such as metallorganic vapor phase epitaxy (MOVPE) or molecular beam epitaxy (MBE). MOVPE consists in passing reactant chemicals at atmospheric pressure in vapour form over a heated substrate. The precursor gases dissociate at the surface of the substrate, depositing atoms at the rate of about one monolayer per second. The high deposition rate makes MOVPE an attractive candidate for large scale solar cell production. However, compositional control does not reach the precision of e.g. MBE, and there is the problem of high unintentional background doping, which can be detrimental to solar cell performance. In MBE, collimated beams of molecules are directed onto a heated substrate situated in an ultra high vacuum growth chamber. The molecular beams are generated in heated crucibles, which contain the precursors in solid or liquid form. Evaporation produces the molecular beam. The molecules dissociate at the surface of the substrate, depositing the metal atoms. Compositional control is achieved by changing the temperature of the solid sources. Very sharp compositional changes of the order of a monolayer are possible simply by placing a shutter in front of any given source. The sample is generally rotated during growth to ensure uniform growth across the wafer. MBE grown samples are very well characterizable and of higher purity, but also substantially

more expensive than those made by MOVPE.

Before the epitaxial structures are of any use as solar cells, they need corresponding processing. In the case of QWSC, usual processing steps include photolithography and etching of the sample to obtain circular mesa photodiodes, followed by the addition of anti-reflection coating, front surface ring contacts and a back surface mirror. A typical device configuration is shown in Fig. 2.6 [19].

The last step before research based on the grown devices can start is the characterization of the latter. This includes measuring the dark-IV profile and the quantum efficiency. Background doping and field dependencies in the QE can be probed qualitatively using monochromatic-IV measurements and fill-factors are determined via IV measurements under illumination. MQW width and composition are obtained from low temperature photocurrent, while X-ray diffraction together with transmission electron microscopy provides a means for determining the barrier thickness. To assess the crystalline and structural quality of the MQW regions, electron beam induced current microscopy is used [14].

2.2.3 Optical and electronic properties

MQW *p-i-n* diodes have been studied extensively in the reverse bias regime for optoelectronic applications [20, 21, 22]. Solar cells however, to deliver power, need to be operated in the forward bias - reverse current regime, hence under conditions that had barely been considered before [23].

There are two main categories of properties that need to be quantified in order to characterize a quantum well solar cell: the *optical* and the *transport* properties. As in any solar cell, the optical properties can be modified via light-management techniques reducing reflection and reemission and enhancing the light-incoupling via anti-reflection coatings, backreflectors and light-trapping textures [24], allowing for an efficient photon recycling [25, 26]; however, these measures do not take advantage of the specific spatial and electronic structure of QWSC, and will therefore not be considered further here.

Absorption in quantum wells

The one optical property that is strongly modified in QWSC due to the presence of quantum wells is the absorption and the luminescent emission of light within the cell. This fact is also exploited in other optoelectronic devices such as interband QW-lasers, superlattice *p-i-n* photodetectors and optical modulators [27, 20]. Compared to continuum absorption in bulk, absorption in quantum wells reflects the lower dimensionality of the density of

states participating in the optical transitions, which is reduced due to one-dimensional confinement; in the case of type I quantum wells³ it also shows stronger excitonic contributions due to larger overlap of electron and hole wave function as a consequence of spatial localization [28], and the absorption edge is shifted towards larger photon energies, the size of the shift depending on the geometry (width and depth) of the well. The built-in field of the *p-i-n* diode, which is required to lie above a critical value for efficient carrier extraction, affects the absorption via the *quantum confined Stark effect* (QCSE), decreasing the electron-hole overlap (Fig. 2.7) and redshifting the confinement levels [29, 30, 31].

Carrier escape from quantum wells

Efficient carrier escape from the quantum wells is one of the main premises for high photovoltaic performance, since for a contribution to photocurrent, the carrier sweep-out rate must exceed the recombination rate in the well. Two principle escape mechanisms have been identified: thermal emission over and tunneling through the confining barrier, where the latter can be assisted thermally or by scattering with phonons [20] or ionized impurities [32]. Both mechanisms depend on material properties and design parameters like width and depth/height of the wells/barriers as well as on external factors like electric field and temperature. In the case of thermionic emission, the escape rate increases with lower barrier and higher temperature [33], where the field dependence enters via the barrier height. Tunneling escape is determined via the quantum-mechanical transmission through the finite height barrier and increases for decreasing barrier thickness, as a consequence of weaker confinement that leads to broader levels corresponding to a shorter lifetime, and growing fields enabling Fowler-Nordheim tunneling [20].

To study carrier escape mechanisms in QWSC, combined temperature and bias dependent photoluminescence and photocurrent studies on *p-i-n* diodes with single quantum well (SQW) [34, 35, 36, 37, 31], double quantum well (DQW) [38] and multi-quantum well (MQW) or superlattice (SL) [39, 40, 41, 29, 42, 43] structures were performed. At very high fields corresponding to reverse bias condition, carrier escape is maximum, since the effective barrier is both narrow and low. At low fields corresponding to forward bias, i.e. for the situation that is relevant for photovoltaic operation, three temperature regimes with specific prevailing carrier escape channels have been established:

1. At very low T, tunneling dominates, since on one hand, there is no significant thermal population of higher levels near the top of the well that would allow thermal emission, and on the other hand the coherence length is increased;

³Unless otherwise stated, the quantum wells that are discussed are of type I.

2. At intermediate T , tunneling becomes thermally assisted, via phonons or ionized impurity scattering;
3. At high (room) temperature, escape is practically purely thermal and leads to an internal quantum efficiency close to unity except for very deep wells [34, 44].

In SQW, tunneling escape is suppressed due to the single large triangular barrier (see, e.g., Fig. 2.7), whereas in DQW and SL, tunneling between adjacent wells is possible and can lead to resonant enhancement of the photocurrent response in properly adjusted barrier-well geometries [11, 45, 38, 41]. In the case of SL with deep wells, resonant tunneling can even become the only efficient escape channel. Resonant tunneling can be either sequential, which requires a sequence of appropriately tuned wells to align the subband levels [11, 45], or involve energy relaxation via inelastic scattering, in which case a non-sequential resonant tunneling process is possible in a regular superlattice [41]. The latter approach has the advantage that tunneling transport is not limited to a few wells and does thus not require the combination of several such periods to obtain sufficient absorption, which would lead to losses due to carrier recapture in subsequent periods. The high efficiency of thermal escape at elevated temperature leads to a favourable temperature dependence of the overall efficiency of the QWSC, which, together with the tunability of the effective band gap via the well width, makes it a suitable candidate for thermophotovoltaic applications, where broadband blackbody radiation is converted into low energy narrowband radiation via a selective emitter [46, 47].

In a steady state situation, in order to conserve current, the carrier species specific escape rates $R_i = \rho_i/\tau_i$, where ρ_i is the carrier density in the quantum well and τ_i the escape lifetime, have to be identical for electrons ($i = e$) and holes ($i = h$). The escape lifetimes strongly depend on band offset and effective masses and differ thus considerably for electrons, light and heavy holes. This leads to an imbalance in the densities of electron and holes, i.e. to an effective charge build-up in the quantum well region that screens the field and hence affects the carrier sweep-out, inhibiting the escape of the faster carrier while enhancing that of the slower carrier [31]. Since both radiative and nonradiative recombination depend on the availability of electron-hole pairs, these processes are controlled by the smaller of the species densities, which in turn corresponds to the carrier species with the fastest escape. In the GaAs-Al_xGa_{1-x}As system with $x < 0.4$, escape is dominated by light holes, which have both low confinement and low effective mass. It was found that the sequence of the subsequently escaping carriers strongly affects the output voltage due to enhanced screening in the case where heavy holes escape prior to electrons [43]. In the InP-InGaAsP with high enough Indium content, the valence band offset exceeds that of the conduction band and escape becomes dominated by electrons [39].

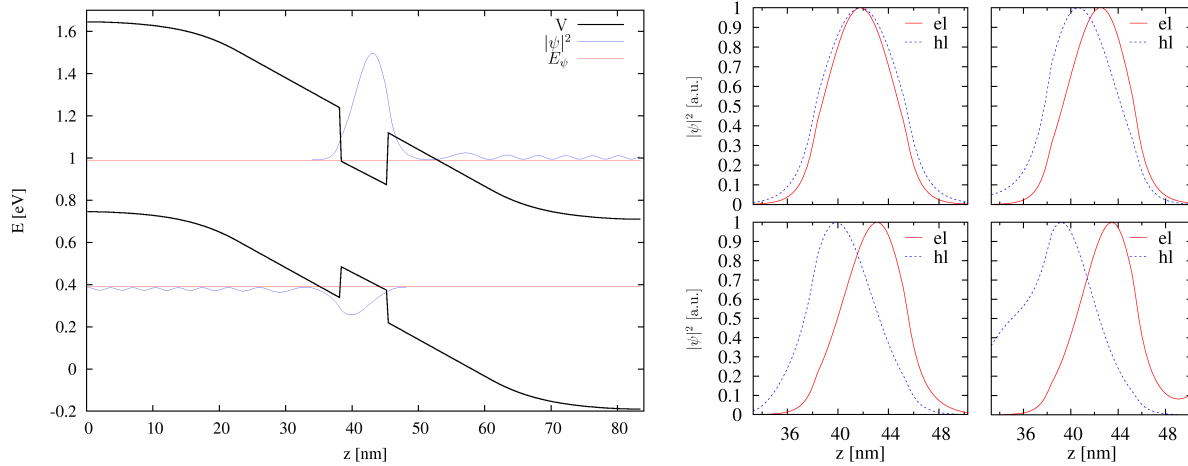


Figure 2.7: (Left) Lowest quasi-bound states in a SQW p - i - n diode; the oscillating wave function tail leaking out of the well illustrates the effect of open boundaries. (Right) The effect of the field on the overlap of the electron (el) and hole (hl) wave function (normalized to unity) of the lowest quasibound state in the QW region (quantum confined Stark effect).

In the case of MQW and SL, carriers that have escaped can be recaptured by subsequent quantum wells. This process is highly desired in light emitting devices, but not in solar cells, since captured carriers are more likely to recombine. Carrier capture rates depend on the available scattering mechanisms (mostly optical phonons), the energy of the unbound carriers and the density of states near the top of the quantum wells, which are related to the structure parameters of barriers and wells [48, 49, 50, 51]. The capture times are usually much smaller than the escape times.

Recombination in quantum wells

In quantum wells at room temperature, both radiative and nonradiative recombination is important [52, 34]. As compared to bulk solar cells, recombination is enhanced due to spatial localization of the carriers [53]. The radiative lifetime increases with temperature as a consequence of the spread in exciton linewidth [54, 55] and decreases with field owing to the shrinking electron-hole overlap, i.e. larger spatial separation of the exciton constituents [56, 53, 57, 58].

Nonradiative recombination in practical QWSC is primarily of the Shockley-Read-Hall type due to appearance of trap states at non-perfect interfaces. It depends on both electron and hole densities and is strongest where they are equal, which in a symmetrically doped p - i - n structure is the case in the center of the intrinsic region, and it can thus be

advantageous to locate the QWs at the edge of this region [59]. Although Auger recombination is an intrinsic loss process, it is estimated to be of minor importance in practical QWSC based on direct gap materials, except for high carrier densities at large forward bias. However, it is the only non-radiative recombination mechanism that needs to be considered in calculations aiming at the ultimate efficiency limit of QWSC. Generally, Auger recombination is more important for low band gap materials and under high injection conditions as prevailing in concentrator systems. The use of SB-QWSC allows to reduce Auger recombination due to lower effective valence band mass, which leads via the smaller asymmetry between electron and hole mass to lower injection at a given separation of the quasi-Fermi levels as compared to unstrained bulk material of the same band gap [46, 60]. Efficient carrier escape reduces both radiative and nonradiative recombination by lowering the carrier population and the degree of localization [61]. In the case of resonant tunneling escape, a reduction of radiative recombination at the resonance due to enhanced carrier escape was observed [40, 41].

Spectral response

The optical and transport properties discussed above are reflected in the spectral, or photocurrent, response (SR) or the related external quantum efficiency, as defined in Eq. (2.1), which represents one of the main footprints of a QWSC that is experimentally accessible. As compared to bulk, the contribution to the photocurrent from the intrinsic region includes a long wave-length component from the quantum well absorption, displaying the characteristic step-like shape and pronounced excitonic peaks right below the subband edges. Carrier capture appears in the SR as a small decrease in the current at wavelengths corresponding to energies above the well, i.e. to barrier contributions. Fig. 2.8 (left) shows a typical SR measurement.

2.2.4 Current-voltage characteristics

The most important, but also most complex characteristics, are provided by the current-voltage relation of a QWSC device, since both current and output voltage are affected by the presence of quantum wells.

Dark current

As in bulk solar cells, dark current contains components from radiative and nonradiative recombination as well as from the diode current driven by terminal voltage. Since the

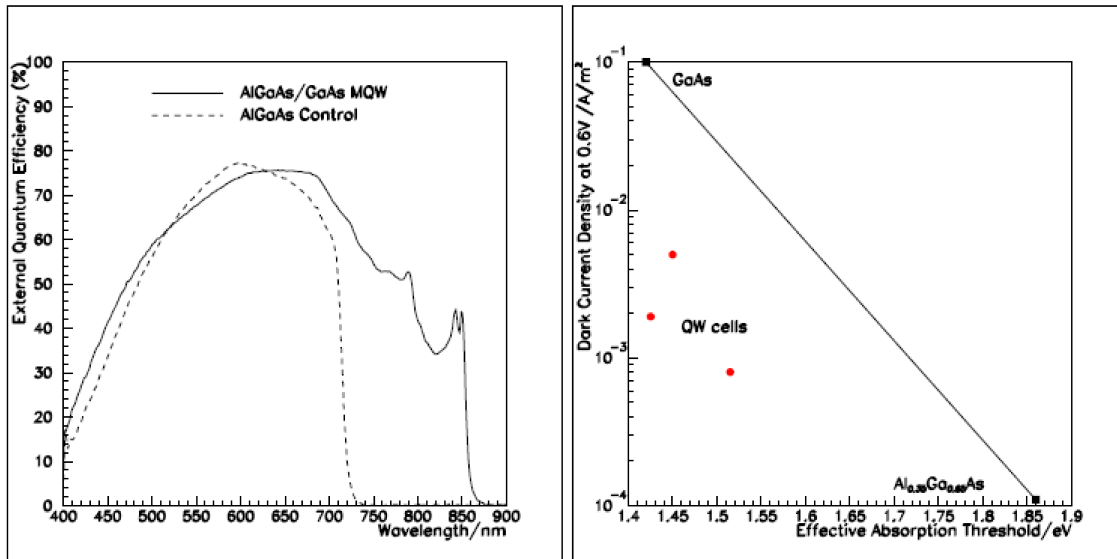


Figure 2.8: *Left: spectral response of a typical QWSC, exhibiting the gain in photocurrent due to the extended absorption range, and the change in the dimensionality of the joint density of states in the spectral region of confined states; Right: measured QWSC dark currents, which are consistently below the linear interpolation of the bulk control indicating the expected value for the corresponding effective absorption edge. From [14].*

radiative dark-current level depends on the intrinsic carrier concentration of the material, dark currents of the QWSC samples were expected to lie below those of the control samples formed from the well material, but above the ones of the barrier control, which was confirmed experimentally [62]. The same argument explains the higher dark currents in wide wells as compared to narrow ones, since weaker confinement leads to a lower effective band gap. However, it was found that QW devices have a dark current more than an order of magnitude lower than the corresponding control samples, i.e., the dark currents are significantly better than would be expected for homogeneous cells with the same effective band gap. This was explained with a suppressed radiative recombination due to efficient carrier escape, as discussed above. It means that there is indeed an increase in dark current by insertion of QW, but not to the extent as to be expected from the lower band gap, as shown in Fig. 2.8 (right). Radiative dark currents can be further reduced via photon-recycling mediated by distributed Bragg-reflectors (DBR).

Dark currents in practical QWSC under unconcentrated illumination have ideality factors near 2, which indicates that, as expected for these materials, the forward dark bias is dominated by nonradiative (SRH) recombination in the QW. In high quality SB-QWSC and at high currents corresponding to concentrator conditions (high bias), there is a tran-

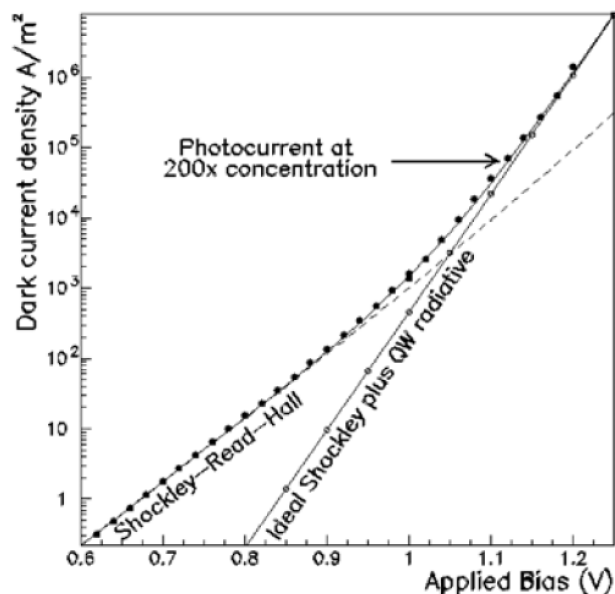


Figure 2.9: Dark current-voltage characteristics of a QWSC: for elevated currents (large bias) corresponding to high concentration, the ideality factor changes from 2 (non-radiative, SRH) to 1 (radiative, ideal diode current). From [64].

sition to ideality factor 1, expressing the fact that recombination starts to be dominated by the increase in radiative transitions that accompanies increased population of the QW subbands [63, 64, 65]. The bias dependent ideality factor observed in strained GaAs-InGaAs could be related to the bias dependent carrier trapping efficiency, which affects the recombination current.

Photocurrent

The increase of photocurrent by the use of quantum wells is the most obvious advantage of QWSC over bulk devices and was confirmed by many experiments [23]. It was also shown experimentally that increasing the number of wells increases the photocurrent linearly whereas dark current increases only sublinearly, and not linearly with the number of wells, due to increased recombination in wells and larger i-region (lower field) [66, 67]. This means that higher efficiencies should be possible with larger number of wells, which was found to be valid up to 50 wells [68]. At higher well numbers, even for the photocurrent growing faster than the dark current, increasing the well number requires longer intrinsic region which means lowering the field and therefore the collection efficiency, which finally results in a reduced overall efficiency.

Output voltage

Next to the short circuit current, which was shown to be enhanced in QWSC as explained above, a possible efficiency enhancement critically depends on the value of open circuit voltage, which was expected to decrease due to higher dark current from increased recombination in the wells. Soon after the demonstration of photocurrent gain, the group at Imperial College was able to show that practical QWSC can indeed have an improved voltage performance compared to conventional single bandgap cells with the same effective absorption bandedge [69]. For lattice matched materials, V_{oc} is related to design parameters like well width and alloy fraction, the latter determining the barrier height. For strained GaAs-InGaAs QWSC, the voltage performance depends on barrier width, since the latter determines strain relaxation and defect formation. In general, the voltage enhancement is larger than what would be expected from the shift in the absorption edge due to the effect of confinement in the wells. The voltage gain over the well material control cell is higher in SQW than in MQW because of the absence of carrier recapture. On the other hand, the decrease in V_{oc} with respect to the barrier material control is smaller than what is to be expected from lower effective band gap due to associated higher recombination, corresponding to the observed dark current behavior [62]. In shallow wells, the voltage decrease is relatively small due to the exponential dependence of radiative recombination on well depth. [70].

2.2.5 Efficiency

As stated above, the efficiency of semiconductor solar cells depends on the effective band gap for absorption, i.e. the energy difference between the highest states in the valence band and the lowest states in the conduction band. In QWSC, the depth and width of the quantum wells can be adjusted such that the effective band gap variation determined by the confinement levels covers the high efficiency region of the solar spectrum. Furthermore, as Barnham and Duggan suggested in their original proposal of the QWSC, an efficiency enhancement over bulk cells should be possible if photocurrent and dark current could be optimized independently, which they assumed could be the case in QWSC if dark current, or recombination, which determines V_{oc} , was primarily controlled by the barrier band gap, and the photocurrent by the effective band gap in the well region [11]. And indeed, the gain in additional photocurrent was demonstrated in several material systems to outweigh the drop in terminal voltage resulting from the increased dark current due to recombination of carriers trapped in the quantum wells, resulting in a higher overall conversion efficiency as compared to a bulk $p-n$ control cell made of the *barrier* material [23], even though

the original hopes concerning the magnitude of the voltage drop turned out to be too optimistic. In the meantime, due to progress in material science and device growth, a 50-well SB-QWSC with efficiency exceeding that of the GaAs well material control has been realized [62]. Due to these experimental findings it is now generally accepted that quantum wells can indeed enhance the efficiency of a solar cell in real, practical systems. However, the question whether the ideal quantum well solar cell can *in principle* achieve a higher efficiency than the ideal single junction bulk cell is still widely debated [71]. Soon after the first proposal of the concept, a detailed balance analysis was put against it that ruled out such a *global* efficiency enhancement in the radiative limit [72, 73, 74], predicting that the conversion efficiency of the quantum-well device would not exceed that of the base-line bulk device. However, the argument was based on the assumption of thermal quasi-equilibrium throughout the entire device, corresponding to constant quasi-Fermi level (QFL) separation given by the applied bias. The following debate led to a series of both experimental and theoretical investigations of QFL-separation (QFLS) in QWSC. On the experimental side, information about bias and temperature dependent QFL-splitting was obtained by fitting calibrated electroluminescence (EL) results for SQW and DQW in the dark to a generalized detailed balance luminescence spectrum depending on the QFL-separation [75, 61, 76, 77, 19, 78]. This procedure revealed both a variation from barrier to well and a significant reduction of the QFL-splitting in the well as compared to the applied bias, i.e. lower dark current was observed than predicted by constant QFLS, and also different QFLS in the two wells of asymmetric DQW (ADQW) systems. The effect was even more pronounced in dark current governed by nonradiative recombination, and it was attributed to suppressed recombination due to efficient escape of photogenerated carriers from the quantum wells, increasing the photocurrent at the expense of dark current and thus enhancing V_{oc} . In the ADQW system, the QFLS seemed to be sensitive to the coupling of the wells at low temperatures, i.e. in the tunneling regime. On the theoretical side, it was shown that efficiency enhancement could indeed be obtained from a QFL-variation [79]. Further theoretical work based on detailed balance with non-uniform QFL suggested that efficiency in multi-QFL systems could be drastically increased if photon-assisted escape were an effective mechanism [80, 81], which seems not to be the case for quantum well system due to the very low intra-subband absorption for the in-plane polarization that is dominant in QWSC. But again, by thermodynamical arguments it was reasoned that, given that the dominant escape mechanism is thermal and phonon-assisted, lower QFLS in the quantum well would lead to a flow of carriers into the well, eventually cancelling the QFLS-gradient [82]. Contrary to predictions based on the same arguments, the QFL-separation remained suppressed in PL experiments under illuminated conditions, which indicates that quasi-equilibrium thermodynamical models might not be able to properly

describe the non-equilibrium steady state carrier escape [83, 84]. Recent experiments suggest that the reduction in QFL-separation and the observed suppression of radiative recombination could be a *hot carrier* effect related to incomplete thermalization of the carriers in the quantum wells [63, 85, 86, 87]. Indeed, a lower quasi-Fermi level separation in the wells can be a stationary solution of the transport equations if the temperature of the confined carriers is higher than that of the lattice, so that a thermoelectric force causes a net flow of carriers out of the well [84].

2.2.6 Fundamental open questions

Although QWSC have been demonstrated to enhance efficiency in practical devices, it is still not clear where exactly the decrease in dark current originates. Concerning the theory of QWSC, two principal questions were raised by Anderson [71], namely

1. under what conditions are continuum thermodynamic models using quasi-Fermi distributions valid for the description of nonequilibrium nanostructures like QWSC under illumination and bias, and
2. to what extent do detailed-balance limits represent realistic target efficiencies in the case of multiband cells ?

To answer these questions, theories where the assumptions underlying the above models are relaxed should be devised and applied to QWSC to obtain a more realistic estimate of an upper bound to efficiency. This applies especially to the distribution of carriers in the quantum wells, which could correspond to higher temperatures or even be non-thermal, i.e. more comprehensive pictures should include both hot carrier and non-equilibrium effects.

Geometry effects

Another experimental evidence that requires further (theoretical) analysis is the impact of geometry on the photovoltaic performance of coupled quantum well structures: the fact that the insertion of quantum wells affects not only the absorption, but also the transport properties of the device has never been addressed thoroughly; the question therefore arises if the photovoltaic device performance cannot be optimized by making use of such design degrees of freedom like geometry and band-offsets, which can be controlled by suitable choice of alloys and alloy-fractions. The idea of a geometry related efficiency enhancement

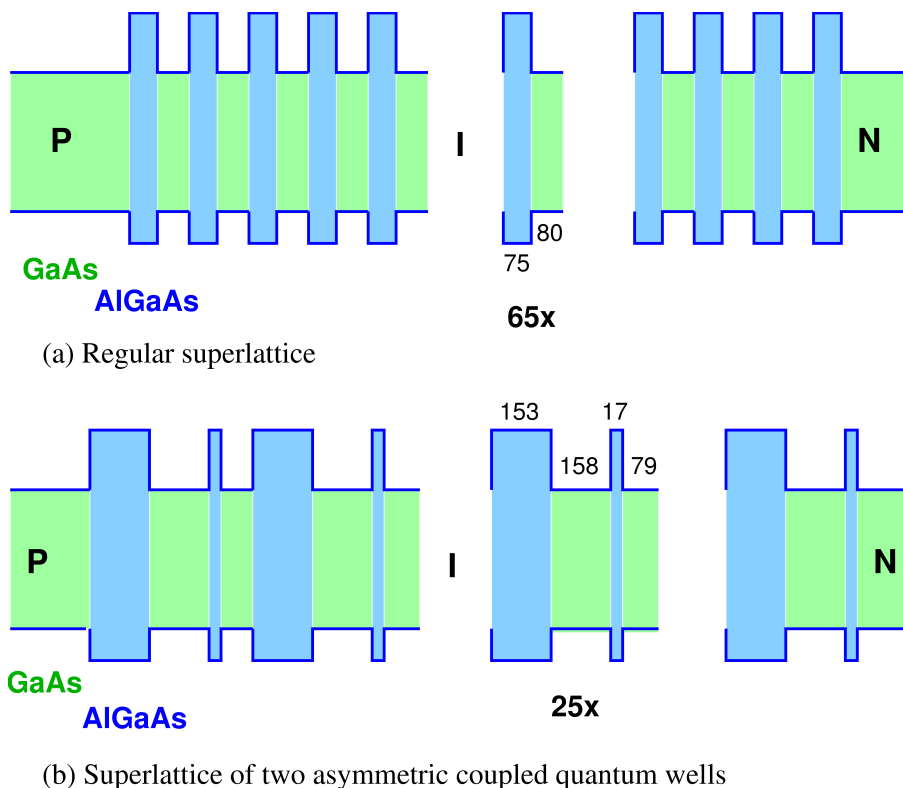


Figure 2.10: The two quantum well structures of different layer geometry investigated by Fox et al. [88]. The layer dimensions are given in Å.

via design optimization is supported by findings of several carrier escape studies on MQW and SL [88], and on ADQW [38, 37].

In the most striking example, Fox and coworkers compare temperature dependent current-voltage characteristics of two different MQW-geometries, shown in Fig. 2.10: a regular, weakly coupled superlattice on one side and a multi - quantum well structure of strongly coupled asymmetric quantum wells on the other side. The two structures show very dissimilar behavior at all temperatures (Fig. 2.11), with a much better performance of the asymmetric structure at room temperature forward-bias - reverse-current conditions, which is the relevant regime for photovoltaic applications. This indicates that even near the operating point of solar cells, i.e. at room temperature and moderate fields, where escape is believed to be entirely thermal, the shape and degree of spatial localization of the wave functions matters, and the structure parameters determining these properties should therefore be chosen to maximize escape and minimize recombination. Such an optimization requires a deeper insight into the nonequilibrium quantum kinetics of confined carriers and the ways these are affected by the variation of design parameters and external conditions.

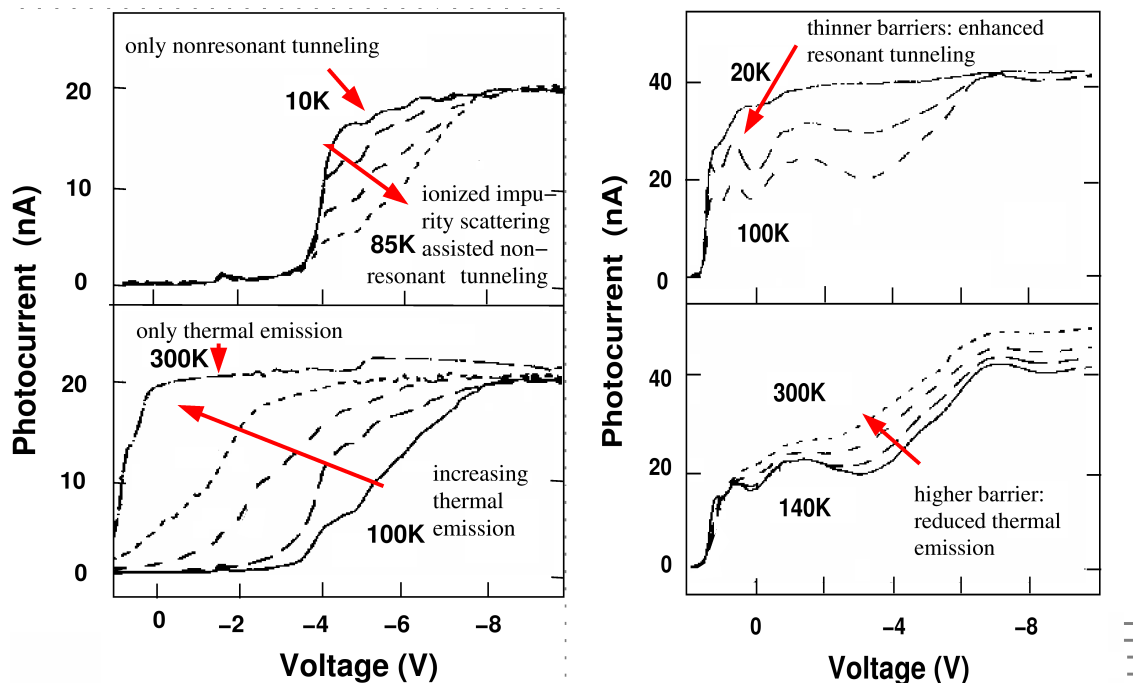


Figure 2.11: Temperature dependent current-voltage characteristics of the quantum well structures in Fig. 2.10. The most interesting feature from the photovoltaic point of view is the much better room-temperature fill-factor in the forward bias regime relevant for photovoltaic applications observed in the asymmetric coupled sample (left) as compared to the one of the regular superlattice. The arrows indicate the effects of dominant escape mechanisms.

2.3 Theoretical models for QWSC

The need for optimized MQW design and the fundamental issues about global efficiency enhancement made the experimental QWSC development be accompanied by a constant modelling effort.

The many different models for QWSC can be roughly categorized in two classes: Thermodynamic or detailed-balance theories, and models based on analytical or numerical solution of the semiconductor transport equations including the source and sink terms for carrier generation and recombination, respectively. While the former rely on highly idealized assumptions and therefore primarily provide upper limiting efficiencies, the latter describe more realistic situations including an estimate of the relevant loss processes and aim at reproducing real device characteristics. Representatives of both categories will be briefly reviewed below.

2.3.1 Thermodynamic and detailed-balance theories

This type of limiting efficiency analysis dates back to the landmark paper of Shockley and Queisser [10], where the current from solar cell with only radiative recombination is calculated as the difference between absorbed flux and emitted radiative flux, making use of the principle of *detailed balance*. This approach assumes infinite mobility corresponding to a constant QFL separation, vanishing reflectivity, complete transparency for photon energies below the band gap and complete absorption for photon energies above it. The original formalism for single junction bulk devices was extended by Henry [89] to the case of multiple band gaps. The detailed balance approach of Corkish and Green [90] treated the QW as an incremental cell in addition to the baseline high bandgap bulk cell, but without any coupling between the two and in a field-free limit. V_{oc} and I_{sc} were then obtained from the superposition of baseline and incremental cell. Araújo and Martí [72] generalized the detailed balance analysis further, taking into account the light path in the device, variation of refractive indices and the angular range of incident and emitted radiation, and showing that for constant QFLS, the emissivity equals the absorptivity, with the consequence that within this limit, QWSC could not exceed the efficiency of an ideal homojunction device. The model of Bremner, Honsberg and Corkish [80], based on ideas proposed by Kettmann and Guillemoles [79], allowed for QFL variations under assumption of radiative transitions between the different levels, which yields considerable efficiency increase, but might not be applicable to the case of QWSC, due to the very small intraband transition matrix elements for in-plane polarization. The origin of the variation in QFLS is not contained in the model, i.e. the QFLS-step is not an emergent feature of the theory.

2.3.2 Macroscopic continuum and hybrid transport models

A simple and intuitive ideal QWSC model was presented by Anderson [91]: his approach, which in philosophy is similar to the model of Corkish and Green [90], is based on the ideal diode current-voltage characteristics for bulk homojunctions, with the quantum well material accounted for by enhancement factors for oscillator strength and DOS, providing the modifications of generation and recombination. The effects of QWs on transport properties are not considered.

Apart from the experimental confirmation of practical effectiveness of QWSC, the group at Imperial College produced also a number of modelling approaches of increasing complexity and comprehensiveness [92, 93, 94, 59, 95]. In their approach, dark currents are obtained by analytical or numerical solution of the electron and hole drift-diffusion equations including

the terms for generation and recombination and the coupling to Poisson's equation. The carrier density is expressed in terms of the corresponding quasi-Fermi levels. In the case of QW, the density is modified by an additional factor to adjust to the two-dimensional DOS calculated from the solution of the effective mass equations in the envelope-function approximation [96] providing the subband energies. To include nonparabolicity of the light-hole band, a 4-band Kane model of the valence band is converted into corresponding 1D effective mass equations for each carrier-type, with the effective mass acquiring an energy dependence. The equations are solved numerically using a transfer-matrix method, which in addition provides the transmission function of the confining barrier. The DOS calculated in this way is also used to obtain the QW absorption that provide the generation rate. Excitonic contributions to absorption are included via parametric models with dimensionality parameters for exciton binding energies and oscillator strengths; the parameters are obtained from a fit to the solution of the effective mass equation for excitons. The absolute excitonic absorption is scaled and convolved with a Lorentzian for homogeneous broadening to fit the experimental data. Layer widths, composition and doping levels are determined from growth record and characterization studies, and the minority carrier diffusion lengths are calculated from layer doping and alloy fraction. The recombination rates are determined by the bulk and QW densities and the recombination times including radiative, SRH and Auger recombination, are obtained from fits to the corresponding bulk control cell dark currents. The carrier escape from QW is described by a separate escape lifetime model including thermionic emission and (thermally assisted) tunneling, where the escape lifetime is derived from the escape current which in turn is determined by the carrier density at a fixed energy, given by the DOS and the occupation, and the transmission function of the confining barrier at that energy. At room temperature and moderate fields, the probability of escape from QWs in the intrinsic region is set to unity, in accordance with carrier escape experiments [34]. In spite of its comprehensiveness, there are several shortcomings in the approach: neglect of valence-band mixing, free-carrier Coulomb interaction and interwell coupling lead to an underestimation of absorption high in the wells, and near the top of the wells, the envelope-function approximation breaks down and QW-absorption gradually becomes bulk-like, which is not reflected in the model. Furthermore, the DOS and correspondingly the absorption above the wells is assumed to be that of homogeneous bulk, which is not the case due to the existence of quasi-bound states and higher resonances.

A similar self-consistent Schrödinger-Poisson-drift-diffusion model for carrier generation, recombination and transport in QWSC was developed by Ramey and Khoie [97]. This approach describes also carrier capture into QW, and the escape model considers the 2D-DOS, the subband energy level structure including valence-band mixing and escape

from direct and indirect valleys, and the field and temperature dependence, but neglects tunneling escape, since it is assumed to be suppressed at room temperatures and low fields. The QW-absorption is obtained from a semiempirical model [98], not considering excitons, bandstructure or field effects. Only non-radiative recombination (SRH) is described. The model of Varonides [99] explicitly takes into account thermionic emission and tunneling in a way very similar to Nelson [34], but tunneling is restricted to the triangular barrier of an isolated well.

While the models reviewed so far did not consider the (resonant) coupling of multiple quantum wells, the inclusion of (coherent) multi-barrier tunneling into the analysis of QWSC performance was accounted for in the model by Mohaidat et. al. [45], in which a numerical solution of the time dependent Schrödinger equation is used to calculate resonant tunneling transport of photogenerated carriers in MQW with thin barriers. However, the model was never embedded into a more comprehensive picture including explicitly carrier generation, recombination and escape channels other than via tunneling.

2.3.3 Conclusions

The present status of QWSC theory can thus be summarized as follows:

- detailed-balance or equilibrium thermodynamic theories considering the possibility of multiple QFL provide an upper limit to QWSC efficiency, which however might not be realistic as thermodynamical implications rule out transitions other than radiative, which is not in accordance with experimental observations that show suppressed intraband coupling and prominent thermal escape;
- comprehensive QWSC models based on the solution of the semiconductor transport equations including generation, recombination, capture and escape, with the quantum well absorption and densities based on the DOS calculated from a microscopic first principle approach involving the solution of the Schrödinger equation to obtain the subband energies, are able to reproduce experimental spectral response and current-voltage characteristics. However, the large number of separate models and fitting parameters that are required obscures the true nature of the (microscopic) mechanisms that provide the potential for efficiency enhancement in practical devices. Furthermore, non of these models considers the effect of inter-well coupling and geometrical asymmetry on both absorption and escape as well as recombination, since this would require a comprehensive microscopic description of all these processes. The effective mass approximation in the envelope function approximation

commonly used to evaluate the QW DOS relevant for absorption, density and escape does not hold in the energy region near the top of the well and right above which does contribute most to the photocurrent near the operating point at room temperature, and the optical transitions involving quasi-bound states and higher resonances are not described properly. Furthermore, scattering is modelled on the level of a relaxation time approximation, even though the microscopic mechanisms of coupling to phonons play a crucial role in capture, escape and thermalization processes.

- Both approaches suffer from the fact that they are based on the assumption of local equilibrium, whereas the the system under operating conditions - large bias and illumination - is driven away from equilibrium. Whereas the assumption of a local equilibrium and corresponding thermal carrier distribution is reasonable for bulk homojunctions due to fast thermalization, it might not apply to quantum well structures where cooling can be slowed down due to phase space restrictions.

From these conclusions it is obvious that the existing models and theories for QWSC are not able to provide the insight required for further optimization of the photovoltaic performance, and the analysis of their shortcomings defines the requirements for a comprehensive theory of QWSC that goes beyond the existing approaches. Before examining the situation, some remarks about the actual challenges are due.

2.3.4 Requirements for novel approaches

Generally speaking, to come up with a comprehensive and hence predictive model for quantum well solar cells is a daunting task. This is due to the fact that in this type of optoelectronic device, both the optical and the electronic properties need to be described at a high level of accuracy, since they have a direct impact on the device characteristics, and do not correspond to an easy accessible near-equilibrium regime. While the QWSC is similar to QW-lasers or resonant tunneling devices in some aspects, there are key differences that prevent a straightforward application of corresponding models and theories: in the case of the QW-laser, the focus is on the light gain due to stimulated emission from an inverted, highly non-equilibrium carrier population, i.e. carriers are supposed to recombine radiatively as quickly and completely as possible, and carrier transport is sought to be minimized. In the case of resonant tunneling diodes (RTD), quantum transport through heterostructures is described in detail, but without consideration of optical properties and other inter-band processes, since the device is monopolar. An example of a similar device that is based on optical as well as transport processes is the quantum cascade laser (QCL), but also there, the device is monopolar and only intraband processes are considered, and

the role of contacts is usually neglected. Hence, due to the unique operating regime of QWSC, it is necessary to combine elements from the fields of semiconductor quantum optics and quantum transport in nanostructures. A further difficulty arises from the presence of two lengthscales in the problem: unlike in nanotransistors, where the channel length is of the order of 10 nm, the quantum region, i.e. the multi-quantum well sector of the device, can easily reach a length of 0.3-0.5 μm , and the whole device dimension normally exceeds the μm range. Both the extended quantum region and the embedding in a μm device environment pose serious challenges and are prone to considerably increase the computational cost of numerical simulations.

The fundamental requirement for a novel theory that captures the physics of QWSC beyond the existing approaches is the ability to provide a consistent picture of the microscopic processes in quantum-well structures under nonequilibrium conditions that are relevant for photovoltaic operation, namely

1. the *optical properties* as well as
2. the *quantum transport* mechanisms in
3. *open systems* of
4. arbitrary *heterostructure potential* that are
5. *out of equilibrium* and where the
6. effects of *scattering* cannot be neglected.

In the following, the above points shall be substantiated further and implications for the theoretical framework be derived:

1. Optical properties The picture of the optical properties should include all types of allowed transitions, i.e. intraband and interband, and between both quasi-bound and quasi-continuum states at energies within and above the quantum wells. The corresponding expressions for absorption and emission also need to consider the occupation of the available states, without any assumptions on the nature of the carrier distribution. The optical matrix elements and the amplitude of the transition should reflect the symmetries of the underlying microscopic model. Since the optical properties of a given material are directly related to its electronic structure via the dielectric function, an accurate model of the band structure is indispensable.

2. Quantum transport: A picture of carrier transport in QWSC needs to include quantum effects such as confinement and tunneling processes arising from spatially inhomogeneous potentials, especially in the case of multi-quantum well structures and superlattices with strong inter-well coupling and for a proper description of the carrier capture and escape mechanisms involving both bound and extended states. It is thus imperative to recur to a quantum transport formalism based on a microscopic model for the electronic structure, which for the sake of consistency should be the same as the one providing the optical properties.

3. Open systems: In order to produce electrical current from the device, carriers need to be injected from and absorbed into contacts. This coupling to the environment induces a finite lifetime and an associated level broadening to the eigenstates of the closed system. It is therefore more appropriate to describe the system in terms of scattering states. The net flow of carriers between device and contacts is controlled by the density and occupation of current carrying states. The desired formalism of quantum transport should consider these properties of mesoscopic conductors. In addition to the exchange of particles with the environment, there is also an exchange respectively dissipation of energy due to the coupling to lattice vibrations and electromagnetic fields.

4. Heterostructure potential: The model of the electronic structure should allow arbitrary spatial variation of heterostructure materials and provide realistic material properties, especially concerning the band offsets which play a major role in the determination of the subband energies.

5. Out of equilibrium: Transport is inherently a non-equilibrium process. In the case of a solar cell, the system is driven out of equilibrium by the illumination. While the short circuit current may be described reasonably well by means of perturbations around the equilibrium state, the operating point of such a device is far from the linear response regime, and simple approximate descriptions are not applicable in this situation. A valid candidate for a consistent QWSC theory should therefore not rely on the assumption of (global) quasi-equilibrium.

6. Scattering effects: To be able to assess the role and degree of thermalization in QWSC, as well as for the description of carrier capture and escape processes, the inclusion of scattering mechanisms is essential. At room temperature, where the device is supposed to operate, the most prominent relaxation mechanism is provided by the scattering with

optical phonons, but the total broadening can also contain contributions from scattering among the carriers, with ionized impurities, due to interface roughness etc. The implication of the presence of scattering process is the considerable increase in complexity and computational expense associated with microscopic theories beyond the ballistic regime.

Since a steady-state quantum transport formalism for open systems is an essential component of the required theory and the feature that is absent in most of the existing approaches, some representative models shall be reviewed and assessed for their usefulness as a basis for the description of QWSC operation.

2.3.5 Quantum transport models for QWSC

On a basic level, the quantum well solar cells represents an optoelectronic device, and as such, any model needs to cover the three aspects shown in Fig. 2.12: using the input from external conditions and material properties, the semiconductor transport equations providing charge and current densities have to be solved self-consistently with Maxwell's equations, which use the latter as internal sources together with external source terms to provide in turn the electromagnetic fields that enter the transport problem. With the

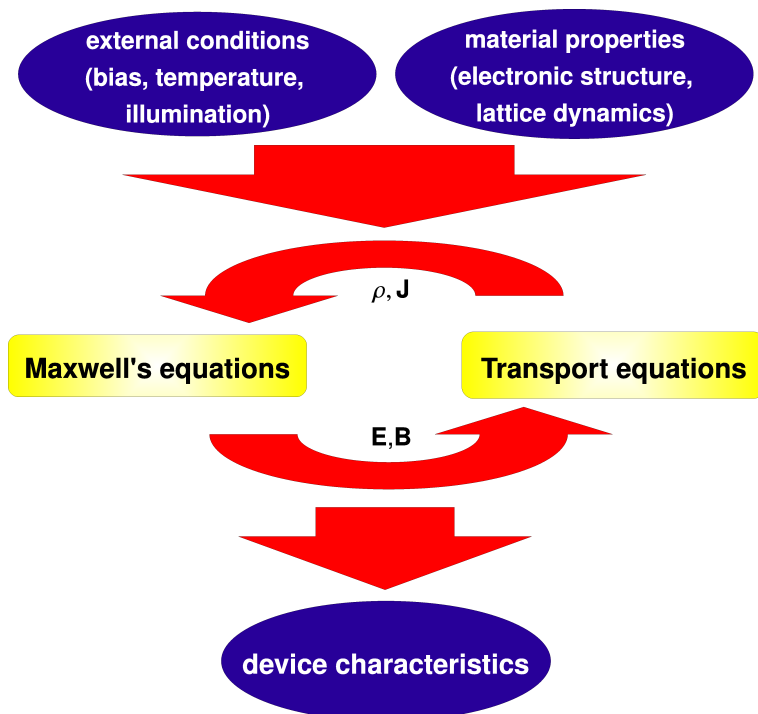


Figure 2.12: *Aspects of optoelectronic device modelling.*

ongoing miniaturization of (opto)electronic devices, novel modelling approaches had to be conceived to include the quantum effects that started to have considerable impact on the device characteristics. In passing to a quantum description of transport, a major difficulty was encountered in the unavoidable coupling of the system to the environment, which means that the system is open, requiring a formalism based on scattering states rather than on the closed system eigenstates. Further complications arise from the loss of coherence due to inelastic scattering causing transitions between quantum states that make it necessary to recur to mixed state or quantum statistical description of the system. For the moment, there is no universal quantum transport model capable of addressing any kind of system where quantum effects are important, comparable to the Boltzmann equation in semi-classical systems, but the choice of the approach strongly depends on the problem at hand. Fig. 2.13 shows a hierarchy of models for quantum transport in semiconductors.

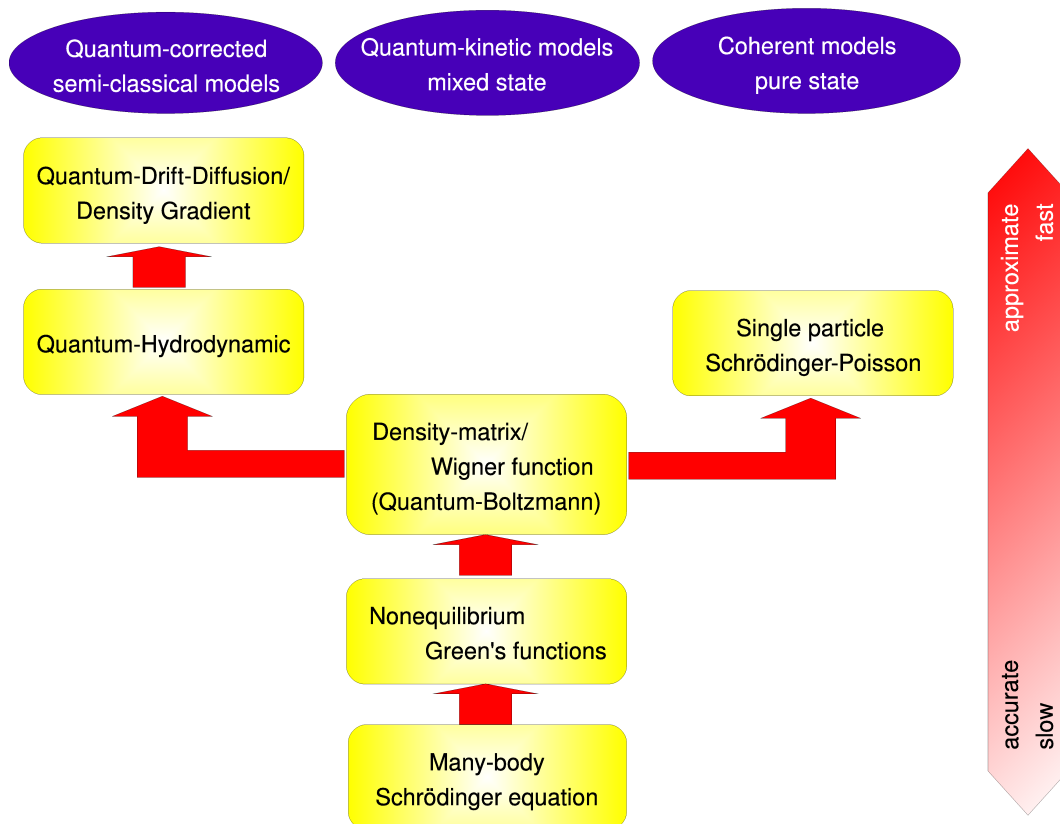


Figure 2.13: *Hierarchy of quantum transport models for semiconductor devices.*

Quantum corrected macroscopic continuum approaches

Most conventional models for solar cells are based on macroscopic continuum approaches to charge transport in semiconductors, such as the drift-diffusion or the hydrodynamic models derived from the Boltzmann equation via a moment expansion using a shifted Maxwellian distribution function [100, 101, 102]. To keep the advantages of this type of approach, both computational (speed and low memory requirements) and conceptual (direct access to physical quantities and classical definition of open-system boundary conditions), quantum effects are included via corrections that correspond to a moment expansion of the Quantum-Boltzmann or Liouville equation with respect to the Wigner function (see below) instead of the Boltzmann distribution function, leading to the quantum-hydrodynamic (QHD) [103] or quantum-drift-diffusion (QDD) equations [104], respectively. While this approach is supposed to yield reasonable results at high temperatures, it does not represent a “true” quantum-transport formalism, and the numerically observed characteristic quantum features like negative differential resistance (NDR) are not in quantitative agreement neither with more advanced models nor with experiments [105], and have even been attributed to an artefact of the model [106]. What remains as a severe limitation for the description of QWSC is the need for an additional microscopic model to quantify the absorption, and the macroscopic quantities this model gives rise to are not likely to be consistent with those obtained from the quantum correction.

Open-boundary Schrödinger-Poisson type wave function based models

To obtain both transport and optical properties from the same microscopic model, direct solutions of the Schrödinger equation can be used. While many-body calculations including correlations are not feasible for systems of realistic dimensions as a complete set of dynamical variables is required for each particle, efficient single-particle formalisms have been devised to calculate the heterostructure subbands for both single and multiband envelope function [107, 108, 109, 96, 110, 111, 112] and tight-binding [113, 114, 115, 116, 117] models. The current carrying states are not the eigenstates of the closed system, but scattering states. These open-system solutions of the Schrödinger equation can be obtained by the transfer-matrix approach [113, 118, 119, 120], which however is numerically unstable for long structures. A common way to impose open boundary conditions that is not subject to these stability issues is the use of the quantum-transmitting-boundary method (QTBM)[121, 122, 123, 124], which provides the wave-function of the scattering region, i.e. the scattering states, depending on the solution of the Schrödinger equation in the homogeneous leads, which can be obtained from the solution of a generalized eigenvalue problem [125, 126]. The scattering states are occupied according to the chemical potentials of the

contacts, which control the level of injection of carriers and enable the simulation of the device behaviour under nonequilibrium conditions. As an alternative to the QTBM, open boundary conditions can be mimicked by the introduction of an artificial non-reflecting contact using the *perfectly matched layer* (PML) method [127, 128, 129, 130], which is much less computationally intensive. The *contact block reduction* (CBR) approach [131, 132] is another efficient method that can be used in the case of ballistic transport in 2D/3D devices with multiple contacts. Here, the transmission function of the open system is obtained from the eigenstates of a corresponding closed system that need to be calculated only once and the solution of a very small linear algebraic system. Once the wave function of the system is known, the optical properties can be derived by methods depending on the type of band structure model [113, 114, 110, 111, 133, 134, 135, 136, 137, 138].

The major drawback of the Schrödinger-Poisson method is that a consistent inclusion of interactions is not straightforward, since the model is based on a pure-state single-particle picture: while carrier-carrier interactions can be treated on the (mean field) Hartree-level by a self-consistent coupling to Poisson's equation [139, 140], the description of phase-breaking scattering processes requires the use of a Pauli-master-equation formalism [141, 142] quantifying the transitions between pure states, i.e. eigenstates of the Hamiltonian. This formalism, however, suffers from the severe problem of continuity violation [122]. Schrödinger-Poisson type models are thus mostly used to describe purely coherent processes such as ballistic transport. In this case, the conductance can be expressed in the Büttiker-Landauer formalism [143, 144, 145] based on the quantum mechanical transmission function.

Although these models are perfectly suited and widely used for the calculation of optical and transport properties of quantum well structures, the difficult inclusion of scattering mechanisms limits their aptitude to serve as a basis for a comprehensive theory of QWSC.

Quantum kinetic models

To incorporate internal force terms arising from incoherent processes like e.g. inelastic electron-phonon scattering, kinetic equations need to be invoked. Quantum kinetic theory thus appears to be the simplest level at which both quantum interference and irreversibility may be described consistently, treating coherent and phase-breaking processes on equal footing. Since transitions between different states are incorporated in a kinetic theory, a mixed state description is required, such as provided by the single-particle reduced *density matrix* including all off-diagonal terms. The equation of motion for the density matrix is the quantum *Liouville* equation. It only describes conservative motion, however, a nonequilibrium steady-state cannot be established in a reversible system. For the descrip-

tion of irreversibility causing dissipative processes at a kinetic level, a collision term would need to be added to the Liouville superoperator. Irreversibility is already introduced into the Liouville equation by the application of open boundary conditions. Thus, for a proper formulation of open-system boundary conditions, time-reversal symmetry must be broken. The boundary conditions themselves need to be irreversible, which can be achieved by distinguishing between particles entering and leaving the system. For that purpose, a phase-space distribution formalism is better suited than the real space density-matrix.

Such a formalism is the one based on the *Wigner function* [146, 147, 122, 148, 149, 150, 151], which can be thought of as the quantum-statistical mechanical analog of the classical phase space distribution and is related to the mixed-state single-particle reduced density matrix via the *Wigner-Weyl* transform, corresponding to the Fourier transform with respect to relative coordinates. The quantum Boltzmann equation for the Wigner function is obtained by the same transform from the Liouville equation. Within the Wigner function formalism, the coupling to the environment via ideal contacts is modelled via setting the distribution function of the injected carriers equal to the reservoir equilibrium distribution characterized by the corresponding electrochemical potentials [122]. Conceptually, the boundary conditions are identical to the QTBM approach, but there is a mathematical difference due to the definition of the variables. Quantum-interference effects enter via the nonlocal potential term, and scattering can be described at different levels of sophistication, from simple relaxation time approximation [152] to a fully quantum-mechanical description based on Wigner-paths [149, 150]. To incorporate the electronic structure of the semiconductor on a higher level, multiband and multivalley schemes have been developed [153, 154], but their use is not very widespread as compared with other microscopic models.

It is also possible to use directly the density matrix as the model function [155, 156], with open boundary conditions obtained from those in for the Wigner function via the inverse Wigner-Weyl transform, but the real-space definition is less well suited to incorporate scattering effects due to the nonlocal nature of the latter, whereas scattering is local in the Wigner function formalism. On the other hand, the Wigner function itself is purely real valued, which simplifies the calculations and the interpretation of the results. Both formalism have been extensively used for the simulation of nonequilibrium quantum transport in open systems like resonant tunneling diodes [157, 158, 159, 152, 160] and in semiconductor quantum optics [161, 162, 156, 163, 164].

Both the Wigner function and the density matrix are single-time quantities, i.e. they are able to describe spatial correlations, but not temporal ones, which is equivalent to say that they have no memory and describe what is called the *Markovian* limit. To include memory

effects, a second time - or energy - variable is required, like in the full kernel or Green's function governing the spatial and temporal evolution of the single-particle wave-function, which leads to the non-equilibrium Green's function formulation of quantum transport representing the highest hierarchy level of quantum transport beyond the exact solution of the many-body Schrödinger equation, and from which the lower level approaches can be obtained via averaging over one time or energy variable, respectively.

The non-equilibrium Green's function (NEGF) method is a versatile and powerful tool to study non-equilibrium properties of nanostructures, since it is based on a quantum field theoretical approach to non-equilibrium statistical mechanics [165, 166, 167, 168, 169]. In the NEGF approach, the Green's functions for the involved particles (electrons, holes, phonons, photons, excitons, plasmons, etc) are the model functions providing all the physical quantities characterizing the system. They correspond to the response of the system to external perturbations, the latter entering the equations of motion for the Green's functions, the *Dyson's* equations, in the form of *self-energies*. The self-energies due to (weak) interactions such as electron-phonon or electron-photon coupling are calculated using standard diagrammatic or operator expansion techniques used in many-body perturbation theory [170]. The coupling to contacts, i.e. the application of open boundary conditions, is provided by a special type of boundary self-energy.

One of the major advantages of the approach is that it is both conceptually sound and easily applicable to the description of all kinds of transport properties in many different types of real mesoscopic systems [171], wherefore it has become among the most popular quantum transport theories in the last years. Apart from the actual nonequilibrium quantum transport phenomena comprising ballistic transport and resonant tunneling in semiconductor multilayers and nanostructures of different dimensionality (quantum wells [172], wires [173, 174] and dots [175]), metallic and molecular conduction [176, 177, 178, 179, 180, 181, 182, 183], phonon mediated inelastic and thermal transport [184, 185, 186, 187, 188], Coulomb-blockade [189, 190] and Kondo-effect [191, 192, 193], it is also used to describe strongly non-equilibrium and interacting regimes in semiconductor quantum optics requiring a quantum kinetic approach [194, 195, 196, 197, 198], with phenomena such as nonequilibrium absorption, interband polarization, spontaneous emission and laser gain. The concept was first adapted to the simulation of transport in open nanoscale devices on the example of tunneling in metal-insulator-metal junctions [199, 200, 201, 202], and has in the following been applied to investigation and modelling of MOSFET [203, 204, 205, 206, 207], CNT-FET [208, 209], resonant tunneling diodes [210, 211, 184, 212, 172, 213] and interband tunneling diodes [214, 215, 216], interband quantum well lasers [217] and intraband quantum cascade lasers [218], as well as infrared photodetectors [219] and CNT-photodiodes [220, 221, 222]. The theory was formulated

both for continuum effective-mass [195, 206] and discrete multiband tight-binding [172, 214] models of the electronic structure, and in the case of molecular conduction it is combined with ab-initio methods such as density functional theory [178, 223, 181].

Conclusions

From the requirements formulated in Sec. 2.3.4 and the properties of the different approaches discussed above it is evident that a comprehensive theory of quantum well photovoltaics needs to be on the quantum kinetic level and combined with a microscopic description of the electronic structure. There, the NEGF formalism offers the best basis to treat all the relevant processes on equal footing under inclusion of an accurate band structure model. For the latter, tight-binding models are more popular in transport problems if multiple bands are required, whereas for optics and extended structures, effective mass models are more favourable due to the continuum nature of the approach. In this thesis, the tight-binding method is used, considering the relative ease in numerical implementation that it offers.

2.3.6 Summary

The basic mechanisms of photovoltaic solar energy conversion in crystalline bulk homojunction cells, i.e. generation, transport and recombination of free charge carriers, are modified in the presence of quantum wells originating from the insertion of lower band gap material in the intrinsic region of a *p-i-n* diode. The generation of photocurrent and thus the value of the short-circuit current I_{sc} is enhanced by the extended absorption range, whereas the dark current increases due to higher recombination, leading to a lower open-circuit voltage V_{oc} . If the current gain outweighs the voltage loss, an increased output power and thus higher efficiency results. This has been achieved experimentally in several III-V semiconductor material systems. On the theoretical side, as the presence of the heterostructure potential introduces strong quantum effects affecting both the optical and transport properties of the device, conventional macroscopic continuum models begin to fail in their ability to deliver a proper picture of the dominating physical processes, such as the escape of photogenerated carriers. A theory of quantum well solar cells able to go beyond the existing approaches needs to be able to describe optical and transport properties of an open, interacting nonequilibrium system on a unified, microscopic level. Out of the available quantum transport models, such a theory is provided best by the nonequilibrium Green's function formalism in a tight-binding representation.

Since the theory and applications of nonequilibrium Green's functions as a tool to under-

stand the operation of open quantum devices far from equilibrium is central to this work, it will be reviewed in more detail in the next chapter.

Chapter 3

Quantum transport with nonequilibrium Green's functions

Abstract: In this chapter, the nonequilibrium Green's functions formalism (NEGF) is reviewed. A brief introduction to the quantum statistical mechanical foundations of the theory is followed by a discussion of the general framework of its application to the field of nanostructure device modelling, and it is shown how it provides the means to describe open interacting system far from equilibrium in a formally appealing and general way.

3.1 Introduction

Many effects in nanoscale condensed matter systems require a microscopic theory for their explanation. Such a description is provided by the formulation of the system Hamiltonian \mathcal{H} . The basic problem to be solved then amounts to the Schrödinger equation

$$i\hbar\partial_t\Psi(\mathbf{r}_1, \mathbf{r}_2, \dots, \mathbf{r}_N, t) = \mathcal{H}\Psi(\mathbf{r}_1, \mathbf{r}_2, \dots, \mathbf{r}_N, t) \quad (3.1)$$

for the many-particle wave function $\Psi(\mathbf{r}_1, \mathbf{r}_2, \dots, \mathbf{r}_N, t)$ that characterizes the system of N particles at coordinates $r_i, i = 1, 2, \dots, N$ by providing expectation values for observables. However, in many cases, especially those involving interactions among the particles, the above equation can only be solved perturbatively. The perturbative evaluation of ensemble averages, e.g. in diagrammatic fashion, has become a standard tool in condensed matter theory. The central object of the method are the Green's functions, that similar to the wave functions contain all the relevant microscopic information about the system. There exist different branches of the theory, depending on the system under consideration, such as the zero-temperature equilibrium theory or the finite-temperature Matsubara technique

[224, 170, 225]. The present work relies on the (finite temperature) non-equilibrium Green's function (NEGF) formalism, introduced by Kadanoff and Baym [167], and Keldysh [168], based on ideas by Schwinger and coworkers [165, 166]. This formalism provides a framework for calculating the non-equilibrium statistical ensemble average of operators acting on many-particle systems driven out of equilibrium. In this thesis, the focus is on the averages of single-particle operators from which physical quantities such as particle density and current can be derived.

Due to the wide range of applications, there exist many topical reviews providing a thorough introduction to the general formalism [226, 227, 228, 229, 195]. Here, only the aspects of the theory that are fundamental or relevant for the use in mesoscopic device modelling shall be reviewed.

This chapter is organized as follows: In the first section, the formalism to evaluate nonequilibrium ensemble averages of general operators is developed along the line of equilibrium theory, with the necessary modifications to satisfy the nonequilibrium conditions. After the representation of the system Hamiltonian in terms of single particle operators in second quantization, the formalism is used in the next section to derive expressions for the nonequilibrium Green's functions. Again in analogy to the equilibrium case, the perturbative evaluation of these expressions is discussed, followed by the derivation of the Dyson's equations corresponding to the equations of motion of the Green's functions. Next, the representation of physical quantities such as density and current in terms of the nonequilibrium Green's functions is discussed. The last section is dedicated to the applications of the formalism in the theory of transport in nanoscale electronic devices. After a discussion of the system partitioning and the treatment of contacts, the self-consistent procedure for the calculation of physical quantities is outlined. The chapter concludes with a discussion of suitable choices of spatial discretization and basis functions depending on the problem at hand.

3.2 Nonequilibrium statistical averages

We consider a system with an equilibrium state described by the time-independent Hamiltonian

$$H = H_0 + H^i, \quad (3.2)$$

with the noninteracting, exactly solvable part H_0 and the interparticle interaction contained in H^i . As an open system, it is connected to a heat-bath of temperature T and a particle reservoir characterized by a chemical potential μ , which implies the choice of the grand canonical ensemble for statistical averaging. The thermodynamic equilibrium state

of the system is then given by the equilibrium density matrix, which for $\mu = 0$ reads

$$\rho(H) = \frac{e^{-\beta H}}{\text{tr}[e^{-\beta H}]} \equiv \mathcal{Z}^{-1} e^{-\beta H}, \quad \beta \equiv (k_B T)^{-1}. \quad (3.3)$$

To describe the nonequilibrium state of the system, the latter is assumed to be instantaneously disconnected from the reservoirs and exposed to a perturbation at a time t_0 , such as e.g. a time varying electromagnetic field or an imbalance of the chemical potentials in the reservoirs coupled to the system. The perturbation is represented by the time-dependent part of the total Hamiltonian \mathcal{H} ,

$$\mathcal{H}(t) = H + H'(t), \quad (3.4)$$

$$H'(t) = 0, \quad t < t_0. \quad (3.5)$$

The nonequilibrium statistical average of an observable $O_{\mathcal{H}}(t)$ in the Heisenberg picture with respect to the grand-canonical ensemble characterized by the density operator $\rho(H)$ is then defined as¹

$$\langle \hat{O}_{\mathcal{H}}(t) \rangle \equiv \text{tr}[\rho(H) O_{\mathcal{H}}(t)]. \quad (3.6)$$

A perturbative evaluation of the above expression requires an analogy to the equilibrium Gell-Mann-Low formula

$$\langle O_{\mathcal{H}}(t) \rangle_{eq} = \frac{\langle T_t \{ S(\infty, -\infty) \hat{O}_{\mathcal{H}}(t) \} \rangle_0}{\langle S(\infty, -\infty) \rangle_0}, \quad (3.7)$$

where $\langle \dots \rangle_0$ denotes the expectation value with respect to the noninteracting ground state at $t = \pm\infty$ and \hat{T}_t is the the *chronological* time-ordering operator defined by

$$\hat{T}_t \{ \hat{A}(t_1) \hat{B}(t_2) \} \equiv \theta(t_1 - t_2) \hat{A}(t_1) \hat{B}(t_2) \mp \theta(t_2 - t_1) \hat{B}(t_2) \hat{A}(t_1), \quad (3.8)$$

where θ is the step function and the minus sign is for fermionic operators. The *antichronological* time-ordering operator \hat{T}_{at} has an analogous definition, with reversal of the ordering. The crucial assumption in equilibrium is the one that the system returns to its initial state for asymptotically large times, which is expressed in the arguments of the time-evolution operator of the interaction representation, $S(\infty, -\infty)$, where

$$S(t, t') \equiv \hat{T}_t \left\{ e^{-\frac{i}{\hbar} \int_{t'}^t d\tau H^i(\tau)} \right\}. \quad (3.9)$$

This assumption does no longer hold in out-of-equilibrium systems, wherefore reference to asymptotically large times has to be replaced by reference to the initial time t_0 . To find an

¹Note that the Hamiltonian in the distribution does not contain the time-dependent perturbation, as discussed e.g. by Mahan [225], p. 216-218.

expression corresponding to Eq. (3.7) for a perturbative evaluation of the nonequilibrium ensemble average starting from Eq. (3.6), the role in the time evolution of the operator \hat{O} played by \mathcal{H} has to be transferred to H_0 , which has a *Wick decomposition*. This corresponds to a transformation of the operator representation from the *Heisenberg picture* into the *interaction picture*. To relate the different representations, it is suitable to express the quantum statistical averages in terms of the time independent Schrödinger operator \hat{O}_S and a time evolution operator $U_h(t)$ corresponding to a time evolution governed by the Hamiltonian h , with the condition that the pictures coincide at time t_0 , i.e. $\hat{O}_h(t_0) = \hat{O}_S$, where the wave function is simply the solution of the Schrödinger equation for the Hamiltonian H_0 . For the Heisenberg picture ($h = \mathcal{H}$), this yields

$$\hat{O}_{\mathcal{H}}(t) \equiv \hat{U}_{\mathcal{H}}^\dagger(t, t_0) \hat{O}_S \hat{U}_{\mathcal{H}}(t, t_0), \quad (3.10)$$

with

$$\hat{U}_{\mathcal{H}}(t, t_0) = \hat{T}_t \left\{ e^{-\frac{i}{\hbar} \int_{t_0}^t dt' \mathcal{H}(t')} \right\}. \quad (3.11)$$

In the same fashion, the time evolution of an operator with respect to the time-independent Hamiltonian H is expressed as

$$\hat{O}_H(t) \equiv \hat{U}_H^\dagger(t, t_0) \hat{O}_S \hat{U}_H(t, t_0). \quad (3.12)$$

with

$$\hat{U}_H(t, t_0) = e^{-\frac{i}{\hbar} H(t-t_0)}. \quad (3.13)$$

and thus

$$\hat{O}_{\mathcal{H}}(t) \equiv \hat{V}_H^\dagger(t, t_0) \hat{O}_H(t) \hat{V}_H(t, t_0) \quad (3.14)$$

where

$$\hat{V}_H(t, t_0) \equiv \hat{U}_H^\dagger(t, t_0) \hat{U}_{\mathcal{H}}(t, t_0) = \hat{T}_t \left\{ e^{-\frac{i}{\hbar} \int_{t_0}^t dt' H'_H(t')} \right\} \quad (3.15)$$

and

$$\hat{V}_H^\dagger(t, t_0) \equiv \hat{U}_{\mathcal{H}}^\dagger(t, t_0) \hat{U}_H(t, t_0) = \hat{T}_t \left\{ e^{-\frac{i}{\hbar} \int_{t_0}^t dt' H'_H(t')} \right\} \equiv \hat{T}_{at} \left\{ e^{-\frac{i}{\hbar} \int_{t_0}^t dt' H'_H(t')} \right\}. \quad (3.16)$$

The time ordering in Eq. (3.14) can be written as ordering along the *contour* branches C_1 and C_2 of the contour C shown in Fig. 3.1, corresponding to chronological and antichronological time ordering, respectively, which means that

$$\hat{V}_H(t, t_0) \equiv \hat{T}_{C_1} \left\{ e^{-\frac{i}{\hbar} \int_{C_1} d\tau H'_H(\tau)} \right\}, \quad (3.17)$$

$$\hat{V}_H^\dagger(t, t_0) \equiv \hat{T}_{C_2} \left\{ e^{-\frac{i}{\hbar} \int_{C_2} d\tau H'_H(\tau)} \right\} \quad (3.18)$$

and thus

$$\hat{O}_{\mathcal{H}}(t) = \hat{T}_C \left\{ e^{-\frac{i}{\hbar} \int_C d\tau H'_H(\tau)} \hat{O}_H(t) \right\} \equiv \hat{T}_C \left\{ S'_H(C) \hat{O}_H(t) \right\}, \quad (3.19)$$

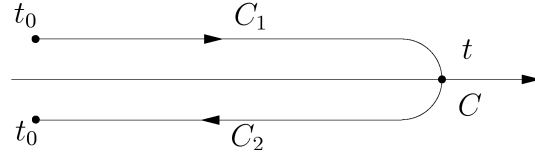


Figure 3.1: The Keldysh contour $C \equiv C_1 \cup C_2$ used in the transformation into a time evolution governed by the time-independent Hamiltonian H . The deviation from the real axis is only to distinguish between the two branches and to illustrate the ordering along the contour.

where the *contour ordering* operator

$$\hat{T}_C\{\hat{A}(t_1)\hat{B}(t_2)\} \equiv \theta_C(t_1, t_2)\hat{A}(t_1)\hat{B}(t_2) \mp \theta_C(t_2, t_1)\hat{B}(t_2)\hat{A}(t_1), \quad (3.20)$$

was introduced, with the following definitions of functions on the contour C

$$\theta_C(t_1, t_2) \equiv \begin{cases} \theta(t_1 - t_2) & t_1 > t_2 \quad \text{and} \quad t_1 \text{ later on } C \\ \theta(t_2 - t_1) & t_2 > t_1 \quad \text{and} \quad t_1 \text{ later on } C \\ \theta(t_2 - t_1) & t_1 > t_2 \quad \text{and} \quad t_2 \text{ later on } C \\ \theta(t_1 - t_2) & t_2 > t_1 \quad \text{and} \quad t_2 \text{ later on } C \end{cases} \quad (3.21)$$

and the derivative

$$\frac{\partial}{\partial t_1}\theta_C(t_1, t_2) \equiv \delta_C(t_1, t_2) = -\frac{\partial}{\partial t_1}\theta_C(t_2, t_1). \quad (3.22)$$

In the interaction picture, the Schrödinger operator is transformed into

$$\hat{O}_{H_0}(t) \equiv \hat{U}_{H_0}^\dagger(t, t_0)\hat{O}_S\hat{U}_{H_0}(t, t_0) \quad (3.23)$$

with

$$\hat{U}_{H_0}(t, t_0) = e^{-\frac{i}{\hbar}H_0(t-t_0)}. \quad (3.24)$$

Replacing the Schrödinger operator by the relation to the Heisenberg representation in Eq. (3.10), we find

$$\hat{O}_{\mathcal{H}}(t) = \hat{V}_{H_0}^\dagger(t, t_0)\hat{O}_{H_0}\hat{V}_{H_0}(t, t_0) \quad (3.25)$$

where

$$\hat{V}_{H_0}(t, t_0) \equiv \hat{U}_{H_0}^\dagger(t, t_0)\hat{U}_{\mathcal{H}}(t, t_0) = \hat{T}_t \left\{ e^{-\frac{i}{\hbar}\int_{t_0}^t dt' H'_{H_0}(t')} e^{-\frac{i}{\hbar}\int_{t_0}^t dt' H_{H_0}^i(t')} \right\}. \quad (3.26)$$

In terms of contour ordered operators, Eq. (3.25) becomes

$$\hat{O}_{\mathcal{H}}(t) = T_C \left\{ S'_{H_0}(C) S_{H_0}^i(C) \hat{O}_{H_0}(t) \right\}, \quad (3.27)$$

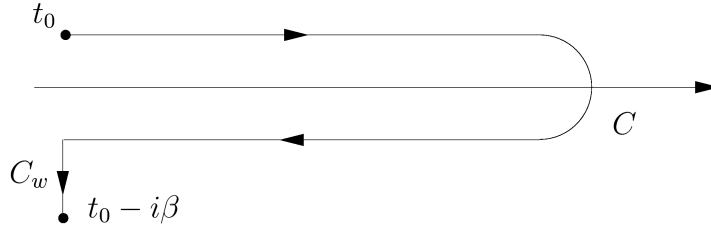


Figure 3.2: The contour $\tilde{C} \equiv C \cup C_w$ used in the transformation to the interaction picture where the time-evolution is governed by the non-interacting Hamiltonian H_0 . The deformation into the complex plane is required for the consideration of initial correlations. In steady state, which is equivalent to $t_0 \rightarrow -\infty$, this deviation is negligible and one can work with the Keldysh contour in Fig. 3.1.

with

$$S'_{H_0}(C) \equiv e^{-\frac{i}{\hbar} \int_C d\tau H'_{H_0}(\tau)}, \quad S^i_{H_0}(C) \equiv e^{-\frac{i}{\hbar} \int_C d\tau H^i_{H_0}(\tau)}. \quad (3.28)$$

To write the quantum statistical ensemble average (3.6) in the interaction picture, the density matrix $\rho(H)$ needs to be replaced by $\rho(H_0)$. This is achieved by noting that

$$e^{\beta H} = e^{\beta H_0} w(t_0 - i\beta, t_0) \quad (3.29)$$

with

$$w(t, t_0) = T_t \left\{ e^{-\frac{i}{\hbar} \int_{t_0}^t dt' H^i_{H_0}(t')} \right\}. \quad (3.30)$$

The modification of the density matrix amounts to a deformation of the integration contour from C to \tilde{C} as shown in Fig. 3.2, by adding the imaginary time strip C_w from t_0 to $t_0 - i\beta$ on which w is defined, and we can write

$$w(t_0 - i\beta, t_0) = T_{\tilde{C}} \left\{ S'_{H_0}(C) S^i_{H_0}(\tilde{C}) \right\}. \quad (3.31)$$

This deformation of the contour also allows for the consideration of initial correlations [230, 231].

One finally arrives at the ensemble average

$$\langle \hat{O}_{\mathcal{H}}(t) \rangle = \frac{\langle \hat{T}_{\tilde{C}} \{ S'_{H_0}(C) S^i_{H_0}(\tilde{C}) \hat{O}_{H_0}(t) \} \rangle_0}{\langle \hat{T}_{\tilde{C}} \{ S'_{H_0}(C) S^i_{H_0}(\tilde{C}) \} \rangle_0} = \frac{\text{Tr}[\rho(H_0) \hat{T}_{\tilde{C}} \{ S'_{H_0}(C) S^i_{H_0}(\tilde{C}) \hat{O}_{H_0}(t) \}]}{\text{Tr}[\rho(H_0) \hat{T}_{\tilde{C}} \{ S'_{H_0}(C) S^i_{H_0}(\tilde{C}) \}]} \quad (3.32)$$

where all the time dependence is determined by the solvable Hamiltonian H_0 and the ensemble average is evaluated with respect to the noninteracting density matrix $\rho(H_0)$. Eq. (3.32) also holds in the case of initial correlations, which may play an important role for the study of transient behaviour in nonequilibrium systems [230, 231].

The steady state, which is the relevant regime for photovoltaic applications, corresponds to a situation that is established after the perturbation has been turned on for a sufficiently long time, i.e. for $t \gg t_0$ or, equivalently, $t_0 \rightarrow -\infty$. In that case,

$$\lim_{t_0 \rightarrow -\infty} w(t_0 - i\beta, t_0) = \lim_{t_0 \rightarrow -\infty} T_{C_w} \left\{ e^{-\frac{i}{\hbar} \int_{t_0}^{t_0 - i\beta} dt' H_{H_0}^i(t')} \right\} = 1, \quad (3.33)$$

which means that in steady state, the integrations along contours C and \tilde{C} coincide.

3.3 Nonequilibrium Green's functions

To evaluate the physical properties of many-body systems far from equilibrium, it is convenient to derive the corresponding single-particle nonequilibrium Green's functions, which are defined as the nonequilibrium ensemble averages of contour ordered field operators

$$G(11') \equiv -\frac{i}{\hbar} \langle \hat{T}_C \{ \hat{\Psi}_{\mathcal{H}}(1) \hat{\Psi}_{\mathcal{H}}^\dagger(1') \} \rangle \quad (3.34)$$

$$= -\frac{i}{\hbar} \left(\theta_C(1, 1') \langle \hat{\Psi}_{\mathcal{H}}(1) \hat{\Psi}_{\mathcal{H}}^\dagger(1') \rangle \mp \theta_C(1', 1) \langle \hat{\Psi}_{\mathcal{H}}^\dagger(1') \hat{\Psi}_{\mathcal{H}}(1) \rangle \right), \quad (3.35)$$

where $\hat{\Psi}_{\mathcal{H}}(1)$ is the field operator in the Heisenberg picture for a single fermion (upper sign in (3.35)) or a single boson (lower sign in (3.35)), and the argument is given in the short hand notation $1 \equiv (\mathbf{r}_1, t_1, \sigma_1)$, where σ is the spin index.

Applying Eq. (3.32) to the average in Eq. (3.35) provides a starting point for a perturbation expansion of the nonequilibrium Green's functions,

$$G(11') = -\frac{i}{\hbar} \frac{\langle \hat{T}_{\tilde{C}} \{ S'_{H_0}(C) S^i_{H_0}(\tilde{C}) \hat{\Psi}_{H_0}(1) \hat{\Psi}_{H_0}^\dagger(1') \} \rangle_0}{\langle \hat{T}_{\tilde{C}} \{ S'_{H_0}(C) S^i_{H_0}(\tilde{C}) \} \rangle_0}, \quad (3.36)$$

in analogy to the equilibrium zero temperature Gell-Mann-Low formula, with the corresponding diagrammatic representation and Feynman rules for the evaluation.

The following discussion is based on the assumption that initial correlations are absent or washed out, i.e. the time evolution is along the Keldysh contour C (Fig. 3.1).

3.3.1 Equations of motion

The equations of motion describing the time evolution of the nonequilibrium Green's functions can be determined via the time derivative of the contour-ordered pair of Heisenberg

field operators,

$$\frac{\partial}{\partial t}G(\mathbf{r}, t, \sigma; \mathbf{r}', t', \sigma') = \frac{\partial}{\partial t}\langle \hat{T}_C\{\hat{\Psi}_{\mathcal{H}}(\mathbf{r}, t, \sigma)\hat{\Psi}_{\mathcal{H}}^\dagger(\mathbf{r}', t', \sigma')\} \rangle \quad (3.37)$$

$$= \left\langle \hat{T}_C \left\{ \left[\frac{\partial}{\partial t} \hat{\Psi}_{\mathcal{H}}(\mathbf{r}, t, \sigma) \right] \hat{\Psi}_{\mathcal{H}}^\dagger(\mathbf{r}', t', \sigma') \right\} \right\rangle \\ + \delta_C(t, t') \left\langle \left[\hat{\Psi}_{\mathcal{H}}(\mathbf{r}, t, \sigma), \hat{\Psi}_{\mathcal{H}}^\dagger(\mathbf{r}', t, \sigma') \right]_{\pm} \right\rangle \quad (3.38)$$

$$= \left\langle \hat{T}_C \left\{ \left[\frac{\partial}{\partial t} S'_H(t_0, t) \right] \hat{\Psi}_H(\mathbf{r}, t, \sigma) S'_H(t, t_0) \hat{\Psi}_{\mathcal{H}}^\dagger(\mathbf{r}', t', \sigma') \right\} \right\rangle \\ + \left\langle \hat{T}_C \left\{ S'_H(C) \left[\frac{\partial}{\partial t} \hat{\Psi}_H(\mathbf{r}, t, \sigma) \right] \hat{\Psi}_{\mathcal{H}}^\dagger(\mathbf{r}', t', \sigma') \right\} \right\rangle \\ + \left\langle \hat{T}_C \left\{ S'_H(t_0, t) \hat{\Psi}_H(\mathbf{r}, t, \sigma) \left[\frac{\partial}{\partial t} S'_H(t, t_0) \right] \hat{\Psi}_{\mathcal{H}}^\dagger(\mathbf{r}', t', \sigma') \right\} \right\rangle \\ + \delta_C(t, t') \delta(\mathbf{r} - \mathbf{r}') \delta_{\sigma, \sigma'}, \quad (3.39)$$

where $[\cdot, \cdot]_{\pm}$ denotes the (anti-)commutator for fermions and bosons, respectively, and Eqs. (3.35), (3.106) and (3.19) were used. The time derivatives of the Heisenberg field operators can now be replaced by the corresponding Heisenberg equation of motion, expressing the time-independent part of the system Hamiltonian $\hat{H} = \hat{H}_0 + \hat{H}^i$ in terms of the field operators, which for the case of an general particle-particle interaction $\hat{H}^i = \hat{V}$ gives the expression

$$\hat{H}(t) = \sum_{\sigma} \int d\mathbf{r} \hat{\Psi}_{\mathcal{H}}^\dagger(\mathbf{r}, t, \sigma) H_0(\mathbf{r}) \hat{\Psi}_{\mathcal{H}}(\mathbf{r}, t, \sigma) \\ + \frac{1}{2} \sum_{\sigma, \sigma'} \int d\mathbf{r} \int d\mathbf{r}' \hat{\Psi}_{\mathcal{H}}^\dagger(\mathbf{r}, t, \sigma) \hat{\Psi}_{\mathcal{H}}^\dagger(\mathbf{r}', t, \sigma') V(\mathbf{r} - \mathbf{r}') \hat{\Psi}_{\mathcal{H}}(\mathbf{r}', t, \sigma') \hat{\Psi}_{\mathcal{H}}(\mathbf{r}, t, \sigma). \quad (3.40)$$

The Heisenberg equation for the field operator with respect to this Hamiltonian is

$$i\hbar \frac{\partial}{\partial t} \hat{\Psi}_H(\mathbf{r}, t, \sigma) = \left[\hat{\Psi}_{\mathcal{H}}(\mathbf{r}, t, \sigma), \hat{\mathcal{H}}(t) \right]_- \quad (3.41)$$

$$= H_0(\mathbf{r}) \hat{\Psi}_{\mathcal{H}}(\mathbf{r}, t, \sigma) + \sum_{\sigma} \int d\mathbf{r}' V(\mathbf{r} - \mathbf{r}') \hat{\Psi}_{\mathcal{H}}^\dagger(\mathbf{r}', t, \sigma) \hat{\Psi}_{\mathcal{H}}(\mathbf{r}', t, \sigma) \hat{\Psi}_{\mathcal{H}}(\mathbf{r}, t, \sigma). \quad (3.42)$$

For the derivative of the time evolution operator, $\frac{\partial}{\partial t} S'_H(t_0, t)$, the perturbation Hamiltonian $\hat{H}'(t)$ also needs to be expressed in second quantization,

$$\hat{H}'_H(t) = \sum_{\sigma} \int d\mathbf{r} \hat{\Psi}_H^\dagger(\mathbf{r}, t, \sigma) U(\mathbf{r}, t) \hat{\Psi}_H(\mathbf{r}, t, \sigma), \quad (3.43)$$

which is used to obtain

$$\begin{aligned} & \left[\frac{\partial}{\partial t} S'_H(t_0, t) \right] \hat{\Psi}_H(\mathbf{r}, t, \sigma) S'_H(t, t_0) + S'_H(t, t_0) \hat{\Psi}_H(\mathbf{r}, t, \sigma) \left[\frac{\partial}{\partial t} S'_H(t, t_0) \right] \\ &= S'_H(C) H'(t) \hat{\Psi}_H(\mathbf{r}, t, \sigma). \end{aligned} \quad (3.44)$$

Inserting these expressions for the time derivatives into Eq. (3.39) and recalling the definition of the Green's function in (3.35) yields the equation of motion for the Green's function with respect to t ,

$$\left(i\hbar \frac{\partial}{\partial t_1} - H_0(\mathbf{r}_1) - U(1) \right) G(11') = \delta(11') - i\hbar \int_C d3V(1-3)G^{(2)}(13^-1'3^+) \quad (3.45)$$

where on the left-hand side, the definition of the Green's function in Eq. (3.34) was used, and on the right-hand side, the two-particle Green's function

$$G^{(2)}(131'3') = \left(-\frac{i}{\hbar} \right)^2 \left\langle \hat{T}_C \left\{ \hat{\Psi}_{\mathcal{H}}(1) \hat{\Psi}_{\mathcal{H}}(3) \hat{\Psi}_{\mathcal{H}}^\dagger(3') \hat{\Psi}_{\mathcal{H}}^\dagger(1') \right\} \right\rangle \quad (3.46)$$

was introduced, together with the definitions

$$\delta(12) \equiv \delta_C(t_1, t_2) \delta(\mathbf{r}_1 - \mathbf{r}_2) \delta_{\sigma_1, \sigma_2}, \quad (3.47)$$

$$V(1-2) \equiv V(\mathbf{r}_1 - \mathbf{r}_2) \delta(t_1 - t_2), \quad (3.48)$$

and the short-hand notation

$$\int_C d1 \equiv \sum_{\sigma} \int_C dt_1 \int d\mathbf{r}_1. \quad (3.49)$$

In (3.45), 1^\pm denotes the coordinates with time infinitesimally smaller or larger than t_1 . A similar equation is found for the derivative with respect to t' ,

$$\left(-i\hbar \frac{\partial}{\partial t'_1} - H_0(\mathbf{r}_{1'}) - U(1') \right) G(11') = \delta(11') - i\hbar \int_C d3V(1'-3)G^{(2)}(13^-1'3^+). \quad (3.50)$$

Eqs. (3.45) and (3.50) induce an infinite hierarchy, since the equation for the two-particle Green's function contains the three-particle Green's function and so on. This hierarchy can be truncated by noting that, following the analogy to the equilibrium case established by Eq. (3.36), the equation of motion for the contour ordered Green's function can be written as the *Dyson's equation*

$$G(1, 1') = G_0(1, 1') + \int_C d2 \int_C d3 G_0(1, 2) \Sigma(2, 3) G(3, 1'), \quad (3.51)$$

where G_0 is the Green's function in the absence of interactions and Σ is the *irreducible self-energy* containing the effects of interactions. The equivalence of (3.51) to Eq. (3.45) with the proper definition of the self-energy is established by considering that the noninteracting Green's function G_0 is the solution of (3.45) without the two particle Green's function, and hence

$$G_0(1, 1')^{-1} = \left(i\hbar \frac{\partial}{\partial t_1} - H_0(\mathbf{r}) - U(1) \right) \delta(1, 1'). \quad (3.52)$$

The equations of motion for the Green's function, Eqs. (3.45) and (3.50) can thus be written as

$$\left(i\hbar \frac{\partial}{\partial t_1} - H_0(\mathbf{r}) - U(1) \right) G(11') = \delta(11') - i\hbar \int_C d3 \Sigma(13) G(31'), \quad (3.53)$$

$$\left(-i\hbar \frac{\partial}{\partial t_1} - H_0(\mathbf{r}') - U(1') \right) G(11') = \delta(11') - i\hbar \int_C d3 G(13) \Sigma(31'). \quad (3.54)$$

The specific form of the self-energy depends on the interaction, and it can be derived by different perturbative approaches such as Feynman diagrams, Wick's decomposition or functional derivatives, and to different levels of approximation, such as Hartree-Fock or second Born. The perturbative expansion of Eq. (3.36) is reviewed in App. E on the example of the type of generic fermion-boson interaction relevant for the interaction of carriers with photons and phonons. The diagrammatic version of the Dysons equation is shown in Fig. 3.3.

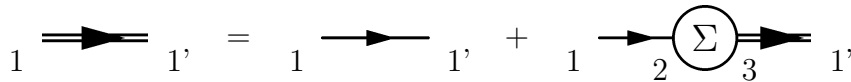


Figure 3.3: Diagrammatic Dyson equation for carrier Green's function.

3.3.2 Analytic continuation

To reduce the unpractical contour integration resulting from the formal perturbation expansion to real-time integrals, rules for analytical continuation are required, such as provided by the mapping of Keldysh [168], which for a given position on the contour C in Fig. 3.4 relates the contour-ordered Green's functions to a specific kind of real-time Green's functions,

$$G(1, 1') \equiv \begin{cases} G^C(11') & t_1, t_{1'} \in C_1, \\ G^>(11') & t_1 \in C_2, t_{1'} \in C_1, \\ G^<(11') & t_1 \in C_1, t_{1'} \in C_2, \\ G^{\tilde{C}}(1, 1') & t_1, t_{1'} \in C_2, \end{cases} \quad (3.55)$$

which are named the *lesser*, *greater*, *chronological* and *antichronological* Green's functions and are defined by

$$G^<(11') \equiv \pm \frac{i}{\hbar} \langle \hat{\Psi}_{\mathcal{H}}^\dagger(1') \hat{\Psi}_{\mathcal{H}}(1) \rangle, \quad (3.56)$$

$$G^>(11') \equiv \mp \frac{i}{\hbar} \langle \hat{\Psi}_{\mathcal{H}}(1) \hat{\Psi}_{\mathcal{H}}^\dagger(1') \rangle, \quad (3.57)$$

$$G^C(11') \equiv \mp \frac{i}{\hbar} \langle \hat{T}_t \{ \Psi_{\mathcal{H}}(1) \hat{\Psi}_{\mathcal{H}}^\dagger(1') \} \rangle, \quad (3.58)$$

$$G^{\tilde{C}}(11') \equiv \mp \frac{i}{\hbar} \langle \hat{T}_{at} \{ \hat{\Psi}_{\mathcal{H}}(1) \hat{\Psi}_{\mathcal{H}}^\dagger(1') \} \rangle, \quad (3.59)$$

where the upper (lower) sign applies to fermions (bosons).

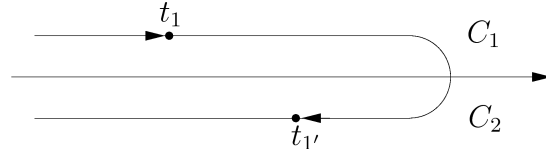


Figure 3.4: Contour for the mapping from contour-ordered to real-time Green's functions.

The chronological and antichronological Green's functions are usually replaced by the *retarded* and *advanced* Green's functions defined by

$$G^R(11') \equiv -\frac{i}{\hbar} \theta(t-t') \langle [\Psi_{\mathcal{H}}(1), \Psi_{\mathcal{H}}^\dagger(1')]_{\pm} \rangle \quad (3.60)$$

$$= \theta(t-t') [G^>(11') - G^<(11')], \quad (3.61)$$

$$G^A(11') \equiv \frac{i}{\hbar} \theta(t'-t) \langle [\Psi_{\mathcal{H}}(1), \Psi_{\mathcal{H}}^\dagger(1')]_{\pm} \rangle \quad (3.62)$$

$$= -\theta(t'-t) [G^>(11') - G^<(11')], \quad (3.63)$$

where $[\dots]_{\pm}$ denotes the anti-commutator (commutator), and which are related to the former via

$$G^C(11') = \theta(t-t') G^>(11') + \theta(t'-t) G^<(11') \quad (3.64)$$

$$= G^<(11') + G^R(11') \quad (3.65)$$

$$= G^>(11') + G^A(11'), \quad (3.66)$$

$$G^{\tilde{C}}(11') = \theta(t'-t) G^>(11') + \theta(t-t') G^<(11') \quad (3.67)$$

$$= G^<(11') - G^A(11') \quad (3.68)$$

$$= G^>(11') - G^R(11'). \quad (3.69)$$

From Eq. (3.55) follows that in the contour integration, depending on the position on the contour, all four Green's functions $G^{R,A,\lessgtr}$ are involved. Although there are four different Green's functions, only three of them are linearly independent; this is expressed in the relation

$$G^R(11') - G^A(11') = G^>(11') - G^<(11'). \quad (3.70)$$

A similar relation holds for other two-time quantities defined on the contour C , such as the self-energy $\Sigma(11')$,

$$\Sigma^R(11') - \Sigma^A(11') = \Sigma^>(11') - \Sigma^<(11'). \quad (3.71)$$

The contour integrations in Eq. (3.51) can be evaluated by decomposition into real time integrations using the rules due to Langreth [169], which are derived in App. A, e.g. for the operator product $C = AB$: the contour convolution

$$C(\tau, \tau') = \int_C d\tau_1 A(\tau, \tau_1) B(\tau_1, \tau') \quad (3.72)$$

has the real-time components

$$C^{R(A)}(t, t') = \int_{-\infty}^{\infty} dt_1 A^{R(A)}(t, t_1) B^{R(A)}(t_1, t'), \quad (3.73)$$

$$C^{\lessgtr}(t, t') = \int_{-\infty}^{\infty} dt_1 [A^R(t, t_1) B^{\lessgtr}(t_1, t') + A^{\lessgtr}(t, t_1) B^A(t_1, t')], \quad (3.74)$$

or, in a compact notation,

$$C^{R(A)} = A^{R(A)} B^{R(A)}, \quad (3.75)$$

$$C^{\lessgtr} = A^R B^{\lessgtr} + A^{\lessgtr} B^A. \quad (3.76)$$

In a similar fashion, the product $D = ABC$ of three operators has the real-time decomposition (again in compact notation)

$$D^{R(A)} = A^{R(A)} B^{R(A)} C^{R(A)}, \quad (3.77)$$

$$D^{\lessgtr} = A^R B^R C^{\lessgtr} + A^R B^{\lessgtr} C^A + A^{\lessgtr} B^A C^A. \quad (3.78)$$

Applying the Langreth rules to the integral formulation of the Dyson's equations in Eq. (3.51) and omitting the integrals, the equation for the retarded and advanced Green's functions simplifies to the form

$$G^{R(A)} = G_0^{R(A)} + G_0^{R(A)} \Sigma^{R(A)} G^{R(A)}, \quad (3.79)$$

which can be rewritten as

$$\left[\left(G_0^{R(A)} \right)^{-1} - \Sigma^{R(A)} \right] G^{R(A)} = \delta. \quad (3.80)$$

The corresponding equation for the lesser and greater functions reads

$$G^{\lessgtr} = G_0^{\lessgtr} + G_0^R \Sigma^R G^{\lessgtr} + G_0^R \Sigma^{\lessgtr} G^A + G_0^R \Sigma^A G^A. \quad (3.81)$$

By iteration with respect to $G^<$, one finds that the infinite order iterate has the form

$$G^{\lessgtr} = (\delta + G^R \Sigma^R) G_0^{\lessgtr} (\delta + G^A \Sigma^A) + G^R \Sigma^< G^A. \quad (3.82)$$

This equation is also called the *Keldysh equation*. It can be further simplified in steady state situations. Reversing Eq. (3.80) yields

$$G^R \left[(G_0^R)^{-1} - \Sigma^R \right] = \delta \quad \Rightarrow \quad \delta + G^R \Sigma^R = G^R \overleftarrow{G}_0^{-1} \quad (3.83)$$

where the arrow indicates the direction in which the operator acts. A similar expression is found for the retarded part. The first term of Eq. (3.82) can hence be written as

$$G^R \overleftarrow{G}_0^{-1} G_0^{\lessgtr} \overrightarrow{G}_0^{-1} G^A. \quad (3.84)$$

If no boundary terms are present, the central terms can be exchanged and the whole term vanishes since $\overrightarrow{G}_0^{-1} G_0^{\lessgtr} = 0$. The first term of Eq. (3.82) therefore corresponds to a boundary term representing initial conditions that contain the memory of the initial state before turning on the interactions and the onset of nonequilibrium dynamics. It is relevant only for the transient behaviour ([228, 232, 195]) and is therefore omitted in steady state calculations, where these initial effects are assumed to be damped; we will adopt this assumption in the subsequent chapters. The equations of motion for the real-time Green's functions are thus given by

$$G^{R(A)}(1, 1') = G_0^{R(A)}(1, 1') + \int d2 \int d3 G_0^{R(A)}(1, 2) \Sigma^{R(A)}(2, 3) G^{R(A)}(3, 1'), \quad (3.85)$$

$$G^{\lessgtr}(1, 1') = \int d2 \int d3 G^R(1, 2) \Sigma^{\lessgtr}(2, 3) G^A(3, 1') \quad (3.86)$$

where

$$\int d1 \equiv \sum_{\sigma_1} \int d\mathbf{r}_1 \int_{-\infty}^{\infty} dt_1. \quad (3.87)$$

3.3.3 Steady state representation

In Eqs. (3.85)-(3.86), the Dyson equations are written in integral form with a pair of real space and time coordinates as the two four vector arguments of the Green's functions. For steady state calculations, only the time *difference* $\tau = t' - t$ is meaningful. Fourier transforming from relative time to *energy* coordinates,

$$O_{\sigma_1\sigma_2}^\alpha(\mathbf{r}_1, \mathbf{r}_2; E) \equiv \int_{-\infty}^{\infty} d\tau e^{\frac{i}{\hbar}E\tau} O_{\sigma_1\sigma_2}^\alpha(\mathbf{r}_1, \mathbf{r}_2; \tau), \quad (3.88)$$

$$O_{\sigma_1\sigma_2}^\alpha(\mathbf{r}_1, \mathbf{r}_2; \tau) \equiv \frac{1}{2\pi\hbar} \int_{-\infty}^{\infty} dE e^{-\frac{i}{\hbar}E\tau} O_{\sigma_1\sigma_2}^\alpha(\mathbf{r}_1, \mathbf{r}_2; E), \quad (3.89)$$

$$O \in \{G, \Sigma\}, \quad \alpha \in \{R, A, <, >\},$$

Eqs. (3.85)-(3.86) can be written as ([233])

$$\begin{aligned} G_{\sigma_1\sigma_{1'}}^{R(A)}(\mathbf{r}_1, \mathbf{r}_{1'}; E) &= (G_0)_{\sigma_1\sigma_{1'}}^{R(A)}(\mathbf{r}_1, \mathbf{r}_{1'}; E) \\ &+ \sum_{\sigma_2, \sigma_3} \int d\mathbf{r}_2 \int d\mathbf{r}_3 (G_0)_{\sigma_1\sigma_2}^{R(A)}(\mathbf{r}_1, \mathbf{r}_2; E) \Sigma_{\sigma_2\sigma_3}^{R(A)}(\mathbf{r}_2, \mathbf{r}_3; E) G_{\sigma_3\sigma_{1'}}^{R(A)}(\mathbf{r}_3, \mathbf{r}_{1'}; E), \end{aligned} \quad (3.90)$$

$$G_{\sigma_1\sigma_{1'}}^{\lessgtr}(\mathbf{r}_1, \mathbf{r}_{1'}; E) = + \sum_{\sigma_2, \sigma_3} \int d\mathbf{r}_2 \int d\mathbf{r}_3 G_{\sigma_1\sigma_2}^R(\mathbf{r}_1, \mathbf{r}_2; E) \Sigma_{\sigma_2\sigma_3}^{\lessgtr}(\mathbf{r}_2, \mathbf{r}_3; E) G_{\sigma_3\sigma_{1'}}^A(\mathbf{r}_3, \mathbf{r}_{1'}; E), \quad (3.91)$$

with the noninteracting Green's function given by

$$\left[G_0^{R(A)} \right]^{-1}(\mathbf{r}, \mathbf{r}', E) = [E + (-)i\eta - H_0(\mathbf{r}) - U(\mathbf{r})] \delta(\mathbf{r} - \mathbf{r}'), \quad \eta \rightarrow 0^+, \quad (3.92)$$

where the small parameter η provides the correct analytical properties. In situations where time reversal symmetry holds, one finds

$$G^R(1, 1') = [G^A(1', 1)]^* \rightarrow G^R(\mathbf{r}, \mathbf{r}', E) = [G^A(\mathbf{r}, \mathbf{r}', E)]^\dagger, \quad (3.93)$$

$$G^{\lessgtr}(1, 1') = -[G^{\lessgtr}(1', 1)]^* \rightarrow G^{\lessgtr}(\mathbf{r}, \mathbf{r}', E) = -[G^{\lessgtr}(\mathbf{r}, \mathbf{r}', E)]^\dagger, \quad (3.94)$$

and the number of independent Green's functions is reduced to two. In equilibrium, the situation simplifies further, since all Green's functions are directly related through ²

$$G^<(E) = \pm if(E)A(E), \quad G^>(E) = i[\pm f(E) - 1]A(E), \quad (3.95)$$

²We omit spin and spatial arguments for clarity, and the upper (lower) sign corresponds to fermions (bosons)

where A is the *spectral function* defined by

$$A(E) \equiv i[G^R(E) - G^A(E)] = i[G^>(E) - G^<(E)], \quad (3.96)$$

and $f(E)$ is the statistical distribution function given by the Fermi-Dirac function in the case of fermions or the Bose-Einstein function for bosons. Eq. (3.95) is called the *fluctuation-dissipation* theorem. For the lesser and greater self-energies, the corresponding identities hold

$$\Sigma^<(E) = \pm i f(E) \Gamma(E), \quad \Sigma^>(E) = \pm i [f(E) - 1] \Gamma(E), \quad (3.97)$$

$$\Gamma(E) \equiv i [\Sigma^R(E) - \Sigma^A(E)] = i [\Sigma^>(E) - \Sigma^<(E)]. \quad (3.98)$$

Relation (3.172) for an energy dependent quantity O is a *Hilbert-transform*,

$$O^R(E) = \int d\tau e^{\frac{i}{\hbar} E \tau} O(\tau) = \int d\tau e^{\frac{i}{\hbar} E \tau} \theta(\tau) [O^>(\tau) - O^<(\tau)] \quad (3.99)$$

$$= \int \frac{dE'}{2\pi\hbar} \hat{\theta}(E' - E) [O^>(E') - O^<(E')] \quad (3.100)$$

$$= i \int \frac{dE'}{2\pi} \frac{O^>(E') - O^<(E')}{E' - E + i\eta}. \quad (3.101)$$

Using the identity

$$\lim_{\eta \rightarrow 0} \frac{1}{x + i\eta} = -i\pi\delta(x) + \mathcal{P} \left\{ \frac{1}{x} \right\}, \quad (3.102)$$

where \mathcal{P} denotes the *Cauchy principal value*, Eq. (3.101) can be rewritten as

$$O^R(E) = \mathcal{P} \int \frac{dE'}{2\pi} \frac{\mathcal{O}(E')}{E' - E} - \frac{i}{2} \mathcal{O}(E), \quad (3.103)$$

where $\mathcal{O}(E) = i[O^>(E) - O^<(E)]$. In this way, the Fourier transform of the retarded Green's function is related to the spectral function by

$$G^R(E) = i \int \frac{dE'}{2\pi} \frac{G^>(E') - G^<(E')}{E' - E + i\eta} = \mathcal{P} \int \frac{dE'}{2\pi} \frac{A(E')}{E' - E} - \frac{i}{2} A(E), \quad (3.104)$$

and the connection between the scattering functions and the retarded self energy becomes

$$\Sigma^R(E) = i \int \frac{dE'}{2\pi} \frac{\Sigma^>(E') - \Sigma^<(E')}{E' - E + i\eta} = \mathcal{P} \int \frac{dE'}{2\pi} \frac{\Gamma(E')}{E' - E} - \frac{i}{2} \Gamma(E). \quad (3.105)$$

We will further need the equivalence

$$\int d\tau e^{iE\tau/\hbar} \equiv \frac{1}{2\pi\hbar} \delta(E) \quad (3.106)$$

and the convolution theorem

$$\widehat{f(\tau) \cdot g(\tau)} = \frac{1}{2\pi\hbar} \{\hat{f} * \hat{g}\}(E) \equiv \int \frac{dE'}{2\pi\hbar} f(E') g(E - E'). \quad (3.107)$$

3.3.4 Physical quantities from NEGF

The real time Green's functions defined above have the following physical interpretation: The retarded Green's function G^R is a single-particle response function, describing particle propagation, while the advanced Green's function G^A describes the propagation of a hole. The spectral function A which combines the information about both types of excitations represents the density of states. The correlation functions $G^<$ and $G^>$ provide the spectral density of particles and holes, respectively. The Green's functions are related directly to physical observables, since the ensemble average of any single-body operator

$$\hat{O}(t) = \int d\mathbf{r} \hat{O}(\mathbf{r}, t) \quad (3.108)$$

$$= \int d\mathbf{r} \sum_{\sigma, \sigma'} \hat{\Psi}_{\mathcal{H}}^\dagger(\mathbf{r}, t, \sigma) O_{\sigma, \sigma'}(\mathbf{r}, t) \hat{\Psi}_{\mathcal{H}}(\mathbf{r}, t, \sigma') \quad (3.109)$$

can be written as [170]

$$\begin{aligned} \langle \hat{O}(\mathbf{r}, t) \rangle &= \text{Tr}[\rho \hat{O}(\mathbf{r}, t)] \\ &= \sum_{\sigma, \sigma'} \text{Tr}[\rho \hat{\Psi}_{\mathcal{H}}^\dagger(\mathbf{r}, t, \sigma) O_{\sigma, \sigma'}(\mathbf{r}, t) \hat{\Psi}_{\mathcal{H}}(\mathbf{r}, t, \sigma')] \\ &= \lim_{\mathbf{r} \rightarrow \mathbf{r}} \lim_{t' \rightarrow t+} \sum_{\sigma, \sigma'} O_{\sigma, \sigma'}(\mathbf{r}, t) \text{Tr}[\rho \hat{\Psi}_{\mathcal{H}}^\dagger(\mathbf{r}', t', \sigma) \hat{\Psi}_{\mathcal{H}}(\mathbf{r}, t, \sigma')] \\ &= \lim_{\mathbf{r} \rightarrow \mathbf{r}} \lim_{t' \rightarrow t+} \sum_{\sigma, \sigma'} O_{\sigma, \sigma'}(\mathbf{r}, t) \langle \hat{\Psi}_{\mathcal{H}}^\dagger(\mathbf{r}', t', \sigma) \hat{\Psi}_{\mathcal{H}}(\mathbf{r}, t, \sigma') \rangle \\ &= \mp \lim_{\mathbf{r} \rightarrow \mathbf{r}} \lim_{t' \rightarrow t+} \text{Tr}[O(\mathbf{r}, t) G^<(\mathbf{r}, t; \mathbf{r}', t')], \end{aligned} \quad (3.110)$$

where in the last line, the upper (lower) sign applies to fermions (bosons), and the trace is over spin indices.

The most relevant macroscopic quantities in the investigation of device characteristics are particle densities and currents. The corresponding operator averages shall thus be derived in the following.

Density

The expressions for particle and hole densities follow directly from the definition of the density operator and the Green's functions in (3.34):

a) particles

$$n(\mathbf{r}, t) = \sum_{\sigma} \langle \hat{\Psi}_{\mathcal{H}}^{\dagger}(\mathbf{r}, t, \sigma) \hat{\Psi}_{\mathcal{H}}(\mathbf{r}, t, \sigma) \rangle \quad (3.111)$$

$$= \mp \lim_{\mathbf{r}' \rightarrow \mathbf{r}} \lim_{t' \rightarrow t+} \sum_{\sigma} i\hbar G^{<}(\mathbf{r}, t, \sigma; \mathbf{r}', t', \sigma); \quad (3.112)$$

$$\text{(steady state)} \quad n(\mathbf{r}) = \mp \lim_{\mathbf{r}' \rightarrow \mathbf{r}} \lim_{t' \rightarrow t+} i\hbar \sum_{\sigma} G_{\sigma\sigma}^{<}(\mathbf{r}, \mathbf{r}'; t - t') \quad (3.113)$$

$$= \mp \lim_{\mathbf{r}' \rightarrow \mathbf{r}} \lim_{t' \rightarrow t+} i\hbar \sum_{\sigma} \int \frac{dE}{2\pi\hbar} e^{\frac{i}{\hbar}E(t-t')} G_{\sigma\sigma}^{<}(\mathbf{r}, \mathbf{r}; E) \quad (3.114)$$

$$= \mp i \sum_{\sigma} \int \frac{dE}{2\pi} G_{\sigma\sigma}^{<}(\mathbf{r}, \mathbf{r}; E) \quad (3.115)$$

b) holes

$$p(\mathbf{r}, t) = \sum_{\sigma} \langle \hat{\Psi}_{\mathcal{H}}(\mathbf{r}, t, \sigma) \hat{\Psi}_{\mathcal{H}}^{\dagger}(\mathbf{r}, t, \sigma) \rangle \quad (3.116)$$

$$= \pm \lim_{\mathbf{r}' \rightarrow \mathbf{r}} \lim_{t' \rightarrow t+} i\hbar \sum_{\sigma} G^{>}(\mathbf{r}, t, \sigma; \mathbf{r}', t', \sigma) \quad (3.117)$$

$$\text{(steady state)} \quad p(\mathbf{r}) = \pm \lim_{\mathbf{r}' \rightarrow \mathbf{r}} \lim_{t' \rightarrow t+} i\hbar \sum_{\sigma} \int \frac{dE}{2\pi\hbar} e^{\frac{i}{\hbar}E(t-t')} G_{\sigma\sigma}^{>}(\mathbf{r}, \mathbf{r}; E) \quad (3.118)$$

$$= \pm i \sum_{\sigma} \int \frac{dE}{2\pi} G_{\sigma\sigma}^{>}(\mathbf{r}, \mathbf{r}; E) \quad (3.119)$$

From the expression of the particle density (3.115) and the equilibrium relation for the particle correlation function (3.95), the density can be written as

$$n(\mathbf{r}) = -i \sum_{\sigma} \int \frac{dE}{2\pi} i f(E) A_{\sigma\sigma}(\mathbf{r}, \mathbf{r}; E) \quad (3.120)$$

$$\equiv \int dE f(E) \mathcal{D}(\mathbf{r}, E), \quad (3.121)$$

which defines the *local density of states* (LDOS) in terms of the spectral function,

$$\mathcal{D}(\mathbf{r}, E) \equiv \frac{1}{2\pi} \sum_{\sigma} A_{\sigma\sigma}(\mathbf{r}, \mathbf{r}; E) \quad (3.122)$$

$$= \frac{1}{2\pi} \sum_{\sigma} \Im\{G_{\sigma\sigma}^R(\mathbf{r}, \mathbf{r}; E)\}. \quad (3.123)$$

Current

Starting point for the derivation of the current in terms of non-equilibrium Green's functions are the Dyson's equations (3.45), (3.50) and (3.53)-(3.54). Taking the difference between the equations of motion with respect to t_1 and t_2 yields

$$\begin{aligned} & i\hbar \left(\frac{\partial}{\partial t_1} + \frac{\partial}{\partial t_2} \right) G(12) + [H_0(\mathbf{r}_1) - H_0(\mathbf{r}_2)] G(12) \\ &= [U(1) - U(2)] G(12) - i\hbar \int_C d3 [V(1-3) - V(2-3)] G^{(2)}(13^- 23^+) \end{aligned} \quad (3.124)$$

$$= [U(1) - U(2)] G(12) + \int_C d3 [\Sigma(13)G(32) - G(13)\Sigma(32)]. \quad (3.125)$$

Taking the limit $\mathbf{r}_2 \rightarrow \mathbf{r}_1$ and $t_2 \rightarrow t_1$, the corresponding equation for the lesser Green's function reads

$$i\hbar \frac{\partial}{\partial t} G^<(\mathbf{r}, t, \sigma; \mathbf{r}, t, \sigma') + \lim_{\mathbf{r}' \rightarrow \mathbf{r}} \frac{1}{2} [H_0(\mathbf{r}) - H_0(\mathbf{r}')] G^<(\mathbf{r}, t, \sigma; \mathbf{r}', t, \sigma') = 0, \quad (3.126)$$

as the rhs of Eq. (3.124) vanishes in this limit. By recalling the definition of the density and introducing the velocity $\mathbf{v}(\mathbf{r}) \equiv -\frac{i}{\hbar} [\mathbf{r}, H_0]$, the above equation can be written as

$$-\frac{\partial}{\partial t} n(\mathbf{r}, t) + \nabla_{\mathbf{r}} \cdot \left[\lim_{\mathbf{r}' \rightarrow \mathbf{r}} \frac{i\hbar}{2} [\mathbf{v}(\mathbf{r}) - \mathbf{v}(\mathbf{r}')] \sum_{\sigma} G^<(\mathbf{r}, t, \sigma; \mathbf{r}', t, \sigma) \right] = 0, \quad (3.127)$$

which, compared to the continuity equation

$$\frac{\partial}{\partial t} n(\mathbf{r}, t) + \nabla_{\mathbf{r}} \cdot \mathbf{J}(\mathbf{r}, t) = 0, \quad (3.128)$$

provides the following expression for the current:

$$\mathbf{J}(\mathbf{r}, t) = \lim_{\mathbf{r}' \rightarrow \mathbf{r}} \frac{i\hbar}{2} [\mathbf{v}(\mathbf{r}') - \mathbf{v}(\mathbf{r})] \sum_{\sigma} G^<(\mathbf{r}, t, \sigma; \mathbf{r}', t, \sigma), \quad (3.129)$$

with the steady-state form

$$\mathbf{J}(\mathbf{r}) = \sum_{\sigma} \int dE \mathbf{J}_{\sigma}(\mathbf{r}; E) = \lim_{\mathbf{r}' \rightarrow \mathbf{r}} \frac{i}{2} [\mathbf{v}(\mathbf{r}) - \mathbf{v}(\mathbf{r}')] \sum_{\sigma} \int \frac{dE}{2\pi} G_{\sigma\sigma}^<(\mathbf{r}, \mathbf{r}'; E). \quad (3.130)$$

Considering the explicit form of the noninteracting (spinless) Hamiltonian,

$$H_0(\mathbf{r}) \equiv \frac{\mathbf{p}_{\mathbf{r}}^2}{2m_0} + \sum_i V(\mathbf{r} - \mathbf{R}_i), \quad (3.131)$$

where $\mathbf{p}_\mathbf{r} = -i\hbar\nabla_\mathbf{r}$ and $V(\mathbf{r} - \mathbf{R}_i)$ the potential from the lattice atoms at positions \mathbf{R}_i , the current acquires the well known form

$$\mathbf{J}(\mathbf{r}, t) = \lim_{\mathbf{r}' \rightarrow \mathbf{r}} \frac{\hbar^2}{2m_0} [\nabla_\mathbf{r} - \nabla_{\mathbf{r}'}] G^<(\mathbf{r}, t; \mathbf{r}', t). \quad (3.132)$$

Based on Eq. 3.126, it is possible to define a steady-state *current operator* [171]

$$\hat{\mathcal{I}}_\sigma(E) \equiv \frac{1}{2\pi\hbar} \left[\hat{H}_0 G_{\sigma\sigma}^< - G_{\sigma\sigma}^< \hat{H}_0 \right], \quad (3.133)$$

such that

$$\mathcal{I}_\sigma(\mathbf{r}, \mathbf{r}; E) = \nabla \cdot \mathbf{J}_\sigma(\mathbf{r}; E) \quad (3.134)$$

With Eqs. (3.90) and (3.91), the current operator can be written as

$$\mathcal{I}(E) \equiv \frac{1}{2\pi\hbar} \left[\Sigma^R G^< - G^R \Sigma^< + \Sigma^< G^A - G^< \Sigma^A \right]. \quad (3.135)$$

The total *current flow* out of a certain volume V is given by

$$\sum_\sigma \int_V d\mathbf{r} \nabla \cdot \mathbf{J}_\sigma(\mathbf{r}; E) = \sum_\sigma \int_V \mathcal{I}_\sigma(\mathbf{r}, \mathbf{r}; E) \equiv \text{Tr}[\mathcal{I}(E)]. \quad (3.136)$$

The validity of the continuity equation and hence current *conservation* demands the equality of Eqs. (3.124) and (3.125), which implies that in the limit $\mathbf{r}_2 \rightarrow \mathbf{r}_1$ and $t_2 \rightarrow t_1$, the lesser part of

$$\int_C d3 [\Sigma(13)G(31) - G(13)\Sigma(31)] \quad (3.137)$$

must vanish, i.e.

$$\int d3 [\Sigma^R(13)G^<(31) + \Sigma^<(13)G^A(31) - G^R(13)\Sigma^<(31) - G^<(13)\Sigma^A(31)] = 0, \quad (3.138)$$

which for steady state conditions takes the form

$$\begin{aligned} \sum_{\sigma_3} \int d\mathbf{r}_3 \int \frac{dE}{2\pi\hbar} \left[\Sigma_{\sigma_1\sigma_3}^R(\mathbf{r}_1, \mathbf{r}_3; E) G_{\sigma_3\sigma_1}^<(\mathbf{r}_3, \mathbf{r}_1; E) + \Sigma_{\sigma_1\sigma_3}^<(\mathbf{r}_1, \mathbf{r}_3; E) G_{\sigma_3\sigma_1}^A(\mathbf{r}_3, \mathbf{r}_1; E) \right. \\ \left. - G_{\sigma_1\sigma_3}^R(\mathbf{r}_1, \mathbf{r}_3; E) \Sigma_{\sigma_3\sigma_1}^<(\mathbf{r}_3, \mathbf{r}_1; E) - G_{\sigma_1\sigma_3}^<(\mathbf{r}_1, \mathbf{r}_3; E) \Sigma_{\sigma_3\sigma_1}^A(\mathbf{r}_3, \mathbf{r}_1; E) \right] = 0. \end{aligned} \quad (3.139)$$

From Eqs. (3.135) and (3.136) it is obvious that this condition corresponds to

$$\int dE \text{Tr}[\mathcal{I}(E)] = 0. \quad (3.140)$$

Eq. (3.139) therefore ensures the conservation of particles, momentum and energy [167], and it must be satisfied by any approximation for the self-energies.

3.4 Application to transport in nanoscale devices

3.4.1 System partitioning, Hamiltonian and self-energies

Starting point for the application of the NEGF formalism to the modelling of a real device is the formulation of the Hamiltonian. For an adequate description, the device is divided into the following sections and the corresponding Hamiltonians [199, 171, 172, 234] (cf. Fig. 3.5):

- **contact regions:** Highly doped regions operating as carrier reservoirs. The carriers are assumed to be in equilibrium (through scattering) with a Fermi-distribution corresponding to chemical potentials $\mu_{L,R}$ and vanishing external potentials U (flat band condition). Apart from the equilibrating effect, interactions are not taken into account explicitly. Carriers are injected into scattering states occupied according to the Fermi-statistics of the contact, i.e. fully thermalized, and absorbed from the device in a nonequilibrium distribution. The idea that the electrodes or contacts in mesoscopic conductors need to be treated as a part of the transport problem dates back to Landauer [143, 235] and forms an essential ingredient of the Landauer-Büttiker transport formalism. It is via the phase-randomization in the contact that the irreversibility required for steady-state transport enters the theory.
- **leads:** Connection between contact regions and the device region. The isolated leads are described by the lead Hamiltonians $H_0^{L,R}$. Interactions are not considered in this region, which is however affected by the physical processes in the device through the spatially varying electrostatic potential U , and also by the coupling to the contacts via $H_0^{LD,RD} \equiv \tau$. It might be necessary to include such a region in cases where the spatial separation of the contacts and the interacting device is such that band-bending effects need to be considered, a situation that is encountered in quantum well solar cells.
- **device:** Interacting non-equilibrium region, subject to different scattering mechanisms involving carriers as well as photons, phonons, impurities, etc., i.e., unlike in the Landauer-Büttiker formalism, dissipative or phase-breaking processes are not restricted to the contacts, which constitutes the main advantage of the NEGF method. The interactions are described in specific terms H_{ep} , $H_{e\gamma}$, etc. of the Hamiltonian H_i . The scattering-free part H_0^D of the Hamiltonian describes ballistic transport: it contains the kinetic energy, the band structure effects and again the one-body potential U .

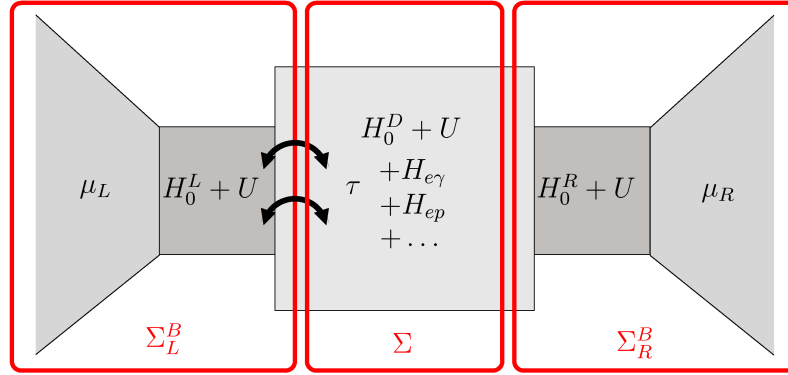


Figure 3.5: Partitioning of a typical device in NEGF modelling: the equilibrium contacts characterized by $\mu_{L,R}$ are connected to the interacting non-equilibrium device through non-interacting non-equilibrium leads. The effects of interactions are absorbed into respective self-energies Σ , while the effects of the coupling to extended contacts give rise to additional boundary self-energy terms Σ^B .

The total Hamiltonian of the overall system thus reads

$$H = H_0 + H_i, \quad (3.141)$$

$$H_0 = H_0^D + \underbrace{H_0^L + H_0^R + H_0^{LD} + H_0^{RD}}_{\rightarrow \Sigma^B}, \quad (3.142)$$

$$H_i = \underbrace{H_{e\gamma} + H_{ep} + \dots}_{\rightarrow \Sigma^I}. \quad (3.143)$$

One of the principal ideas in NEGF device modelling is now to absorb the effects of scattering in the device as well as the coupling to the leads into respective self-energies Σ^I and $\Sigma^B = \Sigma_L^B + \Sigma_R^B$, to appear in the Dyson's equations for the Green's functions in the corresponding regions. While the coupling to the leads, i.e. the effects of open boundaries, can be treated exactly, the self-energies for the different types of scattering in the device usually have to be determined perturbatively.

3.4.2 Basis functions and spatial discretization

A. General formalism

For the numerical evaluation of the Dyson's equations (3.90)-(3.91), the Green's functions first need to be expressed in a suitable basis. This is achieved by writing the field operators in Eq. (3.34) as linear combinations of creation and annihilation operators for a complete

set of orthonormal states $|\nu\rangle$ characterized by quantum numbers ν , with the expansion coefficients given by the corresponding single particle wave functions $\psi_\nu(\mathbf{r}, \sigma) \equiv \langle \mathbf{r}, \sigma | \nu \rangle$,

$$\hat{\Psi}_{\mathcal{H}}(\mathbf{r}, t, \sigma) \equiv \sum_{\nu} \psi_\nu(\mathbf{r}, \sigma) \hat{c}_\nu(t), \quad (3.144)$$

$$\hat{\Psi}_{\mathcal{H}}^\dagger(\mathbf{r}, t, \sigma) \equiv \sum_{\nu} \psi_\nu^*(\mathbf{r}, \sigma) \hat{c}_\nu^\dagger(t). \quad (3.145)$$

The Green's functions in this specific basis then follow as (we omit the spin index in the following)

$$G(11') = \sum_{\nu, \mu} \psi_\nu(\mathbf{r}) \langle \hat{T}_C \{ \hat{c}_\nu(t) \hat{c}_\mu^\dagger(t') \} \rangle \psi_\mu^*(\mathbf{r}') \quad (3.146)$$

$$\equiv \sum_{\nu, \mu} \psi_\nu(\mathbf{r}) G_{\nu\mu}(tt') \psi_\mu^*(\mathbf{r}'), \quad (3.147)$$

$$G_{\nu\mu}(tt') = \int d\mathbf{r} \int d\mathbf{r}' \psi_\nu^*(\mathbf{r}) G(11') \psi_\mu(\mathbf{r}'), \quad (3.148)$$

where, for a discrete basis, $G_{\nu\mu}(tt')$ is now a matrix-valued function. The equations of motion for the steady-state Green's functions $G_{\nu\mu}(E)$ are obtained via the insertion of the steady-state version of Eq. (3.147),

$$G(\mathbf{r}, \mathbf{r}'; E) = \sum_{\nu, \mu} \psi_\nu(\mathbf{r}) G_{\nu\mu}(E) \psi_\mu^*(\mathbf{r}'), \quad (3.149)$$

into Eqs. (3.90)-(3.91). For the retarded Green's function, this yields

$$\begin{aligned} \sum_{\nu, \mu} \psi_\nu(\mathbf{r}_1) G_{\nu\mu}^R(E) \psi_\mu^*(\mathbf{r}_{1'}) &= \sum_{\nu, \mu} \psi_\nu(\mathbf{r}_1) [G_0^R]_{\nu\mu}(E) \psi_\mu^*(\mathbf{r}_{1'}) \\ &+ \int d\mathbf{r}_2 \int d\mathbf{r}_3 \sum_{\substack{\nu_i, \mu_i \\ i=1,2,3}} \psi_{\nu_1}(\mathbf{r}_1) [G_0^R]_{\nu_1\mu_1}(E) \psi_{\mu_1}^*(\mathbf{r}_2) \\ &\times \psi_{\nu_2}(\mathbf{r}_2) \Sigma_{\nu_2\mu_2}^R(E) \psi_{\mu_2}^*(\mathbf{r}_3) \psi_{\nu_3}(\mathbf{r}_3) G_{\nu_3\mu_3}^R(E) \psi_{\mu_3}^*(\mathbf{r}_{1'}) \end{aligned} \quad (3.150)$$

$$\begin{aligned} &= \sum_{\nu, \mu} \psi_\nu(\mathbf{r}_1) [G_0^R]_{\nu\mu}(E) \psi_\mu^*(\mathbf{r}_{1'}) \\ &+ \sum_{\substack{\nu_i, \mu_i \\ i=1,2,3}} \psi_{\nu_1}(\mathbf{r}_1) [G_0^R]_{\nu_1\mu_1}(E) \Sigma_{\nu_2\mu_2}^R(E) G_{\nu_3\mu_3}^R(E) \\ &\times \underbrace{\int d\mathbf{r}_2 \psi_{\mu_1}^*(\mathbf{r}_2) \psi_{\nu_2}(\mathbf{r}_2)}_{\delta_{\mu_1, \nu_2}} \underbrace{\int d\mathbf{r}_3 \psi_{\mu_2}^*(\mathbf{r}_3) \psi_{\nu_3}(\mathbf{r}_3)}_{\delta_{\mu_2, \nu_3}} \end{aligned} \quad (3.151)$$

$$= \sum_{\nu, \mu} \psi_\nu(\mathbf{r}_1) \left\{ [G_0^R]_{\nu\mu}(E) + [\mathbf{G}_0^R \Sigma^R \mathbf{G}^R]_{\nu\mu}(E) \right\} \psi_\mu^*(\mathbf{r}_{1'}) \quad (3.152)$$

which is equivalent to the linear matrix equation

$$\mathbf{G}^R(E) = \mathbf{G}_0^R(E) + \mathbf{G}_0^R(E)\Sigma^R(E)\mathbf{G}^R(E), \quad (3.153)$$

that can also be written as

$$[\{\mathbf{G}_0^R(E)\}^{-1} - \Sigma^R(E)] \mathbf{G}^R(E) = \mathbb{1}, \quad (3.154)$$

providing the expression corresponding to Eq. (3.80), with the noninteracting Green's function \mathbf{G}_0^R given by

$$[G_0^R]_{\nu\mu}^{-1}(E) = \int d\mathbf{r} \int d\mathbf{r}' \psi_\nu^*(\mathbf{r}) [G_0^R]^{-1}(\mathbf{r}, \mathbf{r}'; E) \psi_\mu(\mathbf{r}') \quad (3.155)$$

$$= \int d\mathbf{r} \int d\mathbf{r}' \psi_\nu^*(\mathbf{r}) [E - H_0(\mathbf{r}) - U(\mathbf{r})] \delta(\mathbf{r} - \mathbf{r}') \psi_\mu(\mathbf{r}') \quad (3.156)$$

$$= \int d\mathbf{r} \psi_\nu^*(\mathbf{r}) [E - H_0(\mathbf{r}) - U(\mathbf{r})] \psi_\mu(\mathbf{r}) \quad (3.157)$$

$$= (E + i\eta)\delta_{\nu,\mu} - h_{\nu\mu} - u_{\nu\mu}, \quad \eta \rightarrow 0^+, \quad (3.158)$$

where

$$h_{\nu\mu} \equiv \int d\mathbf{r} \psi_\nu^*(\mathbf{r}) H_0(\mathbf{r}) \psi_\mu(\mathbf{r}), \quad (3.159)$$

$$u_{\nu\mu} \equiv \int d\mathbf{r} \psi_\nu^*(\mathbf{r}) U(\mathbf{r}) \psi_\mu(\mathbf{r}). \quad (3.160)$$

In the same way, the Dyson's equation (3.91) for the correlation functions acquires the form

$$\mathbf{G}^{\lessgtr}(E) = \mathbf{G}^R(E)\Sigma^{\lessgtr}(E)\mathbf{G}^A(E). \quad (3.161)$$

B. Tight-binding approach for layered structures

To accurately describe transport and optical processes in semiconductor quantum well structures, atomic resolution and the use of a realistic band structure are required. For that reason, the Green's functions and self-energies are calculated using an empirical *tight-binding* (TB) basis consisting of linear combinations of localized atomic orbitals and which reflects the layered nature of the compositional structure, since a proper account of dimensionality and symmetry of the problem often helps in reducing computational complexity. In the case of translational invariance in the direction perpendicular to transport and growth, it is possible to define a unit cell with the basis vectors separated into members of the parallel space (preserved periodicity of the crystal) and perpendicular space (translational symmetry broken due to external potential, heterojunction, etc.). This applies to

heterostructures such as quantum wells and superlattices. The Bravais-vector \mathbf{R} is decomposed into parallel and perpendicular components: $\mathbf{R} = \mathbf{R}_\perp + \mathbf{R}_\parallel$, where \mathbf{R}_\parallel defines the transverse Brillouin-zone BZ_\parallel for the transverse wave vectors \mathbf{k}_\parallel . The transverse unit cell may exceed the minimal one in the case materials which have different (but commensurate) unit cells. For the periodic (transverse) dimensions, the Bloch theorem holds and hence allows the restriction of the problem to the unit cell, reducing the number of atoms that need to be considered. The general Ansatz for the basis functions in Eqs. (3.144)-(3.145) is thus of the form

$$\psi_\nu(\mathbf{r}) \rightarrow \psi_{\alpha,L,\mathbf{k}_\parallel}(\mathbf{r}) = \frac{1}{\sqrt{N_\parallel}} \sum_{\mathbf{R}_\parallel^L} \varphi_\alpha(\mathbf{r} - \{\mathbf{R}_\parallel^L, z_L\}) e^{i\mathbf{k}_\parallel \cdot \mathbf{R}_\parallel^L}, \quad (3.162)$$

where $\varphi_\alpha(\mathbf{r} - \{\mathbf{R}_\parallel^L, z_L\})$ is the atomic orbital localized around $(\mathbf{R}_\parallel^L, z_L)$, with α and L labeling the type of orbital and the atomic layer, respectively. N_\parallel is a normalization factor corresponding to the number of unit cells in the parallel space.

A standard multiband TB-model which is suited for providing realistic band structures of *zinc-blende* semiconductors like GaAs, is the nearest neighbor $sp3s^*$ model [236], which uses excited s -orbitals together with the s and $p_{x,y,z}$ orbitals to construct the wave functions. However, the computational cost of such a multiband model is considerable, wherefore simplified approaches were investigated. In the simplest case, a combination of two single band tight-binding models with isotropic and parabolic transverse dispersion, equivalent to the effective mass approach, is used to model conduction and valence bands separately. In this type of model, where the parallel space is considered in the continuum limit, the basis functions have the simple form

$$\psi_{\alpha,L,\mathbf{k}_\parallel}(\mathbf{r}) = \frac{1}{\sqrt{\mathcal{A}}} e^{i\mathbf{k}_\parallel \cdot \mathbf{r}_\parallel} \varphi_\alpha(z - z_L), \quad (3.163)$$

where \mathcal{A} is the area of the transverse cross section. The most basic truly multiband model requires already two different basis orbitals to yield the two bands for electrons and holes. Also in that case, the transverse dispersion is considered via the addition of an isotropic, parabolic energy term corresponding to carriers which are free in the transverse planes. The considered models are presented in more detail in App. C .

To obtain the spatial discretization required for numerical evaluation of the equations of motion for the Green's functions, the device is partitioned into \mathcal{N} model layers of width Δ , with index L , where $L = 1, \dots, n_L$ contain the left contact and lead (H_0^L), layers $n_L + 1, \dots, n_R - 1$ the active device region and layers n_R, \dots, \mathcal{N} the right lead and contact (H_0^R). In general, a model layer (also called *superlayer* or *principal layer* [237]) may contain several atomic layers with different basis atoms of species i , located at $(\mathbf{R}_\parallel + \mathbf{v}_{\parallel,i}, L\Delta + v_{z,i})$,

where $(\mathbf{R}_{\parallel}, \mathbf{R}_{\perp} \equiv L\Delta\hat{z})$ indicates the positions of the model layer reference basis atoms and $\mathbf{v} = (\mathbf{v}_{\parallel,i}, v_{z,i})$ the relative displacement from that position within the unit cell, which depends on the direction of transport with respect to that of the layer growth. The basis is thus formed by linear combinations of the localized atomic orbitals $|\alpha i, L, \mathbf{R}_{\parallel}\rangle$, where α is the orbital label, e.g. s, p_x, p_y, \dots . In the case of zinc-blende compounds, one model layer contains a layer of *cations* (c) and a layer of *anions* (a), e.g. Ga and As in the case of GaAs, as illustrated in Fig. 3.6 for transport in the (001) direction.

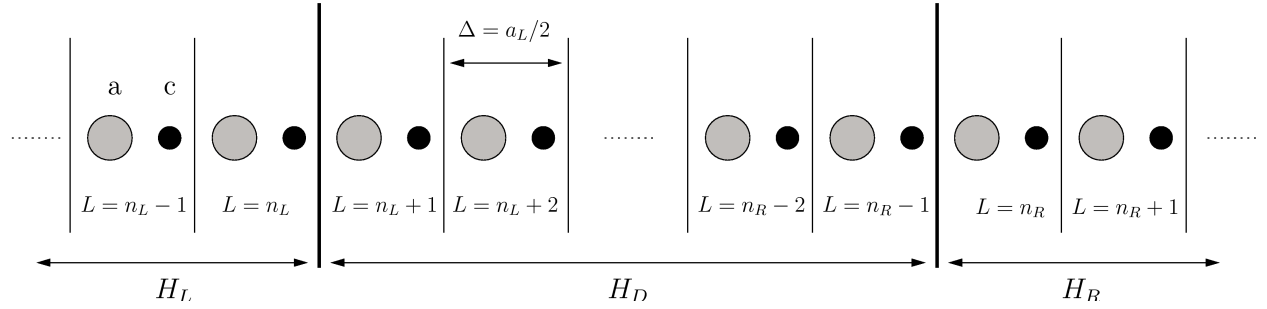


Figure 3.6: *Spatial discretization of a typical zinc-blende multilayer structure in (001) growth direction. The model layer of width $\Delta = a_L/2$, where a_L is the lattice constant, consists of the two atomic layers of the cation and the anion that together form the two-atom basis. The number of bands of the model is determined by the number of orbitals per model layer, which ranges from one (single band model) to ten (sp^3s^*) and more.*

In the single-band model, the anion and cation components are lumped together in one single orbital per layer, while in the two-band model, the cation is occupied by a s -type orbital and the anion by a p_z -type orbital. In a more advanced multiband approach to layered semiconductors, the scattering states are written as linear combinations of planar Bloch sums in the parallel space [237, 238],

$$|E, \mathbf{k}_{\parallel}\rangle = \sum_{\alpha, L} C_{\alpha, L}(E, \mathbf{k}_{\parallel}) |\alpha, L, \mathbf{k}_{\parallel}\rangle, \quad (3.164)$$

with the *planar orbitals*

$$|\alpha, L, \mathbf{k}_{\parallel}\rangle = \frac{1}{\sqrt{N_{\parallel}}} \sum_{\mathbf{R}_{\parallel}} e^{i\mathbf{k}_{\parallel} \cdot \mathbf{R}_{\parallel}} |\alpha, L, \mathbf{R}_{\parallel}\rangle, \quad (3.165)$$

corresponding to the basis functions in Eq. (3.162); to simplify the notation, α labels both the basis atom and the atomic orbital. With the use of the wave functions ($\mathbf{k} \equiv \mathbf{k}_{\parallel}$)

$$\psi_{\alpha, L, \mathbf{k}}(\mathbf{r}) \equiv \langle \mathbf{r} | \alpha, L, \mathbf{k} \rangle \quad (3.166)$$

in Eqs. (3.144)-(3.145), the carrier field operators corresponding to this *planar orbital basis* (POB) are

$$\hat{\Psi}_{\mathcal{H}}(\mathbf{r}, t) = \sum_{\mathbf{k}, L} \sum_{\alpha} \langle \mathbf{r} | \alpha, L, \mathbf{k} \rangle \hat{c}_{\alpha, L, \mathbf{k}}(t), \quad (3.167)$$

$$\hat{\Psi}_{\mathcal{H}}^{\dagger}(\mathbf{r}, t) = \sum_{\mathbf{k}, L} \sum_{\alpha} \langle \alpha, L, \mathbf{k} | \mathbf{r} \rangle \hat{c}_{\alpha, L, \mathbf{k}}^{\dagger}(t), \quad (3.168)$$

where $\hat{c}_{\alpha, L, \mathbf{k}}$ ($\hat{c}_{\alpha, L, \mathbf{k}}^{\dagger}$) is the annihilation (creation) operator for a fermion in state $|\alpha, L, \mathbf{k}\rangle$. The corresponding Green's functions are

$$G_{\alpha, L; \alpha', L'}^{<}(\mathbf{k}; t, t') = \frac{i}{\hbar} \langle c_{\alpha', L', \mathbf{k}}^{\dagger}(t') c_{\alpha, L, \mathbf{k}}(t) \rangle, \quad (3.169)$$

$$G_{\alpha, L; \alpha', L'}^{>}(\mathbf{k}; t, t') = -\frac{i}{\hbar} \langle c_{\alpha, L, \mathbf{k}}(t) c_{\alpha', L', \mathbf{k}}^{\dagger}(t') \rangle, \quad (3.170)$$

$$G_{\alpha, L; \alpha', L'}^R(\mathbf{k}; t, t') = -\frac{i}{\hbar} \theta(t - t') \langle [\hat{c}_{\alpha, L, \mathbf{k}}(t), \hat{c}_{\alpha', L', \mathbf{k}}^{\dagger}(t')]_{+} \rangle \quad (3.171)$$

$$= \theta(t - t') [G_{\alpha, L; \alpha', L'}^{>}(\mathbf{k}; t, t') - G_{\alpha, L; \alpha', L'}^{<}(\mathbf{k}; t, t')], \quad (3.172)$$

$$G_{\alpha, L; \alpha', L'}^A(\mathbf{k}; t, t') = \frac{i}{\hbar} \theta(t' - t) \langle [\hat{c}_{\alpha, L, \mathbf{k}}(t), \hat{c}_{\alpha', L', \mathbf{k}}^{\dagger}(t')]_{+} \rangle \quad (3.173)$$

$$= -\theta(t' - t) [G_{\alpha, L; \alpha', L'}^{>}(\mathbf{k}; t, t') - G_{\alpha, L; \alpha', L'}^{<}(\mathbf{k}; t, t')]. \quad (3.174)$$

The steady-state Green's functions $G_{\alpha, L; \alpha', L'}(\mathbf{k}; E)$, related to the above objects via the Fourier transform in Eq. (3.88), are obtained as the solutions of the Dyson's equations (3.154) and (3.154), which in the chosen basis become the linear equations

$$\mathbf{G}^R(\mathbf{k}, E) = \left[\{ \mathbf{G}_0^R(\mathbf{k}, E) \}^{-1} - \Sigma^R(\mathbf{k}, E) - \Sigma^{RB}(\mathbf{k}, E) \right]^{-1}, \quad (3.175)$$

$$\mathbf{G}_0^R(\mathbf{k}, E) = [(E + i\eta)\mathbb{1} - \mathbf{h}(\mathbf{k})]^{-1}, \quad (3.176)$$

$$\mathbf{G}^A(\mathbf{k}, E) = [\mathbf{G}^R(\mathbf{k}, E)]^{\dagger}, \quad (3.177)$$

$$\mathbf{G}^{\lessgtr}(\mathbf{k}, E) = \mathbf{G}^R(\mathbf{k}, E) [\Sigma^{\lessgtr}(\mathbf{k}, E) + \Sigma^{\lessgtr B}(\mathbf{k}, E)] \mathbf{G}^A(\mathbf{k}, E), \quad (3.178)$$

where the elements of the noninteracting tight-binding Hamiltonian $\mathbf{h}(\mathbf{k})$ are given by

$$h_{\alpha, L; \alpha', L'}(\mathbf{k}) = \int d\mathbf{r} \langle \alpha, L, \mathbf{k} | \mathbf{r} \rangle H_0(\mathbf{r}) \langle \mathbf{r} | \alpha', L', \mathbf{k} \rangle \equiv \langle \alpha, L, \mathbf{k} | \hat{H}_0 | \alpha', L', \mathbf{k} \rangle \quad (3.179)$$

$$= D_{\alpha, L; \alpha', L}(\mathbf{k}) \delta_{L, L'} + (1 - \delta_{L, L'}) t_{\alpha, L; \alpha', L'}(\mathbf{k}). \quad (3.180)$$

The diagonal blocks \mathbf{D} contain the orbital on-site energies, the electrostatic Hartree-potential U and the matrix elements that couple the atoms within the model layer, i.e. the *intra-layer* coupling elements, while the off-diagonal elements \mathbf{t} represent the *inter-layer* coupling. The explicit form of these elements depending on the specific crystal structure

is discussed in the literature, e.g. in [239, 125] for zinc-blende materials. $\Sigma^{i,B}$ are the boundary self-energies due to the coupling of the device to contacts, which will be discussed below, and Σ^i are the self-energies due to the interactions within the device, which may be determined using many-body perturbation theory for the Green's functions in Eqs. (3.169)-(3.174), starting from (3.36)

$$G_{\alpha,L;\alpha',L'}(\mathbf{k}; t, t') \equiv -\frac{i}{\hbar} \langle \hat{T}_C \left\{ e^{-\frac{i}{\hbar} \int_C ds H'(s)} c_{\alpha,L,\mathbf{k}}(t) c_{\alpha',L',\mathbf{k}}^\dagger(t') \right\} \rangle, \quad (3.181)$$

where the Hamiltonian $H'(s)$ of the perturbing interaction is represented in the chosen tight-binding basis, and expanding the exponential to the required order. After evaluation of the expansion terms by means of Feynman diagrams or Wick's theorem, the self energies are then obtained via comparison with their definition in the Dyson's equation (in block matrix notation³)

$$\begin{aligned} G_{L;L'}(\mathbf{k}; t, t') = & \{G_0\}_{L;L'}(\mathbf{k}; t, t') \\ & + \int_C ds \int_C ds' \sum_{L_1} \sum_{L_2} \{G_0\}_{L;L_1}(\mathbf{k}; t, s) \Sigma_{L_1;L_2}(\mathbf{k}; s, s') G_{L_2;L'}(\mathbf{k}; s', t'). \end{aligned} \quad (3.182)$$

The resulting expressions are derived in App. E and discussed in the next chapter for the interactions relevant in quantum well solar cells.

Once the Green's functions are found, physical quantities can be derived according to the expressions in Sec. 3.3.4. The expressions for density and current using the planar orbital basis are derived in App. C from the general expressions in terms of the Green's functions as given by Eqs. (3.119) and (3.130). The average electron (hole) density at layer L results in

$$n^{(p)}_L = -\frac{2i}{\mathcal{A}\Delta} \sum_{\mathbf{k}} \int \frac{dE}{2\pi} \sum_{\alpha} G_{\alpha,L;\alpha,L}^{<(>)}(\mathbf{k}; E) \quad (3.183)$$

$$= -\frac{2i}{\mathcal{A}\Delta} \sum_{\mathbf{k}} \int \frac{dE}{2\pi} \text{Tr}\{G_{L;L}^{<(>)}(\mathbf{k}; E)\}, \quad (3.184)$$

where the trace is over orbital indices. This corresponds to a local density of states at layer L of

$$\rho_L(E) = \frac{1}{\pi\mathcal{A}\Delta} \sum_{\mathbf{k}} \text{Tr}\{A_{L;L}(\mathbf{k}; E)\}, \quad (3.185)$$

³It is often useful to use *block matrix* notation and suppress orbital indices, or even *full matrix* notation, where all indices are omitted.

where $A = i(G^R - G^A)$ is the spectral function, and to a *density matrix*

$$\rho_{\alpha_1, L_1; \alpha_1, L_1}(\mathbf{k}) \equiv \int \frac{dE}{2\pi} \{-iG_{\alpha, L; \alpha', L'}^<(\mathbf{k}; E)\}. \quad (3.186)$$

The electron (hole) current density crossing the plane between layers L and $L+1$ is given by

$$J_L^{n(p)} = (-) \frac{2e}{\hbar \mathcal{A}} \sum_{\mathbf{k}} \int \frac{dE}{2\pi} \text{Tr} \{t_{L; L+1}(\mathbf{k}) G_{L+1; L}^{<(>)}(\mathbf{k}; E) - t_{L+1; L}(\mathbf{k}) G_{L; L+1}^{<(>)}(\mathbf{k}; E)\}, \quad (3.187)$$

and the conservation law corresponding to Eq. (3.139) for vanishing divergence of the electronic current becomes

$$0 = J_L^n - J_{L-1}^n = \frac{2e}{\hbar \mathcal{A}} \sum_{\mathbf{k}} \int \frac{dE}{2\pi} \text{Tr} \left\{ [\Sigma^R \mathbf{G}^< - \mathbf{G}^R \Sigma^< + \Sigma^< \mathbf{G}^A - \mathbf{G}^< \Sigma^A]_{L; L} \right\}. \quad (3.188)$$

3.4.3 Coupling to extended contacts: boundary self-energy treatment

To consider the effect of coupling the device to a large reservoir region, or lead, the overall Hamiltonian is written as [199, 171, 172, 234, 240, 203]

$$\mathbf{H} = \begin{pmatrix} \mathbf{H}_D & \tau \\ \tau^\dagger & \mathbf{H}_R \end{pmatrix}, \quad (3.189)$$

where \mathbf{H}_D and \mathbf{H}_R are the Hamiltonians of the isolated device and the large reservoir in thermal equilibrium, respectively, and τ denotes the coupling matrix between reservoir and device. The corresponding overall retarded Green's function satisfies the equation (corresponding to (3.175))

$$[(E + i\eta)\mathbb{1} - \mathbf{H}] \mathbf{G}^R = \mathbb{1}, \quad (3.190)$$

with $\eta \rightarrow 0^+$, and can thus be expressed as

$$\mathbf{G}^R = [(E + i\eta)\mathbb{1} - \mathbf{H}]^{-1} = \begin{pmatrix} (E + i\eta)\mathbb{1} - \mathbf{H}_D & -\tau \\ -\tau^\dagger & (E + i\eta)\mathbb{1} - \mathbf{H}_R \end{pmatrix}^{-1} \equiv \begin{pmatrix} \mathbf{G}_D^R & \mathbf{G}_{DR}^R \\ \mathbf{G}_{RD}^R & \mathbf{G}_R^R \end{pmatrix}. \quad (3.191)$$

Eq. (3.191), written out in components, can be used to obtain the retarded device Green's function \mathbf{G}_D^R , which is the interesting quantity, in terms of the retarded Green's function

$$\mathbf{g}^R \equiv [(E + i\eta)\mathbb{1} - \mathbf{H}_R]^{-1} \quad (3.192)$$

of the isolated lead which is usually accessible due to the approximations of thermal equilibrium, constant Hartree-potential and absence of interactions, and the model dependent coupling element τ :

$$\begin{pmatrix} (E + i\eta)\mathbb{1} - \mathbf{H}_D & -\tau \\ -\tau^\dagger & [\mathbf{g}^R]^{-1} \end{pmatrix} \cdot \begin{pmatrix} \mathbf{G}_D^R & \mathbf{G}_{DR}^R \\ \mathbf{G}_{RD}^R & \mathbf{G}_R^R \end{pmatrix} = \begin{pmatrix} \mathbb{1} & \mathbf{0} \\ \mathbf{0} & \mathbb{1} \end{pmatrix} \quad (3.193)$$

$$\Rightarrow \mathbf{G}_{DR}^R = \mathbf{G}_D^R \tau \mathbf{g}^R \quad (3.194)$$

$$\Rightarrow \mathbf{G}_D^R = [(E + i\eta)\mathbb{1} - \mathbf{H}_D - \tau^\dagger \mathbf{g}^R \tau]^{-1} \equiv [(E + i\eta)\mathbb{1} - \mathbf{H}_D - \Sigma^{RB}]^{-1}. \quad (3.195)$$

This identity defines the retarded boundary self-energy,

$$\Sigma^{RB} = \tau^\dagger \mathbf{g}^R \tau. \quad (3.196)$$

The correlation functions for device and reservoir follow from the Keldysh relation (3.86), e.g. for the lesser Green's function

$$\mathbf{G}^< = \mathbf{G}^R \Sigma^< \mathbf{G}^A = \begin{pmatrix} \mathbf{G}_D^R & \mathbf{G}_{DR}^R \\ \mathbf{G}_{RD}^R & \mathbf{G}_R^R \end{pmatrix} \cdot \begin{pmatrix} \Sigma_D^< & \Sigma_{DR}^< \\ \Sigma_{RD}^< & \Sigma_R^< \end{pmatrix} \cdot \begin{pmatrix} \mathbf{G}_D^A & \mathbf{G}_{DR}^A \\ \mathbf{G}_{RD}^A & \mathbf{G}_R^A \end{pmatrix}. \quad (3.197)$$

From the assumption of vanishing scattering between contacts and device, i.e. $\Sigma_{DR}^< = \Sigma_{RD}^< = 0$, follows

$$\mathbf{G}^< = \mathbf{G}_D^R \Sigma_D^< \mathbf{G}_D^A + \mathbf{G}_{DR}^R \Sigma_R^< \mathbf{G}_{RD}^A = \mathbf{G}_D^R (\Sigma_D^< + \underbrace{\tau \mathbf{g}^R \Sigma_R^< \mathbf{g}^A \tau^\dagger}_{\mathbf{g}^<}) \mathbf{G}_D^A \quad (3.198)$$

$$\equiv \mathbf{G}_D^R (\Sigma_D^< + \Sigma^{<B}) \mathbf{G}_D^A, \quad (3.199)$$

which corresponds to Eq. (3.178) and defines the boundary term

$$\Sigma^{<B} = \tau \mathbf{g}^< \tau^\dagger. \quad (3.200)$$

An analogous expression is found for $\Sigma^{>B}$. The lesser/greater Green's function of the equilibrium reservoir can be expressed in terms of the retarded and advanced functions using the fluctuation-dissipation theorem,

$$\mathbf{g}^< = -f_\mu(E)[\mathbf{g}^R - \mathbf{g}^A], \quad \mathbf{g}^> = -(1 - f_\mu(E))[\mathbf{g}^R - \mathbf{g}^A], \quad (3.201)$$

where μ is the chemical potential of the reservoir. Alternatively, this result can be obtained directly by the use of the equilibrium relation (3.98) for the boundary self-energies. The whole problem of the coupling to the reservoirs is now reduced to the calculation of the contact Green's function \mathbf{g}^R , which in principle is of infinite dimension, but only needs to be

known in the close vicinity of the device boundary, owing to the reduced dimensionality of the coupling matrix τ , and can therefore be calculated by surface Green's function methods using decimation techniques [241, 242, 243], conformal maps [244] or complex band methods [245, 238, 246, 213]. The method employed in this thesis is reviewed in detail in App. D for a general multiband tight-binding band structure model.

3.4.4 Physical interpretation

The retarded Green's function \mathbf{G}^R describes the coherent evolution of a carrier (electron/hole) between events that destroy coherence, such as scattering, escape to the contacts, etc. The retarded self energy Σ^R can be interpreted as an non-local effective potential describing the effects of coupling to leads and of interactions on the carrier dynamics in the device. It is non-Hermitian, indicator of loss processes. The Dyson's equation (3.175) hence is a Schrödinger-like equation describing the dynamics of quasi-particles as they propagate and decay via scattering processes or escape to the contacts. On the other hand, the correlation functions \mathbf{G}^{\lessgtr} describe the occupation of available states as given by the spectral function A , as well as the scattering of the carriers between different states in and outside the device, the scattering rates being quantified by the scattering functions Σ^{\lessgtr} , comparable to the scattering terms in the Boltzmann equation. The Keldysh equation (3.178) therefore corresponds to a kinetic equation ensuring that the particles which decay are reinjected. Together, the two equations lead to a Boltzmann-like picture of transport that combines quantum dynamics with a probabilistic description of scattering processes.

From the above interpretation of the lesser and greater self-energies, the rate of loss of electrons at a certain energy by scattering can be quantified by the function Γ as defined in (3.98),

$$\Gamma = i[\Sigma^> - \Sigma^<], \quad (3.202)$$

which then can be interpreted as a *broadening function* of the device energy levels, giving the eigenstates a finite lifetime τ , where

$$\frac{1}{\tau} = \frac{1}{\hbar} \text{Tr}\{\Gamma\}. \quad (3.203)$$

A similar interpretation is obtained in the case of current flow as given by Eq. (3.135)

$$\text{Tr}[\mathcal{I}] = \frac{e}{2\pi\hbar} \text{Tr}[\Sigma^R \mathbf{G}^< - \mathbf{G}^R \Sigma^< + \Sigma^< \mathbf{G}^A - \mathbf{G}^< \Sigma^A] \quad (3.204)$$

$$= \frac{e}{2\pi\hbar} \text{Tr}[\Sigma^< \mathbf{G}^> - \Sigma^> \mathbf{G}^<]. \quad (3.205)$$

As $\Sigma^<$ is the rate of inscattering into a state if it is empty and $\mathbf{G}^>$ contains the density of empty states, the term $\Sigma^< \mathbf{G}^>$ represents the actual rate of inscattering. Similarly,

the term $\Sigma^>\mathbf{G}^<$ represents the actual rate of outscattering. In the case of the boundary self-energy due to a given lead or contact, Eq. (3.205) provides the net inflow of charge from this contact. If, on the other hand, the self-energy is due to interactions within the device, (3.205) describes exchange of particles with a conceptual reservoir [171], i.e. no carriers are lost, but their energies may be altered in the exchange process, as e.g. in the case of inelastic scattering with phonons, where power is dissipated.

3.4.5 Self-consistent solution procedure

From Sec. 3.3.4 follows that the derivation of physical quantities like current or density requires the calculation of correlation functions \mathbf{G}^{\lessgtr} . Together with the expressions for the self-energies from boundaries and interactions, and the macroscopic Poisson equation

$$\epsilon_0 \frac{d}{dz} \left[\epsilon(z) \frac{d}{dz} U(z) \right] = n(z) - p(z) - N_{dop}(z), \quad (3.206)$$

relating the Hartree potential $U(z)$ to the doping density $N_{dop}(z)$ and the carrier densities derived from the Green's functions, the Dyson equations (3.175)-(3.178) form a closed set of equations for the latter that have to be solved self-consistently. As only a subset of Green's function matrix elements is needed, a recursive method [247, 211, 248] is computationally more efficient than the solution of the equivalent full linear system [172]. The recursion relations for the required Green's function elements are derived in App. B.

The solution procedure thus consists of the following steps:

1. Evaluation of the boundary terms
 - a) Calculation of the retarded boundary self-energy (Eq. (3.196)) and broadening functions due to the coupling to the contacts: $\Sigma^{(R,A)B} \Rightarrow \Gamma^B$.
 - b) The equilibrium relations (3.98) are used to calculate the boundary scattering functions $\Sigma^{\lessgtr B}$ from Γ^B which provides the carrier escape rates.
2. Calculation of the retarded Green's function \mathbf{G}^R from the Dyson equation (3.175) $\rightarrow \mathbf{G}^A = [\mathbf{G}^R]^\dagger$.
3. Calculation of the correlation functions \mathbf{G}^{\lessgtr} from the new retarded Green's functions and the self-energies Σ^{\lessgtr} , using the Keldysh relation (3.178).
4. Update of the self energies $\Sigma^{R,A,\lessgtr}$ due to the interactions in the device region, using the previously calculated Green's functions \rightarrow if the change is smaller than some threshold, the iteration stops, otherwise steps 2-4 are repeated.

5. Calculation of physical quantities such as density (3.184) and current (3.187) from the correlation function after convergence of the self-consistency iteration for Green's functions and self-energies.
6. To include effects such as charging or depletion due to doping and/or applied external potentials, the carrier densities derived from the Green's functions are used to solve Poisson's equation for an update of the Hartree potential U in an additional self-consistency loop.

The computational scheme is shown in Fig. 3.7.

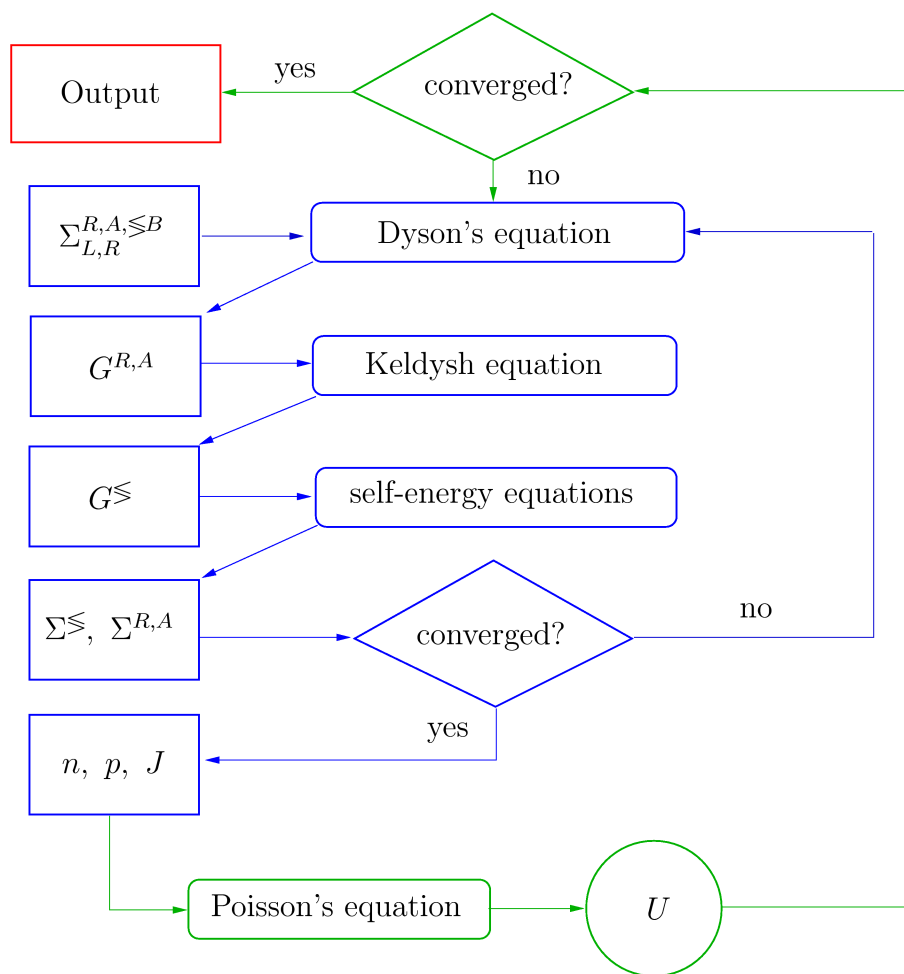


Figure 3.7: Computational scheme for the calculation of physical quantities from Green's functions and self energies. The inner self-consistency loop connects the equations for the Green's functions and the self energies, while the outer loop provides the update of the Hartree potential from the solution of Poisson's equation.

Chapter 4

A NEGF model of quantum well solar cells

Abstract: The general formalism of quantum transport theory with non-equilibrium Green's functions reviewed in the previous chapter is applied to the quantum well solar cell. After general considerations concerning bipolar heterojunction devices, the Hamiltonian of the QWSC system is formulated and discussed. The Hamiltonians of the interactions of electrons and holes with photons, phonons and among themselves are represented in the planar orbital basis, together with the corresponding self-energies.

4.1 Introduction

In order to apply the formalism established in the last chapter to a quantum well solar cell as introduced in Sec. 2.2, the latter is idealized to the elements and processes in Fig. 2.4, i.e. the device that will be described by the NEGF-formalism is a simple p - i - n diode with ohmic contacts at the end of the p and the n regions, some quantum well structure embedded in the intrinsic region, representing the device, and the homogeneous regions between contacts and device serving as bulk leads. The contact layer, where carriers are injected into the leads, is the only part that is considered from the extended reservoirs. This partitioning as illustrated in Fig. 4.1 is actually a compromise between a fully microscopic quantum theory and a model comprising the whole device, since interactions have to be neglected or treated in a very rough approximation in parts of the device, such as the leads, where they are certainly present and should therefore be considered. This for instance applies to both photogeneration and to relaxation processes, which in this partitioning are restricted to the central area. As a consequence, what is extracted from

the present approach is the physics of the central area rather than of the whole device. But since we are mainly interested in the photovoltaic processes occurring in this region, the approximation seems reasonable.

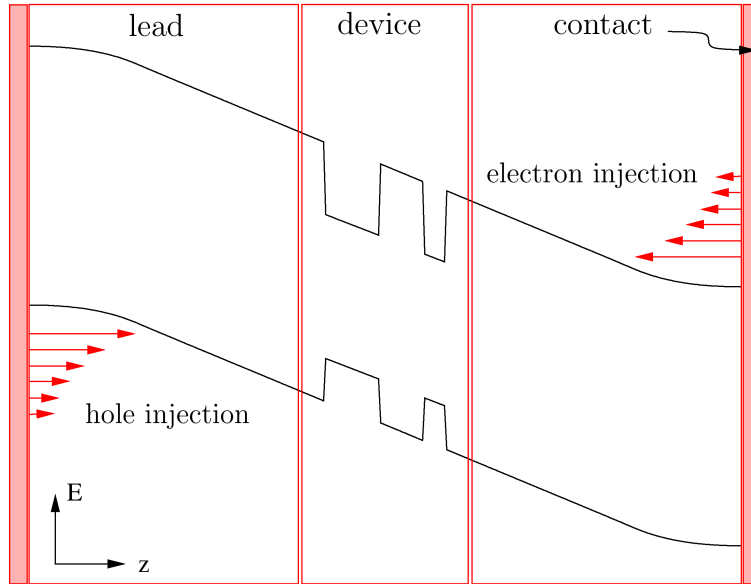


Figure 4.1: Partitioning of the idealized QWSC into contacts, leads and device regions.

QWSC are bipolar devices, in contrast to the nanoscale transistors that form the main area of application of the NEGF-formalism in quantum transport. This has important implications in that electrons and holes need to be treated on equal level, since from the p -contact, there is basically only hole injection into the valence band, while from the n -contact, only electrons are injected into the conduction band. The situation of course changes under large forward bias, i.e. near flat band conditions, where both carrier species start to be injected from both contacts. Another, more technical implication of the pronounced band bending present in bipolar devices is the emergence of spatial dependence in the physical content of the correlation functions G^{\lessgtr} , since for energies corresponding to states in the conduction band, $G^<$ and $G^>$ describe electrons and holes in the conduction band, respectively, and in the same way, $G^<$ and $G^>$ describe electrons and holes in the valence band at corresponding energies. This means that one has to be careful when integrating the Green's functions over energy in Eqs. (3.184) and (3.187) for the densities, since only the mobile charge densities, i.e. electrons in the conduction band and holes in the valence band, are relevant, which requires the introduction of suitable energy cutoffs near the corresponding band edges.

4.1.1 Model Hamiltonian

The full quantum well solar cell system is described in terms of the model Hamiltonian

$$\hat{H} = \hat{H}_e + \hat{H}_\gamma + \hat{H}_p, \quad (4.1)$$

$$\hat{H}_e = \hat{H}_e^0 + \hat{H}_e^i, \quad (4.2)$$

$$\hat{H}_e^i = \hat{H}_{e\gamma} + \hat{H}_{ep} + \hat{H}_{ee}, \quad (4.3)$$

consisting of the coupled systems of electrons (\hat{H}_e), photons (H_γ) and phonons (\hat{H}_p). Since the focus is on the electronic device characteristics, only \hat{H}_e is considered here, however including all of the terms of coupling to the bosonic systems. Within the electronic part, \hat{H}_e^0 provides ballistic transport: it contains the kinetic energy, the (bulk) band structure and band offsets, and also includes the electrostatic potential from the solution of Poisson's equation, which corresponds to the consideration of single species carrier-carrier scattering on the Hartree level. The interaction part \hat{H}_e^i consists of the terms \hat{H}_{ep} , $\hat{H}_{e\gamma}$ and \hat{H}_{ee} for the interactions of electrons with photons, phonons and electrons/holes, respectively.

The electron-photon Hamiltonian $\hat{H}_{e\gamma}$ describes the coupling of light and matter that is essential in the operation of a solar cell, providing the processes of *photogeneration* and *radiative recombination*. The coupling is assumed to be linear in the vector potential of the radiation field, and in a first approach, the dipole approximation is used, neglecting the spatial variation of the latter. In order to provide a starting point for a more general treatment of photons, i.e. on the same level as the carriers, the radiation field is quantized and the photon Green's function is introduced to formulate the self-energy of the interaction. In order to consider optical effects such as photon recycling, the full photon propagator should be evaluated, which corresponds to the evaluation of the photon self-energy and the solution of an additional Dyson equation for the photon Green's function in which the former is contained, and in fact amounts to the full consideration of the photon Hamiltonian \hat{H}_γ . But since in photovoltaics, unlike in laser physics, the light induced perturbation of the equilibrium carrier distribution is weak, it can be treated as a perturbation, and a low order self-energy approach is justified.

The Hamiltonian \hat{H}_{ep} contains contributions from the interaction of electrons with both polar optical and acoustic phonons. While the scattering with acoustic phonons is considered an elastic process which only leads to broadening of the spectral properties due to smearing in transverse momentum space corresponding to momentum relaxation, the interaction with polar optical phonons is inelastic and dissipates energy, resulting in both momentum and energy relaxation. This part of the interaction Hamiltonian thus provides the processes of *thermalization* and phonon assisted escape and capture. The interaction is encoded on the level of the harmonic approximation in respective versions of the Fröhlich

Hamiltonian. The corresponding self-energy exhibits the similarity of the interaction between electrons and phonons to that of electrons and photons, since both correspond to the interaction of fermions with the gauge bosons of some field, the electromagnetic in the case of the photons, and that of the ionic displacement in the case of the phonons. This also means that again, the phonon Green's function is introduced, even though the numerical treatment is kept on the level of a coupling to an equilibrium heat bath corresponding to the use of the equilibrium phonon propagator. The description of effects such as hot phonons would require renormalization of the phonon propagator via the solution of the corresponding Dyson's equation with the phonon self-energy, which amounts to the full consideration of \hat{H}_p .

The inter-carrier interaction Hamiltonian \hat{H}_{ee} contains the Coulomb interaction among electrons and holes. As mentioned above, the Hartree term of the particle-particle mean field approximation corresponds to the solution of Poisson's equation and is absorbed into the noninteracting Hamiltonian. *Excitonic* contributions come about by the particle-hole interaction in higher order terms such as direct-collision and exchange-collision, which are also needed for the description of nonradiative recombination processes such as the Auger effect.

There are of course many other kinds of interaction, like scattering by ionized impurities, alloy composition inhomogeneities or interface roughness, etc., that influence the transport properties. While their implementation is rather straightforward (see, e.g. [172]), in many cases their effect is similar to that of the phonon-scattering discussed above, just adding an additional broadening, and they are not likely to play a key role in the photovoltaic properties of the structures under consideration.

In the remaining of the chapter, the different parts of the interaction Hamiltonian in (4.3) shall be discussed and the corresponding self-energies be derived.

4.2 Electron-photon interaction

In this section, the NEGF formalism is extended to include the effects of electron-photon interactions [219, 220, 221, 222], i.e. the response of the carriers to an external oscillating electromagnetic field, within the context of quantum transport. The interaction with light gives rise to a photocurrent which can be used to quantify the optical and transport properties of a specific heterostructure.

4.2.1 Quantization of the electromagnetic field and photon Green's function

In order to express the interaction of electrons with light in terms of the Green's functions for electrons and photons, the electromagnetic field is represented in the quantized form given given by the field operator [197]

$$\hat{\mathbf{A}}(\mathbf{r}, t) = \sum_{\lambda, \mathbf{q}} \mathbf{A}_0(\lambda, \mathbf{q}) \left[\hat{b}_{\lambda, \mathbf{q}}(t) e^{i\mathbf{q}\mathbf{r}} + \hat{b}_{\lambda, \mathbf{q}}^\dagger(t) e^{-i\mathbf{q}\mathbf{r}} \right] \quad (4.4)$$

$$= \sum_{\lambda, \mathbf{q}} \mathbf{A}_0(\lambda, \mathbf{q}) \left[\hat{b}_{\lambda, \mathbf{q}}(t) + \hat{b}_{\lambda, -\mathbf{q}}^\dagger(t) \right] e^{i\mathbf{q}\mathbf{r}} \quad (4.5)$$

$$\equiv \sum_{\lambda, \mathbf{q}} \hat{\mathbf{A}}(\lambda, \mathbf{q}, t) e^{i\mathbf{q}\mathbf{r}}, \quad (4.6)$$

$$\mathbf{A}_0(\lambda, \mathbf{q}) = \sqrt{\frac{\hbar}{2\epsilon_0 V \omega_{\mathbf{q}}}} \epsilon_{\lambda \mathbf{q}} \quad (4.7)$$

where $\epsilon_{\lambda \mathbf{q}}$ is the polarization of the photon with wave vector \mathbf{q} and energy $\hbar\omega_{\mathbf{q}}$ added to or removed from mode λ by the bosonic creation and annihilation operators

$$\hat{b}_{\lambda, \mathbf{q}}^\dagger(t) = \hat{b}_{\lambda, \mathbf{q}}^\dagger e^{i\omega_{\mathbf{q}} t}, \quad (4.8)$$

$$\hat{b}_{\lambda, \mathbf{q}}(t) = \hat{b}_{\lambda, \mathbf{q}} e^{-i\omega_{\mathbf{q}} t}, \quad (4.9)$$

with

$$[\hat{b}_{\lambda, \mathbf{q}}, \hat{b}_{\lambda', \mathbf{q}'}^\dagger] = \delta_{\lambda, \lambda'} \delta_{\mathbf{q}\mathbf{q}'}, \quad (4.10)$$

$$[\hat{b}_{\lambda, \mathbf{q}}, \hat{b}_{\lambda', \mathbf{q}'}] = [\hat{b}_{\lambda, \mathbf{q}}^\dagger, \hat{b}_{\lambda', \mathbf{q}'}^\dagger] = 0, \quad (4.11)$$

and V is the absorbing volume. This form of the field operator actually corresponds to an optically homogeneous system, an assumption that does not strictly apply to heterostructures. But since we will later adopt the dipole approximation, any spatial dependence in the photon field will drop out of the problem and Eq. (4.4) remains a suitable starting point for the derivation of the interaction.

In terms of the bosonic operators introduced above, the photon Hamiltonian reads

$$\hat{H}_\gamma(t) = \sum_{\lambda, \mathbf{q}} \hbar\omega_{\mathbf{q}} \left(\hat{b}_{\lambda, \mathbf{q}}^\dagger(t) \hat{b}_{\lambda, \mathbf{q}}(t) + \frac{1}{2} \right), \quad (4.12)$$

and the components of the free Green's function of the vector potential are given by (in

momentum space)

$$\mathcal{D}_{\mu\nu}^0(\mathbf{q}; t, t') \equiv -\frac{i}{\hbar} \sum_{\lambda} \left\langle \hat{T}_C \left\{ \hat{A}_{\mu}(\lambda, \mathbf{q}, t) \hat{A}_{\nu}(\lambda, -\mathbf{q}, t') \right\} \right\rangle_0 \quad (4.13)$$

$$= \sum_{\lambda} [\mathbf{A}_0(\lambda, \mathbf{q})]_{\mu} [\mathbf{A}_0(\lambda, -\mathbf{q})]_{\nu} \times \left[-\frac{i}{\hbar} \left\langle \hat{T}_C \left\{ [\hat{b}_{\lambda, -\mathbf{q}}^{\dagger}(t) + \hat{b}_{\lambda, \mathbf{q}}(t)] [\hat{b}_{\lambda, \mathbf{q}}^{\dagger}(t') + \hat{b}_{\lambda, -\mathbf{q}}(t')] \right\} \right\rangle_0 \right] \quad (4.14)$$

$$\equiv \frac{\hbar}{2\epsilon_0 V \omega_{\mathbf{q}}} \sum_{\lambda} [\epsilon_{\lambda \mathbf{q}}]_{\mu} [\epsilon_{\lambda \mathbf{q}}]_{\nu} D_{\lambda}^0(\mathbf{q}; t, t'), \quad (4.15)$$

which defines the bare photon Green's function

$$D_{\lambda}^0(\mathbf{q}; t, t') \equiv -\frac{i}{\hbar} \left\langle \hat{T}_C \left\{ [\hat{b}_{\lambda, -\mathbf{q}}^{\dagger}(t) + \hat{b}_{\lambda, \mathbf{q}}(t)] [\hat{b}_{\lambda, \mathbf{q}}^{\dagger}(t') + \hat{b}_{\lambda, -\mathbf{q}}(t')] \right\} \right\rangle_0. \quad (4.16)$$

The corresponding real-time steady-state expressions, derived in App. E, are

$$D_{\lambda}^{0\leq}(\mathbf{q}, E) = -2\pi i [N_{\lambda, \mathbf{q}} \delta(E \mp \hbar\omega_{\mathbf{q}}) + (N_{\lambda, \mathbf{q}} + 1) \delta(E \pm \hbar\omega_{\mathbf{q}})], \quad (4.17)$$

$$D_{\lambda}^{0R,A}(\mathbf{q}, E) = \frac{1}{E - \hbar\omega_{\mathbf{q}} \pm i\eta} - \frac{1}{E + \hbar\omega_{\mathbf{q}} \pm i\eta}, \quad (4.18)$$

where

$$N_{\lambda, \mathbf{q}} \equiv \langle \hat{b}_{\lambda, \mathbf{q}}^{\dagger} \hat{b}_{\lambda, \mathbf{q}} \rangle_0 \quad (4.19)$$

is the occupation of photon mode (λ, \mathbf{q}) . This photon number depends on the type of radiation field that is described by $\hat{\mathbf{A}}$, as determined by the source of radiation. If the radiation is thermal, as in the case of the sun ($T \approx 6000K$) or the environment ($T \approx 300K$), the occupation is given by the corresponding Bose-Einstein distribution,

$$N_{\lambda, \mathbf{q}} = (e^{\hbar\omega_{\mathbf{q}}/k_B T} - 1)^{-1}. \quad (4.20)$$

The incident spectrum corresponding to a thermal occupation of the boson modes at the temperature of the radiation source is given by the intensity $J^{\gamma}(\hbar\omega_{\mathbf{q}})$.

Blackbody spectrum

For the calculation of absolute ‘‘AM1.5’’ efficiencies¹, the corresponding normalized solar black-body spectrum (shown in Fig. 4.2a) is used, which is given by

$$\frac{dJ_{\gamma}}{dE_{\gamma}} = \frac{d\Omega}{4\pi^3 \hbar^3 c^2} \frac{E_{\gamma}^3}{e^{E_{\gamma}/k_B T_s} - 1} \equiv \phi_{\gamma}(E_{\gamma}) E_{\gamma}, \quad (4.21)$$

¹The absorption effects of the atmosphere resulting in the deviations from the smooth black-body spectrum are neglected.

which defines the photon flux ϕ_γ and where $d\Omega = \pi \sin^2 \theta_s \approx 2.16 \times 10^{-5} \equiv F_s$ is the geometrical factor for the angular range of flat plate, with $\theta_s \approx 0.26$ the half angle subtended by the sun as seen from the earth (Fig. 4.2b), and the temperature of the sun $T_s \approx 5800K$.

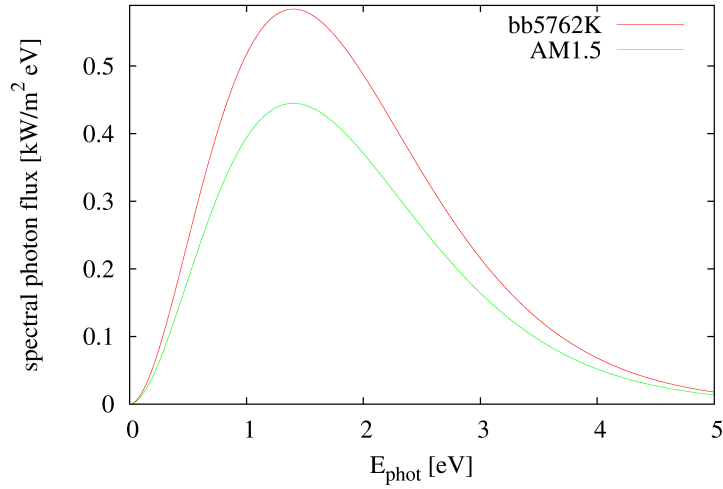


Figure 4.2: Black-body spectrum for $T = 5762K$ corresponding to solar radiation and the normalization to 1 kW/m^2 .

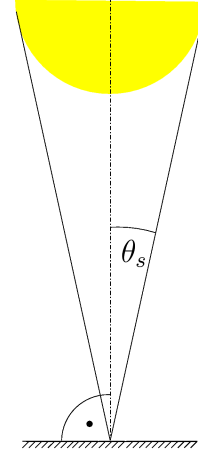


Figure 4.3: Angular range for solar illumination of a flat plate.

The incident power density used to obtain the efficiency in the polychromatic case is the integral of Eq. (4.21),

$$J_\gamma = \int_0^\infty dE_\gamma \phi(E_\gamma) E_\gamma. \quad (4.22)$$

In the case of the AM1.5 spectrum, this incident power density is fixed at 1 kW/m^2 .

Monochromatic illumination

For the investigation of spectral properties, it is sometimes useful to restrict the illumination to monochromatic light. For monochromatic, single-mode photons, the Bose-Einstein distribution $N_{\mathbf{q}}(\hbar\omega_{\lambda,\mathbf{q}})$ in the equilibrium bosonic propagator is replaced by

$$N_{\mathbf{q}}(\hbar\omega_{\lambda,\mathbf{q}}) = N_\gamma \delta(\hbar\omega_{\mathbf{q}} - E_\gamma), \quad (4.23)$$

where $N_\gamma(L)$ is the number of photons occupying the mode with energy $E_\gamma = \hbar\omega_\gamma$ in layer L , which in this case corresponds to the number of photons per layer for the given

radiation power J_γ ,

$$\phi_\gamma(L) = \frac{J_\gamma(L)}{E_\gamma} = \frac{N_\gamma c}{V\sqrt{\mu\varepsilon}} \Rightarrow N_\gamma(L) = \frac{J_\gamma(L)V\sqrt{\mu\varepsilon}}{E_\gamma c}, \quad (4.24)$$

where ε and μ are the (relative) dielectric constant and magnetic permeability of the interacting material, respectively. For a typical light intensity of 1 kW/m² the number of photons in a layer per unit area is $N_\gamma \approx 2.6 \text{ m}^{-2}$ in the case of monochromatic light with $E_\gamma = 0.8 \text{ eV}$. Neglecting the spatial variation of the field, i.e. under the assumptions of the dipole approximation (see below), the monochromatic field operator entering the interaction Hamiltonian has the form

$$\hat{\mathbf{A}}(t) = \sqrt{\frac{\hbar}{2\varepsilon_0 V \omega_\gamma}} \epsilon \left[\hat{b} e^{-i\omega_\gamma t} + \hat{b}^\dagger e^{i\omega_\gamma t} \right]. \quad (4.25)$$

4.2.2 Interaction Hamiltonian for layered systems

The operator $\hat{V}_{e\gamma}$ containing the interaction of light with matter has to first order in the electromagnetic vector potential \mathbf{A} and working in the Coulomb gauge $\nabla \cdot \mathbf{A} = 0$ the form

$$\hat{V}_{e\gamma} = -\frac{e}{m_0} \hat{\mathbf{A}} \cdot \hat{\mathbf{p}} \quad (4.26)$$

with $\hat{\mathbf{p}}$ the momentum operator and $\hat{\mathbf{A}}$ given by Eq. (4.4).

In the planar orbital basis, i.e. in terms of the field operators of Eq. (3.167)-(3.168), the electron-photon Hamiltonian of a layered system reads

$$\hat{H}_{e\gamma}(t) = \int d^3r \hat{\psi}^\dagger(\mathbf{r}, t) \hat{V}_{e\gamma}(\mathbf{r}) \hat{\psi}(\mathbf{r}, t) \quad (4.27)$$

$$= - \int d^3r \sum_{\mathbf{k}, L, \alpha} \sum_{\mathbf{k}', L', \alpha'} \hat{c}_{\alpha, L, \mathbf{k}}^\dagger(t) \langle \alpha, L, \mathbf{k} | \mathbf{r} \rangle \frac{e}{m_0} \hat{\mathbf{A}}(\mathbf{r}) \cdot \hat{\mathbf{p}} | \alpha', L', \mathbf{k}' \rangle \hat{c}_{\alpha', L', \mathbf{k}'}(t). \quad (4.28)$$

In the case of structures that are considerably shorter than the wavelength of the incident illumination, the *dipole approximation* can be used, which amounts to the limit $e^{\pm i\mathbf{q}\mathbf{r}} \approx 1$, where the field operator has no spatial dependence left. In this limit, the Hamiltonian for the electron-photon interaction can be simplified to

$$\begin{aligned} \hat{H}_{e\gamma}(t) &\approx - \sum_{L, L'} \sum_{\alpha, \alpha'} \sum_{\mathbf{k}, \mathbf{k}'} \sum_{\lambda, \mathbf{q}} \langle \alpha, L, \mathbf{k} | \hat{\mathbf{p}} | \alpha', L', \mathbf{k}' \rangle \frac{e}{m_0} \mathbf{A}_0(\lambda, \mathbf{q}) \left\{ \hat{b}_{\lambda, \mathbf{q}}(t) + \hat{b}_{\lambda, -\mathbf{q}}^\dagger(t) \right\} \\ &\quad \times \hat{c}_{\alpha, L, \mathbf{k}}^\dagger(t) \hat{c}_{\alpha', L', \mathbf{k}'}(t) \end{aligned} \quad (4.29)$$

$$= - \sum_{L, L'} \sum_{\alpha, \alpha'} \sum_{\mathbf{k}, \mathbf{q}, \lambda} M_{\alpha, L; \alpha', L'}^\gamma(\mathbf{k}, \mathbf{q}, \lambda) \hat{c}_{\alpha, L, \mathbf{k}}^\dagger(t) \hat{c}_{\alpha', L', \mathbf{k}}(t) (\hat{b}_{\lambda, \mathbf{q}} e^{-i\omega_{\mathbf{q}} t} + \hat{b}_{\lambda, -\mathbf{q}}^\dagger e^{i\omega_{\mathbf{q}} t}), \quad (4.30)$$

where M^γ contains the bandstructure-model dependent momentum-matrix elements

$$M_{\alpha,L;\alpha',L'}^\gamma(\mathbf{k}, \mathbf{q}, \lambda) \equiv \frac{e}{m_0} \mathbf{A}_0(\mathbf{q}, \lambda) \cdot \mathbf{p}_{\alpha,L;\alpha',L'}(\mathbf{k}), \quad (4.31)$$

$$\mathbf{p}_{\alpha,L;\alpha',L'}(\mathbf{k}) \equiv \langle \alpha, L, \mathbf{k} | \hat{\mathbf{p}} | \alpha', L', \mathbf{k} \rangle, \quad (4.32)$$

which can be written in terms of the tight-binding Hamiltonian as [133, 134, 137]

$$\langle \alpha, L, \mathbf{k} | \hat{\mathbf{p}} | \alpha', L', \mathbf{k}' \rangle = \frac{1}{N_{\parallel}} \sum_{\mathbf{R}_{\parallel}^L, \mathbf{R}_{\parallel}^{L'}} e^{i(\mathbf{k}' \mathbf{R}_{\parallel}^{L'} - \mathbf{k} \mathbf{R}_{\parallel}^L)} \langle \alpha, L, \mathbf{R}_{\parallel}^L | \hat{\mathbf{p}} | \alpha', L', \mathbf{R}_{\parallel}^{L'} \rangle, \quad (4.33)$$

$$\langle \alpha, L, \mathbf{R}_{\parallel}^L | \hat{\mathbf{p}} | \alpha', L', \mathbf{R}_{\parallel}^{L'} \rangle = \frac{m_0}{i\hbar} \langle \alpha, L, \mathbf{R}_{\parallel}^L | [\mathbf{r}, H^0] | \alpha', L', \mathbf{R}_{\parallel}^{L'} \rangle = \frac{im_0}{\hbar} (\mathbf{R}^{L'} - \mathbf{R}^L) [H_0]_{\alpha,L;\alpha',L'}. \quad (4.34)$$

For direct transitions, $\mathbf{k}' \approx \mathbf{k}$, in the case of indirect transitions, the carrier wave vectors differ by the phonon momentum, $\mathbf{k}' \approx \mathbf{k} \pm \mathbf{q}_{\parallel}$.

4.2.3 Electron-photon self-energy

The self-energies are obtained from the general expression for the Fock term in the self-consistent first-order Born approximation of the carrier-boson interaction given in App. E, using the Hamiltonian introduced in (4.30). The explicit form of the self-energy depends on the source of the radiation via the corresponding radiation field operator. Here we will consider the two special cases discussed above: monochromatic illumination (e.g. laser light) and blackbody-radiation (e.g. sunlight).

The lesser and greater self-energies read (in full matrix notation)

$$\begin{aligned} \Sigma_{e\gamma}^{\lessgtr}(\mathbf{k}; E) &= \sum_{\lambda, \mathbf{q}} M^\gamma(\mathbf{k}, \mathbf{q}, \lambda) [N_{\lambda, \mathbf{q}} G^{\lessgtr}(\mathbf{k}; E \mp \hbar\omega_{\mathbf{q}}) \\ &\quad + (N_{\lambda, \mathbf{q}} + 1) G^{\lessgtr}(\mathbf{k}; E \pm \hbar\omega_{\mathbf{q}})] M^\gamma(\mathbf{k}, \mathbf{q}, \lambda). \end{aligned} \quad (4.35)$$

Since these self-energies correspond to the scattering functions for the in- and outscattering via optical excitation, the first term of the lesser self-energy can be interpreted as describing the excitation of an electron from energy $E - \hbar\omega_{\mathbf{q}}$ to E via the absorption of a photon of energy $\hbar\omega_{\mathbf{q}}$. In the same way, the second term of this self-energy describes the relaxation of an electron from energy $E + \hbar\omega_{\mathbf{q}}$ to E via the emission of a photon of that energy. The greater self-energy has the same interpretation in terms of holes. As these expressions always contain both the excitation process and its inverse, the principle of detailed balance is automatically respected.

Substituting

$$\sum_{\mathbf{q}} \rightarrow \frac{V}{(2\pi\hbar c)^3} \int dE_\gamma E_\gamma^2 d\Omega_{\mathbf{q}}, \quad (4.36)$$

where $d\Omega_{\mathbf{q}}$ is the solid angle element of the radiation, and assuming normal incidence on a flat plate, the expression becomes

$$\begin{aligned} \Sigma_{e\gamma}^{\lessgtr}(\mathbf{k}; E) = F_s \frac{V}{(2\pi\hbar c)^3} \sum_{\lambda} \int dE_\gamma E_\gamma^2 M^\gamma(\mathbf{k}, E_\gamma, \lambda) & \left[N_\gamma^\lambda G^{\lessgtr}(\mathbf{k}; E \mp E_\gamma) \right. \\ & \left. + (N_\gamma^\lambda + 1) G^{\lessgtr}(\mathbf{k}; E \pm E_\gamma) \right] M^\gamma(\mathbf{k}, E_\gamma, \lambda), \end{aligned} \quad (4.37)$$

and the retarded and advanced self energies are given by

$$\begin{aligned} \Sigma_{e\gamma}^R(\mathbf{k}; E) = F_s \frac{V}{(2\pi\hbar c)^3} \sum_{\lambda} \int dE_\gamma E_\gamma^2 M^\gamma(\mathbf{k}, E_\gamma, \lambda) & \left[(N_\gamma^\lambda + 1) G^R(\mathbf{k}; E - E_\gamma) \right. \\ & + N_\gamma^\lambda G^R(\mathbf{k}; E + E_\gamma) + \frac{1}{2} [G^<(\mathbf{k}; E - E_\gamma) - G^<(\mathbf{k}; E + E_\gamma)] \\ & \left. + i\mathcal{P} \left\{ \int \frac{dE'}{2\pi} \left(\frac{G^<(\mathbf{k}; E - E')}{E' - E_\gamma} - \frac{G^<(\mathbf{k}; E - E')}{E' + E_\gamma} \right) \right\} \right] M^\gamma(\mathbf{k}, E_\gamma, \lambda), \end{aligned} \quad (4.38)$$

$$\begin{aligned} \Sigma_{e\gamma}^A(\mathbf{k}; E) = F_s \frac{V}{(2\pi\hbar c)^3} \sum_{\lambda} \int dE_\gamma E_\gamma^2 M^\gamma(\mathbf{k}, E_\gamma, \lambda) & \left[(N_\gamma^\lambda + 1) G^A(\mathbf{k}; E - E_\gamma) \right. \\ & + N_\gamma^\lambda G^A(\mathbf{k}; E + E_\gamma) + \frac{1}{2} [G^<(\mathbf{k}; E + E_\gamma) - G^<(\mathbf{k}; E - E_\gamma)] \\ & \left. + i\mathcal{P} \left\{ \int \frac{dE'}{2\pi} \left(\frac{G^<(\mathbf{k}; E - E')}{E' - E_\gamma} - \frac{G^<(\mathbf{k}; E - E')}{E' + E_\gamma} \right) \right\} \right] M^\gamma(\mathbf{k}, E_\gamma, \lambda). \end{aligned} \quad (4.39)$$

Numerically it is found that the principle value integral term has a vanishingly small imaginary part and the real part, which corresponds to a level renormalization and does not affect the carrier lifetime, dephasing or relaxation, contributes only to around one percent to the total real part of the retarded self-energy. It is therefore safe to neglect the principle value term altogether in the numerical simulation.

It is important to note that even for monochromatic illumination, the term of spontaneous emission will retain the sum over all photon energies, i.e. spontaneous emission is possible at any energy and is only limited by the joint density of states and the occupation of the states separated by this energy.

4.2.4 Absorption and emission from microscopic polarization

The absorption of light in a semiconductor heterostructure follows from the general behaviour of a light beam propagating in a dielectric medium characterized by a frequency

dependent complex dielectric function $\epsilon(\omega) = \epsilon'(\omega) + i\epsilon''(\omega)$: The equation for the oscillating electromagnetic field results from Maxwell's equations (in SI units)

$$\nabla \times \mathbf{H}(\mathbf{r}, t) = \frac{\partial}{\partial t} \mathbf{D}(\mathbf{r}, t), \quad (4.40)$$

$$\nabla \times \mathbf{E}(\mathbf{r}, t) = - \frac{\partial}{\partial t} \mathbf{B}(\mathbf{r}, t), \quad (4.41)$$

which for $\mathbf{B}(\mathbf{r}, t) \approx \mu_0 \mathbf{H}(\mathbf{r}, t)$ (i.e. $\mu \approx 1$) at optical frequencies yields

$$\nabla \times \nabla \times \mathbf{E}(\mathbf{r}, t) = -\mu_0 \frac{\partial}{\partial t} \nabla \times \mathbf{H}(\mathbf{r}, t) = -\mu_0 \frac{\partial^2}{\partial t^2} \mathbf{D}(\mathbf{r}, t). \quad (4.42)$$

Since $\nabla \times (\nabla \times) = \nabla(\nabla \cdot) - \Delta$, $\mathbf{D}(\mathbf{r}, \omega) = \epsilon_0 \epsilon(\omega) \mathbf{E}(\mathbf{r}, \omega)$ and $\epsilon_0 \mu_0 = 1/c^2$, the equation for a transverse field $\mathbf{E}(\mathbf{r}, t)$ with $\nabla \cdot \mathbf{E}(\mathbf{r}, t) = 0$ becomes

$$\Delta \mathbf{E}(\mathbf{r}, t) - \frac{1}{c^2} \frac{\partial^2}{\partial t^2} \mathbf{D}(\mathbf{r}, t) = 0. \quad (4.43)$$

Under Fourier transformation from time into frequency domain, the resulting equation for the field reads

$$\Delta \mathbf{E}(\mathbf{r}, \omega) + \frac{\omega^2}{c^2} [\epsilon'(\omega) + i\epsilon''(\omega)] \mathbf{E}(\mathbf{r}, \omega) = 0. \quad (4.44)$$

For the solution of Eq. (4.44) corresponding to a plane wave propagating in z -direction with a complex wave vector $k(\omega) + i\kappa(\omega)$, where κ is the *extinction coefficient*, i.e. for

$$\mathbf{E}(\mathbf{r}, \omega) = \mathbf{E}_0(\omega) e^{i[k(\omega) + i\kappa(\omega)]z}, \quad (4.45)$$

the relation between the extinction coefficient describing the (net) absorption and the dielectric function results from Eq. (4.44) to

$$[k(\omega) + i\kappa(\omega)]^2 = \frac{\omega^2}{c^2} [\epsilon'(\omega) + i\epsilon''(\omega)], \quad (4.46)$$

with the corresponding equations for real and imaginary parts

$$k^2(\omega) - \kappa^2(\omega) = \frac{\omega^2}{c^2} \epsilon'(\omega), \quad (4.47)$$

$$2\kappa(\omega)k(\omega) = \frac{\omega^2}{c^2} \epsilon''(\omega). \quad (4.48)$$

The *absorption coefficient* $\alpha(\omega)$ is now defined via

$$\alpha(\omega) \equiv 2\kappa(\omega). \quad (4.49)$$

This definition ensures that the intensity $I \propto |\mathbf{E}|^2$ decays like $e^{-\alpha z}$, i.e. $1/\alpha$ is the length over which the intensity of the light decreases by a factor $1/e$. From Eqs. (4.47)-(4.48),

the *refractive index* $n(\omega)$ defined by $n(\omega) = k(\omega)/k_0$, where $k_0 = \omega/c$ is the wave number in vacuum, is related to the dielectric function via

$$n(\omega) = \sqrt{\frac{1}{2}[\epsilon'(\omega) + \sqrt{\epsilon'^2(\omega) + \epsilon''^2(\omega)}]}. \quad (4.50)$$

With that, the expression for the absorption coefficient can be written as

$$\alpha(\omega) = \frac{\omega}{n(\omega)c} \epsilon''(\omega). \quad (4.51)$$

Now, for $\epsilon''(\omega) \ll \epsilon'(\omega)$, which is often true in semiconductors, expansion of (4.50) yields $n(\omega) \approx \sqrt{\epsilon'(\omega)}$, and if the frequency dependence of the refractive index is weak, the resulting expression is²

$$\alpha(\omega) \approx \frac{\omega}{c\sqrt{\epsilon_b}} \Im\{\epsilon(\omega)\}, \quad (4.52)$$

where ϵ_b is the background dielectric constant. In general crystals, the dielectric function is a tensor valued function, with diagonal transverse part, such that

$$\alpha_\mu(\omega) \approx \frac{\omega}{c\sqrt{\epsilon_b}} \Im\{\epsilon_{\mu\mu}(\omega)\}, \quad (4.53)$$

The (relative) dielectric function as used in (4.52) corresponds to the long wavelength limit $\epsilon(\omega) = \lim_{\mathbf{k} \rightarrow 0} \epsilon(\mathbf{k}, \omega)$ of the transverse dielectric function with components given by [225]

$$\epsilon_{\mu\mu}(\omega) = 1 - \frac{\omega_p}{\omega} - \frac{1}{\epsilon_0 \omega^2} \chi_{\mu\mu}^R(\omega), \quad (4.54)$$

where ω_p is the plasma frequency and $\chi^R(\omega)$ is the retarded form of the *current-current correlation function*, which follows from the *Kubo-Greenwood* formula

$$\chi_{\mu\nu}(\omega) = -\frac{i}{\hbar V} \int_C d\tau e^{i\omega\tau} \langle \hat{T}_C \{ \hat{j}_\mu(\tau) \hat{j}_\nu(0) \} \rangle, \quad (4.55)$$

where the dipole-approximation of the current operator is used,

$$\hat{j}_\mu(t) \equiv \frac{e}{m_0} \hat{p}_\mu(t). \quad (4.56)$$

In the POB-expansion, the momentum operator components are written as

$$\hat{p}_\mu(t) = \sum_{\alpha, \alpha'} \sum_{L, L'} \sum_{\mathbf{k}} p_{\alpha, L; \alpha', L'}^\mu(\mathbf{k}) \hat{c}_{\alpha, L, \mathbf{k}}^\dagger(t) \hat{c}_{\alpha', L', \mathbf{k}}(t), \quad (4.57)$$

²This expression is equivalent to $\alpha = \frac{4\pi}{\lambda_0} \Im\{n(\omega)\}$ often found in textbooks, since $\lambda_0 = 2\pi c/\omega$ and $\Im\{n(\omega)\} \approx \frac{1}{2} \Im\{\epsilon(\omega)\}$.

with the momentum-matrix elements $p_{\alpha,L;\alpha',L'}^{\mu}(\mathbf{k})$ defined in (4.32). Inserting this expression in Eq. (4.55) yields

$$\begin{aligned} \chi_{\mu\nu}(\omega) = & -\frac{ie^2}{m_0^2V\hbar} \sum_{L_1,\dots,L_4} \sum_{\alpha_1,\dots,\alpha_4} \sum_{\mathbf{k},\mathbf{k}'} p_{\alpha_1,L_1;\alpha_2,L_2}^{\mu}(\mathbf{k}) p_{\alpha_3,L_3;\alpha_4,L_4}^{\nu}(\mathbf{k}') \\ & \times \int_C d\tau e^{i\omega\tau} \langle \hat{T}_C \{ \hat{c}_{\alpha_1,L_1,\mathbf{k}}^{\dagger}(\tau) \hat{c}_{\alpha_2,L_2,\mathbf{k}}(\tau) \hat{c}_{\alpha_3,L_3,\mathbf{k}'}^{\dagger}(0) \hat{c}_{\alpha_4,L_4,\mathbf{k}'}(0) \} \rangle. \end{aligned} \quad (4.58)$$

The nonequilibrium ensemble average can be brought into the form

$$\langle \hat{T}_C \{ \hat{c}_{\alpha_1,L_1,\mathbf{k}}^{\dagger}(\tau) \hat{c}_{\alpha_2,L_2,\mathbf{k}}(t) \hat{c}_{\alpha_3,L_3,\mathbf{k}'}^{\dagger}(\tau) \hat{c}_{\alpha_4,L_4,\mathbf{k}'}(t) \} \rangle \quad (4.59)$$

$$= -\langle \hat{T}_C \{ \hat{c}_{\alpha_4,L_4,\mathbf{k}'}(0) \hat{c}_{\alpha_1,L_1,\mathbf{k}}^{\dagger}(\tau) \hat{c}_{\alpha_2,L_2,\mathbf{k}}(\tau) \hat{c}_{\alpha_3,L_3,\mathbf{k}'}^{\dagger}(0) \} \rangle \quad (4.60)$$

$$\equiv \hbar^2 \delta_{\mathbf{k},\mathbf{k}'} G_{\alpha_4,L_4;\alpha_1,L_1}(\mathbf{k}; 0, \tau) G_{\alpha_2,L_2;\alpha_3,L_3}(\mathbf{k}; \tau, 0) \quad (4.61)$$

$$\equiv \hbar^2 \delta_{\mathbf{k},\mathbf{k}'} G_{\alpha_2,L_2;\alpha_3,L_3}(\mathbf{k}; \tau) G_{\alpha_4,L_4;\alpha_1,L_1}(\mathbf{k}; -\tau), \quad (4.62)$$

where for the last line, steady-state conditions were assumed, and thus

$$\begin{aligned} \chi_{\mu\nu}(\omega) = & -\frac{ie^2\hbar}{m_0^2V} \sum_{L_1,\dots,L_4} \sum_{\alpha_1,\dots,\alpha_4} \sum_{\mathbf{k}} p_{\alpha_1,L_1;\alpha_2,L_2}^{\mu}(\mathbf{k}) p_{\alpha_3,L_3;\alpha_4,L_4}^{\nu}(\mathbf{k}) \\ & \times \int_C d\tau e^{i\omega\tau} G_{\alpha_2,L_2;\alpha_3,L_3}(\mathbf{k}; \tau) G_{\alpha_4,L_4;\alpha_1,L_1}(\mathbf{k}; -\tau) \end{aligned} \quad (4.63)$$

Since the linear absorption coefficient follows from Eqs. (4.52) and (4.54) to

$$\alpha_{\mu}(\hbar\omega) = -\frac{1}{\hbar\omega c \epsilon_0 \sqrt{\epsilon_b}} \Im \{ \chi_{\mu\mu}^R(\hbar\omega) \}, \quad (4.64)$$

we need $\Im \{ \chi_{\mu\mu}^R(\hbar\omega) \}$, which can be obtained from

$$\Im \{ \chi_{\mu\mu}^R(\hbar\omega) \} = -\frac{i}{2} [\chi_{\mu\mu}^>(\hbar\omega) - \chi_{\mu\mu}^<(\hbar\omega)], \quad (4.65)$$

where χ^{\lessgtr} follow from Eq. (4.63) via the application of the corresponding Langreth rules,

$$\begin{aligned} \chi_{\mu\nu}^{\lessgtr}(\hbar\omega) = & -\frac{ie^2\hbar}{m_0^2V} \sum_{L_1,\dots,L_4} \sum_{\alpha_1,\dots,\alpha_4} \sum_{\mathbf{k}} p_{\alpha_1,L_1;\alpha_2,L_2}^{\mu}(\mathbf{k}) p_{\alpha_3,L_3;\alpha_4,L_4}^{\nu}(\mathbf{k}) \\ & \times \int dt e^{i\hbar\omega t} G_{\alpha_2,L_2;\alpha_3,L_3}^{\lessgtr}(\mathbf{k}; t) G_{\alpha_4,L_4;\alpha_1,L_1}^{\gtrless}(\mathbf{k}; -t) \end{aligned} \quad (4.66)$$

$$= -\frac{ie^2\hbar}{m_0^2V} \sum_{\mathbf{k}} \int \frac{dE}{2\pi} \text{Tr} \{ \mathbf{p}^{\mu}(\mathbf{k}) \mathbf{G}^{\lessgtr}(\mathbf{k}; E) \mathbf{p}^{\nu}(\mathbf{k}) \mathbf{G}^{\gtrless}(\mathbf{k}; E - \hbar\omega) \}, \quad (4.67)$$

where in the last line, Eq. (3.107) was used, and the trace is over both layer and orbital indices.

From the form of the lesser and greater current correlation functions in terms of the Green's functions it follows that the two terms in Eq. (4.65) describe the *total* absorption and the emission due to radiative recombination, respectively, the difference corresponding to the *net* absorption. This means that the emission can also be obtained directly from the lesser current-correlation function, once the Green's functions are known.

For short active regions, the attenuation of the intensity due to absorption can be neglected. For extended devices with a large number of quantum wells, intensity attenuation and photon recycling needs to be considered, which in a first approximation can be achieved by the calculation of the (local) coefficients for absorption and stimulated emission (photoluminescence). The absorbed flux as a function of the absorption coefficient and penetration depth is given by

$$\phi_{\gamma,abs} = \phi_{\gamma}(1 - \exp \left\{ - \int_0^{L_{abs}} \alpha(z) dz \right\}) \equiv \phi_{\gamma} a_{\gamma} \quad (4.68)$$

where L_{abs} is the thickness of the absorbing material and a_{γ} is termed the *absorptivity* at given photon energy.

If effects that depend on the change in photon-mode occupation, such as photon recycling, have to be considered explicitly and on the same footing as the carriers, an additional Dyson equation has to be solved, which relates the full transverse photon propagator D to the transverse polarization function that plays the role of a photon self-energy, which shall be derived below.

4.2.5 Renormalization of the photon propagator: photon self-energy

The steady-state equation of motion for the photon Green's function is the Dyson equation

$$D_{\lambda}(\mathbf{q}; E) = D_{\lambda}^0(\mathbf{q}; E) + D_{\lambda}^0(\mathbf{q}; E)\Pi(\mathbf{q}; E)D_{\lambda}(\mathbf{q}; E), \quad (4.69)$$

where $\Pi(\mathbf{q}; E)$ is the *transverse polarization function* corresponding to the *photon self-energy*. Eq. (4.69) is a scalar equation and thus readily solved,

$$D_{\lambda}(\mathbf{q}; E) = \frac{D_{\lambda}^0(\mathbf{q}; E)}{1 - D_{\lambda}^0(\mathbf{q}; E)\Pi(\mathbf{q}; E)}. \quad (4.70)$$

In order to determine the photon Green's function, the self-energy $\Pi(\mathbf{q}; E)$ needs to be known. The full non-equilibrium photon Green's function for the interacting system follows from the perturbation expansion

$$D_{\lambda}(\mathbf{q}; t, t') = -\frac{i}{\hbar} \langle \hat{T}_C \{ e^{-\frac{i}{\hbar} \int_C \hat{H}_{e\gamma}(s) ds} [\hat{b}_{\lambda, -\mathbf{q}}^{\dagger}(t) + \hat{b}_{\lambda, \mathbf{q}}(t)] [\hat{b}_{\lambda, \mathbf{q}}^{\dagger}(t') + \hat{b}_{\lambda, -\mathbf{q}}(t')] \} \rangle, \quad (4.71)$$

where the Hamiltonian (4.30) of the dipole-approximation is used. The first order in perturbation theory vanishes, since it has an uneven number of boson operators in the summands

$$D_\lambda^{(1)}(\mathbf{q}; t, t') = \left(-\frac{i}{\hbar}\right)^2 \langle T_C \sum_{L, L'} \sum_{\alpha, \alpha'} \sum_{\mathbf{k}} \sum_{\tilde{\mathbf{q}}, \tilde{\lambda}} \int_C ds M_{\alpha, L; \alpha', L'}^\gamma(\mathbf{k}, \tilde{\mathbf{q}}, \tilde{\lambda}) \hat{c}_{\alpha, L, \mathbf{k}}^\dagger(s) \hat{c}_{\alpha', L', \mathbf{k}}(s) \times [\hat{b}_{\lambda, -\tilde{\mathbf{q}}}^\dagger(s) + \hat{b}_{\tilde{\lambda}, \tilde{\mathbf{q}}}(s)] [\hat{b}_{\lambda, -\mathbf{q}}^\dagger(t) + \hat{b}_{\lambda, \mathbf{q}}(t)] [\hat{b}_{\lambda, \mathbf{q}}^\dagger(t') + \hat{b}_{\lambda, -\mathbf{q}}(t')] \rangle. \quad (4.72)$$

The first contributing terms are thus from second order in the interaction,

$$D_\lambda^{(2)}(t, t') = \left(-\frac{i}{\hbar}\right)^3 \langle \hat{T}_C \sum_{L_1, \dots, L_4} \sum_{\mathbf{k}, \mathbf{k}'} \sum_{\tilde{\mathbf{q}}, \tilde{\mathbf{q}'}} \sum_{\tilde{\lambda}, \tilde{\lambda}'} \sum_{\alpha_1, \dots, \alpha_4} \int_C ds \int_C ds' M_{\alpha_1, L_1; \alpha_2, L_2}^\gamma(\mathbf{k}, \tilde{\mathbf{q}}, \tilde{\lambda}) \times \hat{c}_{\alpha_1, L_1, \mathbf{k}}^\dagger(s) \hat{c}_{\alpha_2, L_2, \mathbf{k}}(s) \hat{c}_{\alpha_3, L_3, \mathbf{k}'}^\dagger(s') \hat{c}_{\alpha_4, L_4, \mathbf{k}'}(s') [\hat{b}_{\lambda, -\tilde{\mathbf{q}}}^\dagger(s) + \hat{b}_{\tilde{\lambda}, \tilde{\mathbf{q}}}(s)] \times [\hat{b}_{\tilde{\lambda}', -\tilde{\mathbf{q}'}}^\dagger(s') + \hat{b}_{\tilde{\lambda}', \tilde{\mathbf{q}'}}(s')] [\hat{b}_{\lambda, -\mathbf{q}}^\dagger(t) + \hat{b}_{\lambda, \mathbf{q}}(t)] [\hat{b}_{\lambda, \mathbf{q}}^\dagger(t') + \hat{b}_{\lambda, -\mathbf{q}}(t')] \times M_{\alpha_3, L_3; \alpha_4, L_4}^\gamma(\mathbf{k}', \tilde{\mathbf{q}'}, \tilde{\lambda}') \rangle \quad (4.73)$$

$$= i\hbar \int_C ds \int_C ds' \sum_{L_1, \dots, L_4} \sum_{\mathbf{k}, \mathbf{k}'} \sum_{\tilde{\mathbf{q}}, \tilde{\mathbf{q}'}} \sum_{\tilde{\lambda}, \tilde{\lambda}'} \sum_{\alpha_1, \dots, \alpha_4} \delta_{\tilde{\lambda}, \lambda} \delta_{\tilde{\lambda}', \lambda} \delta_{\tilde{\mathbf{q}}, \mathbf{q}} \delta_{\tilde{\mathbf{q}'}, -\mathbf{q}} D_\lambda(\tilde{\mathbf{q}}; t, s) \times M_{\alpha_1, L_1; \alpha_2, L_2}^\gamma(\mathbf{k}, \tilde{\mathbf{q}}, \tilde{\lambda}) \delta_{\mathbf{k}, \mathbf{k}'} G_{\alpha_2, L_2; \alpha_3, L_3}(\mathbf{k}; s, s') \delta_{\mathbf{k}, \mathbf{k}'} G_{\alpha_4, L_4; \alpha_1, L_1}(\mathbf{k}; s', s) \times M_{\alpha_3, L_3; \alpha_4, L_4}^\gamma(\mathbf{k}', \tilde{\mathbf{q}'}, \tilde{\lambda}') D_\lambda(\tilde{\mathbf{q}'}; s', t') \quad (4.74)$$

$$= \int_C ds \int_C ds' D_\lambda(\mathbf{q}; t, s) \Pi_\lambda(\mathbf{q}; s, s') D_\lambda(\mathbf{q}; s', t'), \quad (4.75)$$

which yields the photon self-energy

$$\Pi_\lambda(\mathbf{q}; s, s') = i\hbar \sum_{\mathbf{k}} \sum_{L_1, \dots, L_4} \sum_{\alpha_1, \dots, \alpha_4} M_{\alpha_1, L_1; \alpha_2, L_2}^\gamma(\mathbf{k}, \mathbf{q}, \lambda) G_{\alpha_2, L_2; \alpha_3, L_3}(\mathbf{k}; s, s') \times G_{\alpha_4, L_4; \alpha_1, L_1}(\mathbf{k}; s', s) M_{\alpha_3, L_3; \alpha_4, L_4}^\gamma(\mathbf{k}, -\mathbf{q}, \lambda) \quad (4.76)$$

$$= i\hbar \sum_{\mathbf{k}} \text{Tr}\{M^\gamma(\mathbf{k}, \mathbf{q}, \lambda) G(\mathbf{k}; s, s') M^\gamma(\mathbf{k}, -\mathbf{q}, \lambda) G(\mathbf{k}; s', s)\}, \quad (4.77)$$

where the trace is both over orbital and layer indices. This expression is very similar to Eq. (4.63), and following the same procedure, we find the steady-state photon self-energy

$$\Pi_\lambda^\lessgtr(\mathbf{q}; E) = i \sum_{\mathbf{k}} \int \frac{dE'}{2\pi} \text{Tr}\{M^\gamma(\mathbf{k}, \mathbf{q}, \lambda) G^\lessgtr(\mathbf{k}; E') M^\gamma(\mathbf{k}, -\mathbf{q}, \lambda) G^\gtrless(\mathbf{k}; E' - E)\}, \quad (4.78)$$

and the corresponding retarded and advanced self-energies via the Hilbert-transform (3.101).

4.2.6 Quantum efficiency

The efficiency of a QWSC can be considered as formed by a factor for the actual generation of electron-hole pairs, i.e. the absorption process, and one for the following charge separation and collection, i.e. the whole transport process. The *external* quantum efficiency is defined as the normalized spectral response (SR) at zero bias, i.e. the short circuit photocurrent J_{sc} normalized by the current corresponding to the incoming photon flux ϕ_γ . For *monochromatic* illumination, the latter is given by $\phi_\gamma = \frac{J_\gamma}{\hbar\omega}$, where $J_\gamma \sim 1000$ W/m² is the light intensity. This yields for the spectral response and the EQE

$$SR(\hbar\omega) = \frac{J_{sc}(\hbar\omega)}{J_\gamma}, \quad (4.79)$$

$$EQE(\hbar\omega) = \frac{J_{sc}(\hbar\omega)}{\phi_\gamma e} = \frac{J_{sc}(\hbar\omega)}{J_\gamma} \frac{\hbar\omega}{e}. \quad (4.80)$$

The *internal* quantum efficiency (IQE) is obtained by replacing the incoming flux ϕ_γ by the absorbed flux $\phi_{\gamma,abs}$ given in Eq. (4.68). With that, the IQE is written as

$$IQE(\hbar\omega) = \frac{EQE(\hbar\omega)}{a_\gamma} = \frac{J_{sc}(\hbar\omega)}{J_\gamma a_\gamma} \frac{\hbar\omega}{e} \quad (4.81)$$

From this, the maximum current (IQE=1) for given absorptivity a_γ follows as

$$J_{sc}^{max} = e\phi_\gamma a_\gamma. \quad (4.82)$$

For GaAs, the absorption at $\hbar\omega = 1.42$ is $\alpha \approx 10^4$ cm⁻¹, which for a 30 ML thick absorbing region gives an absorptivity $a_\gamma \approx 0.008$. The expected maximum current is then of the order of $J_{sc} \approx 5.6$ Am⁻².

For *full spectrum* illumination, the photon flux is defined by Eq. (4.21), and the maximum generation current is given by

$$J_{sc}^{max} = q \int dE_\gamma \phi(E_\gamma) a(E_\gamma). \quad (4.83)$$

For a sun-temperature black-body spectrum normalized to an integrated intensity of 1000 Wm⁻² and with a high-energy cut-off at 2.11 eV, a maximum current $J_{sc}^{max} \approx 0.86$ Am⁻² results.

4.3 Electron-phonon interaction

In this section, the interaction of charge carriers with phonons is derived based on the nonequilibrium Green's function formalism. As in the case of the photons, we limit the discussion to bulk modes, i.e. the effects of confinement enter solely via the electronic part of the interaction.

4.3.1 Interaction Hamiltonian in planar orbital basis

The potential felt by electrons due to bulk phonons can be written as

$$\hat{V}_{ep}(t) = \frac{1}{\sqrt{V}} \sum_{\mathbf{q}} U_{\mathbf{q}} e^{i\mathbf{q}\cdot\mathbf{r}} \{\hat{a}_{\mathbf{q}}(t) + \hat{a}_{-\mathbf{q}}^{\dagger}(t)\}, \quad (4.84)$$

where \mathbf{r} is the electron coordinate, $\hat{a}_{\mathbf{q}}, \hat{a}_{\mathbf{q}}^{\dagger}$ are the bosonic creation and annihilation operators for a phonon mode with wave vector \mathbf{q} in the first Brillouin zone and $U_{\mathbf{q}}$ is the corresponding Fourier coefficient of the electron-ion potential [225]. In the planar orbital basis (3.165), using the field operators given in Eqs. (3.167)-(3.168), the interaction Hamiltonian in second quantization is

$$\begin{aligned} \hat{H}_{ep}(t) &= \int d\mathbf{r} \hat{\Psi}^{\dagger}(\mathbf{r}, t) \hat{V}_{ep}(t) \hat{\Psi}(\mathbf{r}, t) \\ &= \frac{1}{\sqrt{V}} \sum_{\mathbf{q}} U_{\mathbf{q}} \{\hat{a}_{\mathbf{q}}(t) + \hat{a}_{-\mathbf{q}}^{\dagger}(t)\} \int d^3r \hat{\Psi}^{\dagger}(\mathbf{r}, t) e^{i\mathbf{q}\cdot\mathbf{r}} \hat{\Psi}(\mathbf{r}, t) \\ &= \frac{1}{\sqrt{V}} \sum_{\mathbf{q}} U_{\mathbf{q}} \{\hat{a}_{\mathbf{q}}(t) + \hat{a}_{-\mathbf{q}}^{\dagger}(t)\} \\ &\quad \times \int d^3r \sum_{\mathbf{k}, \mathbf{k}'} \sum_{L, L'} \sum_{\alpha, \alpha'} \langle \alpha, L, \mathbf{k} | \mathbf{r} \rangle e^{i\mathbf{q}\cdot\mathbf{r}} \langle \mathbf{r} | \alpha', L, \mathbf{k}' \rangle \hat{c}_{\alpha, L, \mathbf{k}}^{\dagger}(t) \hat{c}_{\alpha', L', \mathbf{k}'}(t), \end{aligned} \quad (4.85)$$

where α labels the atomic-like orbitals (s, p_z , etc.) as well as the basis atoms (a, c), e.g. $\alpha = a_{p_z}$. For the evaluation of the matrix elements of $e^{i\mathbf{q}\cdot\mathbf{r}}$, the definition (3.165) of the planar orbitals in terms of the localized orbitals is used,

$$\langle \alpha, L, \mathbf{k} | e^{i\mathbf{q}\cdot\mathbf{r}} | \alpha', L', \mathbf{k}' \rangle = \frac{1}{N} \sum_{\mathbf{R}_{\parallel}, \mathbf{R}'_{\parallel}} \sum_{\alpha, \alpha'} \sum_{L, L'} \sum_{\mathbf{k}, \mathbf{k}'} e^{-i\mathbf{k}\cdot(\mathbf{R}_{\parallel} + \mathbf{v}_{\alpha})} \langle \alpha, L, \mathbf{R}_{\parallel} | e^{i\mathbf{q}\cdot\mathbf{r}} | \alpha', L', \mathbf{R}'_{\parallel} \rangle e^{i\mathbf{k}'\cdot(\mathbf{R}'_{\parallel} + \mathbf{v}_{\alpha'})}. \quad (4.86)$$

As Boykin showed in [136], a generally valid representation of the operator $e^{i\mathbf{q}\cdot\mathbf{r}}$ in the (bulk) tight-binding basis (Eq. (C.95))

$$|\alpha_b, \mathbf{k}\rangle = \frac{1}{\sqrt{N}} \sum_{j=1}^N e^{[i\mathbf{k}\cdot(\mathbf{R}_j + \mathbf{v}_{\mu})]} |\alpha_b, \mathbf{R}_j\rangle, \quad (4.87)$$

where the orbitals α are placed on atoms of type b at the positions $\mathbf{R}_j + \mathbf{v}_{\mu}$ and \mathbf{k} denotes a 3D wave vector from the first Brillouin zone, is given by

$$\int d^3r |\mathbf{r}\rangle e^{i\mathbf{q}\cdot\mathbf{r}} \langle \mathbf{r} | \rightarrow \sum_{i, \beta, \nu} |\beta, \nu, \mathbf{R}_i + \mathbf{v}_{\nu}\rangle e^{i\mathbf{q}\cdot(\mathbf{R}_i + \mathbf{v}_{\nu})} \langle \beta, \nu, \mathbf{R}_i + \mathbf{v}_{\nu} |. \quad (4.88)$$

In systems of broken translation symmetry, a corresponding representation has to be found in the planar orbital basis, which is related to (4.87) via

$$|\alpha, \mu, \mathbf{k}\rangle = \frac{1}{\sqrt{N}} \sum_L \sum_{\mathbf{R}_{\parallel}^L} e^{i(\{k_z, \mathbf{k}_{\parallel}\} \cdot \{\mathbf{R}_{\parallel}^L, L\Delta\} + \{\mathbf{v}_{\mu, \parallel}, v_{\mu, z}\})} |\alpha, \mu, \mathbf{R}_j + \mathbf{v}_{\mu}\rangle \quad (4.89)$$

$$= \sum_L e^{ik_z(\Delta L + v_{\tilde{\alpha}, z})} \frac{1}{\sqrt{N}} \sum_{\mathbf{R}_{\parallel}} e^{i\mathbf{k}_{\parallel} \cdot (\mathbf{R}_{\parallel}^L + \mathbf{v}_{\tilde{\alpha}, \parallel})} |\tilde{\alpha}, L, \mathbf{R}_{\parallel}\rangle \quad (4.90)$$

$$= \sum_L e^{ik_z(\Delta L + v_{\tilde{\alpha}, z})} |\tilde{\alpha}, L, \mathbf{k}_{\parallel}\rangle, \quad (4.91)$$

where for the position of the orbitals was used that $\mathbf{R}_j + \mathbf{v}_{\mu} \equiv \{\mathbf{R}_{\parallel}, \Delta L\} + \{\mathbf{v}_{\mu, \parallel}, v_{\mu, z}\}$ for some $\mathbf{R}_{\parallel}, L$, and $\tilde{\alpha} = \{\alpha, \mu\}$ contains both the atom as well as the orbital label. With that, the planar orbital representation of the phase factor is found as

$$\int d^3r |\mathbf{r}\rangle e^{i\mathbf{q} \cdot \mathbf{r}} \langle \mathbf{r}| \rightarrow \sum_{\beta} \sum_L e^{iq_z(L\Delta + v_{\beta, z})} \sum_{\mathbf{R}_{\parallel}} |\beta, L, \mathbf{R}_{\parallel}\rangle e^{i\mathbf{q}_{\parallel} \cdot (\mathbf{R}_{\parallel}^L + \mathbf{v}_{\beta, \parallel})} \langle \beta, L, \mathbf{R}_{\parallel}|, \quad (4.92)$$

and the corresponding matrix elements in (4.85) are

$$\begin{aligned} \langle \alpha, L, \mathbf{R}_{\parallel} | e^{i\mathbf{q} \cdot \mathbf{r}} | \alpha', L', \mathbf{R}'_{\parallel} \rangle &= \sum_{\beta} \sum_{\tilde{L}} \sum_{\tilde{\mathbf{R}}_{\parallel}} e^{iq_z(\tilde{L}\Delta + v_{\beta, z})} \sum_{\tilde{\mathbf{R}}_{\parallel}} e^{i\mathbf{q}_{\parallel} \cdot (\tilde{\mathbf{R}}_{\parallel} + \mathbf{v}_{\beta, \parallel})} \\ &\quad \times \underbrace{\langle \alpha, L, \mathbf{R}_{\parallel} | \beta, \tilde{L}, \tilde{\mathbf{R}}_{\parallel} \rangle}_{=\delta_{\alpha, \beta} \delta_{L, \tilde{L}} \delta_{\mathbf{R}_{\parallel}, \tilde{\mathbf{R}}_{\parallel}}} \underbrace{\langle \beta, \tilde{L}, \tilde{\mathbf{R}}_{\parallel} | \alpha', L', \mathbf{R}'_{\parallel} \rangle}_{=\delta_{\beta, \alpha'} \delta_{\tilde{L}, L'} \delta_{\tilde{\mathbf{R}}_{\parallel}, \mathbf{R}'_{\parallel}}} \end{aligned} \quad (4.93)$$

$$= e^{iq_z(\tilde{L}\Delta + v_{\alpha, z})} e^{i\mathbf{q}_{\parallel} \cdot (\mathbf{R}_{\parallel} + \mathbf{v}_{\alpha, \parallel})} \delta_{\alpha, \alpha'} \delta_{L, L'} \delta_{\mathbf{R}_{\parallel}, \mathbf{R}'_{\parallel}}. \quad (4.94)$$

Inserting this expression in (4.86) yields

$$\begin{aligned} \langle \alpha, L, \mathbf{k} | e^{i\mathbf{q} \cdot \mathbf{r}} | \alpha', L', \mathbf{k}' \rangle &= \frac{1}{N} \sum_{\alpha} \sum_L \sum_{\mathbf{k}, \mathbf{k}'} \sum_{\mathbf{R}_{\parallel}} e^{-i\mathbf{k} \cdot (\mathbf{R}_{\parallel} + \mathbf{v}_{\alpha, \parallel})} e^{iq_z(\tilde{L}\Delta + v_{\alpha, z})} e^{i\mathbf{q}_{\parallel} \cdot (\mathbf{R}_{\parallel} + \mathbf{v}_{\alpha, \parallel})} e^{i\mathbf{k}' \cdot (\mathbf{R}_{\parallel} + \mathbf{v}_{\alpha, \parallel})} \\ &= \frac{1}{N} \sum_{\alpha} \sum_L \sum_{\mathbf{k}, \mathbf{k}'} \left[\underbrace{\sum_{\mathbf{R}_{\parallel}} e^{i(\mathbf{q}_{\parallel} - \mathbf{k} + \mathbf{k}') \cdot (\mathbf{R}_{\parallel} + \mathbf{v}_{\alpha, \parallel})}}_{=N\delta_{\mathbf{k}', \mathbf{k} - \mathbf{q}_{\parallel}}} \right] e^{iq_z(\tilde{L}\Delta + v_{\alpha, z})} \end{aligned} \quad (4.95)$$

which leads to the interaction Hamiltonian

$$\hat{H}_{ep}(t) = \sum_{L, \mathbf{k}} \sum_{\mathbf{q}} \sum_{\alpha} \underbrace{\frac{U_{\mathbf{q}}}{\sqrt{V}} e^{iq_z(\Delta L + v_{\alpha, z})}}_{\equiv M_{\alpha, L}^{ep}(\mathbf{q})} [\hat{c}_{\alpha, L, \mathbf{k}}^{\dagger}(t) \hat{c}_{\alpha, L, \mathbf{k} - \mathbf{q}_{\parallel}}(t)] \left(\hat{a}_{\mathbf{q}}(t) + \hat{a}_{-\mathbf{q}}^{\dagger}(t) \right). \quad (4.96)$$

4.3.2 Scattering self-energies

The general expressions for the scattering functions are given in App. E. With $M(\mathbf{k}, \mathbf{q})_{L,L'} = \delta_{L,L'} M_{\alpha,L}^{ep}(\mathbf{q})$, and shifting the argument $\mathbf{k} - \mathbf{q}$ to the coupling element, the electron-phonon scattering self-energies can be written as

$$\Sigma_{\alpha,L;\alpha',L'}^{\leq,H} = 0, \quad (4.97)$$

$$\begin{aligned} \Sigma_{\alpha,L;\alpha',L'}^{R,H} &= -\delta_{\alpha,\alpha'} \delta_{L,L'} \frac{\hbar}{V} \sum_{\mathbf{k}} \sum_{\alpha_1,L_1} \rho_{\alpha_1,L_1;\alpha_1,L_1}(\mathbf{k}) \\ &\quad \times \sum_{q_z} \frac{2}{\hbar\omega_{\mathbf{q}=(0,q_z)}} |U_{\mathbf{q}=(0,q_z)}|^2 e^{-iq_z\Delta(L-L'+\nu_{\alpha,\alpha'})}, \end{aligned} \quad (4.98)$$

$$\begin{aligned} \Sigma_{\alpha,L;\alpha',L'}^{\leq,F}(\mathbf{k}; E) &= \frac{1}{V} \sum_{\mathbf{q}} |U_{\mathbf{k}-\mathbf{q}}|^2 e^{-iq_z\Delta(L-L'+\nu_{\alpha,\alpha'})} [N_{\mathbf{q}} G_{\alpha,L;\alpha',L'}^{\leq}(\mathbf{q}_{\parallel}; E \mp \hbar\omega_{\mathbf{q}}) \\ &\quad + (N_{\mathbf{q}} + 1) G_{\alpha,L;\alpha',L'}^{\leq}(\mathbf{q}_{\parallel}; E \pm \hbar\omega_{\mathbf{q}})], \end{aligned} \quad (4.99)$$

$$\begin{aligned} \Sigma_{\alpha,L;\alpha',L'}^{R,F}(\mathbf{k}; E) &= \frac{1}{V} \sum_{\mathbf{q}} |U_{\mathbf{k}-\mathbf{q}}|^2 e^{-iq_z\Delta(L-L'+\nu_{\alpha,\alpha'})} \left[(N_{\mathbf{q}} + 1) G_{\alpha,L;\alpha',L'}^R(\mathbf{q}_{\parallel}; E - \hbar\omega_{\mathbf{q}}) \right. \\ &\quad + N_{\mathbf{q}} G_{\alpha,L;\alpha',L'}^R(\mathbf{q}_{\parallel}; E + \hbar\omega_{\mathbf{q}}) + \frac{1}{2} \{ G_{\alpha,L;\alpha',L'}^<(\mathbf{q}_{\parallel}; E + \hbar\omega_{\mathbf{q}}) \\ &\quad \left. - G_{\alpha,L;\alpha',L'}^<(\mathbf{q}_{\parallel}; E - \hbar\omega_{\mathbf{q}}) \} \right], \end{aligned} \quad (4.100)$$

where $\rho_{\alpha_1,L_1;\alpha_1,L_1}(\mathbf{k})$ is the density matrix defined in (3.186), $N_{\mathbf{q}} = (e^{\hbar\omega_{\mathbf{q}}/k_B T} - 1)^{-1}$ is the Bose-Einstein factor for mode \mathbf{q} and ν depends on the details of the atomic orbital basis, e.g. for a two-atom (cation-anion) basis

$$\nu_{\alpha,\alpha'} = \begin{cases} \frac{1}{2} & \alpha = a, \alpha' = c, \\ -\frac{1}{2} & \alpha = c, \alpha' = a, \\ 0 & \text{otherwise.} \end{cases} \quad (4.101)$$

Polar optical phonons The spectrum of optical phonons can be approximated by a single characteristic frequency ω_{op} . The (screened) coupling element is given by [225]

$$|U_{\mathbf{q}}|^2 = \frac{\beta q^2}{(q^2 + q_0^2)^2}, \quad \beta = \frac{e^2 \hbar \omega_{op}}{2\epsilon_0} \left(\frac{1}{\epsilon_{\infty}} - \frac{1}{\epsilon} \right), \quad (4.102)$$

where ϵ the effective dielectric constant (~ 13.1 for GaAs) and ϵ_{∞} the high frequency dielectric constant (~ 10.9 for GaAs). Static screening is introduced via the inverse screening length q_0 , for which we take the inverse Debye screening length [249],

$$q_0 = \left(\frac{\rho e^2}{\epsilon \epsilon_0 k_B T} \right)^{1/2}, \quad (4.103)$$

where ρ is the carrier density of the screening medium.

In the isotropic approximation for the transverse dispersion, which is valid e.g. near the conduction band edge of GaAs, where the bands are nearly spherical, the summation over \mathbf{q} can be turned into an integral over cylindrical coordinates [250],

$$\frac{1}{V} \sum_{\mathbf{q}} |U_{\mathbf{k}-\mathbf{q}}|^2 e^{-iq_z \Delta(L-L'+\nu_{\alpha,\alpha'})} \propto \int \frac{dq_{\parallel} q_{\parallel}}{(2\pi)^2} \int_{-\frac{\pi}{\Delta}}^{\frac{\pi}{\Delta}} \frac{dq_z}{2\pi} e^{-iq_z \Delta(L-L'+\nu_{\alpha,\alpha'})} \underbrace{\int_0^{2\pi} d\theta \frac{|\mathbf{k}-\mathbf{q}|^2}{(|\mathbf{k}-\mathbf{q}|^2 + q_0^2)^2}}_{=I_{\theta}}. \quad (4.104)$$

I_{θ} can be written as an integration over the unit circle in the complex plane by substituting $z = e^{i\theta}$:

$$I_{\theta} = \int_0^{2\pi} d\theta \frac{k^2 + q_{\parallel}^2 + q_z^2 - 2kq_{\parallel} \cos \theta}{(k^2 + q_{\parallel}^2 + q_z^2 + q_0^2 - 2kq_{\parallel} \cos \theta)^2} = \frac{i}{kq_{\parallel}} \oint_{|z|=1} dz \left\{ \frac{1}{z^2 - bz + 1} + \frac{\frac{q_0^2}{kq_{\parallel}} z}{[z^2 - bz + 1]^2} \right\} \quad (4.105)$$

where

$$b = \frac{k^2 + q_{\parallel}^2 + q_z^2 + q_0^2}{kq_{\parallel}}. \quad (4.106)$$

Expression (4.105) is evaluated using the residue theorem,

$$\oint_{|z|=1} dz f(z) = 2\pi i \sum_{|z_0|<1} \text{res}_{z_0} f(z_0). \quad (4.107)$$

In this case, $f = f_1 + f_2$, where

$$f_1 = \frac{1}{z^2 - bz + 1}, \quad f_2 = \frac{\frac{q_0^2}{kq_{\parallel}} z}{[z^2 - bz + 1]^2} \quad (4.108)$$

with poles at $z_0^{\pm} = b \pm \sqrt{b^2 - 1}$, and thus

$$\text{res}_{z_0^-} f_1(z) = (z - z_0^-) f_1(z_0^-), \quad \text{res}_{z_0^-} f_2(z) = \frac{d}{dz} [(z - z_0^-)^2 f_2(z_0^-)], \quad (4.109)$$

which results in

$$I_{\theta}(k^2, q_{\parallel}^2, q_z^2) = -\frac{2\pi}{kq_{\parallel}} \left\{ \frac{1}{z_0^- - z_0^+} + \frac{q_0^2}{kq_{\parallel}} \frac{z_0^+ - z_0^-}{(z_0^+ - z_0^-)^3} \right\} \quad (4.110)$$

$$= 2\pi \left\{ \frac{1}{2\sqrt{(k^2 + q_{\parallel}^2 + q_z^2 + q_0^2)^2 - (kq_{\parallel})^2}} - \frac{q_0^2(k^2 + q_{\parallel}^2 + q_z^2 + q_0^2)}{[(k^2 + q_{\parallel}^2 + q_z^2 + q_0^2)^2 - (kq_{\parallel})^2]^{\frac{3}{2}}} \right\}. \quad (4.111)$$

It remains the integration over the longitudinal component q_z , which can be written as

$$\begin{aligned}
& 2 \int_0^{\frac{\pi}{\Delta}} \frac{dq_z}{2\pi} \cos[q_z \Delta(L - L' + \nu_{\alpha, \alpha'})] I_{\theta}(k^2, q_{\parallel}^2, q_z^2) \\
&= \int_0^{\frac{\pi}{\Delta}} dq_z \frac{\cos[q_z \Delta(L - L' + \nu_{\alpha, \alpha'})]}{\sqrt{(k^2 + q_{\parallel}^2 + q_z^2 + q_0^2)^2 - (kq_{\parallel})^2}} \\
&\quad - \int_0^{\frac{\pi}{\Delta}} \frac{2 \cos[q_z \Delta(L - L' + \nu_{\alpha, \alpha'})] q_0^2 (k^2 + q_{\parallel}^2 + q_z^2 + q_0^2)}{[(k^2 + q_{\parallel}^2 + q_z^2 + q_0^2)^2 - (kq_{\parallel})^2]^{\frac{3}{2}}} \\
&\equiv I_{\alpha, L; \alpha', L'}(k, q_{\parallel}).
\end{aligned} \tag{4.112}$$

$$\equiv I_{\alpha, L; \alpha', L'}(k, q_{\parallel}). \tag{4.113}$$

This provides the final expression for the POP scattering self energies,

$$\Sigma_{\alpha, L; \alpha', L'}^{\leq, H} = 0, \tag{4.114}$$

$$\Sigma_{\alpha, L; \alpha', L'}^{R, H} = -\frac{e^2 \hbar}{\epsilon_0} \left(\frac{1}{\epsilon_{\infty}} - \frac{1}{\epsilon} \right) \sum_{\alpha_1, L_1} \{ I_{\alpha, L; \alpha_1, L_1}(0, 0) \sum_{\mathbf{k}} \rho_{\alpha_1, L_1; \alpha_1, L_1}(\mathbf{k}) \}, \tag{4.115}$$

$$\begin{aligned}
\Sigma_{\alpha, L; \alpha', L'}^{\leq, F}(\mathbf{k}; E) &= \frac{e^2 \hbar \omega_{op}}{2\epsilon_0} \left(\frac{1}{\epsilon_{\infty}} - \frac{1}{\epsilon} \right) \int \frac{d^2 q_{\parallel}}{4\pi^2} I_{\alpha, L; \alpha', L'}(k, q_{\parallel}) \\
&\quad \times [N_{\mathbf{q}} G_{\alpha, L; \alpha', L'}^{\leq}(\mathbf{q}_{\parallel}; E \mp \hbar \omega_{\mathbf{q}}) + (N_{\mathbf{q}} + 1) G_{\alpha, L; \alpha', L'}^{\leq}(\mathbf{q}_{\parallel}; E \pm \hbar \omega_{\mathbf{q}})],
\end{aligned} \tag{4.116}$$

$$\begin{aligned}
\Sigma_{\alpha, L; \alpha', L'}^{R, F}(\mathbf{k}; E) &= \frac{e^2 \hbar \omega_{op}}{2\epsilon_0} \left(\frac{1}{\epsilon_{\infty}} - \frac{1}{\epsilon} \right) \int \frac{d^2 q_{\parallel}}{4\pi^2} I_{\alpha, L; \alpha', L'}(k, q_{\parallel}) \\
&\quad \times \left[(N_{\mathbf{q}} + 1) G_{\alpha, L; \alpha', L'}^R(\mathbf{q}_{\parallel}; E - \hbar \omega_{\mathbf{q}}) + (N_{\mathbf{q}} + 1) G_{\alpha, L; \alpha', L'}^R(\mathbf{q}_{\parallel}; E + \hbar \omega_{\mathbf{q}}) \right. \\
&\quad \left. + \{ G_{\alpha, L; \alpha', L'}^<(\mathbf{q}_{\parallel}; E + \hbar \omega_{\mathbf{q}}) - G_{\alpha, L; \alpha', L'}^<(\mathbf{q}_{\parallel}; E - \hbar \omega_{\mathbf{q}}) \} \right].
\end{aligned}$$

Acoustic phonons For acoustic phonons, the coupling is given by [172]

$$|U_{\mathbf{q}}|^2 = \frac{\hbar D^2}{2\rho c} q, \tag{4.117}$$

where D is the (acoustic) deformation potential, ρ is the density of the semiconductor and c is the sound velocity in the material. For low energy (elastic) scattering and high temperatures, the expression for the equilibrium phonon propagator can be simplified using $n_q \approx n_q + 1 \approx k_B T / \hbar \omega_q \approx k_B T \hbar c q$. The Fock self-energies derived in the appendix thus become

$$\Sigma_{\alpha, L; \alpha', L'}^{\leq, R}(E) = \delta_{L, L'} \eta_{\alpha, \alpha'} \frac{\hbar D^2 k_B T}{\rho c^2 a} \int \frac{d^2 k}{4\pi^2} G_{\alpha, L; \alpha', L'}^{\leq, R}(\mathbf{k}; E), \tag{4.118}$$

with

$$\eta_{\alpha,\alpha'} = \begin{cases} 1 & \{\alpha, \alpha'\} = \{a, a'\} \text{ or } \{c, c'\}, \\ 0 & \text{otherwise.} \end{cases} \quad (4.119)$$

4.3.3 Power dissipation

The energy lost to the phonon bath leads to power dissipation, which can be quantified by considering the outflux of energy into the phonon reservoir as provided by Eq. (3.136)[171],

$$P_p = -\frac{2}{e} \int dE \mathcal{I}_p(E), \quad (4.120)$$

where the net outflow due to inelastic scattering with phonons is

$$\mathcal{I}_p(E) = \frac{e}{2\pi\hbar} \sum_{\mathbf{k}} \text{Tr} \{ \Sigma_{pop}^<(\mathbf{k}; E) \mathbf{G}^>(\mathbf{k}; E) - \Sigma_{pop}^>(\mathbf{k}; E) \mathbf{G}^<(\mathbf{k}; E) \}. \quad (4.121)$$

4.4 Carrier-carrier interaction

The Coulomb interaction among the carriers is essential for the formation of excitonic bound states and in the scattering processes leading to nonradiative recombination, such as the Auger effect.

4.4.1 Hamiltonian in planar orbital basis

The POB Hamiltonian for a general inter-carrier interaction with the Fourier representation

$$V_{cc}(\mathbf{r}) = \frac{1}{V} \sum_{\mathbf{q}} U_{\mathbf{q}} e^{i\mathbf{q}\cdot\mathbf{r}} \quad (4.122)$$

has the form

$$\hat{H}_{cc} = \frac{1}{2} \int d\mathbf{r}_1 \int d\mathbf{r}_2 \hat{\psi}^\dagger(\mathbf{r}_1) \hat{\psi}^\dagger(\mathbf{r}_2) V_{cc}(\mathbf{r}_1 - \mathbf{r}_2) \hat{\psi}(\mathbf{r}_2) \hat{\psi}(\mathbf{r}_1) \quad (4.123)$$

$$= \frac{1}{2} \int d\mathbf{r}_1 \int d\mathbf{r}_2 \sum_{\alpha, L_1, \mathbf{k}_1} \sum_{\beta, L_2, \mathbf{k}_2} \sum_{\gamma, L_3, \mathbf{k}_3} \sum_{\delta, L_4, \mathbf{k}_4} \langle \mathbf{r}_1 | \alpha, L_1, \mathbf{k}_1 \rangle^* \langle \mathbf{r}_2 | \beta, L_2, \mathbf{k}_2 \rangle^* \\ \times \langle \mathbf{r}_2 | \gamma, L_3, \mathbf{k}_3 \rangle \langle \mathbf{r}_1 | \delta, L_4, \mathbf{k}_4 \rangle \hat{c}_{\alpha, L_1, \mathbf{k}_1}^\dagger \hat{c}_{\beta, L_2, \mathbf{k}_2}^\dagger V_{cc}(\mathbf{r}_1 - \mathbf{r}_2) \hat{c}_{\gamma, L_3, \mathbf{k}_3} \hat{c}_{\delta, L_4, \mathbf{k}_4} \quad (4.124)$$

$$= \frac{1}{2V} \sum_{\mathbf{q}} U_{\mathbf{q}} \sum_{\alpha, L_1, \mathbf{k}_1} \sum_{\beta, L_2, \mathbf{k}_2} \sum_{\gamma, L_3, \mathbf{k}_3} \sum_{\delta, L_4, \mathbf{k}_4} \langle \alpha, L_1, \mathbf{k}_1 | \{ \int d\mathbf{r}_1 | \mathbf{r}_1 \rangle e^{i\mathbf{q}\cdot\mathbf{r}_1} \langle \mathbf{r}_1 | \} | \delta, L_4, \mathbf{k}_4 \rangle \\ \times \langle \beta, L_2, \mathbf{k}_2 | \{ \int d\mathbf{r}_2 | \mathbf{r}_2 \rangle e^{-i\mathbf{q}\cdot\mathbf{r}_2} \langle \mathbf{r}_2 | \} | \gamma, L_3, \mathbf{k}_3 \rangle \hat{c}_{\alpha, L_1, \mathbf{k}_1}^\dagger \hat{c}_{\beta, L_2, \mathbf{k}_2}^\dagger \hat{c}_{\gamma, L_3, \mathbf{k}_3} \hat{c}_{\delta, L_4, \mathbf{k}_4} \quad (4.125)$$

Using the planar orbital basis representation (4.92) of the plane waves yields

$$\begin{aligned}
& \langle \alpha, L_1, \mathbf{k}_1 | \{ \int d\mathbf{r}_1 | \mathbf{r}_1 \rangle e^{i\mathbf{q}\cdot\mathbf{r}_1} \langle \mathbf{r}_1 | \} | \delta, L_4, \mathbf{k}_4 \rangle \langle \beta, L_2, \mathbf{k}_2 | \{ \int d\mathbf{r}_2 | \mathbf{r}_2 \rangle e^{-i\mathbf{q}\cdot\mathbf{r}_2} \langle \mathbf{r}_2 | \} | \gamma, L_3, \mathbf{k}_3 \rangle \\
&= \sum_{\mathbf{R}_\parallel^1, \dots, \mathbf{R}_\parallel^4} e^{-i\mathbf{k}_1 \cdot (\mathbf{R}_\parallel^1 + \mathbf{v}_{\alpha, \parallel})} \underbrace{\langle \alpha, L_1, \mathbf{R}_\parallel^1 | \{ \int d\mathbf{r}_1 | \mathbf{r}_1 \rangle e^{i\mathbf{q}\cdot\mathbf{r}_1} \langle \mathbf{r}_1 | \} | \delta, L_4, \mathbf{R}_\parallel^4 \rangle}_{=e^{iq_z(L_1\Delta + v_{\alpha,z})} e^{i\mathbf{q}_\parallel \cdot (\mathbf{R}_\parallel^1 + \mathbf{v}_{\alpha, \parallel})} \delta_{L_1, L_4} \delta_{\alpha, \delta} \delta_{\mathbf{R}_\parallel^1, \mathbf{R}_\parallel^4}} e^{i\mathbf{k}_4 \cdot (\mathbf{R}_\parallel^4 + \mathbf{v}_{\delta, \parallel})} \\
&\quad \times e^{-i\mathbf{k}_2 \cdot (\mathbf{R}_\parallel^2 + \mathbf{v}_{\beta, \parallel})} \underbrace{\langle \beta, L_2, \mathbf{R}_\parallel^2 | \{ \int d\mathbf{r}_2 | \mathbf{r}_2 \rangle e^{-i\mathbf{q}\cdot\mathbf{r}_2} \langle \mathbf{r}_2 | \} | \gamma, L_3, \mathbf{R}_\parallel^3 \rangle}_{=e^{iq_z(L_2\Delta + v_{\beta,z})} e^{i\mathbf{q}_\parallel \cdot (\mathbf{R}_\parallel^2 + \mathbf{v}_{\beta, \parallel})} \delta_{L_2, L_3} \delta_{\beta, \gamma} \delta_{\mathbf{R}_\parallel^2, \mathbf{R}_\parallel^3}} e^{i\mathbf{k}_3 \cdot (\mathbf{R}_\parallel^3 + \mathbf{v}_{\gamma, \parallel})} \quad (4.126)
\end{aligned}$$

$$\begin{aligned}
&= \underbrace{\sum_{\mathbf{R}_\parallel} e^{i[\mathbf{q}_\parallel - \mathbf{k}_1 + \mathbf{k}_4] \cdot (\mathbf{R}_\parallel + \mathbf{v}_{\alpha, \parallel})}}_{=N\delta_{\mathbf{k}_4, \mathbf{k}_1 - \mathbf{q}_\parallel}} e^{iq_z(L\Delta + v_{\alpha,z})} \sum_{\mathbf{R}'_\parallel} \underbrace{e^{i[-\mathbf{q}_\parallel - \mathbf{k}_2 + \mathbf{k}_3] \cdot (\mathbf{R}'_\parallel + \mathbf{v}_{\beta, \parallel})}}_{=N\delta_{\mathbf{k}_3, \mathbf{k}_2 + \mathbf{q}_\parallel}} e^{-iq_z(L'\Delta + v_{\beta,z})}. \quad (4.127)
\end{aligned}$$

With that, the interaction Hamiltonian becomes

$$\hat{H}_{cc} = \frac{1}{2V} \sum_{\alpha, \alpha'} \sum_{L, L'} \sum_{\mathbf{k}, \mathbf{k}'} \sum_{\mathbf{q}} U_{\mathbf{q}} e^{iq_z[(L-L')\Delta + v_{\alpha,z} - v_{\alpha',z}]} \hat{c}_{\alpha, L, \mathbf{k}}^\dagger \hat{c}_{\alpha', L', \mathbf{k}'}^\dagger \hat{c}_{\alpha, L', \mathbf{k} + \mathbf{q}_\parallel} \hat{c}_{\alpha, L, \mathbf{k} - \mathbf{q}_\parallel}. \quad (4.128)$$

4.4.2 First order: Hartree and Fock terms

The first order in the perturbation expansion for \hat{H}_{cc} in

$$G_{\alpha, L; \alpha', L'}(\mathbf{k}; t, t') = \frac{-i}{\hbar} \langle \hat{T}_C e^{\frac{i}{\hbar} \int_C \hat{H}_{cc}(s) ds} \hat{c}_{\alpha, L, \mathbf{k}}(t) \hat{c}_{\alpha', L', \mathbf{k}}^\dagger(t') \rangle \quad (4.129)$$

is given by

$$\begin{aligned}
& - \frac{1}{\hbar^2} \langle \hat{T}_C \sum_{\mathbf{q}} U_{\mathbf{q}} \sum_{\alpha_1, \alpha_2} \sum_{L_1, L_2} \sum_{\mathbf{k}_1, \mathbf{k}_2} e^{iq_z[(L_1 - L_2)\Delta + v_{\alpha_1}^{\alpha_1} - v_{\alpha_2}^{\alpha_2}]} \\
& \times \int_C ds \hat{c}_{\alpha_1, L_1, \mathbf{k}_1}^\dagger(s) \hat{c}_{\alpha_2, L_2, \mathbf{k}_2}^\dagger(s) \hat{c}_{\alpha_2, L_2, \mathbf{k}_2 + \mathbf{q}_\parallel}(s) \hat{c}_{\alpha_1, L_1, \mathbf{k}_1 - \mathbf{q}_\parallel}(s) \hat{c}_{\alpha, L, \mathbf{k}}^\dagger(t) \hat{c}_{\alpha', L', \mathbf{k}}^\dagger(t') \rangle. \quad (4.130)
\end{aligned}$$

The factorization for the ensemble average

$$\begin{aligned}
& \langle \hat{T}_C \hat{c}_{\alpha, L, \mathbf{k}}(t) \hat{c}_{\alpha_1, L_1, \mathbf{k}_1}^\dagger(s) \rangle \langle \hat{T}_C \hat{c}_{\alpha_2, L_2, \mathbf{k}_2 + \mathbf{q}_\parallel}(s) \hat{c}_{\alpha_2, L_2, \mathbf{k}_2}^\dagger(s) \rangle \langle \hat{T}_C \hat{c}_{\alpha_1, L_1, \mathbf{k}_1 - \mathbf{q}_\parallel}(s) \hat{c}_{\alpha', L', \mathbf{k}'}^\dagger(t) \rangle \\
& = \delta_{\mathbf{k}, \mathbf{k}_1} i\hbar G_{\alpha, L; \alpha_1, L_1}(\mathbf{k}; \mathbf{t}, \mathbf{s}) \delta_{\mathbf{k}_2 + \mathbf{q}_\parallel, \mathbf{k}_2} i\hbar G_{\alpha_2, L_2; \alpha_2, L_2}(\mathbf{k}_2; \mathbf{s}, \mathbf{s}) \delta_{\mathbf{k}_1 - \mathbf{q}_\parallel, \mathbf{k}} i\hbar G_{\alpha_1, L_1; \alpha', L'}(\mathbf{k}; \mathbf{s}, \mathbf{t}'), \quad (4.131)
\end{aligned}$$

$$\delta_{\mathbf{k}, \mathbf{k}_1} \delta_{\mathbf{k}_2 + \mathbf{q}_\parallel, \mathbf{k}_2} \delta_{\mathbf{k}_1 - \mathbf{q}_\parallel, \mathbf{k}} = \delta_{\mathbf{k}, \mathbf{k}_1} \delta_{\mathbf{q}_\parallel, 0}.$$

provides the constant, energy and momentum independent Hartree self-energy

$$\Sigma_{\alpha,L;\alpha',L'}^H = \delta_{\alpha,\alpha'} \delta_{L,L'} \frac{-i\hbar}{V} \sum_{q_z} \sum_{\alpha_1} \sum_{\mathbf{k}} \sum_{L_1} U_{q_z} e^{iq_z[(L_1-L')\Delta + v_z^{\alpha_1} - v_z^{\alpha'}]} G_{\alpha_1,L_1;\alpha_1,L_1}(\mathbf{k}; s, s) \quad (4.132)$$

$$= \frac{-i\hbar}{V} \sum_{\alpha_1, L_1, \mathbf{k}} U_z [(L_1 - L')\Delta + v_z^{\alpha_1} - v_z^{\alpha'}] G_{\alpha_1, L_1; \alpha_1, L_1}(\mathbf{k}; s, s). \quad (4.133)$$

With

$$G_{\alpha_1, L_1; \alpha', L'}(\mathbf{k}; s, s) = \frac{1}{\hbar} \int \frac{dE}{2\pi} G_{\alpha_1, L_1; \alpha', L'}^<(\mathbf{k}; E), \quad (4.134)$$

and the definition of the particle density

$$n_L = \sum_{\alpha} n_{\alpha, L}, \quad n_{\alpha, L} = \sum_{\mathbf{k}} \int \frac{dE}{2\pi V} \{-iG_{\alpha, L; \alpha, L}^<(\mathbf{k}; E)\}, \quad (4.135)$$

the Hartree self-energy acquires the mean-field form

$$\Sigma_{\alpha, L; \alpha', L'}^H = \delta_{\alpha, \alpha'} \delta_{L, L'} \sum_{L_1} \sum_{\alpha_1} n_{\alpha_1, L_1} U_z [(L - L_1)\Delta + v_z^{\alpha} - v_z^{\alpha'}] \equiv \delta_{\alpha, \alpha'} \delta_{L, L'} U_L, \quad (4.136)$$

where U_L is the mean-field potential of the particle-pair interaction. For Coulomb interaction, U_L corresponds to the solution of the macroscopic 1D Poisson equation for the potential U_z and density n_L .

The Fock self-energy follows from the factorization

$$\begin{aligned} & \langle \hat{T}_C \hat{c}_{\alpha, L, \mathbf{k}}(t) \hat{c}_{\alpha_1, L_1, \mathbf{k}_1}^\dagger(s) \rangle \langle \hat{T}_C \hat{c}_{\alpha_1, L_1, \mathbf{k}_1 - \mathbf{q}_{\parallel}}(s) \hat{c}_{\alpha_2, L_2, \mathbf{k}_2}^\dagger(s) \rangle \langle \hat{T}_C \hat{c}_{\alpha_2, L_2, \mathbf{k}_2 + \mathbf{q}_{\parallel}}(s) \hat{c}_{\alpha', L', \mathbf{k}}^\dagger(t') \rangle \\ &= \delta_{\mathbf{k}, \mathbf{k}_1} i\hbar G_{\alpha, L; \alpha_1, L_1}(\mathbf{k}; \mathbf{t}, \mathbf{s}) \delta_{\mathbf{k}_2, \mathbf{k}_1 - \mathbf{q}_{\parallel}} i\hbar G_{\alpha_1, L_1; \alpha_2, L_2}(\mathbf{k} - \mathbf{q}_{\parallel}; \mathbf{s}, \mathbf{s}) \delta_{\mathbf{k}_2 + \mathbf{q}_{\parallel}, \mathbf{k}} i\hbar G_{\alpha_2, L_2; \alpha', L'}(\mathbf{k}; \mathbf{s}, \mathbf{t}'), \end{aligned} \quad (4.137)$$

$$\delta_{\mathbf{k}, \mathbf{k}_1} \delta_{\mathbf{k}_2, \mathbf{k}_1 - \mathbf{q}_{\parallel}} \delta_{\mathbf{k}_2 + \mathbf{q}_{\parallel}, \mathbf{k}} = \delta_{\mathbf{k}, \mathbf{k}_1} \delta_{\mathbf{k}_2, \mathbf{k} - \mathbf{q}_{\parallel}},$$

which yields

$$\Sigma_{\alpha, L; \alpha', L'}^F(\mathbf{k}) = \frac{i\hbar}{V} \sum_{\mathbf{q}} U_{\mathbf{q}} e^{iq_z[(L-L')\Delta + v_z^{\alpha} - v_z^{\alpha'}]} G_{\alpha, L; \alpha', L'}^<(\mathbf{k} - \mathbf{q}_{\parallel}; s, s) \quad (4.138)$$

$$\Rightarrow [\Sigma^{F,R}]_{\alpha, L; \alpha', L'}(\mathbf{k}) = \frac{i}{V} \sum_{\mathbf{q}} U_{\mathbf{k} - \mathbf{q}} e^{iq_z[(L-L')\Delta + v_z^{\alpha} - v_z^{\alpha'}]} \int \frac{dE}{2\pi} G_{\alpha_1, L_1; \alpha', L'}^<(\mathbf{k}; E) \quad (4.139)$$

$$= - \sum_{\mathbf{q}} U_{\mathbf{k} - \mathbf{q}} e^{iq_z[(L-L')\Delta + v_z^{\alpha} - v_z^{\alpha'}]} \rho_{\alpha, L; \alpha', L'}(\mathbf{q}_{\parallel}), \quad (4.140)$$

with the density matrix

$$\rho_{\alpha, L; \alpha', L'}(\mathbf{q}_{\parallel}) \equiv \int \frac{dE}{2\pi V} \{-iG_{\alpha_1, L_1; \alpha', L'}^<(\mathbf{q}_{\parallel}; E)\}. \quad (4.141)$$

4.4.3 Second order Born approximation: direct-collision term

The second order term is of the form

$$\begin{aligned}
& \left(-\frac{i}{\hbar}\right)^3 \langle \hat{T}_C \int_C ds \int_C ds' \hat{H}_{cc}(s) \hat{H}_{cc}(s') \hat{c}_{\alpha,L,\mathbf{k}}(t) \hat{c}_{\alpha',L',\mathbf{k}'}^\dagger(t') \rangle \quad (4.142) \\
&= \left(-\frac{i}{\hbar}\right)^3 \langle \hat{T}_C \int_C ds \int_C ds' \frac{1}{4V^2} \sum_{\mathbf{q},\mathbf{q}'} \sum_{L_1,\dots,L_4} \sum_{\alpha_1,\dots,\alpha_4} \sum_{\mathbf{k}_1,\dots,\mathbf{k}_4} U_{\mathbf{q}} U_{\mathbf{q}'} e^{i[q_z(L_1^{\alpha_1}-L_2^{\alpha_2})+q'_z(L_3^{\alpha_3}-L_4^{\alpha_4})]} \\
&\quad \times \hat{c}_{\alpha_1,L_1,\mathbf{k}_1}^\dagger(s) \hat{c}_{\alpha_2,L_2,\mathbf{k}_2}^\dagger(s) \hat{c}_{\alpha_2,L_2,\mathbf{k}_2+\mathbf{q}_{\parallel}}(s) \hat{c}_{\alpha_1,L_1,\mathbf{k}_1-\mathbf{q}_{\parallel}}(s) \hat{c}_{\alpha_3,L_3,\mathbf{k}_3}^\dagger(s') \hat{c}_{\alpha_4,L_4,\mathbf{k}_4}^\dagger(s') \hat{c}_{\alpha_4,L_4,\mathbf{k}_4+\mathbf{q}'_{\parallel}}(s') \\
&\quad \times \hat{c}_{\alpha_3,L_3,\mathbf{k}_3-\mathbf{q}'_{\parallel}}(s') \hat{c}_{\alpha,L,\mathbf{k}}(t) \hat{c}_{\alpha',L',\mathbf{k}'}^\dagger(t'), \quad (4.143)
\end{aligned}$$

where we have introduced the short-hand notation

$$L_i^\alpha \equiv L_i \Delta + v_z^{\alpha i} \quad (4.144)$$

for the longitudinal position. The direct collision diagram corresponds to the factorization

$$\begin{aligned}
& \langle \hat{T}_C \hat{c}_{\alpha,L,\mathbf{k}}(t) \hat{c}_{\alpha_1,L_1,\mathbf{k}_1}^\dagger(s) \rangle \langle \hat{T}_C \hat{c}_{\alpha_4,L_4,\mathbf{k}_4+\mathbf{q}'_{\parallel}}(s') \hat{c}_{\alpha',L',\mathbf{k}'}^\dagger(t') \rangle \langle \hat{T}_C \hat{c}_{\alpha_1,L_1,\mathbf{k}_1-\mathbf{q}_{\parallel}}(s) \hat{c}_{\alpha_4,L_4,\mathbf{k}_4}^\dagger(s') \rangle \\
& \times \langle \hat{T}_C \hat{c}_{\alpha_2,L_2,\mathbf{k}_2+\mathbf{q}_{\parallel}}(s) \hat{c}_{\alpha_3,L_3,\mathbf{k}_3}^\dagger(s') \rangle \langle \hat{T}_C \hat{c}_{\alpha_3,L_3,\mathbf{k}_3-\mathbf{q}'_{\parallel}}(s') \hat{c}_{\alpha_2,L_2,\mathbf{k}_2}^\dagger(s) \rangle \quad (4.145)
\end{aligned}$$

$$\propto \delta_{\mathbf{k},\mathbf{k}_1} \delta_{\mathbf{k},\mathbf{k}_4+\mathbf{q}'_{\parallel}} \delta_{\mathbf{k}_4,\mathbf{k}_1-\mathbf{q}_{\parallel}} \delta_{\mathbf{k}_3,\mathbf{k}_2+\mathbf{q}'_{\parallel}} \delta_{\mathbf{k}_2,\mathbf{k}_3-\mathbf{q}'_{\parallel}} = \delta_{\mathbf{k},\mathbf{k}_1} \delta_{\mathbf{k}_4,\mathbf{k}-\mathbf{q}_{\parallel}} \delta_{\mathbf{k}_3,\mathbf{k}_2+\mathbf{q}_{\parallel}} \delta_{\mathbf{q}_{\parallel},\mathbf{q}'_{\parallel}}, \quad (4.146)$$

and provides the second order contribution in terms of Green's functions as

$$\begin{aligned}
& \int_C ds \int_C ds' \frac{-\hbar^2}{4V^2} \sum_{L_1,\dots,L_4} \sum_{\alpha_1,\dots,\alpha_4} \sum_{\mathbf{q}_{\parallel}} \sum_{q_z,q'_z} \sum_{\mathbf{k}_2} U_{(\mathbf{q}_{\parallel},q_z)} U_{(\mathbf{q}_{\parallel},q'_z)} e^{i[q_z(L_1^{\alpha_1}-L_2^{\alpha_2})+q'_z(L_3^{\alpha_3}-L_4^{\alpha_4})]} \\
& \times G_{\alpha,L;\alpha_1,L_1}(\mathbf{k}; t, s) G_{\alpha_1,L_1;\alpha_4,L_4}(\mathbf{k}-\mathbf{q}_{\parallel}; s, s') G_{\alpha_2,L_2;\alpha_3,L_3}(\mathbf{k}_2+\mathbf{q}_{\parallel}; s, s') G_{\alpha_3,L_3;\alpha_2,L_2}(\mathbf{k}_2; s', s) \\
& \times G_{\alpha_4,L_4;\alpha',L'}(\mathbf{k}; s', t'), \quad (4.147)
\end{aligned}$$

which contains the self-energy

$$\begin{aligned}
[\Sigma_{cc}^{dc}]_{\alpha_1,L_1;\alpha_4,L_4}(\mathbf{k}; s, s') &= -\frac{\hbar^2}{4V^2} \sum_{L_2,L_3} \sum_{\alpha_2,\alpha_3} \sum_{\mathbf{q}_{\parallel}} M_{\alpha_1,L_1;\alpha_2,L_2}^{cc}(\mathbf{q}_{\parallel}) \pi_{23}^{cc}(\mathbf{q}_{\parallel}; s, s') \\
&\quad \times M_{\alpha_3,L_3;\alpha_4,L_4}^{cc}(\mathbf{q}_{\parallel}) G_{\alpha_1,L_1;\alpha_4,L_4}(\mathbf{k}-\mathbf{q}_{\parallel}; s, s'), \quad (4.148)
\end{aligned}$$

where the longitudinal polarization bubble π_{23}^{cc} is given by

$$\pi_{23}^{cc}(\mathbf{q}_{\parallel}; s, s') = \sum_{\mathbf{k}'} G_{\alpha_2,L_2;\alpha_3,L_3}(\mathbf{k}'+\mathbf{q}_{\parallel}; s, s') G_{\alpha_3,L_3;\alpha_2,L_2}(\mathbf{k}'; s', s), \quad (4.149)$$

and the coupling elements are

$$M_{\alpha_1, L_1, \alpha_2, L_2}^{cc}(\mathbf{q}_{\parallel}) = \sum_{q_z} U_{(q_{\parallel}, q_z)} e^{iq_z(L_1^{\alpha_1} - L_2^{\alpha_2})} \quad (4.150)$$

$$\equiv U_z(\mathbf{q}_{\parallel}, L_1^{\alpha_1} - L_2^{\alpha_2}) = \frac{e^2}{2\epsilon} \frac{e^{-\sqrt{q_0^2 + q_{\parallel}^2}(L_1^{\alpha_1} - L_2^{\alpha_2})}}{\sqrt{q_0^2 + q_{\parallel}^2}}. \quad (4.151)$$

The lesser and greater self-energies follow again from the Langreth rules for analytic continuation (App. A), which provide the real time relation

$$G_{23}(s, s')G_{32}(s', s)G_{14}(s, s') \rightarrow G_{23}^<(t, t')G_{32}^>(t', t)G_{14}^<(t, t'). \quad (4.152)$$

The steady state expressions are obtained as the Fourier transform with respect to energy:

$$\Sigma_{14}^{dc, <}(E) = \int d\tau e^{i\frac{E}{\hbar}\tau} \Sigma_{14}^{dc}(\tau) \equiv \widehat{\Sigma_{14}^{dc}(\tau)} \propto \{G_{23}^<(\tau)G_{32}^>(-\tau)G_{14}^<(\tau)\} \quad (4.153)$$

$$= \int \frac{dE_1}{2\pi\hbar} \left\{ \int \frac{dE_2}{2\pi\hbar} G_{23}^<(E_2)G_{32}^>(E_1 - E_2) \right\} G_{14}^<(E - E_1), \quad (4.154)$$

where the transform of the product leads to a twofold convolution. The self-energies are then given by

$$\begin{aligned} [\Sigma_{cc}^{dc, <}]_{\alpha_1, L_1; \alpha', L'}(\mathbf{k}; E) &= -\frac{1}{4V^2} \sum_{L_1, L_2} \sum_{\alpha_1, \alpha_2} \sum_{\mathbf{k}'} \sum_{\mathbf{q}_{\parallel}} M_{\alpha, L; \alpha_1, L_1}^{cc}(\mathbf{q}_{\parallel}) \\ &\times \left[\int \frac{dE_1}{2\pi} \left\{ \int \frac{dE_2}{2\pi} G_{\alpha_1, L_1; \alpha_2, L_2}^<(\mathbf{k}' + \mathbf{q}_{\parallel}; E_2) G_{\alpha_2, L_2; \alpha_1, L_1}^>(\mathbf{k}'; E_1 + E_2) \right\} \right. \\ &\times \left. G_{\alpha, L; \alpha', L'}^<(\mathbf{k} - \mathbf{q}_{\parallel}; E - E_1) \right] M_{\alpha_2, L_2; \alpha', L'}^{cc}(\mathbf{q}_{\parallel}) \end{aligned} \quad (4.155)$$

$$\begin{aligned} &= -\frac{1}{4V^2} \sum_{L_1, L_2} \sum_{\alpha_1, \alpha_2} \sum_{\mathbf{q}_{\parallel}} M_{\alpha, L; \alpha_1, L_1}^{cc}(\mathbf{q}_{\parallel}) \\ &\times \left[\int \frac{dE_1}{2\pi} \pi_{12}^<(\mathbf{q}_{\parallel}; E) G_{\alpha, L; \alpha', L'}^<(\mathbf{k} - \mathbf{q}_{\parallel}; E - E_1) \right] M_{\alpha_2, L_2; \alpha', L'}^{cc}(\mathbf{q}_{\parallel}), \end{aligned} \quad (4.156)$$

where

$$\pi_{12}^<(\mathbf{q}_{\parallel}; E) = \sum_{\tilde{\mathbf{k}}} \int \frac{d\tilde{E}}{2\pi} G_{\alpha_1, L_1; \alpha_2, L_2}^<(\tilde{\mathbf{k}} + \mathbf{q}_{\parallel}; \tilde{E}) G_{\alpha_2, L_2; \alpha_1, L_1}^>(\tilde{\mathbf{k}}; \tilde{E} - E). \quad (4.157)$$

The expressions for retarded and advanced self-energies are again obtained via the Hilbert-transform (3.101).

Chapter 5

Numerical results

Abstract: In a first section, the NEGF-formalism, in the specific form adapted in the previous chapter for the description of photovoltaic heterojunction-devices, is applied to nanoscale bulk *p-i-n* diodes as a test device to assess the capabilities of the approach. It is shown that in the considered parameter range even such a simple device shows a behaviour that differs considerably from the semiclassical bulk picture. In a second part, the effect of a single quantum well in the intrinsic region on the photovoltaic properties of the junction is investigated. In addition to the (quasi) continuum states of the bulk junction, there is now the contribution of the quantized and spatially rather localized well states to consider. The impact of geometry on the photovoltaic performance of a multi-quantum-well structure is the subject of the last part of the chapter. It is demonstrated on the example of various double quantum wells of different geometry how the confinement level structure and the degree of localization of the quantum well states modifies absorption and transport in these structures already in the radiative limit.

5.1 Introduction

The many advantages the NEGF-formalism offers have their price. The major drawback of the method, apart from its conceptual complexity, is the heavy requirement of computational resources. This can be inferred from the size of the basic objects that need to be computed, i.e. the Green's functions and self-energies. This size is given by the size of the tight-binding matrix $N_{TB} = (N_b \cdot N_L) \times (N_b \cdot N_L)$, N_b being the number of bands or orbitals and N_L the number of model layers, the number N_E of energies as well as points N_k in the transverse Brillouin zone for which the Dyson's equations need to be solved. The total size is the product $N_{tot} = N_{TB} \times N_E \times N_k$. If one considers e.g. the quantum

well solar cell device in Fig. 2.6 of Chap. 2, the total thickness amounts to $\sim 1 - 2 \mu m$, which corresponds to $N_L \approx 3500 - 7000$ atomic monolayers. From Figs. 2.4 and 4.1, it is obvious that the energy range that needs to be used in a calculation of density and current must cover at least the whole width of both bands, depending on the length of the device and the built-in field at short circuit conditions. Furthermore, since the quantum well states are strongly bound, their linewidth is small, even at room temperature and in the presence of scattering, which results in increased resolution requirements. For a 1-2 micron AlGaAs-GaAs structure, this means that $\sim 3.5 - 4 eV$ need to be resolved at a resolution of less than $0.01 eV$, i.e. $N_E \gtrsim 350 - 400$. Inhomogeneous energy grids might lower this number somewhat, however the implementation for cases where inelastic processes that couple states at different energies are present is involved. If a realistic bandstructure should be considered, then a considerable part of the irreducible wedge in the transverse Brillouin zone is needed, together with a multiband-model, at least on the level of the ten-band model discussed in App. C, i.e. $N_k \gtrsim 20$ and $N_b \geq 10$. Also here, inhomogeneous meshes could be used, with the same drawback for processes where momentum transfer occurs. The total size of the Green's functions to compute for this device thus amounts to $N_{tot} \gtrsim (10 \cdot 3500)^2 \times 350 \times 20 \approx 8.5 \times 10^{12}$, which is far beyond the actual resource limitations. Even for a 2-band model and considering that for the present purpose, only the diagonal and first off-diagonal blocks of the Green's functions need to be evaluated, corresponding to banded matrices with $4N_b - 1$ (off)diagonals, the total size is still of the order of 10^8 . Quantitative analysis of realistic systems including interactions thus constitutes a considerable computational challenge.

Due to the limitations arising from the above analysis, in a first approach the discussion is limited to qualitative features in systems of reduced size, such as single and double quantum well structures embedded in nanoscale *p-i-n* junctions of total length $\sim 70 - 120 nm$, and simplified band structure models are used, such as the two-band model with isotropic and parabolic transverse dispersion, or even a model composed of two single-band components. Assuming smaller band-gaps of 0.5-0.8 eV, the energy-range is considerably reduced. Since the heterostructure band offsets play a crucial role in the determination of the confinement levels, they retain realistic values, as well as the effective masses for the parabolic transverse dispersion. The most severe caveat of this approach is the much too large built-in field resulting from the shrinking of the intrinsic region, if the doping is kept at the level of long structures. This has consequences for all the field-dependent effects in quantum well structures, such as the quantum confined Stark-effect and the escape via field-enhanced tunneling. Since an applied forward bias counteracts this field, the bias dependence is much more pronounced than in structures of realistic length. In order to obtain more realistic fields, the doping density can be reduced. Ideally, this is achieved by

making the highly doped regions very thin (20 ML). Care has to be taken to preserve a sufficiently extended depletion region, since it is strongly reduced by the lowering of the dopant concentration.

Apart from the structural restrictions discussed above, the investigations are confined to the radiative limit (no Auger or trap recombination), and we do not consider excitons at this stage. As discussed in chapter 4, both photons and phonons are treated in a homogeneous bulk approximation, not considering renormalization effects like photon recycling or hot phonons, or confinement effects like cavity modes and zone folding. Neglecting the excitonic contributions to absorption is not a severe limitation in the case of the nanoscale bulk junction discussed in the first section, but it might considerably modify the picture in the quantum well case.

5.2 Photovoltaic properties of nanoscale bulk *p-i-n* diodes

5.2.1 Introduction

In order to assess the capabilities of the chosen approach, standard structures of limited extension and simple geometry should be investigated, where the physics is well understood. Since the basic device underlying the quantum well solar cell is a standard bulk *p-i-n*-diode, we chose a nanoscale version of this device as the test object.

There are several external parameters that determine the device characteristics, and whose effects on the latter should therefore be investigated. The principle ones are the illumination, characterized by the spectrum I^γ , and the terminal voltage, V_{bias} . Further are of relevance the strength of the coupling to phonons for the relaxation and dissipative processes, and the effects of the built-in field due to doping.

Since the device characteristics are usually assumed to obey additivity, i.e. the total current at a given voltage is obtained as the sum of bias dependent dark current and bias independent short circuit current (Eq. (2.3)), the following investigation considers first the device properties in the dark ($I^\gamma = 0, V_{bias} \neq 0$) and under illumination at short circuit conditions ($I^\gamma > 0, V_{bias} = 0$), before passing to the general situation ($I^\gamma > 0, V_{bias} \neq 0$).

5.2.2 Device characterization

The device under consideration is schematically shown in Fig. 5.1. An extended intrinsic region is sandwiched between a positively and a negatively doped contact, which leads to the formation of a built-in bias V_{bi} of the order of the band gap energy. The depleted space-charge region present in pn -junctions due to the rearrangement of the free carriers, is enlarged by the intrinsic layer. The following results for the bulk p - i - n diode were obtained using the 2-band model (see App. C) with the parameters given in table 5.1 for the device shown in Fig. 5.1, unless specified otherwise. The bulk material is that of the barrier.

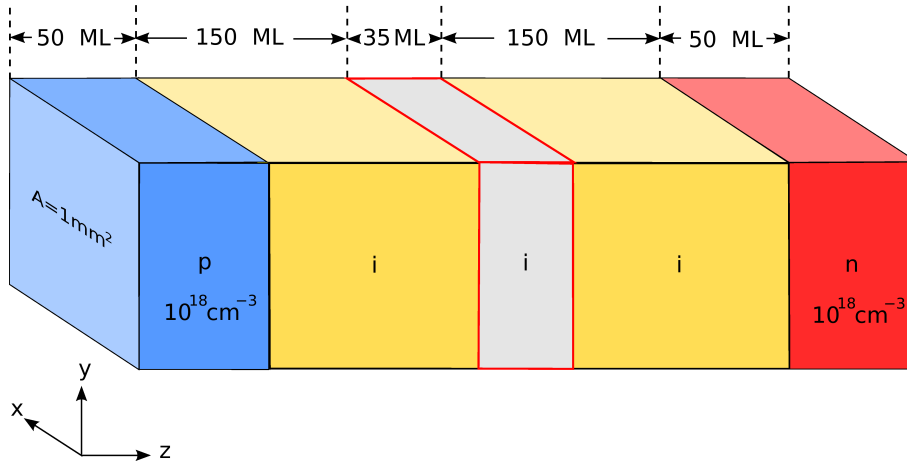


Figure 5.1: Layout of the device studied in this section, indicating the geometrical dimensions and doping densities. The thickness of one monolayer is $\Delta \approx 2.8\text{\AA}$. The central intrinsic part is the interacting region.

5.2.3 Numerical considerations

The simulation parameters that are not related to material or geometry are given in Tab. 5.2. We will motivate the specific values in the following.

Energy and contact Fermi level The energy resolution of 8 meV is a good compromise between speed and accuracy, given high (i.e. room) temperature and strong scattering, which both broaden the spectral features. The required energy range is determined as the union of the support of finite valued spectral quantities, i.e. the current spectrum or the spectral density, at each spatial position of the computational domain. This amounts

to the band width plus an additional energy range of $\sim 0.3 - 0.5$ eV above and below the band edge extrema, depending on the temperature and the position of the contact Fermi level. In principle, the exact value of the latter does not matter, since for charge neutrality, it will be corrected by the boundary value of the Hartree potential. However, to speed up convergence of the Poisson loop, this correction should be kept small. For doping densities of $\sim 10^{18}$ cm $^{-3}$, this is achieved with a chemical potential close to the band edge, as an electron concentration of similar magnitude is produced. For the two band model with parameters in Tab. 5.1, $\mu_{low} = 0.49$ eV and $\mu_{high} = 0.74$ eV are suitable choices for the Fermi levels at the contacts of bulk diodes made from low and high band gap material, respectively. The total energy range above the band edge in the interacting region should be high enough, such that the calculation of optical quantities at photon energies exceeding the band gap does not suffer from disturbing boundary effects. This becomes important at high forward bias, where the bandwidth is small due to low total field.

Transverse momentum The transverse momentum resolution should in principle be as high as possible, if spectral quantities have to be determined. As shown later in this section, integral quantities in bulk devices are rather insensitive to the resolution both in energy and transverse momentum. This is related to the observation that in bulk, there are hardly any sharp spectral features, and hence the spectral weight varies quite smoothly. Hence, a resolution of $\Delta k \approx 0.003\pi/\Delta$ yields already good results. The fraction of the transverse Brillouin zone that needs to be considered increases with scattering strength,

Table 5.1: *Material parameters used in simulations*

	barrier	well	
E_s	0.75	0.5	s -orbital onsite energy [eV]
E_p	-0.15	0	p_z -orbital onsite energy [eV]
V_{sp}	2.0	2.5	layer coupling element [eV]
m_{Cb}^*/m_0	0.1087	0.067	effective mass in conduction band
m_{Vb}^*/m_0	0.29	0.23	effective mass in valence band
ϵ	12.2	13.1	(relative) static dielectric constant
ϵ_∞	10.9	10.9	(relative) high frequency dielectric constant
μ	1	1	(relative) magnetic permeability
$\hbar\omega_{LO}$	0.036 eV	0.036	energy of polar optical phonons [eV]
D_{ap}	0.0296	0.0296	acoustic deformation potential

Table 5.2: *Model parameters*

ΔE	0.008	energy resolution [eV]
Δk	0.003	transverse momentum resolution [π/Δ]
k_{max}	0.14	maximum transverse momentum [π/Δ]
μ_{low}	0.49	well material contact Fermi level [eV]
μ_{high}	0.74	barrier material contact Fermi level [eV]
n_d	10^{18}	<i>n</i> -contact doping density [cm^{-3}]
n_a	10^{18}	<i>p</i> -contact doping density [cm^{-3}]

bias and the length of the interacting region. For the device and parameters used in this section, $k_{max} \approx 0.14\pi/\Delta$ covers the range of finite current and density components.

Convergence criteria Since there are two self-consistency iterations, one for the Poisson equation and another for the interaction self-energies, we need suitable convergence criteria where the iterations are truncated. In the presence of highly doped contacts, the Poisson iteration converges very quickly - in about four to five steps - to a potential correction δU of less than 5 mV, which is taken as terminating condition. The case of the self-consistent self-energy calculation is more complicated. Since the final result of the computation are the current-voltage characteristics of the simulated device, the terminating condition is provided by the relative change in the total current at the lead-device boundary. In bulk and for moderate scattering strength, convergence is reasonably fast, to about less than 0.0001% in 20 iterations.

5.2.4 Equilibrium and non-equilibrium properties in the dark

In the dark, the expected behaviour is that of a diode. However, the very small dimension and correspondingly high fields result in optical and transport properties that differ considerably from the usual bulk picture.

Carrier density, Hartree potential, built-in field and local density of states

Fig. 5.2a shows the densities of electrons and holes for a given doping profile both in equilibrium and for an applied bias voltage V_{bias} . Due to the absence of background doping, the carrier density in the interacting part of the intrinsic region is very low at zero bias ($\sim 10^{17} \text{ m}^{-3}$). Under forward external bias ($V_{bias} < 0$), the chemical potential in the

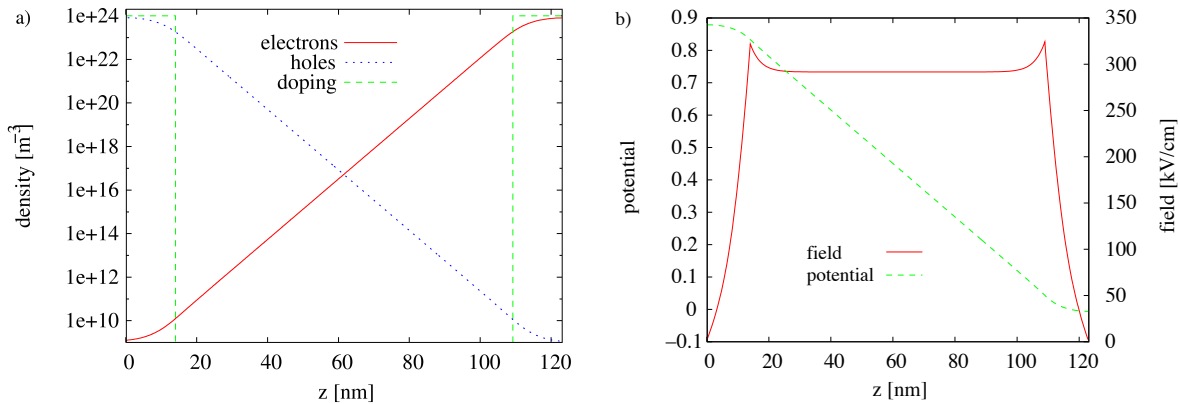


Figure 5.2: a) Electron, hole and doping density in the ballistic limit at zero bias. b) Built-in potential and corresponding field resulting from the solution of Poisson's equation with the doping profile from a).

right contact is shifted upwards by the applied voltage. This modifies the densities and consequently the value of the built-in potential obtained from the solution of Poisson's equation, shown in Fig. 5.2b together with the corresponding field, which is constant over a large part of the intrinsic region and vanishes at the contacts, as required by local charge neutrality. The elevated field strength is a consequence of the reduced length of the junction.

The momentum resolved local density of states $\mathcal{D}_L(\mathbf{k}; E) = \frac{1}{\pi} \text{Tr}\{A_{L;L}(\mathbf{k}, E)\}$ of the non-interacting system is shown in Fig. 5.3 for $\mathbf{k} = 0$. The absence of phase breaking processes leads to coherent superposition of the boundary scattering states. In the finite field region, the states incoming from the right are reflected due to the built-in potential, producing a characteristic stripe-like interference pattern. The interference disappears in the continuum above the maximum of the conduction band edge and below the minimum of the valence band edge due to the absence of reflection. The cut through the center of the intrinsic region reveals the corresponding oscillations in the LDOS, which give way to a constant density of states in the energy region where no states are reflected. In this way, a continuum and a quasi-continuum region can be distinguished that differ in their joint density of states and therefore in their contribution to the photocurrent.

Current spectrum, local current, current conservation and IV-characteristics

In the absence of scattering, the current is the ideal diode current with ideality factor $m \approx 1$ (for definition see Eq.(2.2)), as shown in Fig. 5.4 which displays the current-voltage (I-V)

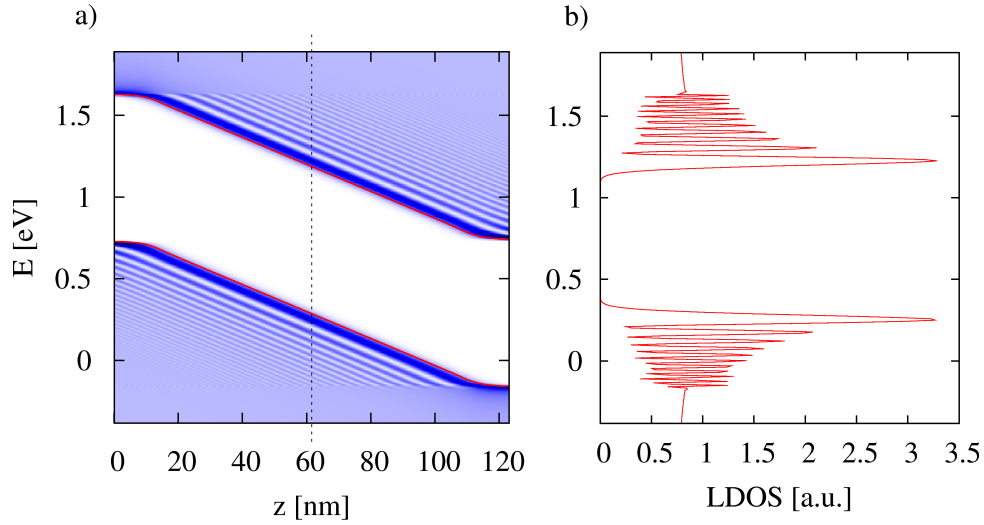


Figure 5.3: a) Local density of states ($k_{\parallel} = 0$) in the ballistic limit. A characteristic interference pattern forms due to the coherent superposition of the wave functions for carriers injected from the contacts and reflected from the barrier formed by the junction potential. b) Cut of the local density of states in a) at the center of the device region. The interference region and the continuum are clearly distinguishable.

characteristics. The current is obtained by integration of the current spectrum given by

$$\mathcal{J}_L^{n(p)}(E) = \sum_{\mathbf{k}} \text{Tr}\{t_{L;L+1}(\mathbf{k})G_{L+1;L}^{<(>)}(\mathbf{k}; E) - t_{L+1;L}(\mathbf{k})G_{L;L+1}^{<(>)}(\mathbf{k}; E)\}, \quad (5.1)$$

which is displayed in Fig. 5.5a for the whole device region and in Fig. 5.5b for the two lead-device interfaces separately. The current spectrum at the lead-device interface reflects the density of states and the distribution of the carriers in the contacts from which they are injected and is thus energetically confined to a narrow region above the band edge. The ballistic dark current shows no spatial variation in the energy band of current carrying states, due to the absence of processes contributing to relaxation. In this situation, where the bands are not coupled due to photoexcitation or recombination, current is conserved for both electrons and holes separately, which is illustrated in Fig. 5.5c .

In the ballistic case, the terminal current as calculated within the NEGF-formalism from Eq. (3.187) can be related to the Landauer picture of transport by writing it as

$$J = \frac{e}{\hbar\mathcal{A}} \sum_{\mathbf{k}} \int \frac{dE}{\pi} T(\mathbf{k}; E)[f_{\mu_L}(E) - f_{\mu_R}(E)], \quad (5.2)$$

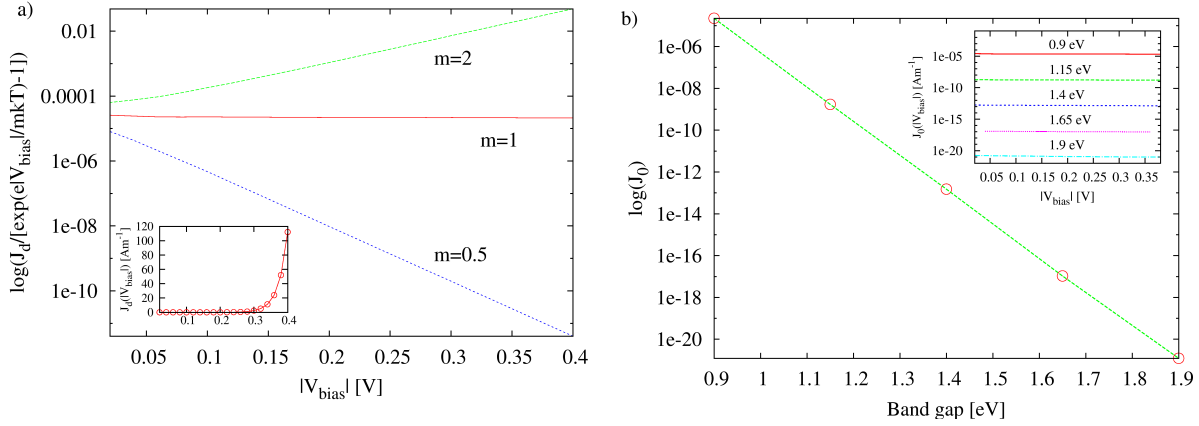


Figure 5.4: a) The ballistic dark current of a nanoscale p - i - n junction as calculated within the NEGF-formalism is in good agreement with the ideal Shockley diode current (ideality-factor $m = 1$). The IV-characteristics is shown in the inset. b) The prefactor of the dark injection current, corresponding to the saturation current, depends exponentially on the band gap, which is the energy governing the thermal activation of current. This dependence is shown for five different values of the band gap.

where the generalized transmission function is defined as [251]

$$T(\mathbf{k}; E) = \text{Tr}\{\Gamma_L^B(\mathbf{k}; E)\mathbf{G}^R(\mathbf{k}; E)\Gamma_R^B(\mathbf{k}; E)\mathbf{G}^A(\mathbf{k}; E)\}. \quad (5.3)$$

The transmission function calculated via this formula is shown in the inset of Fig. 5.5b: it is one above the maximum of the conduction band edge, spatially located at the p -contact, and below the minimum of the valence band edge, located at the n -contact, and zero in between.

5.2.5 Effects of relaxation due to scattering with phonons

The coupling of carriers to acoustic (AC) phonons is assumed to be approximately elastic in the momentum range of interest in transport problems, and leads therefore merely to a weak broadening of the spectral features, while inelastic scattering with polar optical (POP) phonons introduces energy and momentum relaxation effects such as phonon satellite peaks, as depicted in Fig. 5.6 on the example of the current spectrum at the lead-device interfaces. The combined effect of scattering with AC and POP phonons thus leads to a broadened distribution of carriers occupying current carrying states of lower energy and results in a *reduced* dark current, the kinetic energy of the carriers being reduced by the heat that is dissipated in the equilibrium phonon bath.

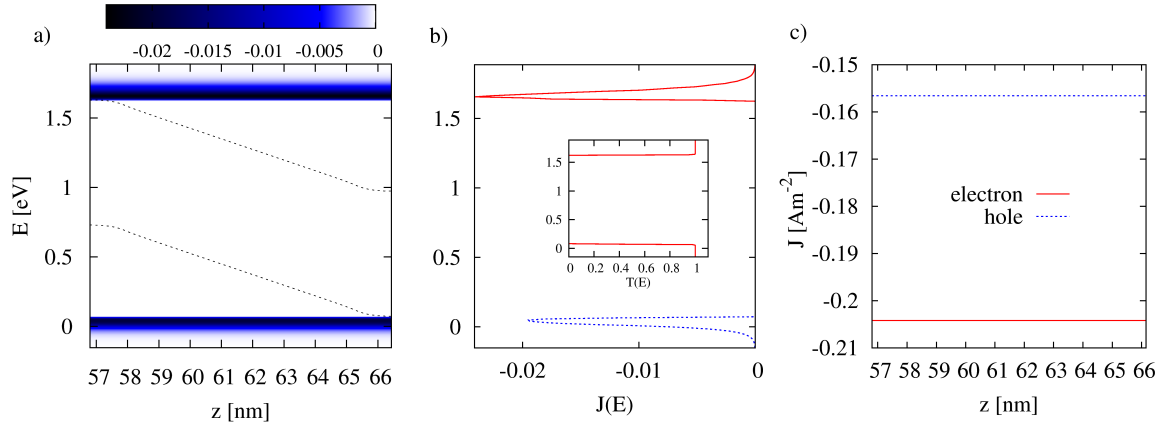


Figure 5.5: a) Current spectrum in the device region at $V_{bias} = 0.25$ V. As indicated by the projection of the band edges, dark injection current can exist only above the maximum of the conduction band edge (electrons) and below the minimum of the valence band edge (holes), i.e. in the reflectionless region of finite transmission (inset in b)). b) Current spectrum at the device boundaries, reflecting the spectrum of states from which carriers are injected at the contacts. The sharp cut-off toward the band gap stems from the step-like onset of the transmission function as shown in the inset. c) The current density in the device is constant for both electrons and holes separately, as imposed by the continuity equation in steady-state for the case of uncoupled bands.

Since the number of scattering events increases with the extension of the traversed interacting region, the effects of relaxation are expected to be most pronounced at the lead interface opposite to the injection region, i.e. at the p -lead-device interface for electrons and at the n -lead-device interface for holes, assuming a net reverse current. In the case of bipolar devices, the large decrease in the density of scatterers away from the majority injection contact overcompensates the increase in scattering events, wherefore the largest scattering effects are observed in the vicinity of the injector contacts. This behaviour is displayed in Fig. 5.7.

Even though the effects of scattering are clearly recognizable, the total amount of relaxation is very small, and transport has to a large extent ballistic characteristics. As a consequence, at the present field strength, the distribution of carriers near the band edge is nearly unperturbed at low to intermediate bias, i.e. from close to short circuit conditions up to the operating point for unconcentrated illumination.

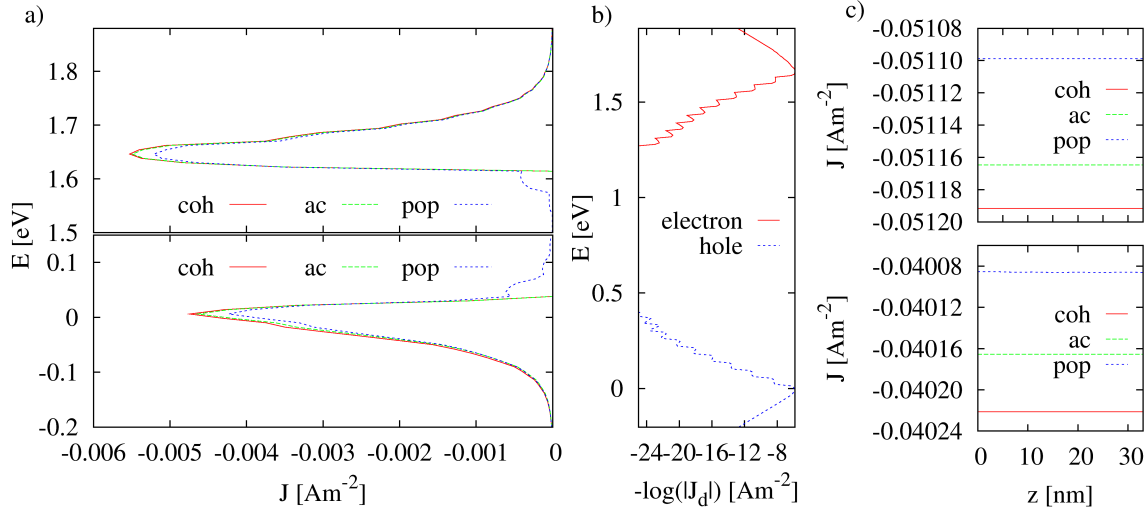


Figure 5.6: *a)* Current spectrum at the lead-device interface opposite to the injection contact (i.e. p for electrons, n for holes) and for different transport regimes: ballistic, with elastic (ac) and inelastic (pop) phonon scattering. While elastic scattering introduces only a weak broadening, the inelastic scattering causes the appearance of satellite peaks at lower energy. *b)* In the fully converged steady state situation, the current spectrum at the lead-device interfaces has a characteristic staircase shape due to the subsequent emission of optical phonons with energy $E_{pop} = \hbar\omega_{LO} \approx 0.036$ eV. *c)* Dark current decreases due to dissipation of energy in the phonon heat bath and transfer of momentum from longitudinal to transverse. The decrease is only minimal for acoustic phonons, but substantial for inelastic scattering with polar-optical phonons. The current is conserved for both electrons and holes separately.

5.2.6 Properties under illumination at short circuit conditions

Illumination leads to the population of current carrying states in the valence and the conduction band. The characteristics of the photocurrent generated by this excess concentration of mobile carriers depends on the energy of the excitation (i.e. the photon energy) and the local spectral properties of absorption (joint density of states and occupation) and transport (local mobility) in the interaction region.

Absorption, emission and photocurrent response

As follows from Eq. (4.67) the total absorption consists of the integrated contribution of several layers, corresponding to the trace of the local interband polarization, which is

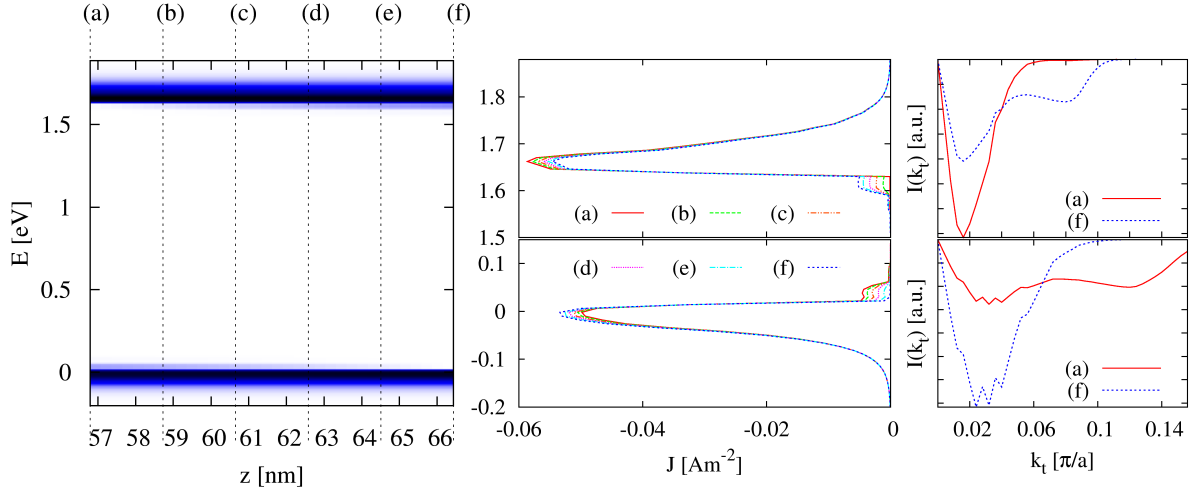


Figure 5.7: *The relaxation of carriers via inelastic scattering with optical phonons results in a redistribution of the carriers in current carrying states from higher to lower energy, leading to the formation of phonon satellite peaks below the noninteracting band edge. The relaxation depends on the local availability of scatterers and the number of scattering events; in p-i-n diodes, these two factors compete and the former dominates, wherefore the phonon satellites are more pronounced in the vicinity of the majority injection contacts, as shown in the central figure, which displays the current spectrum in the locations indicated by the cuts of the left figure. Due to momentum transfer, phonon satellite peaks also show up in the transverse momentum current dispersion (right figure), depending on the location as previously discussed, i.e. the phonon satellite builds up towards the injection contact.*

displayed in Fig. 5.8a)¹. The absorption as obtained from Eq. (4.64) for the present bulk diode is shown in Fig. 5.8b. Both polarization and absorption have the expected smooth shape associated with bulk transitions, with the exception of the onset tail at low energies extending below the fundamental absorption edge, which is one of the signatures of the bulk *Franz-Keldysh* effect that is due to the large field. The dependence of the absorption on the total field is shown in the inset of Fig. 5.8b, where the field is increased via reducing the length of the intrinsic region or reduced via applying a forward bias.

From the derivation of the absorption in Chap. 4 follows that the intensity of emitted radiation and thus the radiative dark current is related to the lesser part of the interband

¹The finite energy range $E \in [E_{min}, E_{max}]$ used in the numerical evaluation of the electron-photon self-energies and the absorption restricts the range of validity to photons with $E_{phot} < E_g + \min(E_V - E_{min}, E_{max} - E_C)$, where E_g is the barrier band gap, $E_{C,V}$ are the conduction and valence band edges, respectively, and the minimum is over the interacting region.

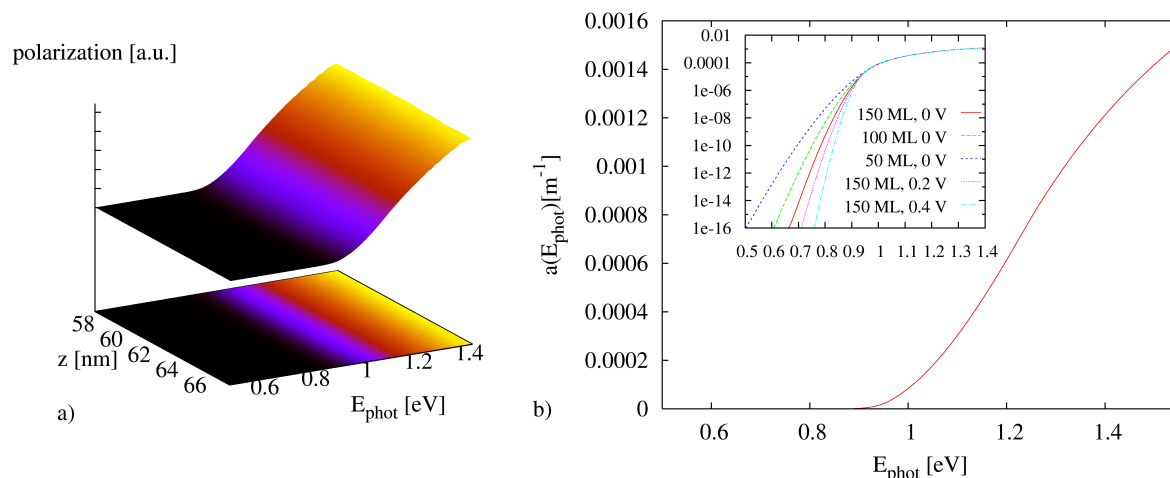


Figure 5.8: *a) Local transverse polarization function reflecting the joint density of states and the (nonequilibrium) occupation of the states near the band edge. b) Integrated absorption spectrum at zero bias. The inset shows the variation of the absorption with the internal field for three different lengths of the intrinsic regions and for forward bias of 0, 0.2 and 0.4 V. At large fields (equivalent to a short intrinsic region or reverse bias), the absorption develops a tail in the band gap (Franz-Keldysh effect).*

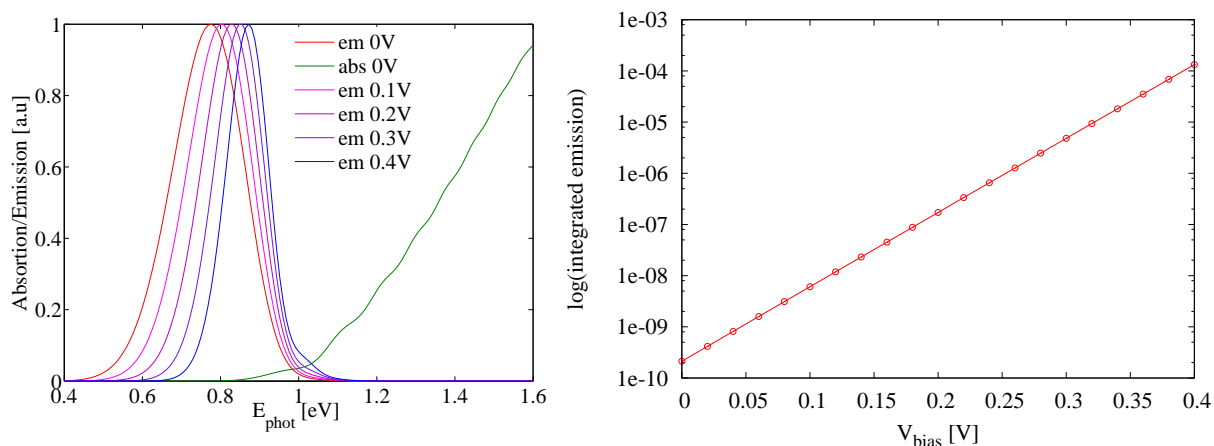


Figure 5.9: *(Left figure) Normalized emission spectra of a short bulk diode at different bias voltage. The effect of the internal field, which decreases with increasing bias voltage, is to broaden and to red-shift the emission line. For comparison, the normalized absorption at zero bias is given. (Right figure) Exponential bias dependence of the radiative dark current (integrated emission spectrum).*

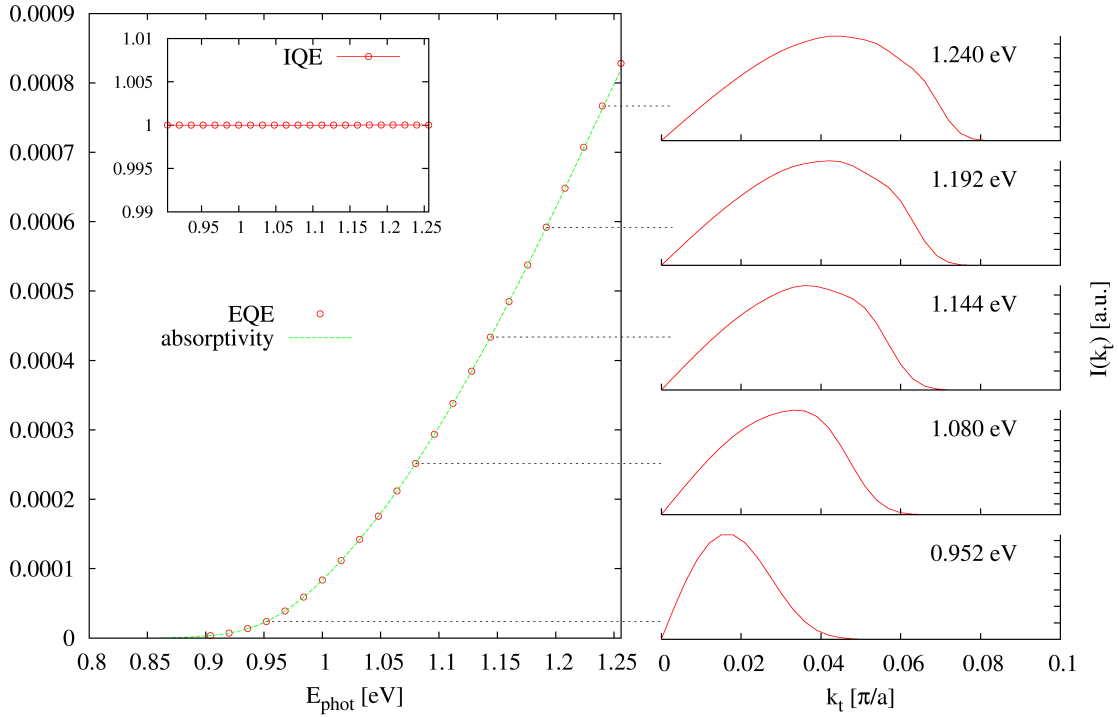


Figure 5.10: Photocurrent response (external quantum efficiency) and absorptivity: for ballistic transport, they must coincide, resulting in unit internal quantum efficiency (inset). At photon energies exceeding the band gap, the maximum weight current component is shifted to larger values of transverse momentum.

polarization function, $I_{em}(\hbar\omega) \propto \Pi^<(\hbar\omega)$. Fig. 5.9 (left) shows the normalized emission at different bias for a short device (high internal field). For comparison, the absorption at zero bias is given. The main features are the pronounced quenching and blue shift with increasing bias voltage corresponding to a decreasing internal field. The exponential dependence of the radiative dark current on bias voltage is verified in Fig. 5.9 (right).

The ballistic photocurrent response for bulk p - i - n diodes is an image of the interband absorption, since for short structures, no carriers are lost due to radiative recombination, and no energy is dissipated. In this situation, the photocurrent response, i.e. the external quantum efficiency (EQE), should equal the absorptivity, which corresponds to an internal quantum efficiency (IQE) of one. This is verified in Fig. 5.10 which shows the absorptivity, the EQE and the IQE (inset) for a range of photon energies above the band gap value. At energies exceeding the band gap, the direct transition occurs away from the band minimum, i.e. at higher values of the transverse momentum, as shown on the right hand side of Fig. 5.10, which displays the shift of the weight in the corresponding transverse

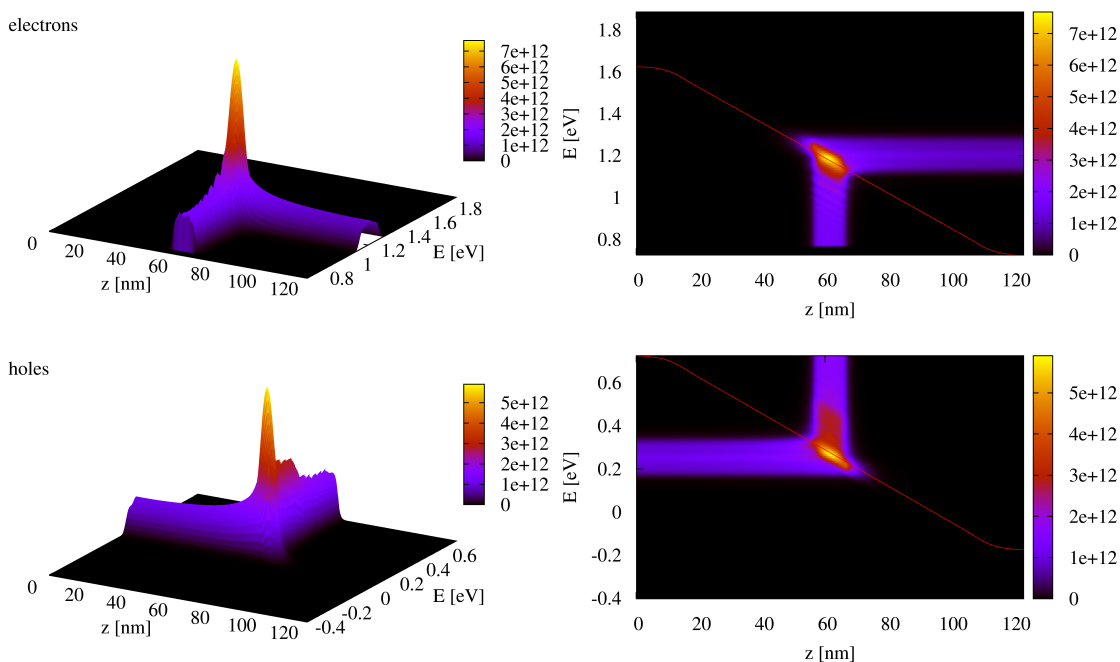


Figure 5.11: *Photogenerated spectral carrier density for illumination with $E_{\text{phot}} = 0.952 \text{ eV}$ at $I_{\gamma} = 1000 \text{ W/m}^2$. At such excitation levels, the density of photocarriers is very small compared to the concentration in the dark (Fig. 5.12). The excess spectral density is strongly localized near the band edge, with a tail towards the contact due to the field driven sweep-out.*

current components. The transverse spectrum is broader and the total current larger at higher photon energy since more initial and final states can be connected.

The photogenerated additional non-equilibrium carrier density is very small for illumination intensities of 1 sun (Fig. 5.12). As shown in Fig. 5.11, the carrier density is modified primarily in close vicinity of the band edge, but as a consequence of the unhindered carrier drift and the extended nature of the continuum states, a finite excess carrier density is still found at the contacts. The spatially resolved current spectrum in Fig. 5.13 reflects the joint density of the states that are involved in the optical transition, i.e. the combined density of states near the band edge, as well as their occupation. Depending on the mismatch between band gap and photon energy, the band edge peaks in the current spectrum are separated. Since photocurrent is generated at each atomic site of the interacting region and the photogenerated carriers drift in the built-in field, the electron and hole photocurrent components grow towards the respective contacts, adding up the local contributions,

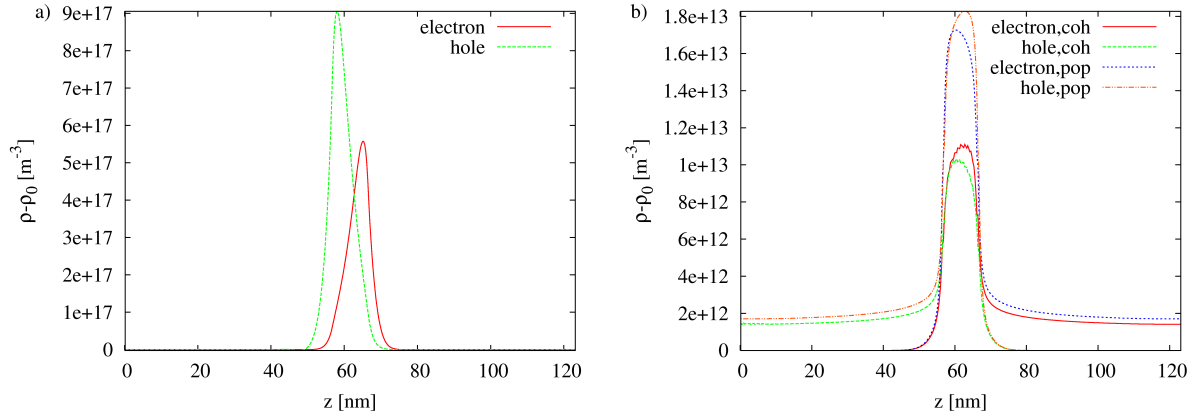


Figure 5.12: *The differential density due to interactions in the device region for a) electron-phonon scattering and b) photoexcitation, with and without electron-phonon scattering. Even though both interactions are restricted to the central device region, the illumination modifies also the density in the leads, since it does not correspond to a mere redistribution of the spectral weight within the same band, like in the case of the scattering with phonons, but to the addition of extra minority carriers that drift to the respective majority contact. It is interesting to note that the phonons modify not only the amount of photogenerated excess carriers, but also their spatial distribution.*

which results in a spatially varying photocurrent spectrum (Fig. 5.14). Unlike in the case of the dark current, the bands are coupled via the photoexcitation process, and therefore only the *total* current, i.e. the sum of electron and hole photocurrent components, is conserved (Fig. 5.13c).

Effects of electron-phonon scattering

From the study of the scattering effects on dark current, one would expect a similar behaviour under illumination, namely a deterioration of the photocurrent as compared to the ballistic case, due to thermalization of the carriers. However, the central observation in this case is that photocurrent is actually *enhanced* by the action of phonons, especially the inelastic scattering with polar optical phonons. This finding is readily explained by the additional 'indirect' transitions that become available through the participation of phonons. The joint density of states is thus increased, and correspondingly the absorption (Fig. 5.15). This photocurrent enhancement is much larger than the reduction of the current due to relaxation observed in the dark case, and should hence also exceed the effects of thermalization of the photocurrent. The effects of scattering on the optical

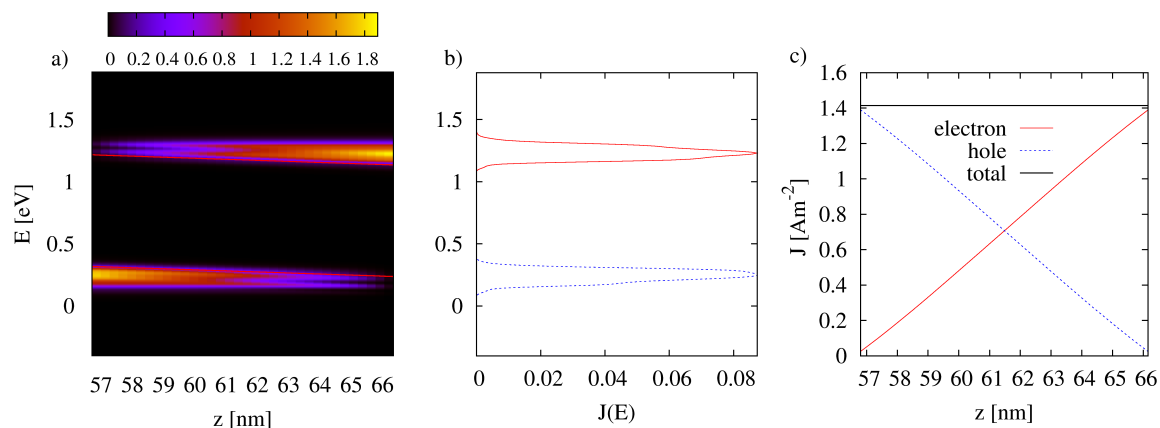


Figure 5.13: *a) Spatially resolved photocurrent spectrum for a photon energy of $E_{\text{phot}} = 1$ eV (including phonon scattering). Each layer contributes according to the local joint density of states and occupation of initial and final states, and since the photogenerated carriers drift to the contact all the contributions add up to the terminal spectrum. b) Photocurrent spectrum at the lead-device interface, reflecting the joint density of the initial and final states of the optical interband transitions. c) Electron and hole photocurrent components grow towards the respective contacts, while their sum is conserved.*

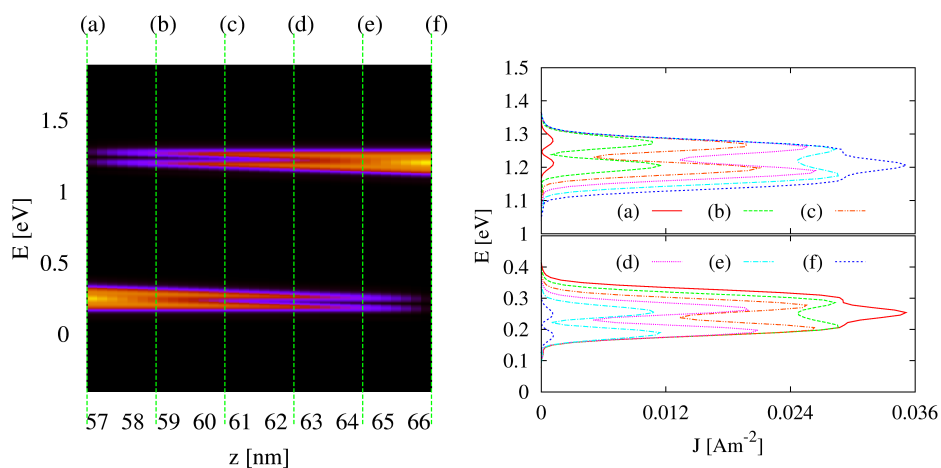


Figure 5.14: *Local variation of the ballistic photocurrent spectrum at $E_{\gamma} = 0.952$ eV. The splitting is due to the mismatch of the photon and the band gap energies.*

properties thus dominate those on transport in the bulk case.

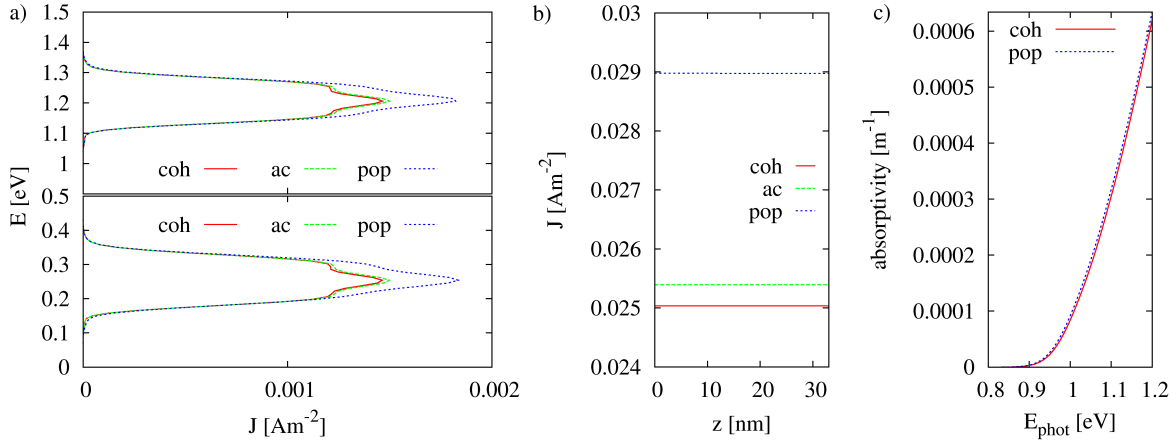


Figure 5.15: a) Photocurrent spectrum at the majority carrier lead-device interfaces for ballistic transport, elastic and inelastic scattering. Unlike in the dark, the photocurrent is enhanced by the scattering, as the phase space of the transition is enlarged. b) In the case of photocurrent, it the enhancement which is minimal for acoustic phonons, but substantial for inelastic scattering with polar-optical phonons. The total current is conserved also in the case where both phonons and photons interact with the charge carriers. c) The enhanced photocurrent is due to a larger joint density of states, which leads to a higher absorption.

5.2.7 Current-voltage characteristics

The results obtained for dark current and short circuit photocurrent can now be combined to analyze the device behaviour at finite terminal voltage and under illumination.

Fig. 5.16 shows the current-voltage characteristics under illumination of ~ 1 sun. Near short circuit conditions (Fig. 5.16b), current is purely photocurrent. At increasing bias, the diode current evolves exponentially (Fig. 5.16c,d), until it compensates the photocurrent at the open circuit voltage V_{oc} .

The effects of bias on the photocurrent enter via the field dependence of the absorption, which is quite weak for bulk, as can be inferred from Fig. 5.17. Since the effect of the built-in field is to broaden the density of states, the shape of the photocurrent reflecting the joint DOS is modified correspondingly with increasing bias.

Effect of simulation parameters and external conditions

As shown in Fig. 5.18, neither the resolution in energy nor in transverse momentum is critical in the evaluation of the current-voltage characteristics, which is to be expected for

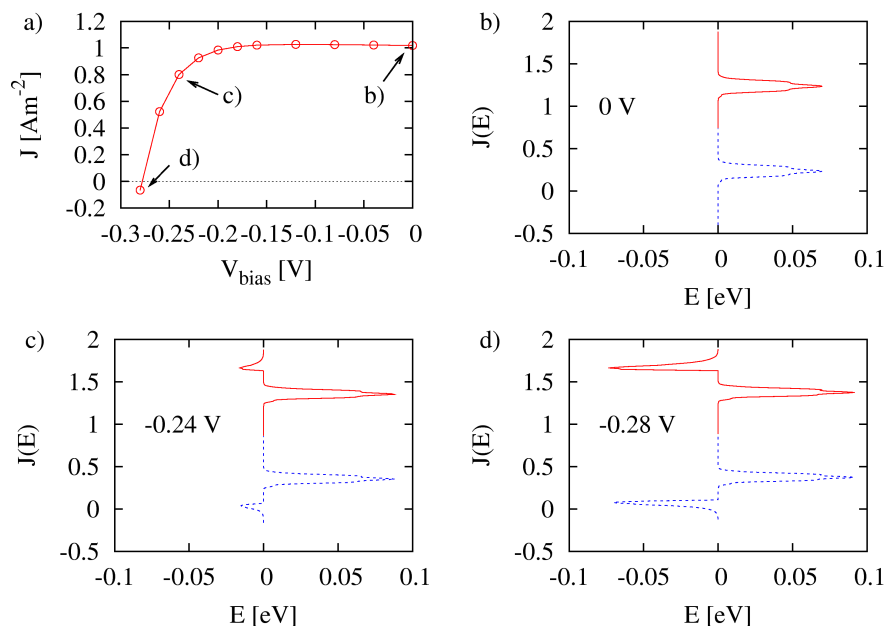


Figure 5.16: *a)* Current voltage characteristics of the p - i - n junction device under illumination of 1000 W/m^2 at $E_{\text{phot}} = 1 \text{ eV}$. The photocurrent spectrum at the lead-device interfaces is shown for *b)* short circuit conditions, *c)* near the maximum power point, and *d)* near the open circuit voltage. Note that the displayed photocurrent spectrum shows only the dominant photocurrent contribution, e.g. the electron component at the n -interface, and not the total current, which in this case would add from the hole component the same amount of dark current but only a vanishingly small photocurrent contribution.

bulk and at room temperature. This is generally true for integral quantities, like current and densities, but not for spectral quantities, like the LDOS or the absorption, which require a finer resolution, depending on the broadening via scattering, field, etc.

Variation in temperature has a direct impact on the distribution of the carriers in the contacts, but also on the population of phonons. Dark current is thus strongly reduced at low temperature, while the photocurrent is barely affected (Fig. 5.19a).

Under unconcentrated illumination of ~ 1 sun, the dependence of the photocurrent on the light intensity is linear, as shown in Fig. 5.19b. In principle, the non-equilibrium Green's function formalism is also ideally suited for the description of highly excited semiconductors, as its widespread use in laser theory demonstrates. However, for high excitation levels, e.g. under concentration, a perturbative treatment of the electron-photon interaction might no longer be appropriate.

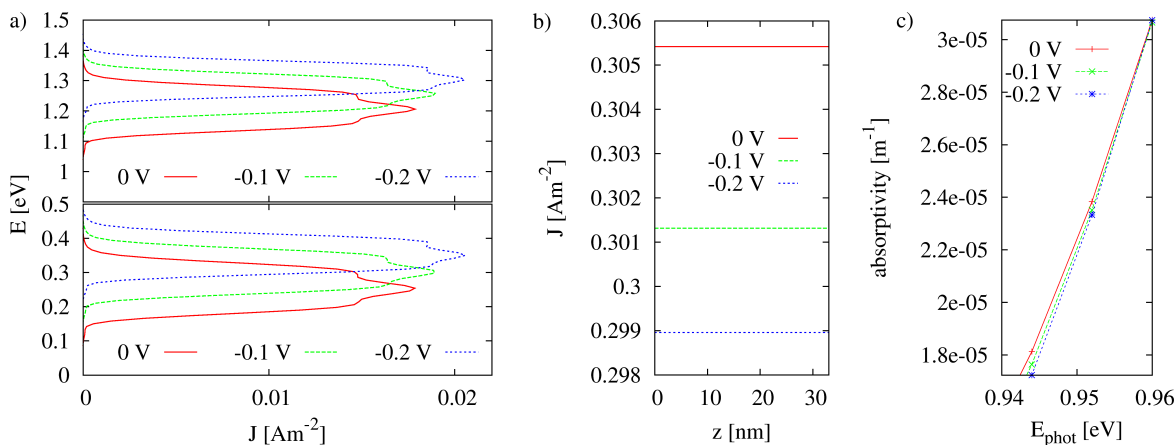


Figure 5.17: a) Photocurrent spectrum at the majority carrier lead-device interfaces at bias voltage of 0 V (short circuit), -0.1 V and -0.2 V. The effect of the decreasing field with growing forward bias is to quench the current spectrum. b) Even though the form of the spectrum is drastically altered by the change in the field, the current resulting from integration of the spectrum decreases only slightly for larger bias. c) In consistency with the decrease of the photocurrent, the absorption at $E_{\text{phot}} = 0.952$ eV is slightly lower for higher forward bias.

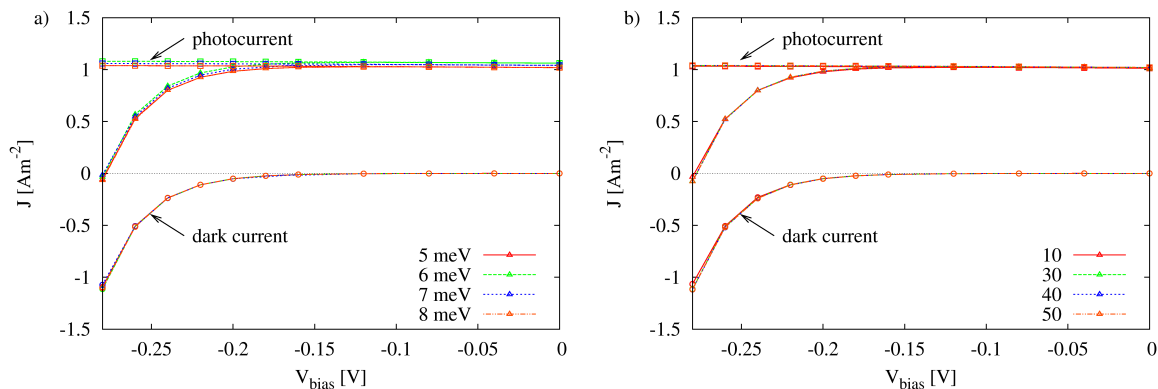


Figure 5.18: a) Dependence of dark and photocurrent on the energy resolution. In the present bulk case, both currents are rather insensitive to the resolution above, as long as it is below 10 meV. b) Dark and photocurrent for different numbers of k_{\parallel} -points in the fixed region of the transverse Brillouin zone that yields a significant contribution. Also here, convergence is reached very quickly.

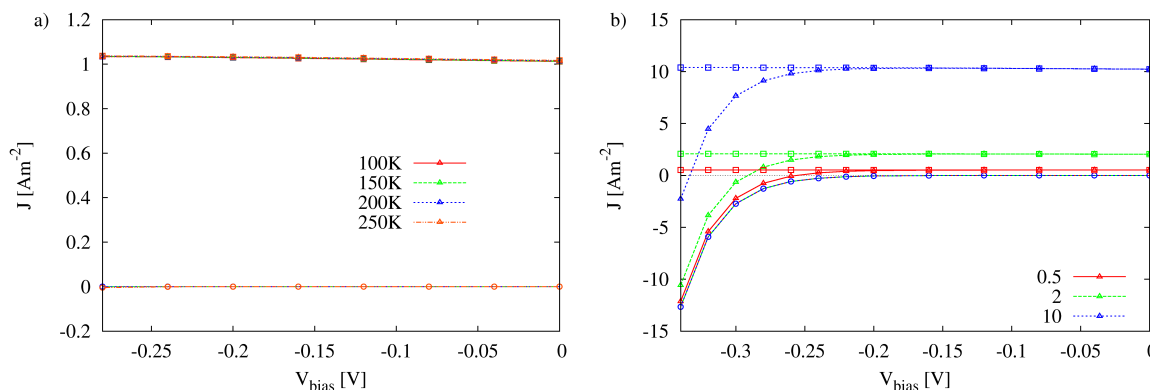


Figure 5.19: a) Temperature dependence of dark current (squares), photocurrent (circles) and total current (triangles). While dark current is completely frozen out, the photocurrent is barely affected. b) Linear dependence of the photocurrent on the illumination intensity. The labels are the same as in a).

5.2.8 Bandstructure effects: comparison with sp^3s^* multiband model

To evaluate the qualitative validity of the approximate band structure models, their predictions are compared to those of a more accurate multiband model able to consistently resolve the transverse band structure and to provide the corresponding dipole matrix elements for transverse polarization, as derived in App. C.

The results presented in the figures of this section were obtained using the parametrization of *Vogl et al.* [236](see App. C). The main difference to the two-band model is the presence of additional bands in the energy relevant for transport and optical excitation. Especially the fact that $\text{Al}_x\text{Ga}_{1-x}\text{As}$ for $x \sim 0.3$ is close to an indirect semiconductor strongly affects the transport properties, since not only carriers from the Γ -valley are injected, but also from the X -valley. The local density of states (at $\mathbf{k}_{\parallel} = 0$) in Fig. 5.20 displays the peaks corresponding to the edges of higher bands. These steps are also reflected in the absorptivity (Fig. 5.22).

The short circuit photocurrent spectrum at a photon energy of $E_{\text{phot}} = 2 \text{ eV}$ (Fig. 5.21a) is in good qualitative agreement with the photocurrent for the two-band model, and so is the transverse momentum dependence of the photocurrent (Fig. 5.23), which is to be expected for photon energies near the band gap value. The excellent conservation of ballistic photocurrent is a further proof of consistency for the present approach.

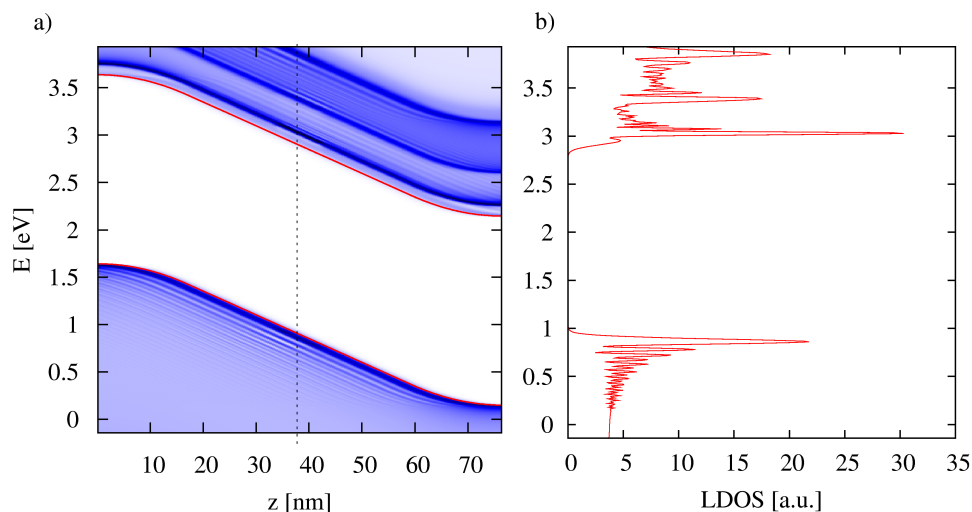


Figure 5.20: Local density of states ($k_{\parallel} = 0$) in the ballistic limit. In addition to the carriers from the Γ_6 -valley, there are the X_6 -valley and the X_7 -valley contributions appearing at higher energies.

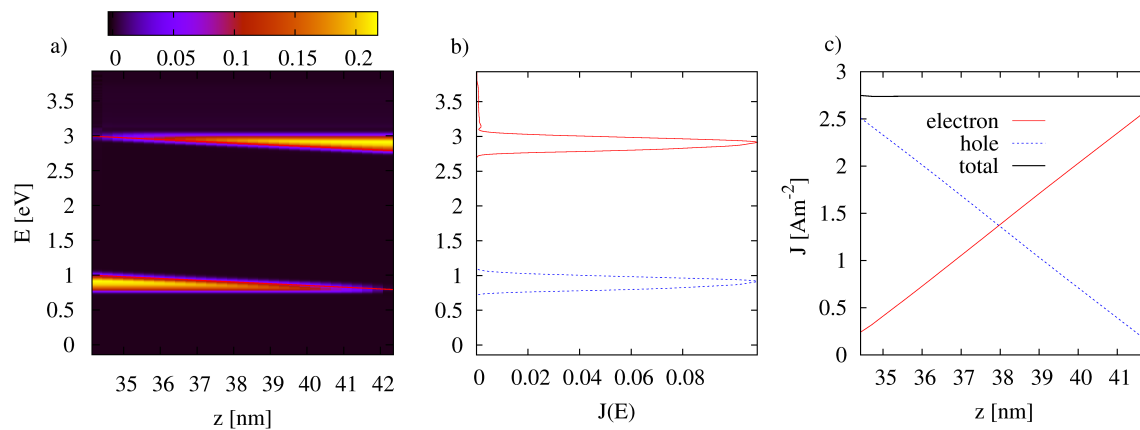


Figure 5.21: Illumination with $E_{\text{phot}} = 2$ eV at short circuit conditions: a) spatially resolved spectral current, b) current spectrum at the contacts, c) conservation of total current.

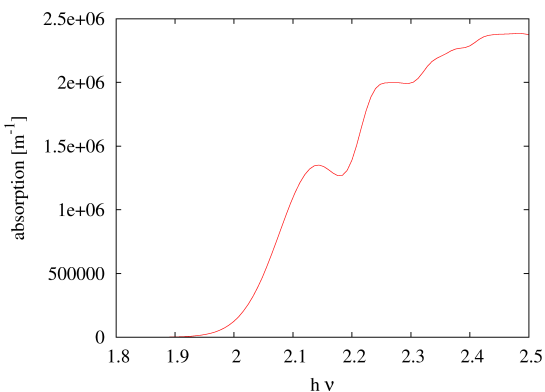


Figure 5.22: Absorption spectrum of the $Al_{0.3}Ga_{0.7}As$ p - i - n diode at short circuit conditions (large field).

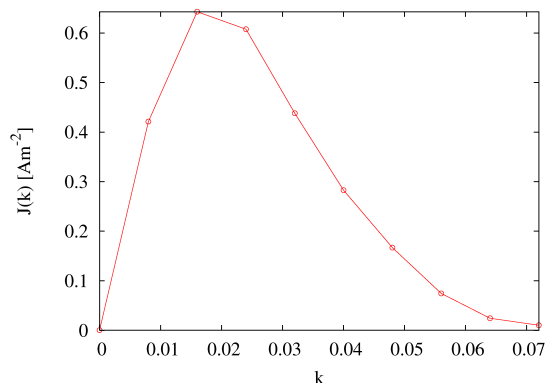


Figure 5.23: Transverse components of the photocurrent in Fig. 5.21.

5.2.9 Summary and conclusions

The nanoscale longitudinal extension of the investigated p - i - n -diode leads to various deviations from semiclassical behaviour. There are pronounced interference effects in the local density of states due to coherent superposition of scattering states. For electrons and light holes, transport is to a large extent ballistic. The strong internal field leads to a pronounced electroabsorption tail below the fundamental edge. The spatial evolution of the photocurrent follows the local joint density of states and occupation. Dark current is conserved for electrons and holes separately, while it is the sum of the currents which is conserved under illumination. Current conservation is excellent even in presence of both electron-phonon and electron-photon interaction. While the scattering with phonons decreases the diode current due to dissipation, it increases the photocurrent via extension of the available phase space.

While the NEGF-formalism provides insight into a wide range of microscopic processes and quantities, the qualitative current-voltage characteristics are still consistent with the picture provided by a semiclassical, macroscopic model. The full power of the present theory becomes evident when dealing with structures that are not accessible to these conventional approaches, like the single quantum well p - i - n diodes that will be considered next.

5.3 Photogeneration and transport in single quantum well p - i - n diodes

5.3.1 Introduction

Apart from the effects due to the ultra-small device dimensions, which appear already in the nanoscale bulk p - i - n junctions considered in the previous section, additional complexity arises with the introduction of quantum wells into the interacting region. To identify these new features, single quantum well (SQW) structures are investigated from the same points of view as for the bulk case.

Device geometry

The generic structure used throughout this section, shown in Fig. 5.24, consists in a single quantum well of 25 ML width, sandwiched between 65 ML of undoped barrier material, of which 5 ML form part of the device region, and 50 ML highly doped barrier material contacts. The inclusion of the barrier layers into the interacting region is necessary due to the finite decay length of the probability amplitude within the barrier material, on which there is still a contribution to the local absorption. The material parameters and the doping concentration are the same as for the bulk diode in the previous section (Tab. 5.1). The offsets resulting from the use of the band structure parameters given in Tab.

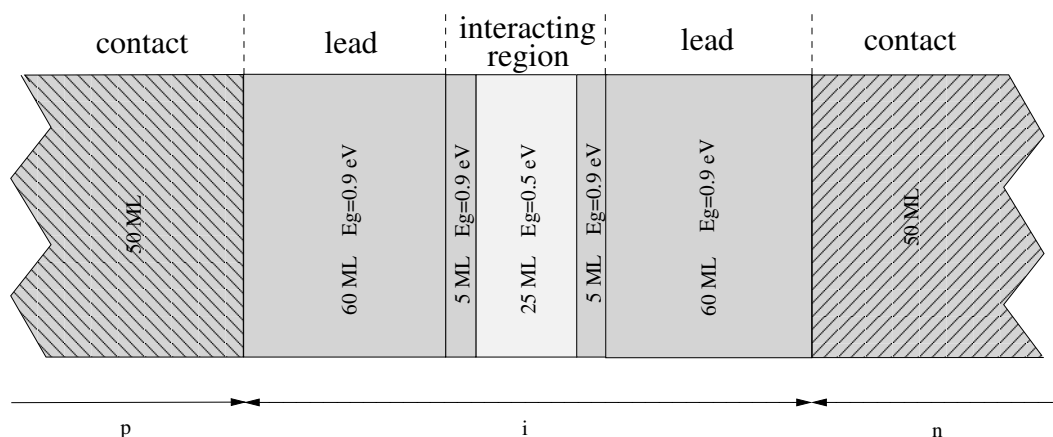


Figure 5.24: Geometrical configuration of the single quantum well device used in the simulations. The interacting region is formed by the 25 ML QW and the 5ML of the adjacent barrier material.

5.1 are 0.25 eV for the conduction band and 0.15 eV for the valence band. This leads to an asymmetric situation with stronger confinement of the electrons, which however is partially compensated by the larger effective mass of the holes.

Numerical considerations

When it comes to the numerical simulation of quantum confined systems, a substantial problem arises from the presence of very sharp features in the spectral quantities, such as the the local density of states of bound states at fixed transverse momentum, which appears also in the optical quantities due to the impact on the joint density of states. Correspondingly, at low temperatures or for the investigation of weakly inelastic transport involving strongly confined states, a much finer resolution is required both for energy and transverse momentum. Even the integral quantities may be largely affected if the resolution of the bound state contribution is insufficient. This problem becomes worse with increasing forward bias, or, equivalently, shrinking total field, since the field helps to delocalize and thus to broaden the confined states. The sharpness of the feature and the high degree of localization in quantum wells has also a detrimental effect on the convergence of the inelastic current, which can be both very slow and inhomogeneous, depending on the excitation energy and the degree of confinement. Inhomogeneous means here that it converges more quickly for the less confined carriers, which are the holes in the case of the symmetric two-band approximation.

5.3.2 Electronic properties in the dark

Local density of states: confinement effects

The transverse momentum resolved local density of states $\mathcal{D}_L(\mathbf{k}; E) = \frac{1}{\pi} \text{Tr}\{A_{L;L}(\mathbf{k}, E)\}$ for a 25 ML SQW at $\mathbf{k} = 0$ and $V_{bias} = -0.01$ V is shown in Fig. 5.25. It reflects the probability amplitude given by the square of the wave function, and reveals the different regimes of states specifically affected by the presence of the well, from the strongly localized states in the quantum wells and in the lead close to the well to higher resonances and the nearly homogeneous extended states of the quasi-continuum. The system being open, there are no true bound states, but all states acquire a finite linewidth corresponding to a finite lifetime. The confinement levels are further broadened by the coupling to phonons, and in the case of strong scattering, phonon satellite peaks form in the LDOS next to the confinement level peaks. The LDOS is obtained after integration over transverse momentum (Fig. 5.25a) and displays the characteristic step-like shape in the quantum well reflecting the lower dimensionality of the mobile carriers. It is more pronounced in the deeper well of the conduction band, where the states are stronger bound and hence sharper than in the shallow valence band well. The confinement energy of the lowest states is inferred from the difference to the corresponding bulk band edge indicated by dashed lines. The onset of the continuum states is much higher than expected from the barrier bulk band edge.

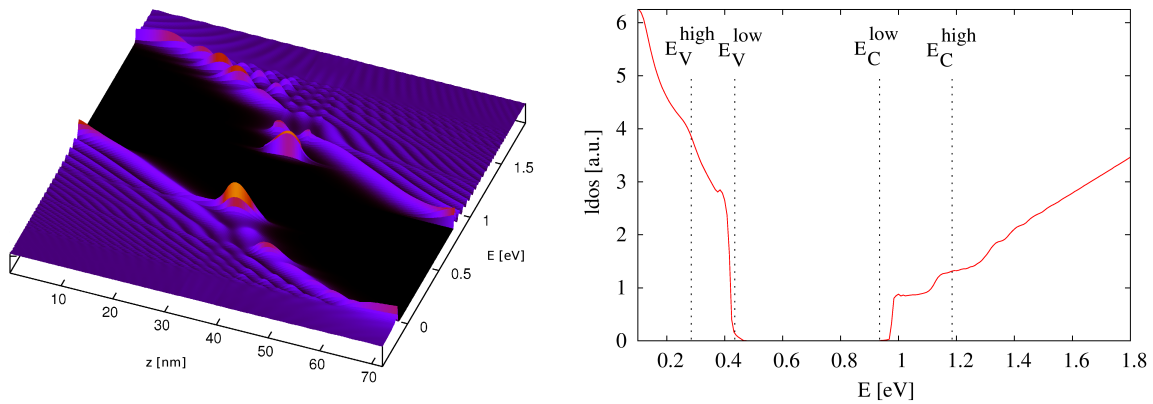


Figure 5.25: a) The local density of states for a 25 ML SQW, reflecting the probability amplitude for quasi-bound to quasi-continuum states. b) The local density of states in the center of the well, integrated over transverse momentum, showing the signs of change in dimensionality due to quantum confinement.

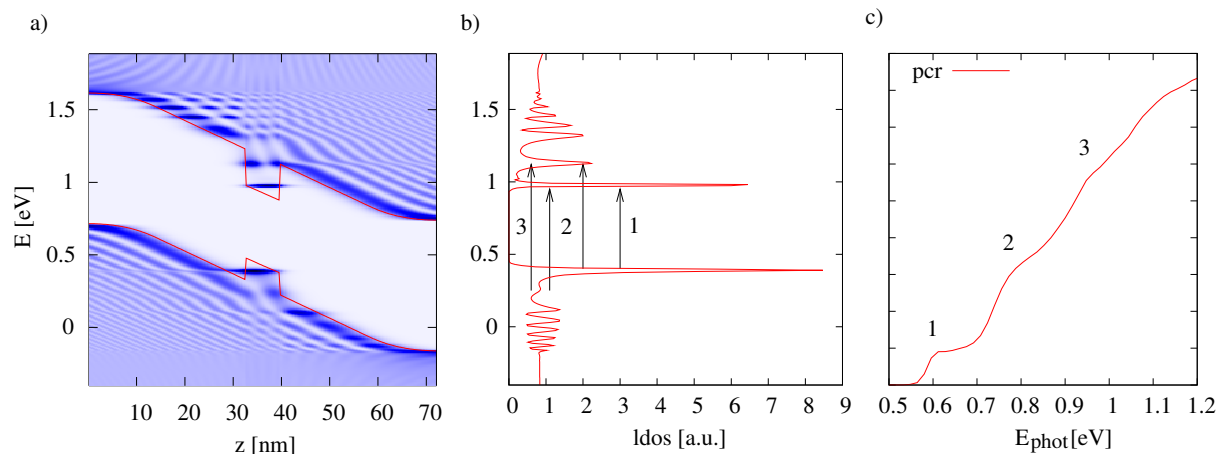


Figure 5.26: *a) Momentum resolved local density of states (LDOS) at $\mathbf{k} = 0$ for a 25 ML SQW pin -diode at $V_{bias} = -0.01$ V. b) Momentum resolved LDOS at the well center and optical transitions between confinement levels. c) Photocurrent response reflecting the density of the states participating in the corresponding optical transitions.*

In the case of the 25 ML SQW, two sharp confinement levels are present and contribute to the photocurrent. The high lying state is only weakly bound and broad, corresponding to a faster carrier escape as compared to the more strongly bound and sharper low lying state². This quantum well geometry is thus ideally suited to study carrier escape from both deep and high levels, which are furthermore well separated in energy. In addition to the confined states, there is a variety of quasi-bound states and transmission resonances above the well, which influence the photovoltaic properties of the structure and might explain the enhanced absorption of QWSC observed at photon energies above the higher band gap. This pattern of quasi-bound states and higher transmission resonances in the well region resulting from quantum confinement is superimposed to the stripe-like interference pattern originating from the built-in field exactly as in the bulk case, i.e. due to reflection of carriers injected below the maximum of the band edge at the minority carrier contacts. Above this maximum, the LDOS acquires the expected uniform value of the quasi-continuum, that however is still affected by the presence of the well. A further interesting characteristic displayed by the LDOS is the appearance of “notch” states between well and the corresponding contacts, as are usually observed in the presence of barriers. Since these states are also of quasi-bound nature, they will strongly modify the spectral response for photon energies right above the value of the barrier band gap.

²It is one of the advantages of the present approach that the linewidth and with it the lifetime comes about naturally and does not have to be determined by an additional model and then be inserted by hand

Potential, field and carrier density

The Hartree potential U resulting from Poisson's equation and the corresponding total electric field \mathcal{E} and displacement \mathcal{D} are shown in Fig. 5.27 a) and b), respectively, at applied forward bias voltage of 0 V, 0.2 V and 0.4 V. The Hartree potential is compared to the corresponding data for bulk. At high voltages, charging effects through accumulation of carriers in the quantum well region leads to corrections that produce a finite band bending in the active area. The total electric field decreases with growing forward bias, since in this case, the external field has opposite sign of the built-in field. The quantum well device consists of media with differing dielectric constants, and hence the electric field \mathcal{E} is discontinuous. The associated continuous macroscopic quantity is the electric displacement \mathcal{D} , also shown in Fig. 5.27 b).

The corresponding electron and hole densities as well as the conduction and valence band edges are displayed in Fig. 5.28 a) and b), respectively, again for an applied forward bias voltage of 0 V, 0.2 V and 0.4 V. The band edge is given by the Hartree potential and the respective band offset. The density in the quantum well is considerably higher than in the barrier region due to the contribution of the localized states, and it varies over several orders of magnitude under the application of bias. At high forward bias voltage (-0.4 V), it becomes comparable to the density in the corresponding majority carrier contact.

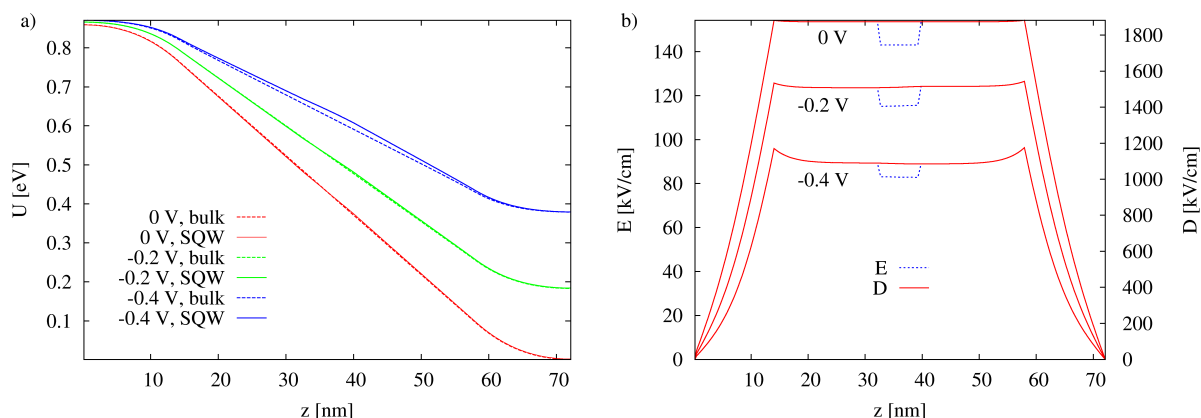


Figure 5.27: a) Hartree potential for bulk and SQW and b) the corresponding total electric field \mathcal{E} and displacement \mathcal{D} for the SQW diode, at applied forward bias voltage of 0 V, 0.2 V and 0.4 V.

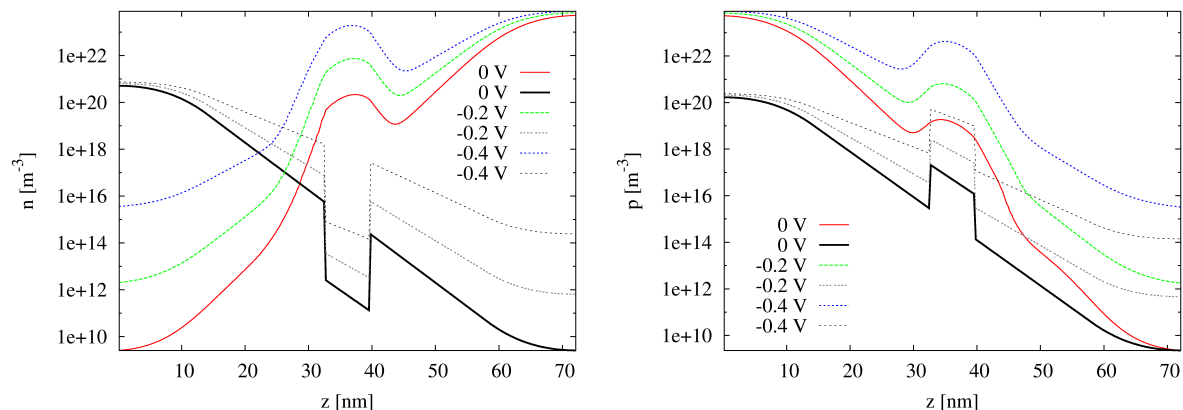


Figure 5.28: a) Electron density and conduction band edge, and b) hole density and valence band edge, respectively, at applied forward bias voltage of 0 V, 0.2 V and 0.4 V.

Effects of scattering on dark current

The effects of scattering on the dark current of a SQW are shown in Fig. 5.29. While qualitatively, no new features appear in the dark spectrum, there is a quantitative difference in the degree of relaxation which is due to the different effective mass of the carriers interacting with the phonons in the quantum well region as compared to the scattering in the barrier material. This change in carrier mass affects all the states irrespective of their energy, including the high continuum states which carry the dark injection current.

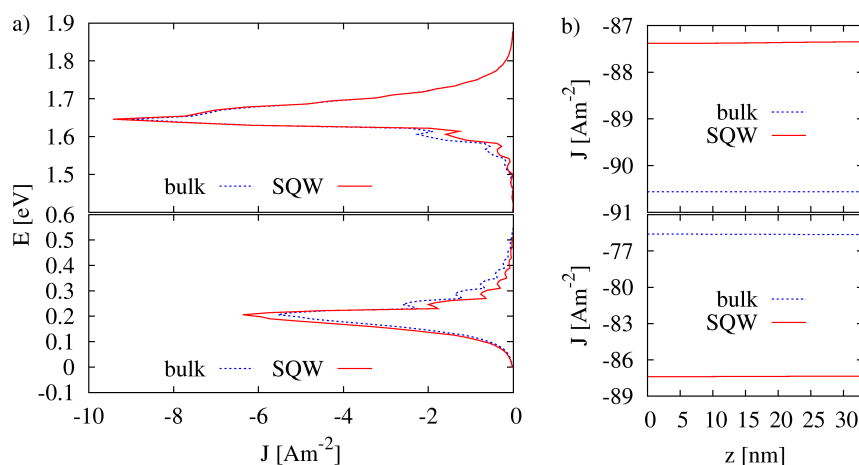


Figure 5.29: a) Dark electron (upper figure) and hole current spectrum at the lead-device interfaces, for SQW and bulk, respectively, assuming the same total field for both configurations. b) Local dark current for bulk and SQW.

Comparison with multiband model

Fig. 5.30 shows the LDOS for a SQW p - i - n diode obtained with the 10-band sp^3s^* model for $\text{Al}_{0.3}\text{Ga}_{0.7}\text{As}$, again using the parametrization of *Vogl. et al* [236](App. C). In this parametrization, the difference of the bulk band gaps is $\Delta E_g \approx 0.445$ eV. The valence band offset at the Γ valley is $\Delta E_V \approx 0.147$ eV, which leaves $\Delta E_V \approx 0.298$ eV for the conduction band offset. The offsets of the X -valleys from barrier to well material are very small, such that the effects of confinement are negligible. The confinement level structure if the Γ -valley quantum well is very similar to the one obtained from the two-band approximation, in terms of number and spacing. In the absence of electron-phonon interaction, the lowest state in the conduction band well is extremely narrow, such that a very fine energy grid is required to resolve it. In the valence band well, the use of the 10-band model allows the resolution of the splitting between the lowest heavy and light-hole levels.

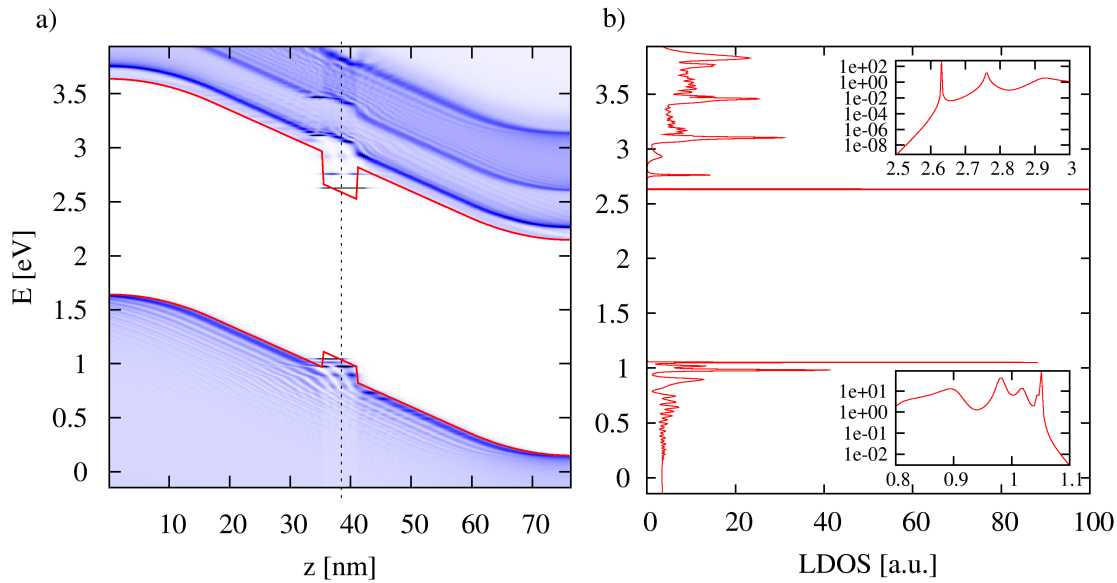


Figure 5.30: Local density of states ($k_{\parallel} = 0$) of a 20 ML SQW, calculated using the 10-band sp^3s^* model. In the ballistic limit shown in the figure, the low lying confinement levels are extremely sharp. The insets show the resolution of the confined states. The effects of confinement are significant only for the well formed by the Γ -point offset. In the valence band, the splitting of the lowest levels for heavy and light holes can be observed.

5.3.3 Optoelectronic properties under illumination

Optical transitions, absorption and photocurrent response

Due to the finite depth of the well, the considerable field and the interaction with phonons, there are no strictly forbidden transitions like in the idealized, flatband situation. The different optical transitions between confined states, quasi-bound states, higher resonances and the continuum can be identified in the photocurrent response (Fig. 5.26c), which at short circuit conditions corresponds to the external quantum efficiency, i.e. the short circuit current normalized by the incoming photon flux. The PCR strongly resembles the absorptivity, which is shown in Fig. 5.31. As in the bulk case, both the absorption and the external quantum efficiency reflect the joint density of states, with its 2D characteristics for the confined states and a more 3D-like shape for higher transitions. In the case of photogeneration of carriers on confinement levels, however, the charge separation is slowed down by the escape process, especially at low fields, corresponding to high bias voltage. This leads to small but finite radiative recombination resulting in an internal quantum efficiency below unity. The transverse momentum resolved current contributions (Fig. 5.32) also reflect the transition from bound-state to quasi-continuum excitations in the shifting of the weight from the peak at small momentum for low energy photons, corresponding to contributions from confined states, to the broadened components of high-lying, weakly

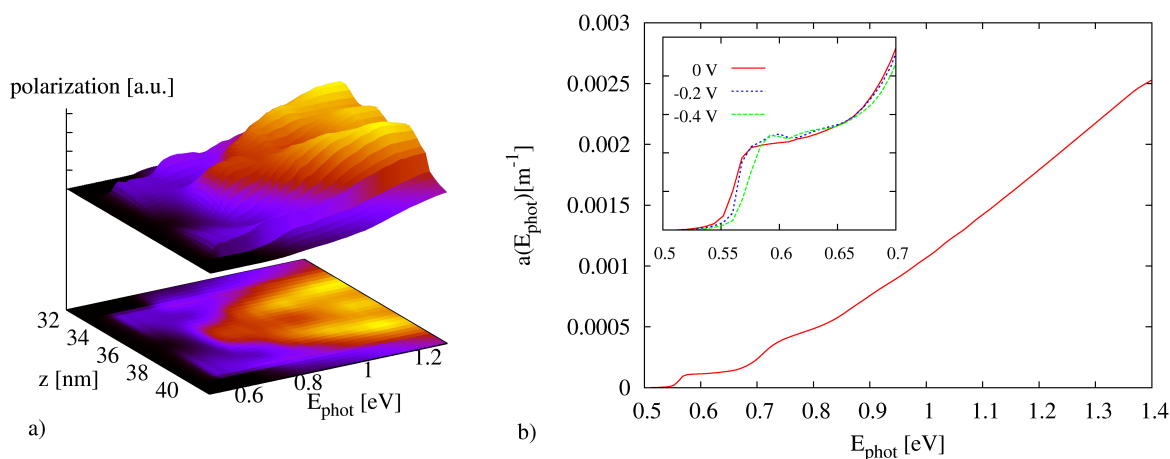


Figure 5.31: a) The local transverse polarization function reflects the local structure of the electron and hole wave functions in the well. b) Integrated absorption spectrum at zero bias. The inset shows the variation of the absorption with the internal field for forward bias of 0, 0.2, and 0.4 V.

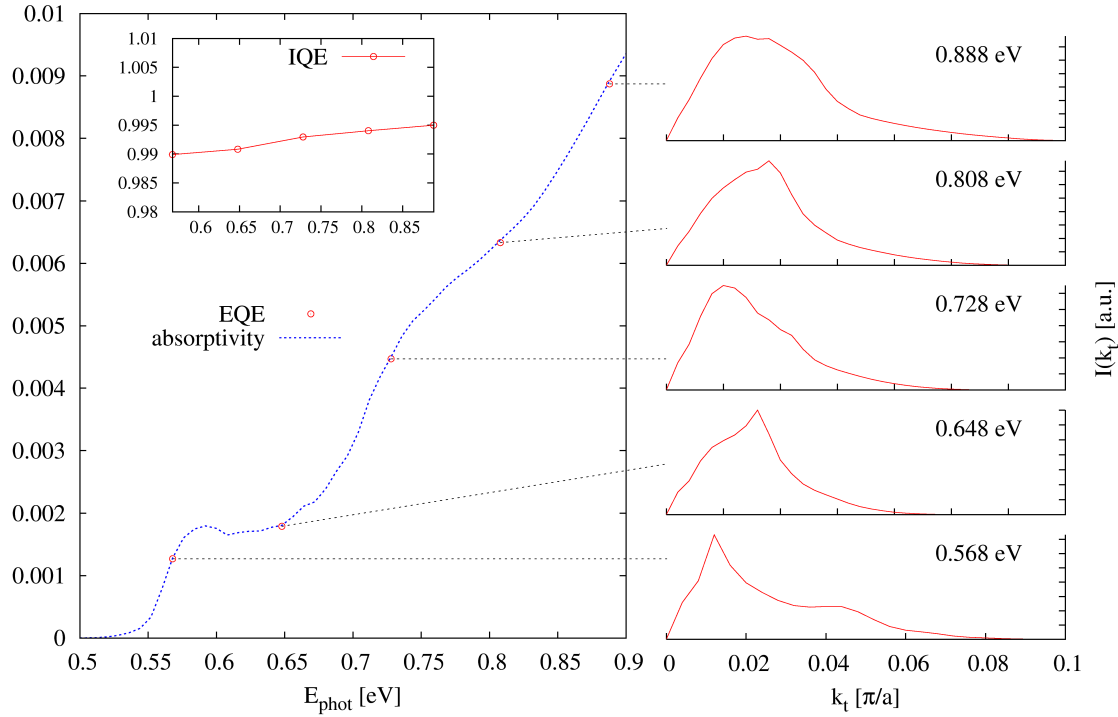


Figure 5.32: a) Absorptivity, external and internal quantum efficiency. The EQE shows the same spectral characteristics as the absorptivity. b) Transverse momentum resolved current contributions.

bound states.

The emission spectra associated with the shown absorption are displayed in Fig. 5.33 (left) for different values of the applied bias voltage. The emission line, which is centered around the energy of the lowest bound state transition, is narrower than in the bulk case, but shows the same behaviour under bias, namely a quenching of the linewidth and a blueshift of the peak position. The exponential bias dependence is shown in Fig. 5.33 (right).

Excess carrier concentration and nonequilibrium occupation

Fig. 5.34 shows the photogenerated excess carrier density $\delta n = n_{\text{light}} - n_{\text{dark}}$ for the SQW diode. There are several differences to the situation in bulk. First of all, the excess density is several orders of magnitude larger. Owing to the localized nature of the states which are occupied, the fraction of the carriers that drifts to the contact is much smaller, especially in the case of the electrons, which are more confined than the holes. The

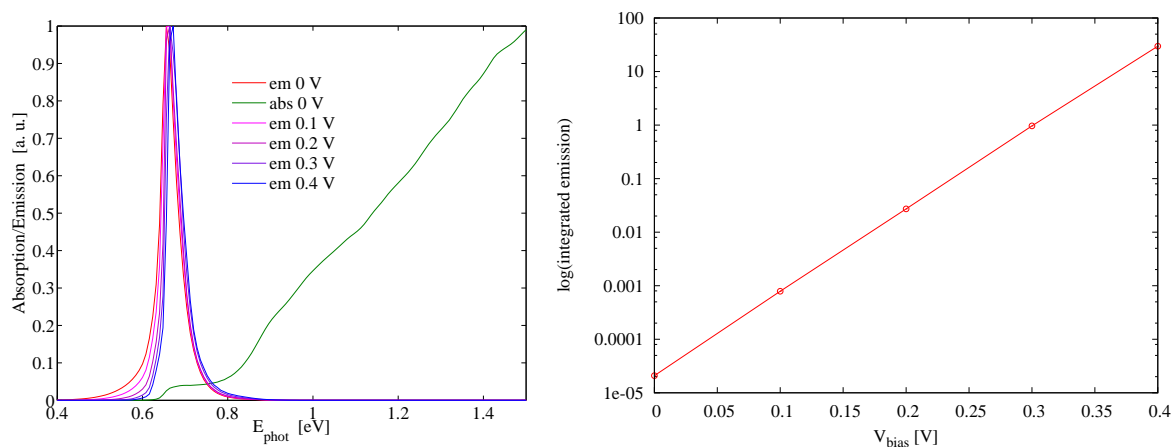


Figure 5.33: (Left image) Emission spectra of a short SQW diode at different bias voltage. As in the bulk case, the emission line is quenched and blue-shifted under the action of the external applied bias, which decreases the internal field. (Right image) Exponential bias dependence of the radiative dark current.

higher electron concentration is a consequence of the longer escape times of the electrons resulting from this stronger confinement. It is further interesting to notice that while the hole concentration follows the increase in photocurrent with larger photon energy, this is not the case for the electron concentration. This observation is explained by the stronger increase in escape channels for electrons at higher excitation energies as compared to the situation of the holes, where the enhancement sets in at lower energies.

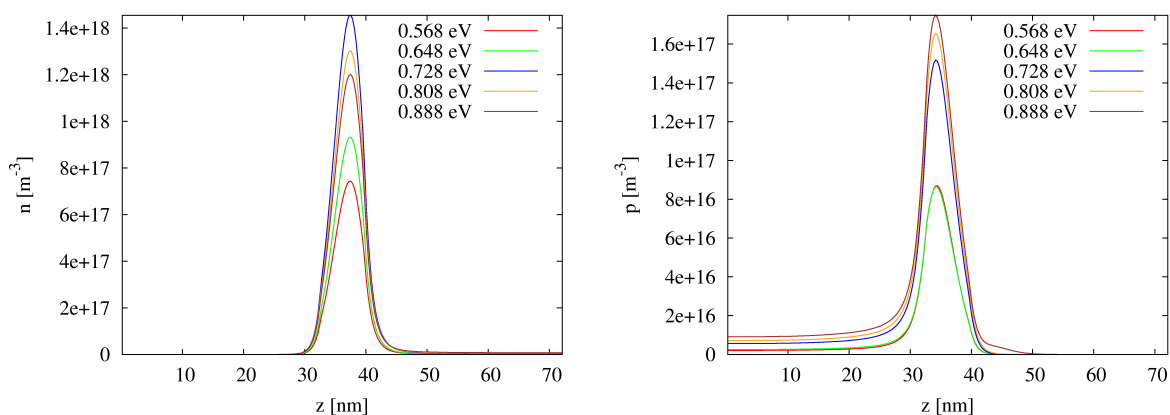


Figure 5.34: Photogenerated excess carrier density for different photon energies at $V_{bias} = -0.01V$. The electronic density exceeds the hole concentration due to stronger confinement and resulting reduced carrier escape.

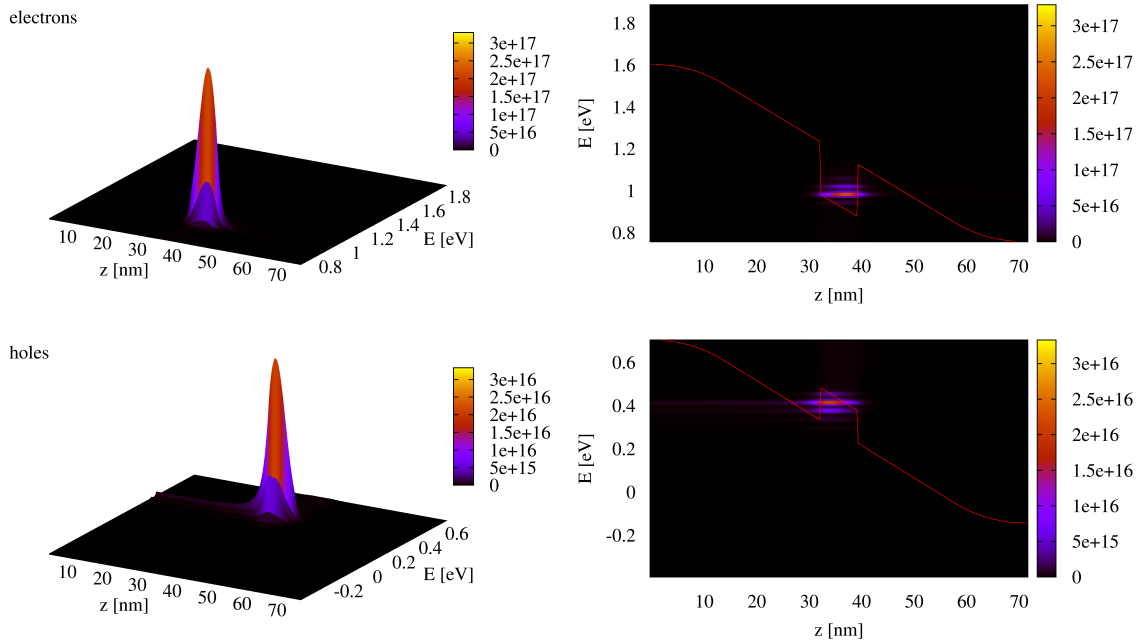


Figure 5.35: Photogenerated excess carrier spectral density for illumination with $E_{phot} = 0.568$ eV (bound state transition), at $V_{bias} = -0.01$ V.

To investigate the occupation of available states by the photogenerated excess carriers, their distribution in energy $\delta\rho_L(E)$ is computed for different excitation energies. In Fig. 5.35, the photogenerated excess carrier spectral density for illumination with $E_{phot} = 0.568$ eV (bound state transition) is displayed. At this low energy, the photogenerated carriers occupy only the lowest subband. This means that not only the dark carrier concentration, but also the photogenerated carrier density is strongly localized in energy around the lowest level, and the occupation of higher and lower energy states via phonons produces pronounced satellite peaks, both in the conduction band well and the valence band well. The photogenerated excess carrier spectral density for illumination with $E_{phot} = 0.888$ eV (quasi-bound state transition) is shown in Fig. 5.36. At this photon energy, states high in the quantum well are occupied by the photoexcitation process, which are broad due to fast escape. Subsequent carrier relaxation via emission of phonons leads to the occupation of the lower confinement levels, which then provide the main contribution to the spectral density. Due to the width of the states of initial occupation, the final excess carrier spectrum exhibits only smooth features. This smoothing of the phonon satellite peaks with increasing excitation energy and the accumulation of density on the lowest confinement levels can also be seen in Fig. 5.37, which shows a cut of the spectral excess

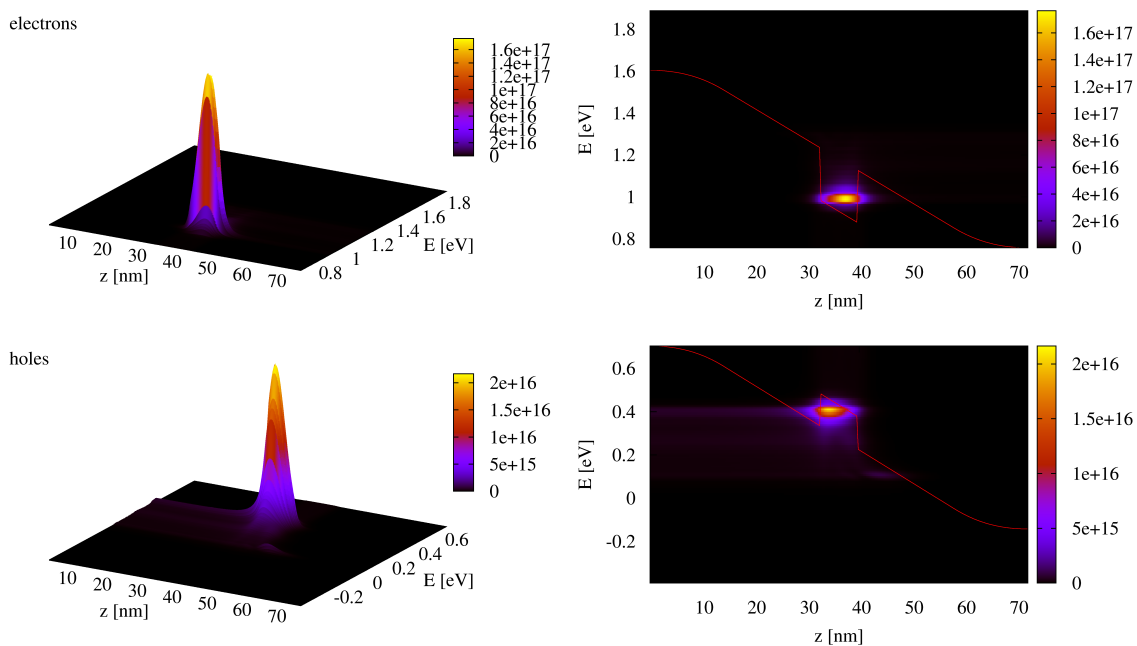


Figure 5.36: Photogenerated excess carrier spectral density for illumination with $E_{\text{phot}} = 0.888 \text{ eV}$ (quasi-bound state transition), at $V_{\text{bias}} = -0.01 \text{ V}$.

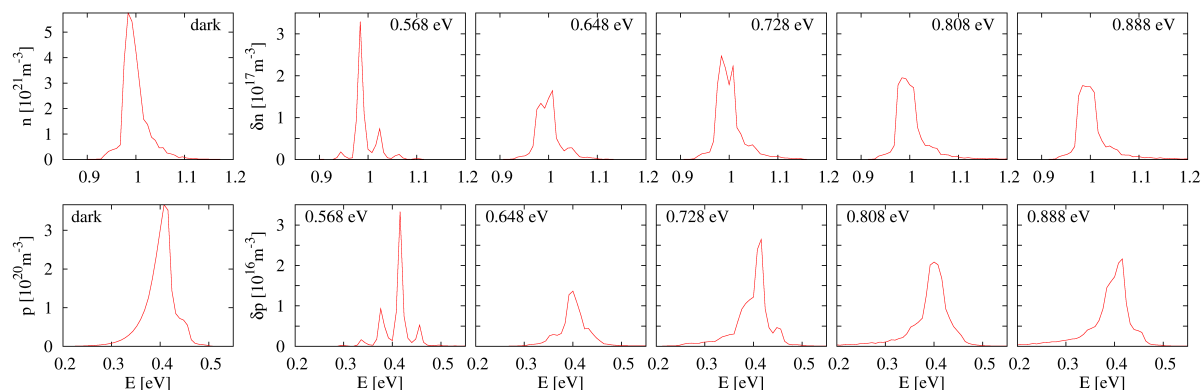


Figure 5.37: Spectral resolution of the excess carrier density for different photon energies (cut at position of maximum in the quantum well). For comparison, the carrier concentration in the dark is given for the same position in the quantum well. While the phonon satellite peaks get smoothed at higher excitation energies due to occupation of broadened states, the highest weight remains always on the lowest confinement level.

carrier concentration at the position of its maximum in the well. What is interesting to notice in this figure is the large difference in the degree of thermionic emission between electrons and holes: while the excess carrier density in the valence band has a tail that extends far above the effective barrier edge at ~ 0.35 eV, the corresponding density is very low in conduction band well at the effective barrier edge of ~ 1.15 eV, even at the highest excitation energies.

It is possible to define an effective local carrier distribution function $\tilde{f}_L(E)$ via

$$\tilde{f}_L(E) \equiv \frac{\rho_L(E)}{\mathcal{D}_L(E)} = \frac{-i \sum_{\mathbf{k}_{\parallel}} \text{Tr}\{G_{L;L}^<(\mathbf{k}_{\parallel}; E)\}}{\sum_{\mathbf{k}_{\parallel}} \text{Tr}\{A_{L;L}(\mathbf{k}_{\parallel}; E)\}}, \quad (5.4)$$

where $\rho_L(E)$ is the spectral density and $\mathcal{D}_L(E)$ the local density of states at layer L . Fig. 5.38 shows this distribution at the majority carrier contact ($L = N_z$ for electrons, $L = 1$ for holes) under small forward bias ($V = -0.01$ V), in the dark and under illumination, with comparison to the equilibrium Fermi distribution $f_{\mu}(E)$ of the contacts with chemical potential μ . In the dark, the only evidence of non-equilibrium giving rise to a deviation $\delta f = \tilde{f} - f_{\mu}$ from the equilibrium distribution is the signature of the injection current from the opposite contact, which is characterized by a chemical potential μ' that differs from μ by the applied bias voltage, $\mu' = \mu + V_{bias}$. Under illumination, there is an additional deviation from equilibrium which reflects the distribution of the photogenerated excess carriers.

Current spectrum and IV-characteristics

For monochromatic illumination in the energy range below quasi-continuum transitions, the photocurrent spectrum reflects the joint density of states of the dominant transition between subbands. Unlike the LDOS in the well, the current spectrum shows a strong asymmetry between electrons and holes: in the conduction band well, the main contribution to current comes from the higher level, while it is the lower one that dominates the current in the valence band well. This demonstrates the impact of carrier escape probability on the current, the latter no longer being characterized by the LDOS alone as in bulk structures.

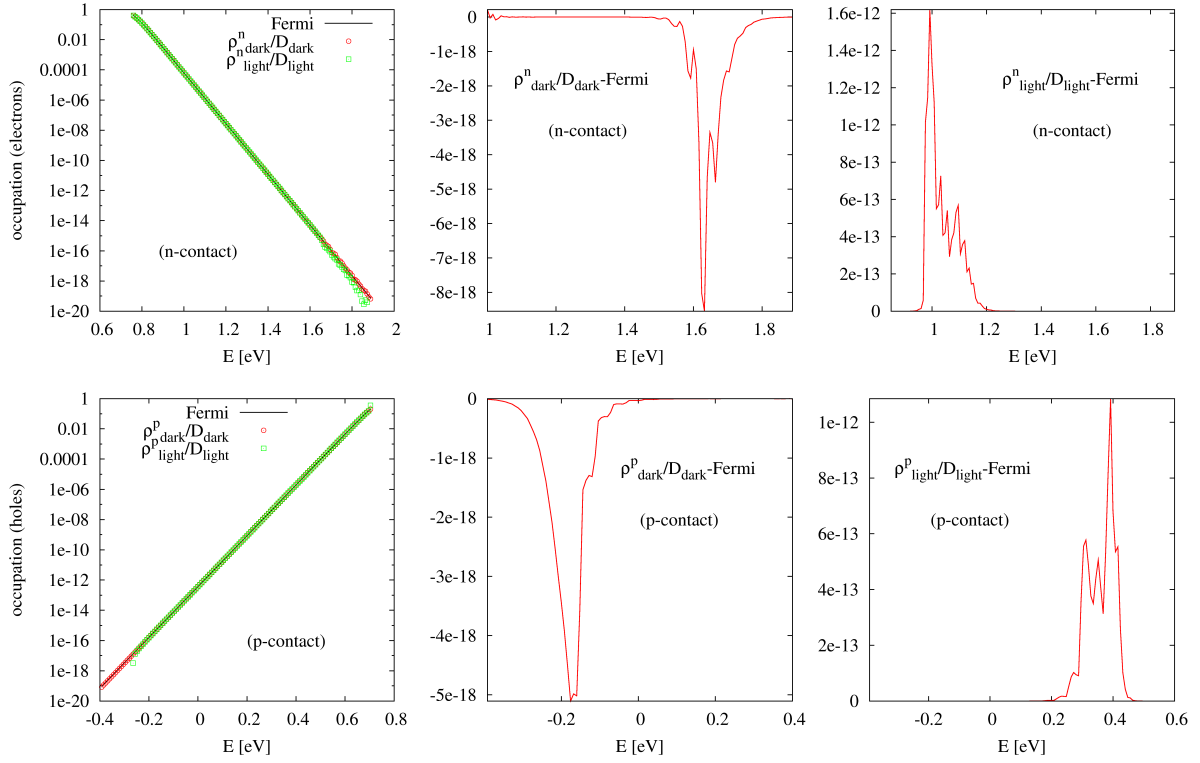


Figure 5.38: (left) Distribution function $\tilde{f}_L(E) \equiv \rho_L(E)/\mathcal{D}_L(E)$ at the majority carrier contact ($L = N_z$ for electrons, $L = 1$ for holes) under small forward bias ($V = -0.01$ V), in the dark and under illumination, with comparison to the equilibrium Fermi distribution $f_\mu(E)$ of the contacts with chemical potential μ . (center) Deviation $\delta f = \tilde{f} - f_\mu$ from the equilibrium distribution in the dark. (right) Deviation from equilibrium under illumination.

To investigate the effects of elastic and inelastic scattering on the photocurrent of the SQW, the hole current³ is determined near short circuit conditions ($V_{\text{bias}} = -0.01$ V) for $E_{\text{phot}} = 0.728$ eV and different types of scattering (Fig. 5.40): elastic only, inelastic only and both elastic and inelastic. Like in the bulk case, current is most strongly enhanced by inelastic scattering. The spectrum of the hole current at the p -contact exhibits the phonon-staircase resulting from the absorption and emission of optical phonons (inelastic scattering), which is smoothed by the scattering with acoustic phonons (elastic scattering).

Fig. 5.41 shows the local density of states and energy resolved local photocurrent at $V_{\text{bias}} = -0.01$ V, illustrating the carrier escape channels at different photon energies: at $E_{\text{phot}} = 0.568$ eV, only the lowest subbands are occupied (see also Figs. 5.32 and 5.35). In the case of such a short structure and at low forward bias, escape from this level is

³We take the hole current due to its faster convergence to the nonequilibrium steady state value.

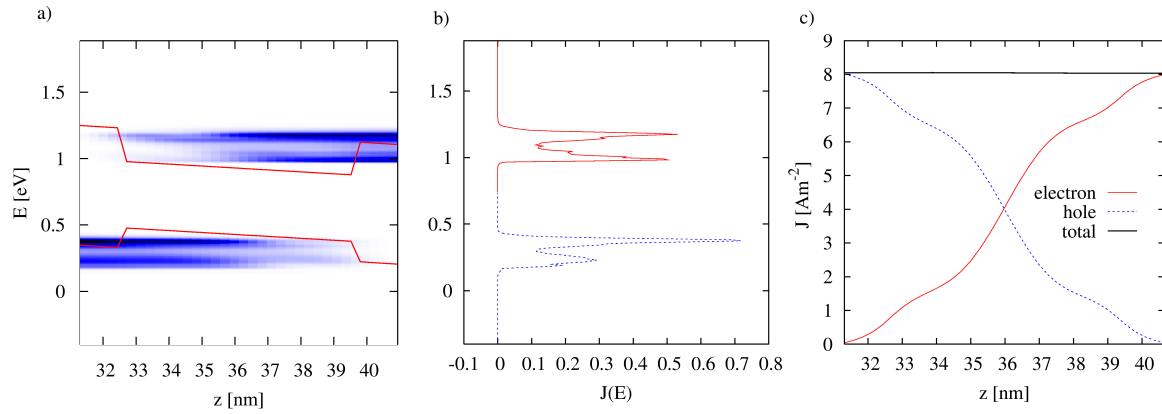


Figure 5.39: *a) Spatially resolved photocurrent spectrum (at zero bias voltage) in the QW region and b) at the interface to the n-contact (electrons) and to the p-contact (holes): the spectrum reflects the joint density of states for the contributing transitions between the confinement levels, modified by the probability for escape, which is suppressed in the case of the deep electronic level. c) Like in the bulk case, electron and hole components of the photocurrent grow towards the respective contacts, while the total current is conserved; in the QW-case, photocurrent does not increase linearly, but depending on the local excess carrier density.*

possible via field enhanced tunneling. At $E_{phot} = 0.648 \text{ eV}$, the occupation is increased, but transport is still restricted to the lowest levels. This means that thermionic emission is not an efficient escape channel for such deep levels, and the emission via phonon absorption is limited by the large separation of the subbands. At $E_{phot} = 0.728 \text{ eV}$, the occupation of the higher subbands has set in. From there, escape is efficient since the states are no longer strictly confined to the well, and thermionic emission is possible. The high level current increases further at $E_{phot} = 0.808 \text{ eV}$, and at $E_{phot} = 0.888 \text{ eV}$, additional quasi-bound states have started to contribute. The lower levels still contribute, but only a part of the subband carries current. An important result of this investigation is the observation that in the present case, where tunneling from low levels is possible, this channel completely dominates the carrier escape, i.e. the contribution of thermionic emission is negligible in comparison.

Fig. 5.42 shows the current-voltage characteristics for the 25 ML SQW structure, together with the current spectrum near short circuit conditions, the maximum power point and the open circuit voltage. The modification of the photocurrent spectrum due to the Stark effect is more pronounced than in the bulk. Like in the bulk case, the spectrum of the

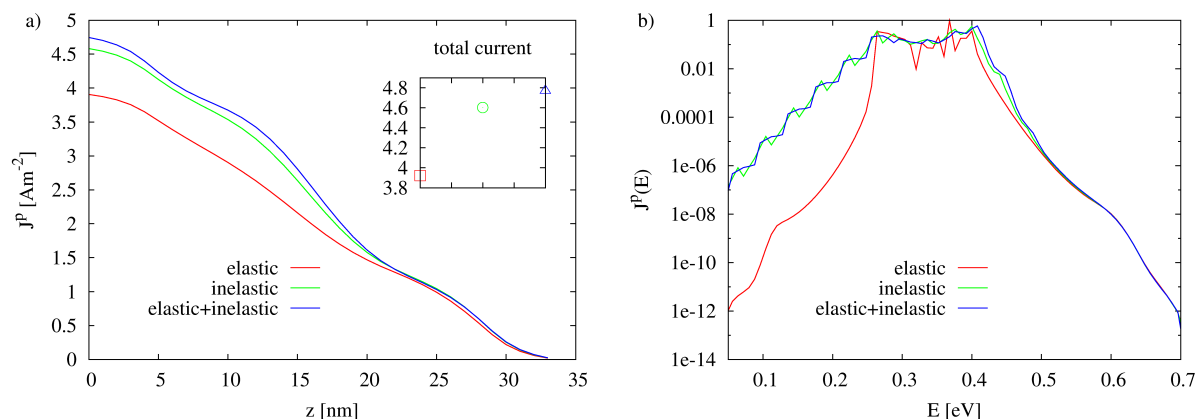


Figure 5.40: a) Hole current near short circuit conditions ($V_{bias} = -0.010$ V) for $E_{phot} = 0.728$ eV and elastic, inelastic and both types of scattering. The characteristic action of the scattering is the same as in bulk: while inelastic scattering leads to the formation of phonon satellites and strongly increases photocurrent, the elastic scattering has mainly a smoothing and broadening effect.

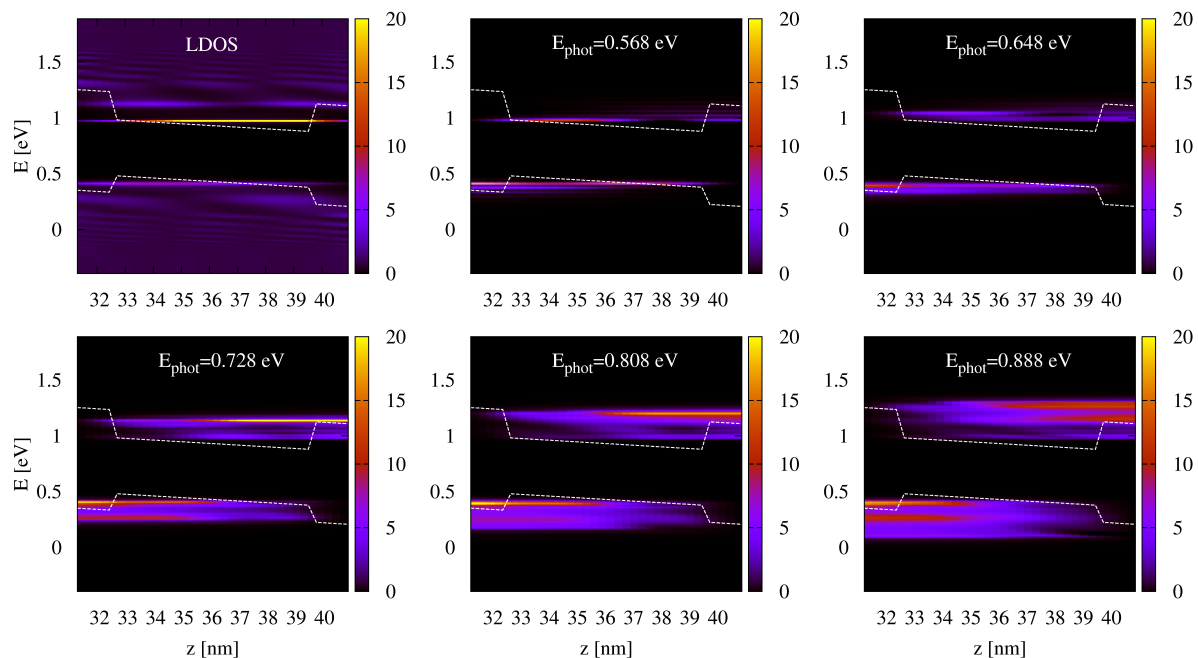


Figure 5.41: Local density of states and energy resolved local photocurrent at $V_{bias} = -0.01$ V, illustrating the carrier escape channels at different photon energies.

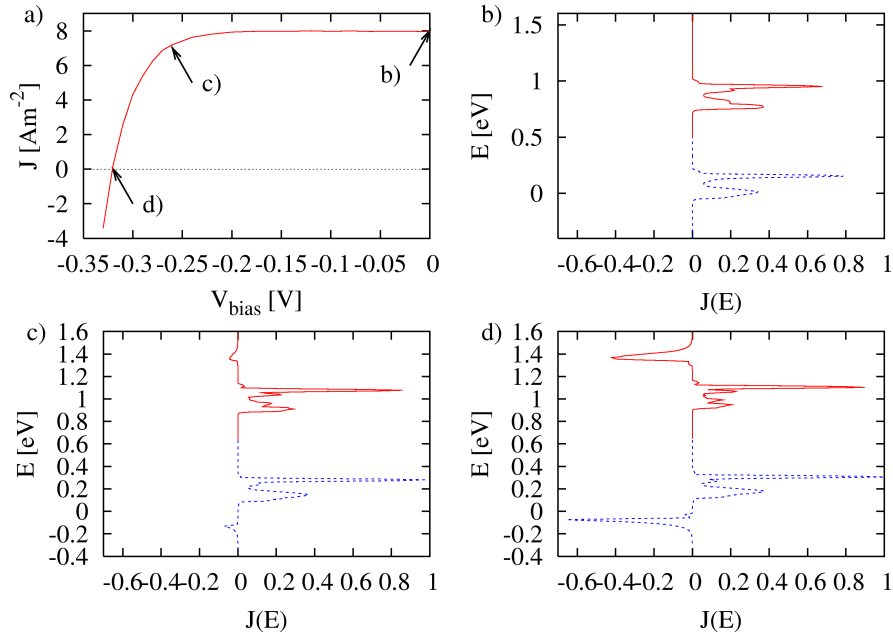


Figure 5.42: a) *IV-characteristics for a 25 ML SQW structure and the current spectrum at the lead-device interface for b) 0 V (short circuit conditions), c) -0.26 V (near the maximum power point), d) -0.32 V (near the open circuit voltage).*

exponentially increasing diode current reflects the density of states and the distribution of the carriers in the bulk contacts, modified by the effects of relaxation due to inelastic scattering in the active region, which leads to the formation of phonon satellites (weakly recognizable near the band edge).

5.3.4 Summary and conclusions

The insertion of quantum wells in the intrinsic region modifies drastically the density of states in the active area, and the effects of confinement in the form of quasi-bound states are found up to the high energies of the quasi-continuum. In absence of nonradiative recombination, the behaviour in the dark is hardly affected: only at high forward bias, charge build-up in the quantum well leads to a modification of the potential in terms of band bending effects similar to those produced via modulation doping, and the different effective mass of the well material modifies the strength of the interaction with phonons. The largest impact is on the optical transitions and on the photocurrent spectrum, since these quantities are directly related to the joint density of states in the interacting region. Depending on the excitation energy, the photogenerated carrier density is strongly local-

ized in the well, especially in the case of the electrons, since relaxation due to scattering concentrates the excess carriers on the lowest available states. The chosen asymmetry in confinement and effective mass for electrons and holes leads to completely different behaviour concerning carrier escape, which can be inferred from the convergence of the terminal current to its non-equilibrium steady state value. While the escape of the holes is fast at all excitation energies due to the low activation barrier, it is very slow for electrons at low photon energies, since only the lowest subbands are occupied, from where escape via tunneling is suppressed and emission over the barrier requires the absorption of many phonons. As a consequence, excess charge is accumulated in the quantum well. This effect is most pronounced under large forward bias, where the field is strongly reduced and hence the confinement increased.

From the analysis in this section follows that the escape of carriers generated in the lowest subbands of deep and narrow isolated quantum wells is not efficient, especially at bias voltages near the operating point. In the next section, it is shown how the transport of photogenerated carriers out of deep wells can be improved via the coupling of quantum wells with different thickness, i.e. via the choice of a specific device geometry.

5.4 Geometry effects in coupled quantum well systems

5.4.1 Introduction

The ability to describe carrier excitation and transport in quantum well structures with atomistic resolution opens the door to microscopic investigations of the effects of geometrical configuration on the photovoltaic properties of quantum wells that are strongly coupled, i.e. separated by barriers of a few monolayers only, such that the carriers are no longer localized in a single quantum well. The final goal of such an investigation would be to find structures that show both the signatures of quantum well absorption and of enhanced transport via the combination of tunneling and thermal emission. Since at the present stage, we are not able to consider at a realistic level the competition between recombination and escape, we will limit the discussion to the distinction of the effects that different geometries have on the absorption from those they have on transport properties.

We consider two geometry parameters that are likely to affect the photovoltaic behaviour, namely the coupling and the asymmetry of the quantum wells, and compare the power density characteristics $P(V) = J(V) \cdot V$, where $J(V)$ is the terminal current density as a function of the terminal voltage $V = V_{bias}$ corresponding to the separation of the chemical potentials at the contacts, which is usually due to the load resistance, but can also be established by application of an external bias. Since the devices considered in this investigation are short, photocurrent is limited by the absorption, and it is therefore essential to normalize physical quantities to the absorptivity in order to allow a comparison of different structures. In this way it is possible to separate transport from optical properties.

5.4.2 Device

The following results were obtained for *p-i-n* junctions with 50 ML highly doped (10^{18} cm^{-3}) contacts and 50 ML intrinsic spacer regions in addition to the intrinsic quantum well structures (Fig. 5.43). 0.9 eV and 0.5 eV were chosen for the high and low band gaps, respectively, with a conduction band offset of 0.25 eV (deep wells) and correspondingly 0.15 eV offset in the valence band. The two-band tight-binding model that was used provides a band structure with equal effective mass for electrons and holes, which was fixed at the value of the GaAs electron mass ($m^*=0.063 m_0$). All the simulations were performed at room temperature (300 K).

The investigated coupled and uncoupled geometries comprise well thicknesses from 5 to

25 ML, which in isolated condition sustain one to two subbands, respectively, where the transition from one to two subbands is from 15 to 20 ML.

The resulting power curves are displayed for five different excitation energies ranging from 0.656 eV, which corresponds to the absorption edge given by the lowest confinement levels, up to 0.912 eV, which is close to the energy of continuum transitions.

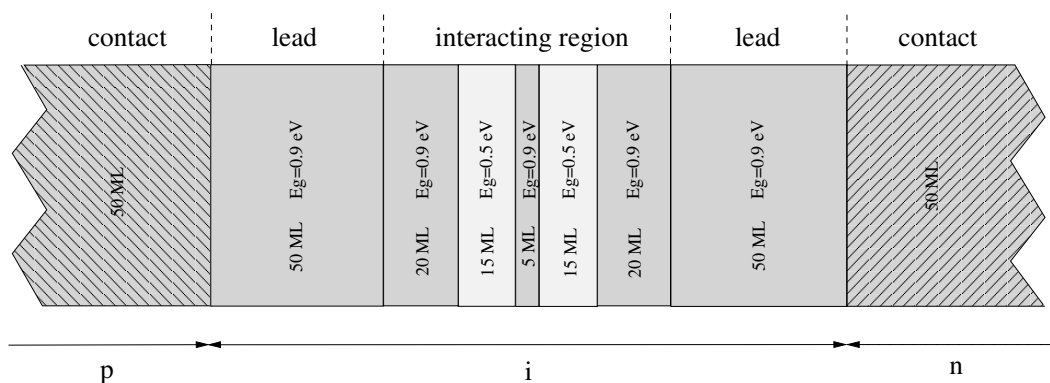


Figure 5.43: *Typical device configuration used in the simulations.*

5.4.3 Coupling

The coupling between the wells directly affects the transport properties through the degree of localization of the carrier wave function, which is also reflected in the absorption spectrum of the DQW. Generally, the beginning of miniband formation associated with strong interwell coupling leads to a broadening of the bound state transition resonance features in the photocurrent response due to the additional transitions that become available. The more important it is thus to separate transport from absorption. The increasing extension of the confined states with shrinking barrier shows up in the local density of states, which is displayed in Fig. 5.44 for the four considered configurations.

Fig. 5.45 (left panel) shows the output power vs. bias voltage for DQW structures of 15 ML wells with barriers of 5 ML (strong coupling), 10 ML, 15 ML and 20 ML (isolated wells). The results seem to indicate that the answer to the question about geometry related efficiency enhancement strongly depends on the photon energy, respectively on the absorptivity of a specific structure at the given excitation energies. Indeed, the picture becomes much more transparent if we consider the power curves normalized by the absorptivity (right panel): the resulting reduction to transport properties underlines the importance

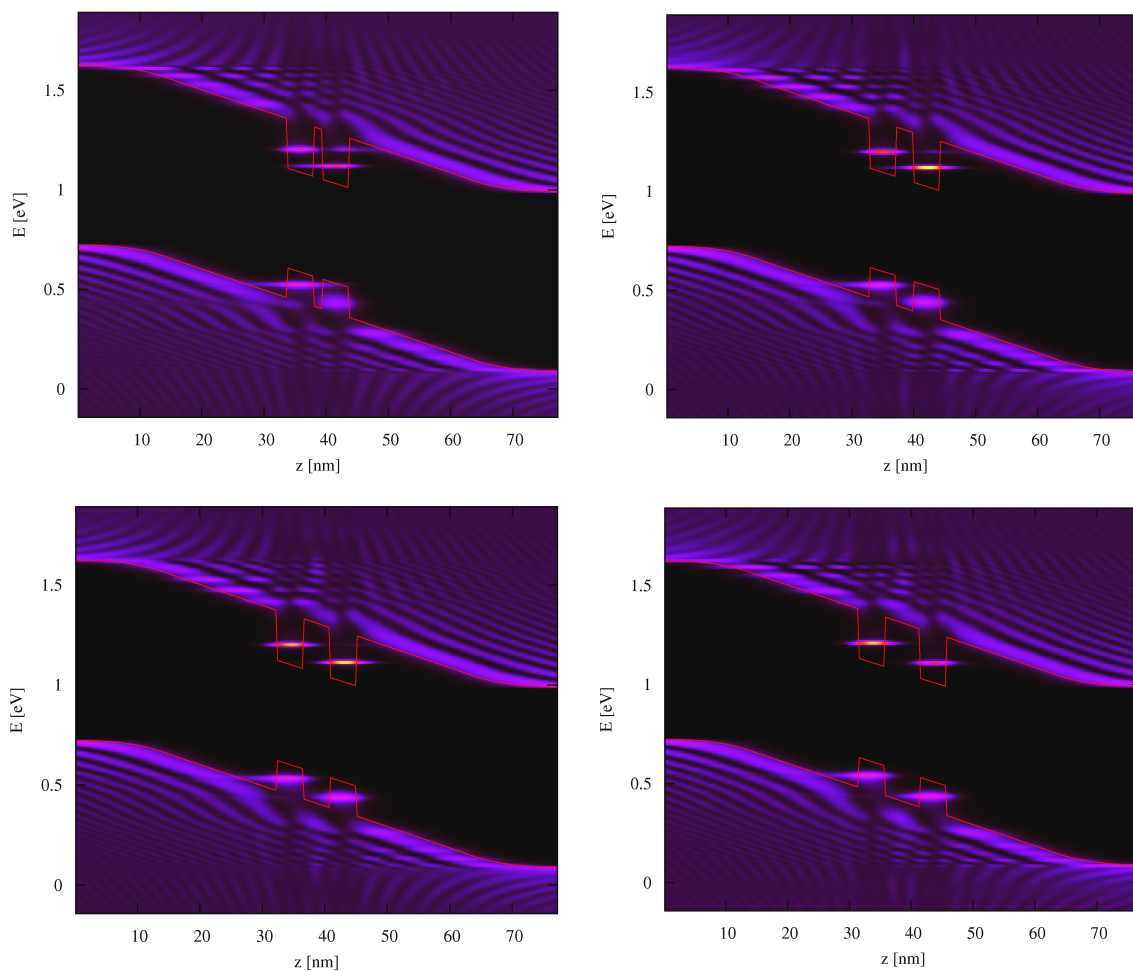


Figure 5.44: Local density of states at zero transverse momentum ($k_{\parallel} = 0$) and at low bias for a double 15 ML quantum well with barrier thickness of 5 (strongly coupled), 10, 15 and 20 ML (isolated single quantum wells). While the states are extended over both wells in the coupled case, they are strongly localized in the isolated configuration.

of geometry for low levels and its negligible effect at energies near the edge of the well, where thermal emission dominates carrier escape. As seen in the top graph on the right side of Fig. 5.45, corresponding to the lowest photon energy, carrier escape is considerably enhanced via the coupling of the wells. This can be explained by the existence of the additional subband in the right well, which via the introduction of intermediate states facilitates the emission via phonon absorption.

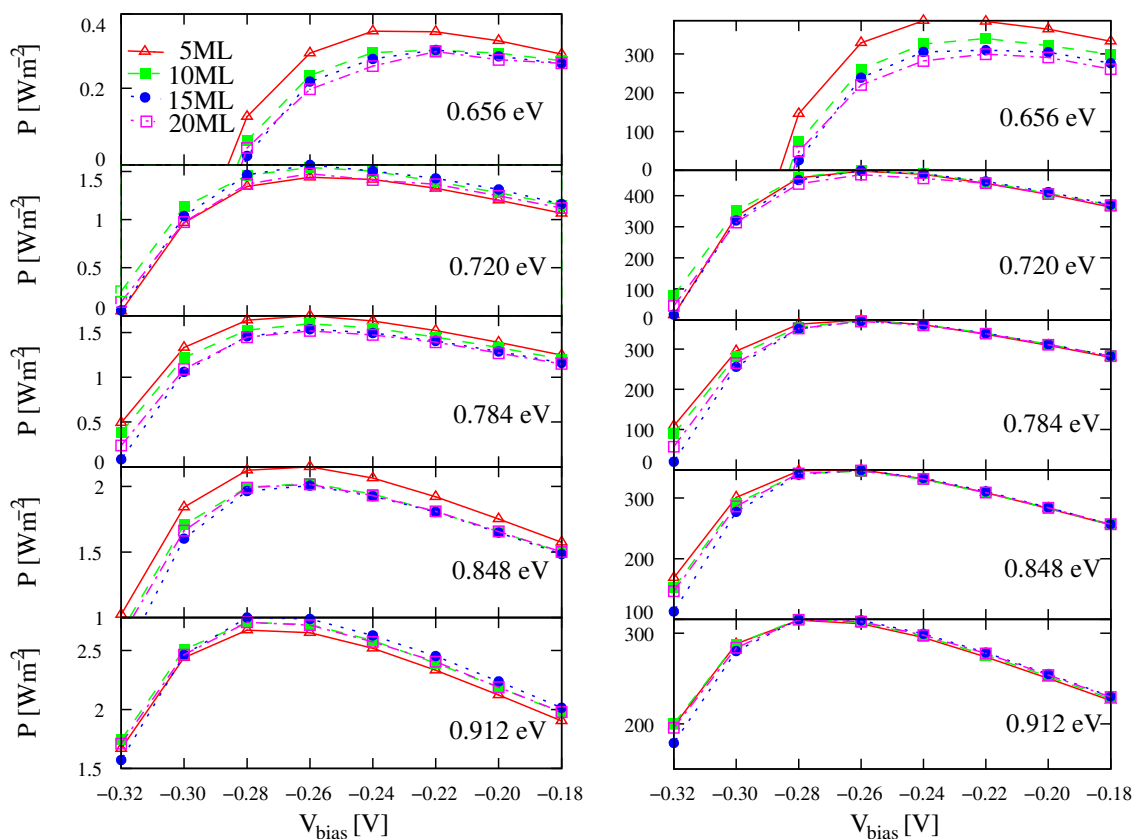


Figure 5.45: Power vs. bias voltage for DQW systems with different degree of coupling, corresponding to a barrier thickness of 5, 10, 15 and 20 ML, respectively. While the dependence on the geometry varies with photon energy in the original curve (left panel), it is pronounced at low energies and vanishes for large energies under renormalization to the absorptivity (right panel), indicating a significant impact of coupling on transport only for very low levels, from where escape is only possible via tunneling.

5.4.4 Asymmetry

The five configurations that were compared include two wide-narrow, a symmetric and two narrow-wide DQW structures, with well widths of 25 ML or 20 ML for the wide well, 15 ML in the symmetric case and 10 ML or 5 ML for the narrow well, respectively. The barrier thickness is 5 ML, which guarantees the coupling of the wells. The corresponding densities of states are displayed in Fig. 5.46. Fig. 5.47 shows again the calculated power density as a function of applied bias voltage displayed for the five different photon energies, exhibiting a decreasing geometry dependence with growing excitation energy, i.e. in the case where higher states are populated, which is to expect due to efficient thermal escape

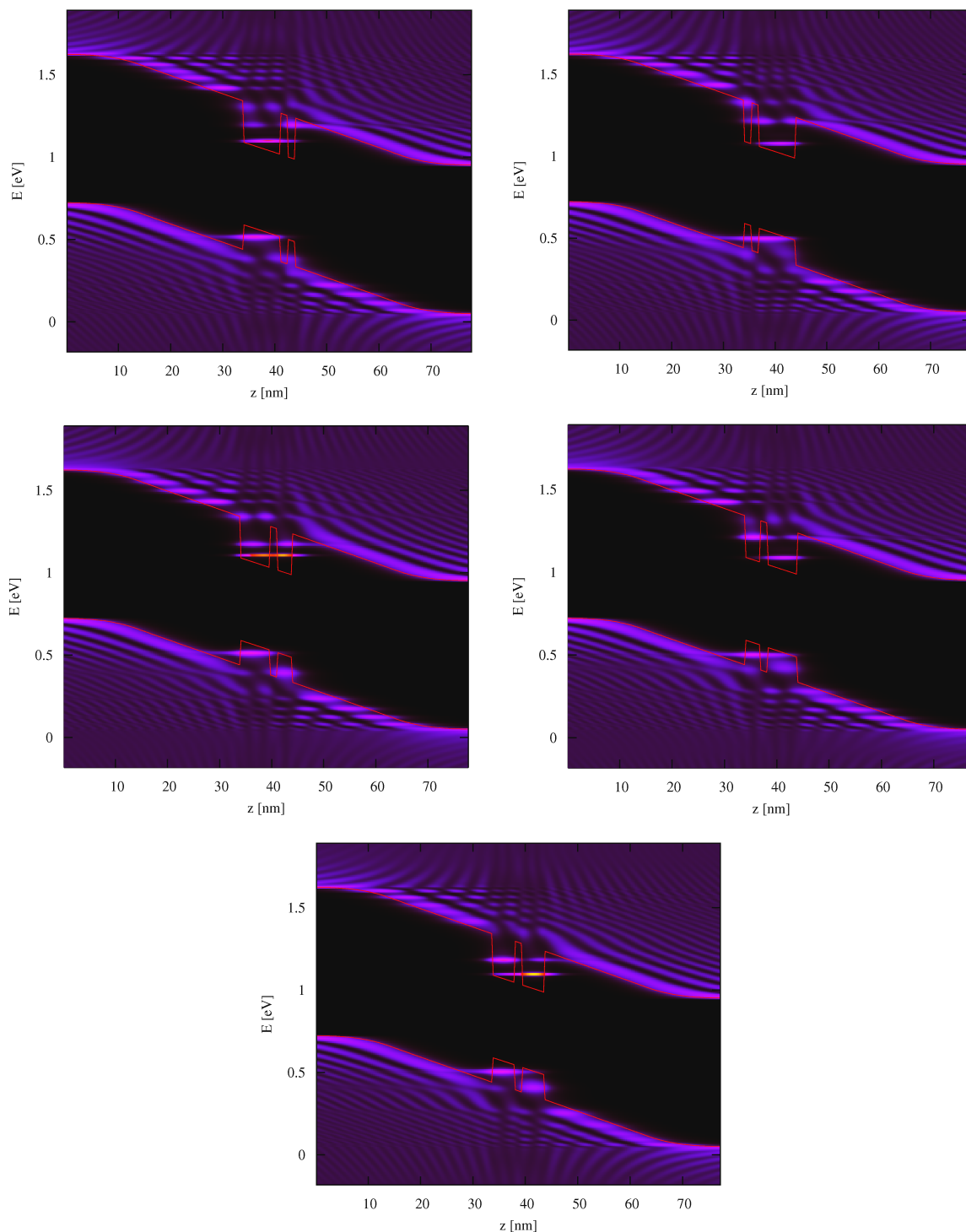


Figure 5.46: Local density of states ($k_{\parallel} = 0$) for the considered configuration corresponding to the different arrangements of the wide and narrow quantum wells. The built-in asymmetry due to doping leads to completely different situations concerning the escape probabilities, especially for deep levels.

from these levels. In the unnormalized graph (left figure), there is once more no general trend recognizable for the change in efficiency from one specific geometry to another, but contrary to the case of variation in coupling, the geometry dependence is not removed by normalization to the absorptivity even at moderate excitation energies, which localizes the origin of this dependence in the differing transport properties. Furthermore, the polarity of the asymmetry affects the V_{oc} , especially for low photon energies, as can be inferred from the normalized graph (right figure). The observed impact of geometry on the transport properties can again be explained by the considerable differences in the subband structure, even though the analysis is complicated by the fact that, unlike the coupling, the asymmetry has contrary effects for electrons and holes, respectively. In general, since the hole escape is faster, it dominates the transport properties, and thus the latter will profit

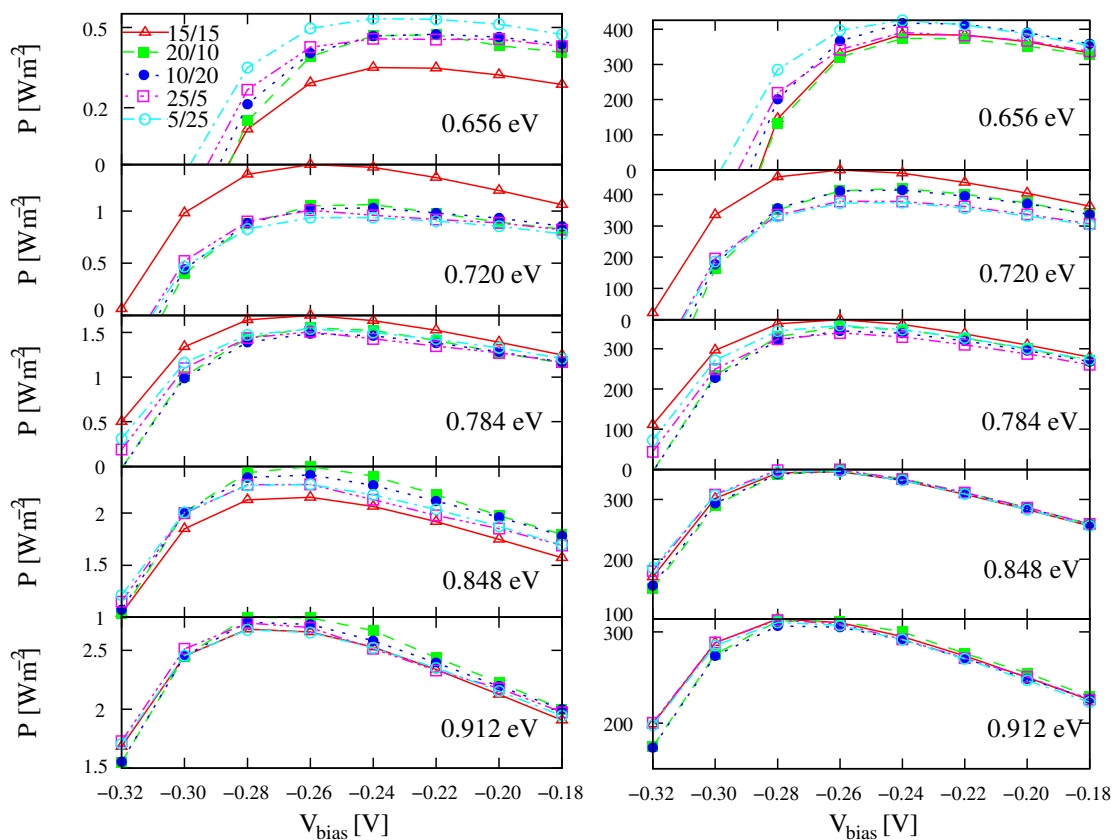


Figure 5.47: Power vs. bias voltage for double quantum well systems with different asymmetry concerning the well width. The geometry dependence does not disappear with normalization to the absorptivity, which is shown in the right figure, indicating that the effect is due to transport rather than to absorption properties of a given structure.

most from an enhancement in the hole escape channels. This fact already explains the observed polarity effect: since the narrow wells in the asymmetry configurations facilitate the emptying of lower subbands from the adjacent wide well only if they are placed on the contact side, i.e. on the right for electrons and on the left for holes, the wide-narrow combinations show the best performance at the lowest excitation energies. At intermediate photon energies, the symmetric DQW is by far the most efficient, which can be explained via the absence of truly deep levels.

5.4.5 Summary and conclusions

Numerical simulations based on a TB-NEGF theory of QWSC confirm the dominant role of thermal escape at room temperature for the case of shallow wells or large excitation energies corresponding to the occupation of high subbands. Apart from the determination of the activation energies, QW geometry becomes important in the tunneling regime, i.e. for low-lying levels where thermal escape is prevented by the large barrier height; in this case, coupling of wells can provide efficient escape channels via tunneling to a spatial location from where escape via thermionic emission or phonon absorption is easier.

Future consideration of the impact of QW geometry on the magnitude and spatial variation of non-radiative recombination may give further directions towards optimal QWSC design.

Chapter 6

Summary and Outlook

In this thesis, a first step was made towards a comprehensive microscopic theory describing the photovoltaic properties of nanostructures dominated by quantum effects, which finally is on a level attained a long time ago in the field of semiconductor lasers. Unlike other theories for quantum well solar cells, it treats absorption, transport and relaxation on equal footing and within a sound theoretical framework based on non-equilibrium quantum statistical mechanics. It is a “first-principles” approach in that the only parameters that enter apart from the external conditions are those characterizing the electronic, vibronic and optical properties of the *bulk*. Owing to the generality of the underlying theory and the use of an atomistic model for the electronic structure, the effects of confinement on optical and transport properties can be resolved for quasi one-dimensional multilayers with arbitrary heterostructure potentials.

While transport of carriers is not considered in the theory of bipolar QW-lasers and most quantum transport investigations are limited to monopolar devices, the model developed in this thesis describes transport of both electrons and holes in strongly doped *p-i-n* junctions, coupled via the interaction with the radiation field.

The investigation of nanoscale *p-i-n* junctions reveals the effects of ultra-small dimensions, like high degree of ballisticity in the transport of electrons and light holes and a pronounced Franz-Keldysh effect in the absorption spectra due to the strong field at low bias. Both optical and electronic properties are strongly affected by the presence of inelastic scattering. A key observation is that the photocurrent enhancement due to an increase in absorption by the scattering is considerably larger than the thermalization loss in the transport process, resulting in an increased total current and correspondingly a higher V_{oc} . From the analysis of the transverse momentum dependence of dark and photocurrent can further be concluded that even for direct gap semiconductors, the conventional restriction to the center of the transverse Brillouin zone ($\mathbf{k} = 0$) is a questionable simplification,

especially if scattering needs to be considered.

In the simulation of a generic single quantum well embedded in such a $p-i-n$ junction, the discussion is extended to include the effects of quantum confinement. The analysis of the local density of states sheds new light on the quantum well absorption, which has characteristics ranging from two- to three-dimensional and includes the effects of higher resonances. The discussion of the spatially resolved photocurrent spectrum represents an “ab-initio” approach to the escape of photogenerated carriers from quantum wells. It is shown how escape channels become active at increasing occupation levels, depending on the photon energy. At low bias corresponding to high fields, tunneling via the decaying tail of a quasi-confined state dominates the escape. The analysis of the energy distribution of photogenerated carriers shows that the thermal tail extending above the barrier is indeed small for deep levels, such that thermal emission from these states is negligible. At higher photon energies, escape happens mainly via emission above the barrier and Fowler-Nordheim tunneling.

One of the advantages of the approach presented in this thesis is the ability to simulate structures of arbitrary planar geometry, including coupled well structures with physical properties that are determined by potentials varying on the scale of a few monolayers. Applied to double quantum well structures, the theory predicts the appearance of new escape channels for deep levels via the coupling to narrow wells on the contact side. The effect is especially pronounced at low excitation energy where only the lowest subbands are occupied.

Even though a variety of effects and interactions have been included in detail, some basic ingredients required to complete the picture are still missing. Furthermore, in the present form the description is not suited for practical modelling purposes, due to the heavy requirement of computational resources and the corresponding necessary approximations and limitations to mesoscopic dimensions.

On the fundamental side, the most restricting approximations are the absence of excitonic contributions to absorption and transport and the neglect of nonradiative recombination processes. While the former strongly modifies the spectral response and thus the short circuit current, the latter has a crucial impact on the bias dependence of the dark current and hence on the open circuit voltage. Both effects are expected to be modified by the phase space restriction in quantum wells due to the lower dimensionality.

The effects of exciton formation and dissociation on single particle transport properties can be studied by the inclusion of higher order terms in the perturbative derivation of the Coulomb-interaction carrier self-energy. Excitonic absorption spectra require a more advanced treatment of the photons including vertex corrections in a Bethe-Salpeter equation

for the photon self-energy.

The route to a microscopic model of nonradiative recombination strongly depends on the specific process. The Auger recombination as an intrinsic effect can be obtained within the presented formalism from higher order diagrams of the perturbation theory for Coulomb interaction, including the phonons for the phonon assisted transition. However, apart from the exceedingly high computational cost of the resulting self-energy terms, realistic, i.e. quantitative predictions are only possible with the use of a realistic band structure that provides a suitable description of highly excited states and high energy intraband transitions. This last requirement comes at its own cost, adding up to the already heavy computation. In the case of recombination via defect states in the band gap, i.e. *Shockley-Read-Hall*-type recombination, an additional model including the microscopic description of the defect atoms is needed.

A further approximation is made in the use of the equilibrium Green's function for a homogeneous isotropic medium when treating photons and phonons. In the case of the photons, consideration of reabsorption and reemission processes requires the renormalization of the propagator via the solution of Dyson's equation with the photon self-energy as derived in Chap. 4, under additional consideration of the waveguide or cavity modes existing in the structure and the spatial variation of the refractive index. While nonlinear optical properties are not expected to arise under low level excitation, the spatial homogeneity will give way to the particular occupation spectrum corresponding to the local absorption, emission and transmission properties. Similarly, the phonon propagator can be evaluated for confined modes and renormalized via the solution of a Dyson's equation with the corresponding phonon self-energy, providing the appropriate non-equilibrium propagator. This non-equilibrium treatment of confined phonons might turn out to be crucial when investigating the question of the quasi-Fermi level separation in QWSC or the properties of solar cells based on the transport of hot carriers. The study of hot carrier transport, i.e. the absence or slowing down of thermalization in nanoscale systems is thus a further field of application of the formalism.

One of the quantitative side, the interacting region needs to be extended to the whole device of realistic extensions, i.e. in the μm -range. On the same time, a suitable multiband formalism providing quantitatively correct confinement energies and optical transition matrix elements imposing the proper selection rules for absorption and emission is indispensable. For structures with weakly coupled, wide quantum wells, the use of a $k \cdot p$ -model on an inhomogeneous spatial grid might be appropriate. If a realistic spectrum is to be used, the energy range has to be extended far beyond the range of validity of a single band or effective mass approximation.

Finally, while the theory presented in this thesis was developed on the example of quantum well structures, it is not limited to those systems, but represents a natural candidate for the investigation photovoltaic effects in other low dimensional nanostructures such as quantum wires and quantum dots. To mention two examples, the NEGF approach could be used in a coupled mode space form to calculate photocurrent in radial quantum well antennas, and it provides a suitable basis for the inclusion microscopic processes such as multiple exciton generation or intrasubband transitions in a model of transport in the quantum dot superlattice of an intermediate band solar cell.

Appendix A

Analytic continuation: Langreth's theorem and the Keldysh formalism

A.1 Introduction

To obtain real time expressions from the contour integrations appearing in the evaluation of Dyson's equations and self-energies, different strategies of analytic continuation have been applied. The most common ones are those due to Langreth [169] and the original formalism developed by Keldysh [168]. The two approaches shall be reviewed below, with focus on the former, since it is used extensively in this thesis.

A.2 Langreth's theorem

The first type of terms to evaluate have the form

$$C(t_1, t_2) = \int_{\mathcal{C}} d\tau A(t_1, \tau) B(\tau, t_2), \quad (\text{A.1})$$

where A and B are defined on the Keldysh contour \mathcal{C} (Fig. 3.1) with the steady state limit $t_0 \rightarrow -\infty$. The derivation of the real-time components of C shall be shown on the example of the lesser components $C^<$. In that case, t_1 lies on the chronological branch of \mathcal{C} and t_2 on the antichronological branch. Contour \mathcal{C} is now deformed into the partial contours \mathcal{C}_1 and \mathcal{C}_2 containing t_1 and t_2 as shown in Fig. A.1, such that the two times define the chronological and antichronological parts of the separate contours. Since for the arguments follows $\tau < t_1$ in B on \mathcal{C}_1 and $\tau > t_1$ in A on \mathcal{C}_2 , the lesser component $C^<$

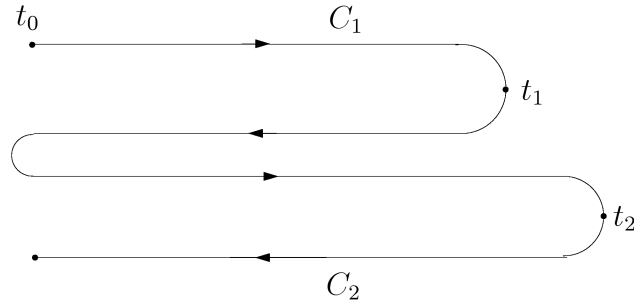


Figure A.1: Deformed Keldysh contour used in the Langreth formalism for the derivation of real time components.

can be written

$$C^<(t_1, t_2) = \int_{C_1} d\tau A(t_1, \tau) B^<(\tau, t_2) + \int_{C_2} d\tau A^<(t_1, \tau) B(\tau, t_2). \quad (\text{A.2})$$

The first term can be split into two parts,

$$\int_{C_1} d\tau A(t_1, \tau) B^<(\tau, t_2) = \int_{-\infty}^{t_1} dt A^>(t_1, \tau) B^<(t, t_2) + \int_{t_1}^{-\infty} dt A^<(t_1, \tau) B^<(t, t_2) \quad (\text{A.3})$$

$$\equiv \int_{-\infty}^{\infty} dt A^R(t_1, t) B^<(\tau, t). \quad (\text{A.4})$$

Combining this result with the expression found from a similar procedure for the second term yields the final expression for the real time component,

$$C^<(t_1, t_2) = \int_{-\infty}^{\infty} dt [A^R(t_1, t) B^<(t, t_2) + A^<(t_1, t) B^A(t, t_2)]. \quad (\text{A.5})$$

The greater component follows simply by replacing “<” with “>” in the above expression. The retarded and advanced components of the Green’s function product C are obtained by repeated use of the definition and the results for the correlation functions,

$$C^R(t_1, t_2) \equiv \theta(t_1 - t_2) [C^>(t_1, t_2) - C^<(t_1, t_2)] \quad (\text{A.6})$$

$$= \theta(t_1 - t_2) \int_{-\infty}^{\infty} dt \left\{ A^R(t_1, t) [B^>(t, t_2) - B^<(t, t_2)] \right. \quad (\text{A.7})$$

$$\left. + [A^>(t_1, t) - A^<(t_1, t)] B^A(t, t_2) \right\} \quad (\text{A.8})$$

$$= \theta(t_1 - t_2) \left\{ \int_{-\infty}^{t_1} dt [A^>(t_1, t) - A^<(t_1, t)] [B^>(t, t_2) - B^<(t, t_2)] \right. \quad (\text{A.9})$$

$$\left. + \int_{-\infty}^{t_2} dt [A^>(t_1, t) - A^<(t_1, t)] [B^<(t, t_2) - B^>(t, t_2)] \right\} \quad (\text{A.10})$$

$$= \int_{t_2}^{t_1} dt A^R(t_1, t) B^R(t, t_2), \quad (\text{A.11})$$

and the corresponding advanced expression replacing “ R ” with “ A ”.

Expressions (A.5) and (A.11) are readily generalized to products of more Green's functions. Using a compact notation, in which (A.5) and (A.11) are written as

$$C^< = A^R B^< + A^< B^A, \quad (\text{A.12})$$

$$C^R = A^R B^R. \quad (\text{A.13})$$

In this notation, a contour-ordered average of the form $D = ABC$ has the real-time components

$$D^< = A^R B^R C^< + A^R B^< C^A + A^< B^A C^A, \quad (\text{A.14})$$

$$D^R = A^R B^R C^R. \quad (\text{A.15})$$

The proof consists of the repeated application of the the rules for a single product.

In the evaluation of self energies, e.g. via diagrammatic perturbation expansion, often terms of the form

$$C(\tau, \tau') = A(\tau, \tau') B(\tau, \tau'), \quad (\text{A.16})$$

$$D(\tau, \tau') = A(\tau, \tau') B(\tau', \tau) \quad (\text{A.17})$$

appear. The lesser and greater parts follow directly from their definition,

$$C^{\lessgtr}(t, t') = A^{\lessgtr}(t, t') B^{\lessgtr}(t, t'), \quad (\text{A.18})$$

$$D^{\lessgtr}(t, t') = A^{\lessgtr}(t, t') B^{\gtrless}(t', t). \quad (\text{A.19})$$

The retarded and advanced components are obtained by procedures similar to those leading to Eq. (A.11),

$$C^R(t, t') \equiv \theta(t - t') [C^>(t, t') - C^<(t, t')] \quad (\text{A.20})$$

$$= \theta(t - t') [A^>(t, t') B^>(t, t') - A^<(t, t') B^<(t, t')] \quad (\text{A.21})$$

$$= \theta(t - t') [A^>(t, t') B^>(t, t') - A^<(t, t') B^>(t, t') \\ + A^<(t, t') B^>(t, t') - A^<(t, t') B^<(t, t')] \quad (\text{A.22})$$

$$= A^R(t, t') B^>(t, t') + A^<(t, t') B^R(t, t') \quad (\text{A.23})$$

$$= A^R(t, t') B^>(t, t') - A^R(t, t') B^<(t, t') \\ + A^R(t, t') B^<(t, t') + A^<(t, t') B^R(t, t') \quad (\text{A.24})$$

$$= A^R(t, t') B^R(t, t') + A^R(t, t') B^<(t, t') + A^<(t, t') B^R(t, t'), \quad (\text{A.25})$$

$$C^A(t, t') = A^A(t, t') B^A(t, t') + A^A(t, t') B^>(t, t') + A^>(t, t') B^A(t, t') \quad (\text{A.26})$$

$$= -A^A(t, t') B^A(t, t') + A^A(t, t') B^<(t, t') + A^<(t, t') B^A(t, t'), \quad (\text{A.27})$$

$$D^R(t, t') = A^R(t, t') B^<(t, t') + A^<(t, t') B^R(t, t'), \quad (\text{A.28})$$

$$D^A(t, t') = A^A(t, t') B^>(t, t') + A^>(t, t') B^A(t, t'). \quad (\text{A.29})$$

Table A.1 summarizes the rules provided by the Langreth theorem.

A.3 Keldysh formalism

An alternative, but completely analogous formulation is that of *Keldysh* [168]: Defining a GF matrix

$$\mathbf{G} = \begin{pmatrix} G^C & G^< \\ G^> & G^{\tilde{C}} \end{pmatrix} \quad (\text{A.30})$$

and the corresponding self-energy matrix

$$\mathbf{\Sigma} = \begin{pmatrix} \Sigma^C & \Sigma^< \\ \Sigma^> & \Sigma^{\tilde{C}} \end{pmatrix}, \quad (\text{A.31})$$

the Dyson's equations can be written as

$$\mathbf{G}(1, 1') = \mathbf{G}_0(1, 1') + \int d2d3 \mathbf{G}_0(1, 2) \mathbf{\Sigma}(2, 3) \mathbf{G}(3, 1'). \quad (\text{A.32})$$

The components of this equation correspond to those obtained from the application of the Langreth rules.

contour	real time
$C = \int_C AB$	$C^< = \int (A^R B^< + A^< B^A)$
	$C^R = \int A^R B^R$
$D = \int_C ABC$	$D^< = \int (A^R B^R C^< + A^R B^< C^A + A^< B^A C^A)$
	$D^R = A^R B^R C^R$
$C(\tau, \tau') = A(\tau, \tau') B(\tau, \tau')$	$C^<(t, t') = A^<(t, t') B^<(t, t')$
	$C^R(t, t') = A^R(t, t') B^>(t, t') + A^<(t, t') B^R(t, t')$
	$= A^R(t, t') B^R(t, t') + A^R(t, t') B^<(t, t') + A^<(t, t') B^R(t, t')$
$D(\tau, \tau') = A(\tau, \tau') B(\tau', \tau)$	$D^<(t, t') = A^<(t, t') B^>(t, t')$
	$D^R(t, t') = A^<(t, t') B^A(t, t') + A^R(t, t') B^<(t, t')$

Table A.1: Rules for the analytic continuation as provided by the Langreth theorem.

Appendix B

The recursive Green's function formalism

We start from the equation of motion for G^R and $G^<$,

$$\{(E + i\eta)\mathbb{1} - H_0 - \Sigma^R - \Sigma^{RB}\} G^R = \mathbb{1}, \quad (\text{B.1})$$

$$\{(E + i\eta)\mathbb{1} - H_0 - \Sigma^R - \Sigma^{RB}\} G^< = (\Sigma^< + \Sigma^{<B})G^A. \quad (\text{B.2})$$

We denote with g^{Rr} the retarded Green's function that couples only to the right, i.e. the Green's function takes into account everything on the right exactly while the coupling elements to the left are set to zero. The equation of motion for the right connected Green's function g^{Rr} reads

$$\begin{pmatrix} T_{nn} & T_{n,n+1:N} \\ T_{n+1:N,n} & T_{n+1:N,n+1:N} \end{pmatrix} \cdot \begin{pmatrix} g_{nn}^{Rr} & g_{n,n+1:N}^{Rr} \\ g_{n+1:N,n}^{Rr} & g_{n+1:N,n+1:N}^{Rr} \end{pmatrix} = \begin{pmatrix} 1 & \mathbf{0}_{n,n+1:N} \\ \mathbf{0}_{n+1:N,n} & \mathbb{1}_{n+1:N,n+1:N} \end{pmatrix} \quad (\text{B.3})$$

with $\mathbf{T} = E\mathbb{1} - H_0 - \Sigma^R$ and $T_{n,n+1:N} = [T_{nn+1} \ 0 \ \dots \ 0]$, $T_{n+1:N,n} = [T_{n+1n} \ 0 \ \dots \ 0]^\dagger$. This yields the equations

$$T_{nn}g_{nn}^{Rr} + T_{n,n+1:N}g_{n+1:N,n}^{Rr} = 1, \quad (\text{B.4})$$

$$T_{n+1:N,n}g_{nn}^{Rr} + T_{n+1:N,n+1:N}g_{n+1:N,n}^{Rr} = \mathbf{0}_{n+1:N,n}. \quad (\text{B.5})$$

From the first equation follows

$$T_{nn}g_{nn}^{Rr} + T_{n+1n}g_{n+1n}^{Rr} = 1, \quad (\text{B.6})$$

and from the second, with $T_{n+1:N,n+1:N} = (g_{n+1:N,n+1:N}^{Rr})^{-1}$,

$$(g_{n+1:N,n+1:N}^{Rr})^{-1}g_{n+1:N,n}^{Rr} = -T_{n+1:N,n}g_{nn}^{Rr}, \quad (\text{B.7})$$

$$\Rightarrow g_{n+1:N,n}^{Rr} = -g_{n+1:N,n+1:N}^{Rr}T_{n+1:N,n}g_{nn}^{Rr}, \quad (\text{B.8})$$

$$\Rightarrow g_{n+1,n}^{Rr} = -g_{n+1n+1}^{Rr}T_{n+1n}g_{nn}^{Rr}. \quad (\text{B.9})$$

The combination of the two results yields a recursion relation for g^{Rr} ,

$$\boxed{g_{nn}^{Rr} = (T_{nn} - T_{nn+1}g_{n+1n+1}^{Rr}T_{n+1n})^{-1}}. \quad (\text{B.10})$$

The boundary element on the right, $g_{N,N}^{Rr}$, is derived in Appendix D.

The equation of motion for the exact Green's function G^R is

$$\begin{pmatrix} T_{nn} & T_{n,n+1:N} \\ T_{n+1:N,n} & T_{n+1:N,n+1:N} \end{pmatrix} \cdot \begin{pmatrix} G_{nn}^R & G_{n,n+1:N}^R \\ G_{n+1:N,n}^R & G_{n+1:N,n+1:N}^R \end{pmatrix} = \begin{pmatrix} 1 & \mathbf{0}_{n,n+1:N} \\ \mathbf{0}_{n+1:N,n} & \mathbb{1}_{n+1:N,n+1:N} \end{pmatrix}, \quad (\text{B.11})$$

and also

$$\begin{pmatrix} G_{nn}^R & G_{n,n+1:N}^R \\ G_{n+1:N,n}^R & G_{n+1:N,n+1:N}^R \end{pmatrix} \cdot \begin{pmatrix} T_{nn} & T_{n,n+1:N} \\ T_{n+1:N,n} & T_{n+1:N,n+1:N} \end{pmatrix} = \begin{pmatrix} 1 & \mathbf{0}_{n,n+1:N} \\ \mathbf{0}_{n+1:N,n} & \mathbb{1}_{n+1:N,n+1:N} \end{pmatrix}, \quad (\text{B.12})$$

The equations coupling $G_{1:n,1:n}$ and $G_{n+1:N,n+1:N}$ that can be extracted from the above systems are

$$T_{n+1:N,1:n}G_{1:n,n+1:N}^R + T_{n+1:N,n+1:N}G_{n+1:N,n+1:N}^R = \mathbb{1}_{n+1:N,n+1:N}, \quad (\text{B.13})$$

$$G_{1:n,1:n}^R T_{1:n,n+1:N} + G_{1:n,n+1:N}^R T_{n+1:N,n+1:N} = \mathbf{0}_{1:n,n+1:N}. \quad (\text{B.14})$$

From the first of these equations and Eq. (B.3), one obtains

$$G_{n+1:N,n+1:N} = g_{n+1:N,n+1:N}^{Rr} - g_{n+1:N,n+1:N}^{Rr} T_{n+1:N,1:n} G_{1:n,n+1:N}^R, \quad (\text{B.15})$$

and from the second

$$G_{1:n,n+1:N}^R = -G_{1:n,1:n}^R T_{1:n,n+1:N} g_{n+1:N,n+1:N}^{Rr}, \quad (\text{B.16})$$

and from the combination of the two follows

$$G_{n+1:N,n+1:N}^R = g_{n+1:N,n+1:N}^{Rr} + g_{n+1:N,n+1:N}^{Rr} T_{n+1:N,1:n} G_{1:n,1:n}^R T_{1:n,n+1:N} g_{n+1:N,n+1:N}^{Rr}. \quad (\text{B.17})$$

For a tri(block)diagonal matrix \mathbf{T} , the recursion relation for the diagonal elements of G^R follows as

$$\boxed{G_{n+1n+1}^R = g_{n+1n+1}^{Rr} + g_{n+1n+1}^{Rr} T_{n+1n} G_{nn}^R T_{nn+1} g_{n+1n+1}^{Rr}}. \quad (\text{B.18})$$

The boundary element G_{11}^R follows from

$$T_{11}G_{11} + T_{12}G_{21}^R = 1, \quad (\text{B.19})$$

where the coupling to the left lead is absorbed into the corresponding boundary selfenergy Σ_L^{RB} contained in Σ_{11}^R . To determine G_{11}^R , G_{21}^R has to be eliminated. From Eq. (B.11), one has

$$T_{n+1:N,1:n}G_{1:n,1:n} + T_{n+1:N,n+1:N}G_{n+1:N,1:n} = \mathbf{0}_{n+1:N,1:n}, \quad (\text{B.20})$$

which can be written as

$$G_{n+1:N,1:n} = -g_{n+1:N,n+1:N}^{Rr} T_{n+1:N,1:n} G_{1:n,1:n}^R, \quad (\text{B.21})$$

providing the off-diagonal elements of G^R ,

$$\boxed{\begin{aligned} G_{n+1n} &= -g_{n+1n+1}^{Rr} T_{n+1n} G_{nn}^R, \\ G_{nn+1} &= -G_{nn}^R T_{nn+1} g_{n+1n+1}^{Rr}. \end{aligned}} \quad (\text{B.22})$$

The first element is

$$G_{n+11}^R = -g_{n+1n+1}^{Rr} T_{n+1n} G_{n1}^{Rr}, \quad (\text{B.23})$$

which provides G_{21}^R , the boundary element thus follows as

$$\boxed{G_{11}^R = (T_{11} - T_{12} g_{22}^{Rr} T_{21})^{-1}}. \quad (\text{B.24})$$

The lesser Green's function are calculated from Eq. (B.2). Again, a right connected lesser Green's function $g^{<r}$ is introduced. The equations of motion for $g^{<r}$ can be written as

$$\begin{pmatrix} T_{nn} & T_{n,n+1:N} \\ T_{n+1:N,n} & T_{n+1:N,n+1:N} \end{pmatrix} \cdot \begin{pmatrix} g_{nn}^{<r} & g_{n,n+1:N}^{<r} \\ g_{n+1:N,n}^{<r} & g_{n+1:N,n+1:N}^{<r} \end{pmatrix} = \quad (\text{B.25})$$

$$\begin{pmatrix} \Sigma_{nn}^{<} & \Sigma_{n,n+1:N}^{<} \\ \Sigma_{n+1:N,n}^{<} & \Sigma_{n+1:N,n+1:N}^{<} \end{pmatrix} \cdot \begin{pmatrix} g_{nn}^{Ar} & g_{n,n+1:N}^{Ar} \\ g_{n+1:N,n}^{Ar} & g_{n+1:N,n+1:N}^{Ar} \end{pmatrix} \quad (\text{B.26})$$

where $\Sigma_{n,n+1:N}^{<} = [\Sigma_{nn+1}^{<} \ 0 \ \dots \ 0]$, $\Sigma_{n+1:N,n}^{<} = [\Sigma_{n+1n}^{<} \ 0 \ \dots \ 0]^\dagger$. From Eq. (B.26), two coupled equations can be extracted,

$$T_{nn} g_{nn}^{<r} + T_{n,n+1:N} g_{n+1:N,n}^{<r} = \Sigma_{nn}^{<} g_{nn}^{Ar} + \Sigma_{n,n+1:N}^{<} g_{n+1:N,n+1:N}^{Ar}, \quad (\text{B.27})$$

$$T_{n+1:N,n} g_{nn}^{<r} + T_{n+1:N,n+1:N} g_{n+1:N,n}^{<r} = \Sigma_{n+1:N,n}^{<} g_{nn}^{Ar} + \Sigma_{n+1:N,n+1:N}^{<} g_{n+1:N,n}^{Ar}. \quad (\text{B.28})$$

Using again $T_{n+1:N,n+1:N} = (g_{n+1:N,n+1:N}^{Rr})^{-1}$, the second equation becomes

$$g_{n+1:N,n}^{<r} = -g_{n+1:N,n+1:N}^{Rr} T_{n+1:N,n} g_{nn}^{<r} \quad (\text{B.29})$$

$$+ g_{n+1:N,n+1:N}^{Rr} (\Sigma_{n+1:N,n}^{<} g_{nn}^{Ar} + \Sigma_{n+1:N,n+1:N}^{<} g_{n+1:N,n}^{Ar}). \quad (\text{B.30})$$

With Eq.(B.9) for $g_{n+1:N,n}^{Ar}$,

$$g_{n+1:N,n}^{Ar} = -g_{n+1:N,n+1:N}^{Ar} T_{n+1:N,n}^* g_{nn}^{Ar} \quad (\text{B.31})$$

and

$$\Sigma_{n+1:N,n+1:N}^{Ar} g_{n+1:N,n+1:N}^{Ar} = T_{n+1:N,n+1:N} g_{n+1:N,n+1:N}^{<r}, \quad (\text{B.32})$$

the second part of Eq. (B.30) can be simplified as follows:

$$g_{n+1:N,n+1:N}^{Rr} \Sigma_{n+1:N,n+1:N}^{<} g_{n+1:N,n}^{Ar} = -g_{n+1:N,n+1:N}^{Rr} \Sigma_{n+1:N,n+1:N}^{<} g_{n+1:N,n+1:N}^{Ar} T_{n+1:N,n}^* g_{nn}^{Ar} \quad (\text{B.33})$$

$$= -g_{n+1:N,n+1:N}^{Rr} T_{n+1:N,n+1:N} g_{n+1:N,n+1:N}^{<r} T_{n+1:N,n}^* g_{nn}^{Ar} \quad (\text{B.34})$$

$$= -g_{n+1:N,n+1:N}^{<r} T_{n+1:N,n}^* g_{nn}^{Ar}. \quad (\text{B.35})$$

Eq. (B.30) becomes

$$g_{n+1:N,n}^{<r} = -g_{n+1:N,n+1}^{Rr} T_{n+1,n} g_{nn}^{<r} - g_{n+1:N,n+1}^{<r} T_{n+1,n}^* g_{nn}^{Ar} + g_{n+1:N,n+1:N}^{Rr} \Sigma_{n+1:N,n}^{<} g_{nn}^{Ar}, \quad (\text{B.36})$$

which is then inserted into the first equation of (B.28) to obtain a recursion relation for $g^{<r}$:

$$\underbrace{(T_{nn} - T_{nn+1} g_{n+1n+1}^{Rr} T_{n+1n})}_{(g_{nn}^{Rr})^{-1}} g_{nn}^{<r} = T_{nn+1} g_{n+1n+1}^{<r} T_{n+1n}^* g_{nn}^{Ar} - T_{nn+1} g_{n+1n+1}^{Rr} \Sigma_{n+1n}^{<} g_{nn}^{Ar} \quad (\text{B.37})$$

$$+ \Sigma_{nn}^{<} g_{nn}^{Ar} - \Sigma_{nn+1}^{<} g_{n+1n+1}^{Ar} T_{n+1n}^* g_{nn}^{Ar}, \quad (\text{B.38})$$

yielding

$$g_{nn}^{<r} = g_{nn}^{Rr} \left[T_{nn+1} g_{n+1n+1}^{<r} T_{n+1n}^* - T_{nn+1} g_{n+1n+1}^{Rr} \Sigma_{n+1n}^{<} - \Sigma_{nn+1}^{<} g_{n+1n+1}^{Ar} T_{n+1n}^* + \Sigma_{nn}^{<} \right] g_{nn}^{Ar}. \quad (\text{B.39})$$

The equations of motion for the exact GF $G^{<}$ are

$$\begin{pmatrix} T_{1:n,1:n} & T_{1:n,n+1:N} \\ T_{n+1:N,1:n} & T_{n+1:N,n+1:N} \end{pmatrix} \cdot \begin{pmatrix} G_{1:n,1:n}^{<} & G_{1:n,n+1:N}^{<} \\ G_{n+1:N,1:n}^{<} & G_{n+1:N,n+1:N}^{<} \end{pmatrix} = \quad (\text{B.40})$$

$$\begin{pmatrix} \Sigma_{1:n,1:n}^{<} & \Sigma_{1:n,n+1:N}^{<} \\ \Sigma_{n+1:N,1:n}^{<} & \Sigma_{n+1:N,n+1:N}^{<} \end{pmatrix} \cdot \begin{pmatrix} G_{1:n,1:n}^A & G_{1:n,n+1:N}^A \\ G_{n+1:N,1:n}^A & G_{n+1:N,n+1:N}^A \end{pmatrix} \quad (\text{B.41})$$

or

$$\begin{pmatrix} G_{1:n,1:n}^{<} & G_{1:n,n+1:N}^{<} \\ G_{n+1:N,1:n}^{<} & G_{n+1:N,n+1:N}^{<} \end{pmatrix} \cdot \begin{pmatrix} T_{1:n,1:n}^* & T_{1:n,n+1:N}^* \\ T_{n+1:N,1:n}^* & T_{n+1:N,n+1:N}^* \end{pmatrix} = \quad (\text{B.42})$$

$$\begin{pmatrix} G_{nn}^R & G_{n,n+1:N}^R \\ G_{n+1:N,n}^R & G_{n+1:N,n+1:N}^R \end{pmatrix} \cdot \begin{pmatrix} \Sigma_{nn}^{<} & \Sigma_{n,n+1:N}^{<} \\ \Sigma_{n+1:N,n}^{<} & \Sigma_{n+1:N,n+1:N}^{<} \end{pmatrix} \quad (\text{B.43})$$

The two equations that one extracts to find the recursion relation between $G_{n+1n+1}^<$ and $G_{nn}^<$ are

$$T_{n+1:N,1:n}G_{1:n,n+1:N}^< + T_{n+1:N,n+1:N}G_{n+1:N,n+1:N}^< = \Sigma_{n+1:N,n+1:N}^< G_{n+1:N,n+1:N}^A + \Sigma_{n+1:N,1:n}^< G_{1:n,n+1:N}^A, \quad (\text{B.44})$$

$$G_{1:n,1:n}^< T_{1:n,n+1:N}^* + G_{1:n,n+1:N}^< T_{n+1:N,n+1:N}^* = G_{1:n,n+1:N}^R \Sigma_{n+1:N,n+1:N}^< + G_{1:n,1:n}^R \Sigma_{1:n,n+1:N}^<. \quad (\text{B.45})$$

The first equation provides

$$G_{n+1:N,n+1:N}^< = g_{n+1:N,n+1:N}^{Rr} \left[-T_{n+1:N,1:n}G_{1:n,n+1:N}^< + \Sigma_{n+1:N,n+1:N}^< G_{n+1:N,n+1:N}^A + \Sigma_{n+1:N,1:n}^< G_{1:n,n+1:N}^A \right], \quad (\text{B.46})$$

$$+ \Sigma_{n+1:N,n+1:N}^< G_{n+1:N,n+1:N}^A + \Sigma_{n+1:N,1:n}^< G_{1:n,n+1:N}^A], \quad (\text{B.47})$$

and from the second follows

$$G_{1:n,n+1:N}^< = \left[-G_{1:n,1:n}^< T_{1:n,n+1:N}^* + G_{1:n,n+1:N}^R \Sigma_{n+1:N,n+1:N}^< \right. \quad (\text{B.48})$$

$$\left. + G_{1:n,1:n}^R \Sigma_{1:n,n+1:N}^< \right] g_{n+1:N,n+1:N}^{Ar}. \quad (\text{B.49})$$

With the further relations

$$G_{1:n,n+1:N}^A = -G_{1:n,1:n}^A T_{1:n,n+1:N}^* g_{n+1:N,n+1:N}^{Ar} \quad (\text{B.50})$$

and

$$g_{n+1:N,n+1:N}^{<r} = g_{n+1:N,n+1:N}^{Rr} \Sigma_{n+1:N,n+1:N}^< G_{n+1:N,n+1:N}^A, \quad (\text{B.51})$$

the seeked recursion relation follows as

$$\boxed{G_{n+1n+1}^< = g_{n+1n+1}^{<r} + g_{n+1n+1}^{Rr} T_{n+1n} G_{nn}^< T_{nn+1}^* g_{n+1n+1}^{Ar} + g_{n+1n+1}^{Rr} T_{n+1n} G_{nn}^R T_{nn+1} g_{n+1n+1}^{<r} + g_{n+1n+1}^{<r} T_{n+1n}^* G_{nn}^A T_{nn+1}^* g_{n+1n+1}^{Ar} - g_{n+1n+1}^{Rr} T_{n+1n} G_{nn}^R \Sigma_{nn+1}^< g_{n+1n+1}^{Ar} - g_{n+1n+1}^{Rr} \Sigma_{n+1n}^< G_{nn}^A T_{nn+1}^* g_{n+1n+1}^{Ar}.} \quad (\text{B.52})$$

The off-diagonal elements are obtained from the remaining equations of (B.41):

$$G_{n+1:N,1:n}^< = g_{n+1:N,n+1:N}^R \left[-T_{n+1:N,1:n}G_{1:n,1:n}^< + \Sigma_{n+1:N,1:n}^< G_{1:n,1:n}^A + \Sigma_{n+1:N,n+1:N}^< G_{n+1:N,1:n}^A \right], \quad (\text{B.53})$$

$$G_{1:n,n+1:N}^< = \left[-G_{1:n,1:n}^< T_{1:n,n+1:N}^* + G_{1:n,n+1:N}^R \Sigma_{n+1:N,n+1:N}^< + G_{1:n,1:n}^R \Sigma_{1:n,n+1:N}^< \right] g_{n+1:N,n+1:N}^A, \quad (\text{B.54})$$

which yields

$$\boxed{G_{n+1n}^< = -g_{n+1n+1}^{Rr} T_{n+1n} G_{nn}^< - g_{n+1n+1}^{<r} T_{n+1n}^* G_{nn}^A + g_{n+1n+1}^{Rr} \Sigma_{n+1n}^< G_{nn}^A,} \quad (\text{B.55})$$

$$G_{nn+1}^< = -G_{nn}^< T_{nn+1}^* g_{n+1n+1}^{Ar} - G_{nn}^R T_{nn+1} g_{n+1n+1}^{<r} + G_{nn}^R \Sigma_{nn+1}^< g_{n+1n+1}^{Ar}.$$

The starting values at the boundaries are given by

$$\boxed{g_{NN}^{<r} = -f_N (g_{NN}^{Rr} - g_{NN}^{Ar})} \quad (\text{B.56})$$

and

$$\boxed{G_{11}^{<} = g_{11}^{<r}}. \quad (\text{B.57})$$

Appendix C

Multiband formalism

C.1 Introduction

To properly describe interband transitions, a multiband model is required. III-V materials like GaAs or $\text{Al}_x\text{Ga}_{1-x}\text{As}$ have been described by various empirical tight-binding (ETB) models of increasing sophistication, from a simple two-band nearest neighbor model [126] to next-nearest neighbor twenty-band sp^3s^* including the effects of spin-orbit coupling [125].

In this appendix, the basic principles of the tight-binding approach to the investigation of electronic and optical properties of semiconductors are reviewed, focusing on models for layered systems.

C.2 Bulk Hamiltonian and band structure

Due to the periodical nature of crystalline solids, their electronic structure follows from the solution of an eigenvalue problem of the form [252]

$$[\hat{H} - \epsilon_n(\mathbf{k})]|n, \mathbf{k}\rangle = 0, \quad n = 1, 2, \dots, N_b \quad (\text{C.1})$$

which gives the dispersion $\epsilon_n(\mathbf{k})$ of the N_b bands and the corresponding Bloch states $|n, \mathbf{k}\rangle$. In the ETB approach, the actual Hamiltonian \hat{H} is replaced by a pseudo-Hamiltonian which involves only a small number of atomic-like pseudo-orbitals [236], which in the case of symmetrically orthogonalized atomic orbitals are called the Löwdin orbitals [253] and provide the basis

$$|\alpha b, \mathbf{k}\rangle = \frac{1}{\sqrt{N}} \sum_{j=1}^N e^{i\mathbf{k}\cdot\mathbf{R}_j + \mathbf{v}_b} |\alpha b, \mathbf{R}_j\rangle, \quad (\text{C.2})$$

where α labels the atomic-like orbitals, b the basis atoms of a unit cell and \mathbf{v}_b the displacement vector of the basis atoms. N is the number of atoms, which corresponds to the number of wave vectors \mathbf{k} in the first Brillouin zone.

In the basis (C.2), the Bloch equation (C.1) takes the form

$$\sum_{\alpha', b'} \{ \langle \alpha b, \mathbf{k} | \hat{H} | \alpha' b', \mathbf{k} \rangle - \epsilon_n(\mathbf{k}) \delta_{\alpha, \alpha'} \delta_{b, b'} \} \langle \alpha' b', \mathbf{k} | n, \mathbf{k} \rangle = 0. \quad (\text{C.3})$$

The solutions $|n, \mathbf{k}\rangle$ can be expressed in terms of the $|\alpha b, \mathbf{k}\rangle$ -basis via

$$|n, \mathbf{k}\rangle = \sum_{\alpha, b} |\alpha b, \mathbf{k}\rangle \langle \alpha b, \mathbf{k} | n, \mathbf{k} \rangle \equiv \sum_{\alpha, b} C_{\alpha b}^n(\mathbf{k}) |\alpha b, \mathbf{k}\rangle. \quad (\text{C.4})$$

Eq. (C.3) can therefore be written as

$$\sum_{\alpha', b'} [H_{\alpha b; \alpha' b'}(\mathbf{k}) - \epsilon_n(\mathbf{k}) \delta_{\alpha, \alpha'} \delta_{b, b'}] C_{\alpha' b'}^n(\mathbf{k}) = 0. \quad (\text{C.5})$$

The coefficients $C_{\alpha b}^n(\mathbf{k})$ are the entries of the eigenvectors of $H_{\alpha b; \alpha' b'}$ which result from the diagonalization providing the band dispersions $\epsilon_n(\mathbf{k})$.

To obtain the Hamiltonian in terms of tight-binding matrix elements using the localized atomic orbitals, the expansion of the Bloch basis (C.2) is used in Eq. (C.3) to find

$$H_{\alpha b, \alpha' b'}(\mathbf{k}) \equiv \langle \alpha b, \mathbf{k} | \hat{H} | \alpha' b', \mathbf{k} \rangle = \frac{1}{N} \sum_{j, j'} \langle \alpha b, \mathbf{R}_j | \hat{H} | \alpha' b', \mathbf{R}_{j'} \rangle e^{i\mathbf{k} \cdot (\mathbf{R}_{j'} - \mathbf{R}_j)} \quad (\text{C.6})$$

$$= \sum_j \langle \alpha b, \mathbf{R}_0 | \hat{H} | \alpha' b', \mathbf{R}_j \rangle e^{i\mathbf{k} \cdot (\mathbf{R}_j - \mathbf{R}_0)} \quad (\text{C.7})$$

$$\equiv \sum_j [H(\mathbf{R}_j - \mathbf{R}_0)]_{\alpha b, \alpha' b'} e^{i\mathbf{k} \cdot (\mathbf{R}_j - \mathbf{R}_0)}, \quad (\text{C.8})$$

where $[H(\mathbf{R}_j - \mathbf{R}_0)]_{\alpha b, \alpha' b'}$ are the tight-binding matrix elements of the Hamiltonian. In practical applications, the sum over real space indices is restricted to unit cells with non-negligible overlap, e.g. nearest-neighbors.

C.3 Optical matrix elements

As shown by several authors [133, 134, 137], the optical matrix elements can be derived directly from the tight-binding representation of the Hamiltonian \hat{H}_0 making use of the *Feynman-Hellman* theorem,

$$\mathbf{p}_{\alpha b, \alpha' b'}(\mathbf{k}) = \frac{m_0}{\hbar} \nabla_{\mathbf{k}} H_{\alpha b, \alpha' b'}(\mathbf{k}), \quad H_{\alpha b, \alpha' b'}(\mathbf{k}) \equiv \langle \alpha b, \mathbf{k} | \hat{H}_0 | \alpha' b', \mathbf{k} \rangle \quad (\text{C.9})$$

$$= \frac{im_0}{\hbar} \frac{1}{N} \sum_{\mathbf{R}, \mathbf{R}'} e^{i\mathbf{k} \cdot (\mathbf{R}' - \mathbf{R})} (\mathbf{R}' - \mathbf{R}) \langle \alpha b, \mathbf{R} | \hat{H}_0 | \alpha' b', \mathbf{R} \rangle. \quad (\text{C.10})$$

To obtain the elements corresponding to the various interband transitions with respect to the different bands, the momentum matrix elements are transformed into the band basis,

$$\mathbf{p}_{nm}(\mathbf{k}) = \sum_{\alpha b, \alpha' b'} C_{\alpha b}^n(\mathbf{k})^* C_{\alpha' b'}^m(\mathbf{k}) \mathbf{p}_{\alpha b, \alpha' b'}(\mathbf{k}), \quad (\text{C.11})$$

where n, m are the band indices and with the coefficients $C_{\alpha b}^i$ given by Eq. (C.5).

C.4 Tight-binding model for layered semiconductors: planar orbital basis

C.4.1 Basis functions and representation of the Hamiltonian

In layered structures such as (multi) quantum well systems or superlattices, the characteristic behavior is due to the existence of parallel planar defects or interfaces along the growth axis z . The atomic planes parallel to the interfaces are grouped into layers L , and the orbitals α of the atoms in a given atomic plane i form the so called *planar orbitals* [238] in terms of the sum of localized atomic orbitals $|\alpha i, L, \mathbf{R}_{\parallel}\rangle$ centered at $\mathbf{R}^L = (\mathbf{R}_{\parallel} + v_{\parallel, i}^{\alpha}, L\Delta + v_{z, i}^{\alpha})$ and weighted by the phase factor $e^{i\mathbf{k}\cdot(\mathbf{R}_{\parallel} + v_{\parallel, i}^{\alpha})}$,

$$|\alpha i, L, \mathbf{k}_{\parallel}\rangle = \frac{1}{\sqrt{N_{\parallel}}} \sum_{\mathbf{R}_{\parallel}} e^{i\mathbf{k}_{\parallel}\cdot(\mathbf{R}_{\parallel} + v_{\parallel, i}^{\alpha})} |\alpha i, L, \mathbf{R}_{\parallel}^L\rangle, \quad (\text{C.12})$$

where \mathbf{R}^L denotes the lattice position of the atoms, \mathbf{k}_{\parallel} and \mathbf{R}_{\parallel} are the transverse¹ component of momentum and position, respectively, and N_{\parallel} is the number of points in the transverse Brillouin zone. In the planar orbital basis (POB), the matrix elements of the noninteracting Hamiltonian H_0 acquire the general form

$$\langle \alpha i, L, \mathbf{k}_{\parallel} | H_0 | \alpha' i', L', \mathbf{k}_{\parallel} \rangle = D_{\alpha i, \alpha' i'; L}(\mathbf{k}_{\parallel}) \delta_{L, L'} - t_{\alpha i, L; \alpha' i', L'}(\mathbf{k}_{\parallel}) (1 - \delta_{L', L}). \quad (\text{C.13})$$

where the diagonal block \mathbf{D} contains the orbital on-site energies, the electrostatic potential U and the anion-cation coupling matrix elements, while the off-diagonal elements \mathbf{t} represent the interlayer coupling², as given by the matrix elements with respect to the localized basis states $|\alpha i, L, \mathbf{R}_{\parallel}\rangle$. To obtain the Hamiltonian matrix elements in the planar orbital

¹Transverse means normal to the direction of current flow

²It is often convenient to use *block matrix* notation and suppress orbital indices, or even *full matrix* notation, where all indices are suppressed.

basis (C.12), the latter is related to the bulk Hamiltonian in the orbital Bloch basis $|\alpha i, \mathbf{k}\rangle$ via [239]

$$|\alpha i, L, \mathbf{k}_{\parallel}\rangle = \frac{1}{\sqrt{L_{BZ}}} \int dk_z e^{-ik_z(L\Delta + v_{z,i}^{\alpha})} |\alpha i, \mathbf{k}\rangle, \quad (\text{C.14})$$

where L_{BZ} is the size of the 1D longitudinal Brillouin zone. The Hamiltonian elements in (C.13) follow as

$$\langle \alpha i, L, \mathbf{k}_{\parallel} | H_0 | \alpha' i', L', \mathbf{k}_{\parallel} \rangle = \frac{1}{L_{BZ}} \int dk_z e^{ik_z[(L-L')\Delta + v_{z,i}^{\alpha} - v_{z,i'}^{\alpha'}]} [H(\mathbf{k})]_{\alpha i, \alpha' i'} \quad (\text{C.15})$$

with $H(\mathbf{k})$ given in (C.8). This integration modifies the \mathbf{k} -dependent phase factors of the bulk Hamiltonian.

C.4.2 Dipole-matrix elements for optical transitions

The POB representation of the momentum matrix elements is given by

$$\mathbf{p}_{\alpha, L; \alpha', L'}(\mathbf{k}_{\parallel}) \equiv \langle \alpha, L, \mathbf{k}_{\parallel} | \hat{\mathbf{p}} | \alpha', L', \mathbf{k}_{\parallel} \rangle \quad (\text{C.16})$$

$$= \frac{1}{N_{\parallel}} \sum_{\mathbf{R}_{\parallel}, \mathbf{R}'_{\parallel}} e^{i\mathbf{k}_{\parallel} \cdot (\mathbf{R}'_{\parallel, \alpha'} - \mathbf{R}_{\parallel, \alpha})} \langle \alpha, L, \mathbf{R}_{\parallel} | \hat{\mathbf{p}} | \alpha', L', \mathbf{R}'_{\parallel} \rangle, \quad (\text{C.17})$$

$$\langle \alpha, L, \mathbf{R}_{\parallel} | \hat{\mathbf{p}} | \alpha', L', \mathbf{R}'_{\parallel} \rangle = \frac{m_0}{i\hbar} \langle \alpha, L, \mathbf{R}_{\parallel} | [\hat{\mathbf{r}}, \hat{H}_0] | \alpha', L', \mathbf{R}'_{\parallel} \rangle \quad (\text{C.18})$$

$$= \frac{m_0}{i\hbar} \left[(\mathbf{R}'_{\parallel} + \mathbf{v}_{\parallel, b'}^{\alpha'}, L'\Delta + v_{z, b'}^{\alpha'}) - (\mathbf{R}_{\parallel} + \mathbf{v}_{\parallel, b}^{\alpha}, L\Delta + v_{z, b}^{\alpha}) \right] \\ \times \langle \alpha, L, \mathbf{R}_{\parallel} | \hat{H}_0 | \alpha', L', \mathbf{R}'_{\parallel} \rangle, \quad (\text{C.19})$$

where $\mathbf{R} = (\mathbf{R}_{\parallel} + \mathbf{v}_{\parallel, i}^{\alpha}, L\Delta + v_{z, i}^{\alpha}) \equiv (\mathbf{R}_{\parallel}^{\alpha}, L^{\alpha}\Delta)$ (i.e. the atomic and orbital indices i and α' are merged into a single index α) and $N = N_{\parallel} \cdot N_z$. This result can also be derived from the expression for the bulk transition elements given in (C.10) by integrating in the growth direction,

$$\mathbf{p}_{\alpha, L; \alpha', L'}(\mathbf{k}_{\parallel}) = \frac{1}{\underbrace{L_{BZ}}_{N_z}} \int dk_z e^{ik_z L^{\alpha} \Delta} \int dk'_z e^{-ik'_z L^{\alpha'} \Delta} \langle \alpha, \mathbf{k}_{\parallel}, k_z | \hat{\mathbf{p}} | \alpha', \mathbf{k}_{\parallel}, k'_z \rangle \quad (\text{C.20})$$

$$= \frac{1}{N} \sum_{\tilde{L}, \tilde{L}'} \sum_{\tilde{\mathbf{R}}_{\parallel}, \tilde{\mathbf{R}}'_{\parallel}} N_z \underbrace{\int dk_z e^{ik_z (L^{\alpha} - \tilde{L}^{\alpha}) \Delta}}_{\delta_{L^{\alpha}, \tilde{L}^{\alpha}}} \underbrace{\int dk'_z e^{-ik'_z (L^{\alpha'} - \tilde{L}^{\alpha'}) \Delta}}_{\delta_{L^{\alpha'}, \tilde{L}^{\alpha'}}} \\ \times e^{i\mathbf{k}_{\parallel} \cdot (\tilde{\mathbf{R}}'_{\parallel, \alpha'} - \tilde{\mathbf{R}}_{\parallel, \alpha})} (\tilde{\mathbf{R}}' - \tilde{\mathbf{R}}) \langle \alpha, \tilde{L}, \tilde{\mathbf{R}}_{\parallel} | \hat{H}_0 | \alpha', \tilde{L}', \tilde{\mathbf{R}}'_{\parallel} \rangle \quad (\text{C.21})$$

$$= \frac{im_0}{\hbar} \frac{1}{N_{\parallel}} \sum_{\mathbf{R}_{\parallel}, \mathbf{R}'_{\parallel}} e^{i\mathbf{k}_{\parallel} \cdot (\mathbf{R}'_{\parallel, \alpha'} - \mathbf{R}_{\parallel, \alpha})} (\mathbf{R}' - \mathbf{R}) \langle \alpha, L, \mathbf{R}_{\parallel} | \hat{H}_0 | \alpha', L', \mathbf{R}'_{\parallel} \rangle, \quad (\text{C.22})$$

which corresponds exactly to the expression (C.19). The POB expressions for the optical matrix elements can therefore be obtained in a form similar to the bulk case,

$$\mathbf{p}_{\alpha,L;\alpha',L'}(\mathbf{k}_{\parallel}) = \frac{m_0}{\hbar} [\nabla H_0]_{\alpha,L;\alpha',L'}(\mathbf{k}_{\parallel}), \quad (\text{C.23})$$

$$[\nabla H_0]_{\alpha,L;\alpha',L'}(\mathbf{k}_{\parallel}) \equiv \frac{1}{L_{BZ}} \int dk_z e^{-ik_z[(L'-L)\Delta + v_z^{\alpha'} - v_z^{\alpha}]} \nabla_{\mathbf{k}} H_{\alpha,\alpha'}(\mathbf{k}). \quad (\text{C.24})$$

C.4.3 Green's functions

The Green's functions and self-energies are found using the planar orbital representation of the field operators (3.144)-(3.145) (neglecting spin)

$$\hat{\Psi}(\mathbf{r}, t) = \sum_{\mathbf{k}, L} \sum_{\alpha} \langle \mathbf{r} | \alpha, L, \mathbf{k} \rangle \hat{c}_{\alpha,L,\mathbf{k}}(t), \quad (\text{C.25})$$

$$\hat{\Psi}^{\dagger}(\mathbf{r}, t) = \sum_{\mathbf{k}, L} \sum_{\alpha} \langle \alpha, L, \mathbf{k} | \mathbf{r} \rangle \hat{c}_{\alpha,L,\mathbf{k}}^{\dagger}(t), \quad (\text{C.26})$$

where $\hat{c}_{\alpha,L,\mathbf{k}}(t)$ ($\hat{c}_{\alpha,L,\mathbf{k}}^{\dagger}(t)$) is the annihilation (creation) operator for an electron in state $|\alpha, L, \mathbf{k}\rangle$ at time t , and $\mathbf{k} \equiv \mathbf{k}_{\parallel}$. From Eq. (3.147), the Green's functions follow as

$$G(1, 1') = \sum_{\mathbf{k}, \mathbf{k}'} \sum_{L, L'} \sum_{\alpha, \alpha'} \langle \alpha, L, \mathbf{k} | \mathbf{r} \rangle G_{\alpha,L;\alpha',L'}(\mathbf{k}, t; \mathbf{k}', t') \langle \mathbf{r}' | \alpha', L', \mathbf{k}' \rangle \quad (\text{C.27})$$

with

$$G_{\alpha,L;\alpha',L'}(\mathbf{k}, t; \mathbf{k}', t') \equiv \langle \hat{T}_C \{ \hat{c}_{\alpha,L,\mathbf{k}}(t) \hat{c}_{\alpha',L',\mathbf{k}'}^{\dagger}(t') \} \rangle \quad (\text{C.28})$$

Using the definition of the planar orbitals in (C.12) and since the atomic orbitals are very localized, the wave functions can be written as

$$\langle \mathbf{r} | \alpha, L, \mathbf{k} \rangle \equiv \frac{1}{\sqrt{N_{\parallel}}} \sum_{\mathbf{R}_{\parallel}} e^{i\mathbf{k} \cdot (\mathbf{R}_{\parallel} + v_{\parallel}^{\alpha})} \langle \mathbf{r}_{\parallel}, z | \alpha, L, \mathbf{R}_{\parallel} \rangle \quad (\text{C.29})$$

$$\approx \frac{1}{\sqrt{N_{\parallel}}} \sum_{\mathbf{R}_{\parallel}} e^{i\mathbf{k} \cdot (\mathbf{R}_{\parallel} + v_{\parallel}^{\alpha})} \delta(z - \{L\Delta + v_z^{\alpha}\}) \delta(\mathbf{r}_{\parallel} - \{\mathbf{R}_{\parallel} + v_{\parallel}^{\alpha}\}) |\alpha\rangle, \quad (\text{C.30})$$

which, inserted in Eq.(C.27), yields

$$\begin{aligned} G(1, 1') &= \sum_{\mathbf{k}, \mathbf{k}'} \sum_{L, L'} \sum_{\alpha, \alpha'} \frac{1}{N_{\parallel}} \sum_{\mathbf{R}_{\parallel}, \mathbf{R}'_{\parallel}} e^{i[\mathbf{k}' \cdot (\mathbf{R}'_{\parallel} + v_{\parallel}^{\alpha'}) - \mathbf{k} \cdot (\mathbf{R}_{\parallel} + v_{\parallel}^{\alpha})]} \delta(z - \{L\Delta + v_z^{\alpha}\}) \delta(\mathbf{r}_{\parallel} - \{\mathbf{R}_{\parallel} + v_{\parallel}^{\alpha}\}) \\ &\quad \times \delta(z' - \{L'\Delta + v_z^{\alpha'}\}) \delta(\mathbf{r}'_{\parallel} - \{\mathbf{R}'_{\parallel} + v_{\parallel}^{\alpha'}\}) \langle \alpha | \alpha' \rangle G_{\alpha,L;\alpha',L'}(\mathbf{k}, t; \mathbf{k}', t') \end{aligned} \quad (\text{C.31})$$

$$\begin{aligned} &= \sum_{\mathbf{k}, \mathbf{k}'} \sum_{L, L'} \sum_{\alpha, \alpha'} \frac{1}{N_{\parallel}} \sum_{\mathbf{R}_{\parallel}, \mathbf{R}'_{\parallel}} e^{i[\mathbf{k}' \cdot (\mathbf{R}'_{\parallel} + v_{\parallel}^{\alpha'}) - \mathbf{k} \cdot (\mathbf{R}_{\parallel} + v_{\parallel}^{\alpha})]} \delta(z - \{L\Delta + v_z^{\alpha}\}) \delta(\mathbf{r}_{\parallel} - \{\mathbf{R}_{\parallel} + v_{\parallel}^{\alpha}\}) \\ &\quad \times \delta(z' - \{L'\Delta + v_z^{\alpha'}\}) \delta(\mathbf{r}'_{\parallel} - \{\mathbf{R}'_{\parallel} + v_{\parallel}^{\alpha'}\}) G_{\alpha,L;\alpha',L'}(\mathbf{k}, t; \mathbf{k}', t'), \end{aligned} \quad (\text{C.32})$$

Due to the lattice periodicity in the transverse plane, the Green's function is invariant under $\mathbf{r}_{\parallel} \rightarrow \mathbf{r}_{\parallel} + \mathbf{R}_{\parallel} + v_{\parallel}^{\alpha}$, $\mathbf{r}'_{\parallel} \rightarrow \mathbf{r}'_{\parallel} + \mathbf{R}_{\parallel} + v_{\parallel}^{\alpha}$, and replacing $\mathbf{R}'_{\parallel} = \mathbf{R}_{\parallel} + \tilde{\mathbf{R}}_{\parallel}$, the above expression becomes

$$\begin{aligned} & \sum_{\mathbf{k}, \mathbf{k}'} \sum_{L, L'} \sum_{\alpha} \sum_{\tilde{\mathbf{R}}_{\parallel}} e^{i\mathbf{k}' \cdot \tilde{\mathbf{R}}_{\parallel}} \overbrace{\frac{1}{N_{\parallel}} \sum_{\mathbf{R}_{\parallel}} e^{i(\mathbf{k}' - \mathbf{k}) \cdot (\mathbf{R}_{\parallel} + v_{\parallel}^{\alpha})}}^{\equiv \delta_{\mathbf{k}, \mathbf{k}'}} \delta(z - \{L\Delta + v_z^{\alpha}\}) \delta(\mathbf{r}_{\parallel}) \\ & \times \delta(z' - \{L'\Delta + v_z^{\alpha}\}) \delta(\mathbf{r}'_{\parallel} - \tilde{\mathbf{R}}_{\parallel}) G_{\alpha, L; \alpha, L'}(\mathbf{k}, t; \mathbf{k}', t') \end{aligned} \quad (\text{C.33})$$

$$\begin{aligned} & = \sum_{\mathbf{k}} \sum_{L, L'} \sum_{\alpha} \sum_{\tilde{\mathbf{R}}_{\parallel}} e^{i\mathbf{k} \cdot \tilde{\mathbf{R}}_{\parallel}} \delta(z - \{L\Delta + v_z^{\alpha}\}) \delta(\mathbf{r}_{\parallel}) \\ & \times \delta(z' - \{L'\Delta + v_z^{\alpha}\}) \delta(\mathbf{r}'_{\parallel} - \tilde{\mathbf{R}}_{\parallel}) G_{\alpha, L; \alpha, L'}(\mathbf{k}; t, t'), \end{aligned} \quad (\text{C.34})$$

or, for steady state,

$$\begin{aligned} G(\mathbf{r}, \mathbf{r}'; E) & = \sum_{\mathbf{k}} \sum_{L, L'} \sum_{\alpha} \frac{1}{N_{\parallel}} \sum_{\tilde{\mathbf{R}}_{\parallel}} e^{i\mathbf{k} \cdot \tilde{\mathbf{R}}_{\parallel}} \delta(z - \{L\Delta + v_z^{\alpha}\}) \delta(\mathbf{r}_{\parallel}) \\ & \times \delta(z' - \{L'\Delta + v_z^{\alpha}\}) \delta(\mathbf{r}'_{\parallel} - \tilde{\mathbf{R}}_{\parallel}) G_{\alpha, L; \alpha, L'}(\mathbf{k}; E). \end{aligned} \quad (\text{C.35})$$

C.4.4 Density and current

Within the layer or slab model, the average steady state density at layer L is given by the integration of the density over the layer volume $V = \mathcal{A}\Delta$, where \mathcal{A} is the transverse cross section,

$$n_L = \frac{1}{\mathcal{A}\Delta} \int_{V_L} d\mathbf{r} n(\mathbf{r}). \quad (\text{C.36})$$

Inserting expression (3.115) for the steady-state density in terms of the Green's functions yields

$$n_L = \frac{-2i}{\mathcal{A}\Delta} \int_{V_L} d\mathbf{r} \int \frac{dE}{\pi} G^<(\mathbf{r}, \mathbf{r}; E) \quad (\text{C.37})$$

$$\begin{aligned} & = \frac{-2i}{\mathcal{A}\Delta} \int \frac{dE}{\pi} \sum_{\mathbf{k}} \sum_{L'} \sum_{\alpha} \sum_{\tilde{\mathbf{R}}_{\parallel}} e^{i\mathbf{k} \cdot \tilde{\mathbf{R}}_{\parallel}} \underbrace{\int d\mathbf{r}_{\parallel} \delta(\mathbf{r}_{\parallel}) \delta(\mathbf{r}_{\parallel} - \tilde{\mathbf{R}}_{\parallel})}_{\delta_{\mathbf{R}_{\parallel}, 0}} \\ & \times \underbrace{\int_{z_L} dz \delta(z - \{L'\Delta + v_z^{\alpha}\})}_{\delta_{L, L'}} G_{\alpha, L; \alpha, L'}^<(\mathbf{k}; E) \end{aligned} \quad (\text{C.38})$$

$$= \frac{-2i}{\mathcal{A}\Delta} \sum_{\mathbf{k}} \sum_{\alpha} \int \frac{dE}{\pi} G_{\alpha, L; \alpha, L}^<(\mathbf{k}; E) = \frac{-2i}{\mathcal{A}\Delta} \sum_{\mathbf{k}} \int \frac{dE}{\pi} \text{Tr}\{G_{L; L}^<(\mathbf{k}; E)\}, \quad (\text{C.39})$$

where the trace is over orbital indices.

The current density within the layer model is derived in a similar fashion: starting from Eq. (C.27), but expanding into localized orbitals, and using the abbreviated notation

$$\varphi_\nu(\mathbf{r}) \equiv \langle \mathbf{r} | \alpha^\nu, L^\nu, \mathbf{R}_\parallel^\nu \rangle \quad (\text{C.40})$$

for the localized orbital basis functions, Eq. (3.129) for the current can be written (including a factor two to account for spin degeneracy)

$$\mathbf{J}(\mathbf{r}) = \lim_{\mathbf{r}' \rightarrow \mathbf{r}} \frac{1}{N_\parallel} \sum_{\mathbf{k}, \mathbf{k}'} \sum_{\nu, \mu} e^{i(\mathbf{k}' \cdot \mathbf{R}_\parallel^\mu - \mathbf{k} \cdot \mathbf{R}_\parallel^\nu)} ([H_0(\mathbf{r}), \mathbf{r}] - [H_0(\mathbf{r}'), \mathbf{r}']) G_{\mu\nu}^< \varphi_\nu(\mathbf{r}) \varphi_\mu^*(\mathbf{r}'). \quad (\text{C.41})$$

To express the velocity operator in the planar orbital basis, the equation is multiplied with unity operators from the orthogonality and completeness relations of the basis,

$$\int d\mathbf{r}_1 \delta(\mathbf{r} - \mathbf{r}_1) = \int d\mathbf{r}_1 \sum_{\alpha} \varphi_\alpha(\mathbf{r}) \varphi_\alpha^*(\mathbf{r}_1), \quad (\text{C.42})$$

$$\int d\mathbf{r}_2 \delta(\mathbf{r}' - \mathbf{r}_2) = \int d\mathbf{r}_2 \sum_{\beta} \varphi_\beta(\mathbf{r}_2) \varphi_\beta^*(\mathbf{r}'), \quad (\text{C.43})$$

which yields

$$\begin{aligned} \mathbf{J}(\mathbf{r}) &= \lim_{\mathbf{r}' \rightarrow \mathbf{r}} \frac{1}{N_\parallel} \sum_{\mathbf{k}, \mathbf{k}'} \sum_{\nu, \mu} \sum_{\alpha, \beta} e^{i(\mathbf{k}' \cdot \mathbf{R}_\parallel^\mu - \mathbf{k} \cdot \mathbf{R}_\parallel^\nu)} \int d\mathbf{r}_1 \int d\mathbf{r}_2 \varphi_\alpha(\mathbf{r}) \varphi_\alpha^*(\mathbf{r}_1) \varphi_\beta(\mathbf{r}_2) \varphi_\beta^*(\mathbf{r}') \\ &\quad \times ([H_0(\mathbf{r}_1), \mathbf{r}_1] - [H_0(\mathbf{r}_2), \mathbf{r}_2]) G_{\mu\nu}^< \varphi_\nu(\mathbf{r}_1) \varphi_\mu^*(\mathbf{r}_2) \end{aligned} \quad (\text{C.44})$$

$$\begin{aligned} &= \lim_{\mathbf{r}' \rightarrow \mathbf{r}} \frac{1}{N_\parallel} \sum_{\mathbf{k}, \mathbf{k}'} \sum_{\nu, \mu} \sum_{\alpha, \beta} e^{i(\mathbf{k}' \cdot \mathbf{R}_\parallel^\mu - \mathbf{k} \cdot \mathbf{R}_\parallel^\nu)} [(\mathbf{r}_\nu - \mathbf{r}_\alpha) H_{0,\alpha\nu} \delta_{\mu\beta} \\ &\quad - (\mathbf{r}_\mu - \mathbf{r}_\beta) H_{0,\beta\mu}^* \delta_{\nu\alpha}] G_{\nu\mu}^< \varphi_\alpha(\mathbf{r}) \varphi_\beta^*(\mathbf{r}') \end{aligned} \quad (\text{C.45})$$

$$\begin{aligned} &= \lim_{\mathbf{r}' \rightarrow \mathbf{r}} \frac{1}{N_\parallel} \sum_{\mathbf{k}, \mathbf{k}'} \sum_{\nu, \mu} e^{i(\mathbf{k}' \cdot \mathbf{R}_\parallel^\mu - \mathbf{k} \cdot \mathbf{R}_\parallel^\nu)} \left[\sum_{\alpha} (\mathbf{r}_\nu - \mathbf{r}_\alpha) H_{0,\alpha\nu} G_{\nu\mu}^< \varphi_\alpha(\mathbf{r}) \varphi_\mu^*(\mathbf{r}') \right. \\ &\quad \left. - \sum_{\beta} (\mathbf{r}_\mu - \mathbf{r}_\beta) H_{0,\beta\mu}^* G_{\nu\mu}^< \varphi_\nu(\mathbf{r}) \varphi_\beta^*(\mathbf{r}') \right] \end{aligned} \quad (\text{C.46})$$

$$\begin{aligned} &\approx \frac{1}{N_\parallel} \sum_{\mathbf{k}, \mathbf{k}'} \sum_{\nu, \mu} e^{i(\mathbf{k}' \cdot \mathbf{R}_\parallel^\mu - \mathbf{k} \cdot \mathbf{R}_\parallel^\nu)} \left[\sum_{\alpha} (\mathbf{r}_\nu - \mathbf{r}_\alpha) H_{0,\alpha\nu} G_{\nu\mu}^< \delta_{\alpha,\mu} \delta(\mathbf{r} - \mathbf{r}_\mu) \right. \\ &\quad \left. - \sum_{\beta} (\mathbf{r}_\mu - \mathbf{r}_\beta) H_{0,\mu\beta} G_{\nu\mu}^< \delta_{\beta,\nu} \delta(\mathbf{r} - \mathbf{r}_\nu) \right] \end{aligned} \quad (\text{C.47})$$

$$\begin{aligned} &= \frac{1}{N_\parallel} \sum_{\mathbf{k}, \mathbf{k}'} \sum_{\nu, \mu} e^{i(\mathbf{k}' \cdot \mathbf{R}_\parallel^\mu - \mathbf{k} \cdot \mathbf{R}_\parallel^\nu)} \left[(\mathbf{r}_\nu - \mathbf{r}_\mu) H_{0,\mu\nu} G_{\nu\mu}^< \delta(\mathbf{r} - \mathbf{r}_\mu) - (\mathbf{r}_\mu - \mathbf{r}_\nu) H_{0,\mu\nu} G_{\nu\mu}^< \delta(\mathbf{r} - \mathbf{r}_\nu) \right] \end{aligned} \quad (\text{C.48})$$

$$= \frac{1}{N_\parallel} \sum_{\mathbf{k}, \mathbf{k}'} \sum_{\nu, \mu} e^{i(\mathbf{k}' \cdot \mathbf{R}_\parallel^\mu - \mathbf{k} \cdot \mathbf{R}_\parallel^\nu)} (\mathbf{r}_\mu - \mathbf{r}_\nu) \left[H_{0,\nu\mu} G_{\mu\nu}^< - G_{\nu\mu}^< H_{0,\mu\nu} \right] \delta(\mathbf{r} - \mathbf{r}_\nu), \quad (\text{C.49})$$

which in planar geometry notation is

$$\begin{aligned}
\mathbf{J}(\mathbf{r}, t) &= \frac{1}{N_{\parallel}} \sum_{\mathbf{k}, \mathbf{k}'} \sum_{L, L'} \sum_{\alpha, \alpha'} \sum_{\mathbf{R}_{\parallel}, \mathbf{R}'_{\parallel}} e^{i(\mathbf{k}' \cdot \mathbf{R}'_{\parallel} - \mathbf{k} \cdot \mathbf{R}_{\parallel})} \left[\mathbf{R}'_{\parallel} - \mathbf{R}_{\parallel}, (L' - L)\Delta \right] \\
&\times \left(\langle \alpha, L, \mathbf{R}_{\parallel} | \hat{H}_0 | \alpha', L', \mathbf{R}'_{\parallel} \rangle G_{\alpha', L'; \alpha, L}^<(\mathbf{k}, t; \mathbf{k}', t') \right. \\
&\left. - G_{\alpha, L; \alpha', L'}^<(\mathbf{k}, t; \mathbf{k}', t') \langle \alpha', L', \mathbf{R}'_{\parallel} | \hat{H}_0 | \alpha, L, \mathbf{R}_{\parallel} \rangle \right) \delta(\mathbf{r}_{\parallel} - \mathbf{R}_{\parallel}) \delta(z - L\Delta). \quad (\text{C.50})
\end{aligned}$$

In the slab model, the current passing from layer L to layer $L+1$ is obtained via integrating the current density component perpendicular to the planes in the shifted slab between the two layer centers, which corresponds to the layer current density

$$\begin{aligned}
J_L(t) &= \frac{2}{\mathcal{A}\Delta} \int_{V_L} d\mathbf{r} J^z(\mathbf{r}, t) \quad (\text{C.51}) \\
&= \frac{1}{2\mathcal{A}\Delta} \sum_{\mathbf{k}, \mathbf{k}'} \sum_{L_1, L_2} \sum_{\alpha, \alpha'} \frac{1}{\sqrt{N_{\parallel}}} \sum_{\tilde{\mathbf{R}}_{\parallel}} e^{i\mathbf{k} \cdot \tilde{\mathbf{R}}_{\parallel}} \delta_{\mathbf{k}, \mathbf{k}'} (L_2 - L_1)\Delta \\
&\times \left(\langle \alpha, L_1, \tilde{\mathbf{R}}_{\parallel} | \hat{H}_0 | \alpha', L_2, \mathbf{0} \rangle G_{\alpha', L_2; \alpha, L_1}^<(\mathbf{k}, t; \mathbf{k}', t') \right. \\
&\left. - G_{\alpha, L_1; \alpha', L_2}^<(\mathbf{k}, t; \mathbf{k}', t') \langle \alpha', L_2, \mathbf{0} | \hat{H}_0 | \alpha, L_1, \tilde{\mathbf{R}}_{\parallel} \rangle \right) \\
&\times \underbrace{\int d\mathbf{r}_{\parallel} \delta(\mathbf{r}_{\parallel} - \tilde{\mathbf{R}}_{\parallel})}_1 \underbrace{\int dz \delta(z - L_1\Delta)}_{\delta_{L_1, L} + \delta_{L_1, L+1}} \quad (\text{C.52}) \\
&= \frac{1}{2\mathcal{A}\Delta} \sum_{\mathbf{k}} \sum_{L'} \sum_{\alpha, \alpha'} \left[(L' - L)\Delta \left\{ [H_0]_{\alpha, L'; \alpha', L'}(\mathbf{k}) G_{\alpha', L'; \alpha, L}^<(\mathbf{k}; t, t') \right. \right. \\
&\left. \left. - G_{\alpha, L'; \alpha', L'}^<(\mathbf{k}; t, t') [H_0]_{\alpha', L'; \alpha, L}(\mathbf{k}) \right\} \right. \\
&\left. + [L' - (L + 1)\Delta] \left\{ [H_0]_{\alpha, L+1; \alpha', L'}(\mathbf{k}) G_{\alpha', L'; \alpha, L+1}^<(\mathbf{k}; t, t') \right. \right. \\
&\left. \left. - G_{\alpha, L+1; \alpha', L'}^<(\mathbf{k}; t, t') [H_0]_{\alpha', L'; \alpha, L+1}(\mathbf{k}) \right\} \right]. \quad (\text{C.53})
\end{aligned}$$

Since only the current flow within the slab is considered, the restriction $L' \in \{L, L + 1\}$ holds, and we obtain the expression

$$J_L(t) = \frac{1}{\mathcal{A}} \sum_{\mathbf{k}} \text{Tr} \left\{ [H_0(\mathbf{k})]_{L; L+1} G_{L+1; L}^<(\mathbf{k}; t, t') - G_{L; L+1}^<(\mathbf{k}; t, t') [H_0(\mathbf{k})]_{L+1; L} \right\}, \quad (\text{C.54})$$

where the trace is over orbital indices, with the steady state form

$$J_L = \frac{1}{\hbar\mathcal{A}} \sum_{\mathbf{k}} \int \frac{dE}{\pi} \text{Tr} \left\{ [H_0(\mathbf{k})]_{L; L+1} G_{L+1; L}^<(\mathbf{k}; E) - G_{L; L+1}^<(\mathbf{k}; E) [H_0(\mathbf{k})]_{L+1; L} \right\}. \quad (\text{C.55})$$

Since for both transport and direct optical transitions the vicinity of the transverse band extrema at $k_{\parallel} = 0$ is most important, the dispersion is expanded around that point,

$$H(\mathbf{k}_{\parallel}, k_z) \approx H(0, k_z) + \frac{1}{2} \left(\frac{\partial^2}{\partial k_x^2} H(\mathbf{k}) \Big|_{k_{\parallel}=0} k_x^2 + \frac{\partial^2}{\partial k_y^2} H(\mathbf{k}) \Big|_{k_{\parallel}=0} k_y^2 \right) \quad (\text{C.63})$$

$$\approx 4V_{ss}g_0(0, k_z) + \epsilon_s + \frac{\hbar^2 k_{\parallel}^2}{2m_{\parallel}^*(k_z)}, \quad (\text{C.64})$$

where the definition of the effective mass and the assumption of isotropy of the transverse dispersion were used. The relation between tight-binding parameters and effective mass theory is found from the expression for longitudinal effective mass,

$$m_z^* = \hbar^2 \left[\frac{\partial^2 E}{\partial k_z^2} \right]^{-1} \Big|_{\mathbf{k}=0} = \frac{\hbar^2}{2a_L^2} \frac{1}{V_{ss}} \Rightarrow V_{ss} = -\frac{\hbar^2}{2m_z^* a_L^2}. \quad (\text{C.65})$$

The corresponding value for the on-site energy is obtained from the normalization $E(0) = 0$, which yields $\epsilon_s = -12V_{ss}$. The first term in (C.64) thus becomes

$$H(0, k_z) = 8V_{ss} \left[\cos(k_z \frac{a_L}{2}) - 1 \right]. \quad (\text{C.66})$$

Defining the hopping element $t \equiv -4V_{ss} = \frac{\hbar^2}{2m_z^* \Delta^2}$ with the computational layer width $\Delta \equiv \frac{a_L}{2}$, the quasi-1D effective Hamiltonian with isotropic, parabolic transverse dispersion yields the band structure

$$\epsilon(\mathbf{k}_{\parallel}, k_z) = -2t [\cos(k_z \Delta) - 1] + \frac{\hbar^2 k_{\parallel}^2}{2m_{\parallel}^*} \quad (\text{C.67})$$

$$= D(\mathbf{k}_{\parallel}) - 2t \cos(k_z \Delta) \quad (\text{C.68})$$

where $D(\mathbf{k}_{\parallel}) = 2t + \frac{\hbar^2 k_{\parallel}^2}{2m_{\parallel}^*}$. We thus recover the dispersion of the single orbital quasi-one-dimensional chain.

C.5.1 Boundary self energies

The general form of the boundary self-energy for tight-binding models is derived in App. D and reads, e.g. for the left contact

$$\Sigma_{1;1}^{RB} = -t_{1;0} (U_- \Lambda_z^{-1} U_-^{-1})^{-1}, \quad (\text{C.69})$$

where $t_{1;0}$ is the hopping element between device and contact, U_- contains the left-propagating Bloch states of the contact and Λ_z the corresponding propagation factors.

In the case of the single orbital model, all these quantities are scalars, and the boundary self-energy simplifies to

$$\Sigma_{1;1}^{RB} = -t_{1;0} e^{ik_z^L \Delta}. \quad (\text{C.70})$$

with the longitudinal wave vector determined from the dispersion relation (C.68),

$$k_z^L(\mathbf{k}_{\parallel}; E) = \frac{1}{\Delta} \arccos \left(\frac{D_{1;1}(\mathbf{k}_{\parallel}) - E}{2t_{0;1}} \right). \quad (\text{C.71})$$

This is identical to the self-energy of a semi-infinite quasi-one-dimensional tight-binding chain, which is often used as a simple model for an ideal electrode with finite band-width. The self energy can be written as

$$\Sigma_{1;1}^{RB}(\mathbf{k}_{\parallel}; E) \equiv \Delta(\mathbf{k}_{\parallel}; E) - \frac{i}{2} \Gamma(\mathbf{k}_{\parallel}; E) \quad (\text{C.72})$$

where

$$\Delta(\mathbf{k}_{\parallel}; E) = -t_{1;0} \cos [k_z^L(\mathbf{k}_{\parallel}; E) \Delta] \quad (\text{C.73})$$

$$\equiv -t_{1;0} e^{-|\Im\{\arccos[(D_{1;1}(\mathbf{k}_{\parallel}) - E)/(|2t_{0;1}|\Delta)]\}| \Delta} \cos(\Re\{\arccos[(D_{1;1}(\mathbf{k}_{\parallel}) - E)/(|2t_{0;1}|\Delta)]\}) \quad (\text{C.74})$$

is the level renormalization and

$$\Gamma(\mathbf{k}_{\parallel}; E) = 2t_{1;0} \sin [k_z^L(\mathbf{k}_{\parallel}; E) \Delta] \quad (\text{C.75})$$

$$\equiv 2t_{1;0} e^{-|\Im\{\arccos[(D_{1;1}(\mathbf{k}_{\parallel}) - E)/(|2t_{0;1}|\Delta)]\}| \Delta} \sin(\Re\{\arccos[(D_{1;1}(\mathbf{k}_{\parallel}) - E)/(|2t_{0;1}|\Delta)]\}) \quad (\text{C.76})$$

is the rate of carrier escape into the contact. Fig. C.2 shows the dependence on energy of the two parts, normalized by the band-width $|2t|$ and at $\mathbf{k}_{\parallel} = 0$.

Due to the isotropic dispersion relation for transverse momentum, the summation over transverse momentum can be approximated by a one dimensional integration up to some cutoff,

$$\sum_{\mathbf{k}} \approx \frac{\mathcal{A}}{(2\pi)^2} \int_{BZ_{\perp}} d^2k = \frac{\mathcal{A}}{2\pi} \int dk k \approx \frac{\mathcal{A}}{2\pi} \sum_k k \Delta k, \quad (\text{C.77})$$

where \mathcal{A} is the device cross section, BZ_{\perp} is the projected Brillouin zone and $k = |\mathbf{k}|$ is the absolute value of the transverse momentum.

C.5.2 Single orbital two-band model

To describe transport and optical transitions within the same theoretical framework, both electrons and holes have to be represented by the microscopic theory. The single orbital

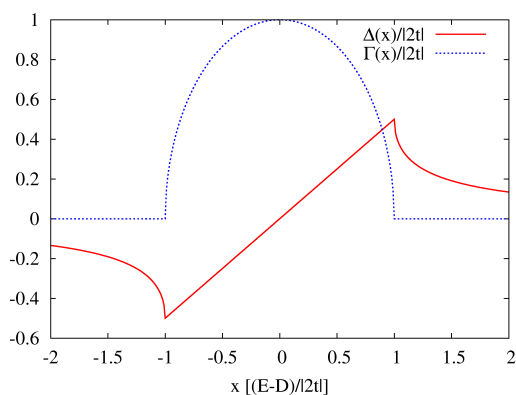


Figure C.2: Level renormalization Δ and escape rate Γ for the contact self-energy in the single orbital tight binding model.

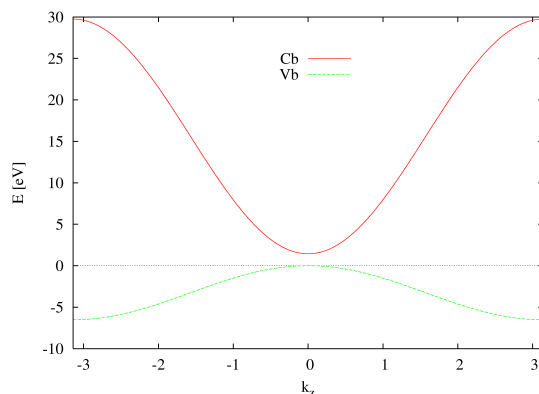


Figure C.3: Two-band dispersion relation for a model made of two single orbital tight binding components. The hole-branch corresponds to heavy holes.

model derived above also applies to the description of holes in the valence band, if the electronic effective mass is replaced by a corresponding negative value, both in the longitudinal and transverse direction. In the following, the zero of energy is placed at the valence band maximum, and the on-site energy of the electrons is shifted upwards in energy by the value E_g of the band gap. Fig. C.3 shows the longitudinal single-orbital two-band dispersion for GaAs: while the parameters are chosen to reproduce the effective mass at the Γ -point, the deviation from the physical gap is considerable near the boundary of the Brillouin zone. To improve this behaviour, more orbitals need to be included.

C.6 Diatomic two-band model

Multiband tight-binding models are obtained by placing multiple orbitals on the same atomic site or by choosing a multi-atom basis for the unit cell. The simplest multiband tight-binding model to approximate the conduction and valence band structure of direct semiconductors like e.g. GaAs is the diatomic model with a two-atom basis. In this model, a two-band dispersion is produced by placing an s -type orbital on the cation (Ga) and a p_z -type orbital on the anion (As). The tight-binding parameters which determine the dispersion relation in the (001) direction are the onsite-energies and hopping parameters displayed in table C.6. For further simplification, the transverse band structure is replaced by the parabolic approximation in a similar way as for the single-band model, replacing the

E_s	cation on-site energy
E_p	anion on-site energy
V_s	inter-layer coupling of s-orbitals
V_p	inter-layer coupling of p-orbitals
$V_{sp} = -V_{ps}$	inter-orbital coupling

electronic effective mass by the corresponding hole effective mass in the case of the valence band and performing the integration over transverse momentum using the isotropic one dimensional approximation of Eq. (C.77). What remains in the direction of propagation is a sp_z model with $\mathbf{k} = 0$, which is equivalent to a linear chain of atoms, with the cation layers at $z = La_L/2$ and the anion layers at $z = (La_L/2 + a_L/4)$, where $L \in \mathbb{N}$ labels the monolayer of thickness $\Delta = a_L/2$, with a_L the lattice constant of the binary compound, i.e. 5.65 \AA in the case of GaAs. In terms of the parameters in table C.6, the elements of the TB-Hamiltonian (C.58), including parabolic transverse energy, are given by

$$D_L \equiv H_{LL} = \begin{pmatrix} E_s + \frac{\hbar k^2}{2m_{el}^*} & -V_{sp} \\ -V_{sp} & E_p - \frac{\hbar k^2}{2m_{hl}^*} \end{pmatrix}, \quad (\text{C.78})$$

$$t_{LL+1} \equiv -H_{LL+1} = \begin{pmatrix} -V_p & 0 \\ -V_{sp} & -V_s \end{pmatrix}, \quad t_{LL-1} \equiv -H_{LL-1} = \begin{pmatrix} -V_p & -V_{sp} \\ 0 & -V_s \end{pmatrix}. \quad (\text{C.79})$$

where $m_{el/hl}^*$ is the effective electron and hole mass, respectively. Via Eq. (C.8), this yields the bulk Hamiltonian

$$H(\mathbf{k}, k_z) = \begin{pmatrix} E_s + 2V_s \cos(k_z \frac{a_L}{2}) + \frac{\hbar k^2}{2m_{el}^*} & 2iV_{sp} \sin(k_z \frac{a_L}{4}) \\ -2iV_{sp} \sin(k_z \frac{a_L}{4}) & E_p + 2V_p \cos(k_z \frac{a_L}{2}) - \frac{\hbar k^2}{2m_{hl}^*} \end{pmatrix}. \quad (\text{C.80})$$

which for $k = 0$ gives rise to the dispersion relation

$$\det[H(k_z) - E] = 0 \quad \Rightarrow \quad E^{Cb, Vb}(k_z) = \frac{1}{2} \left[E_p + E_s + 2(V_p + V_s) \cos(k_z \frac{a_L}{2}) \right] \quad (\text{C.81})$$

$$\pm \sqrt{\left(E_p - E_s + 2(V_p - V_s) \cos(k_z \frac{a_L}{2}) \right)^2 + 16V_{sp}^2 \sin^2(k_z \frac{a_L}{4})}, \quad (\text{C.82})$$

For the GaAs TB-parameters, the two bands shown in Fig. C.4 are produced.

To fit a specific band structure, the measured effective masses for electrons and heavy holes at the Γ -point and the electronic X -point mass are used together with the band gap E_g and some arbitrary zero-energy reference level, which is chosen at the valence band

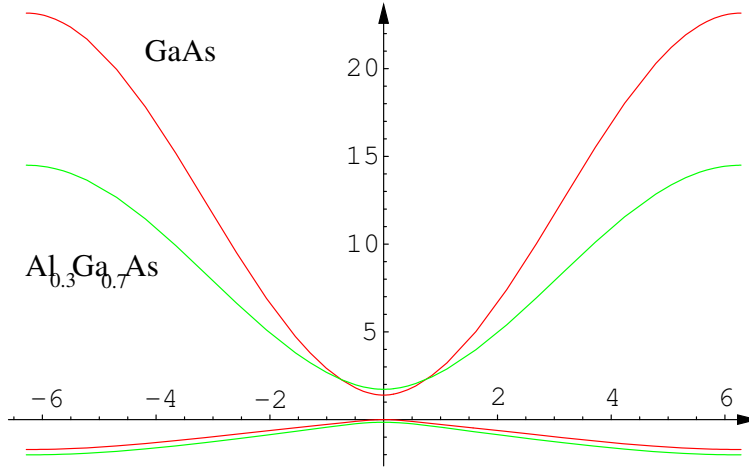


Figure C.4: Dispersion of the 2-band model with parameters adjusted to fit the effective masses of GaAs and $\text{Al}_{0.3}\text{Ga}_{0.7}\text{As}$ at the Γ -point.

edge. The band gap is given in terms of the TB-parameters as

$$E_g = |E_p - E_s + 2(V_p - V_s)|, \quad (\text{C.83})$$

and the effective mass m_z^* is obtained from the longitudinal dispersion relation, as $m_z^* = \frac{\hbar^2}{m_0} \left[\frac{\partial^2 E_z}{\partial k_z^2} \right]^{-1}$, with E_z resulting from the secular equation $\det[H_0(k_z) - E_z] = 0$, where $H_0(k_z) = H(\mathbf{k}) - \frac{\hbar^2 \mathbf{k}_{\parallel}}{2m_{\parallel}^*}$. From Eq. (C.82), one finds the relation between the effective mass and the tight-binding parameters,

$$m_{el,z}^{*\Gamma} = \frac{\hbar^2 a^2}{m_0 4} \left[-(V_p + V_s) + \frac{-(E_p - E_s + 2(V_p - V_s))(V_p - V_s) + 2V_{sp}^2}{|E_p - E_s + 2(V_p - V_s)|} \right]^{-1}, \quad (\text{C.84})$$

$$m_{el,z}^{*X} = \frac{\hbar^2 a^2}{m_0 4} \left[(V_p + V_s) + \frac{(E_p - E_s - 2(V_p - V_s))(V_p - V_s) - 2V_{sp}^2}{\sqrt{(E_p - E_s - 2(V_p - V_s))^2 + 16V_{sp}^2}} \right]^{-1}, \quad (\text{C.85})$$

$$m_{hl,z}^{*\Gamma} = \frac{\hbar^2 a^2}{m_0 4} \left[-(V_p + V_s) + \frac{(E_p - E_s + 2(V_p - V_s))(V_p - V_s) - 2V_{sp}^2}{|E_p - E_s + 2(V_p - V_s)|} \right]^{-1}. \quad (\text{C.86})$$

To obtain the optical matrix elements from the standard Hellman-Feynman theorem (Eq. (C.24)) in the case of longitudinal polarization is straightforward:

$$\mathbf{p}_{\alpha,L;\alpha',L'}(\mathbf{k}_{\parallel}) = \frac{m_0}{i\hbar} [(L' - L)\Delta + v_z^{\alpha'} - v_z^{\alpha}] H_{\alpha,L;\alpha',L'}(\mathbf{k}_{\parallel}). \quad (\text{C.87})$$

For transverse polarization, the transverse Hamiltonian $H(\mathbf{k}_{\parallel})$ for free carriers needs to be replaced by a more realistic term that reproduces the right \mathbf{k}_{\parallel} -dependence. One possibility

would be to take the sp_z -elements as derived from a sp^3s^* model (see below), which provides the correct transverse band structure. A simpler approach is to assume the same band structure in the transverse direction as along the growth axis (except for the additional homogeneity in composition), which means that the same sp_z -model is used for the transverse Hamiltonian. In contrast to the previous case of z -polarized light, there is no direct light induced modification of the inter-plane coupling, and the summation over the transverse atomic positions leads to the optical element for bulk:

$$\mathbf{p}_{\alpha,L;\alpha',L'}^{\parallel}(\mathbf{k}_{\parallel}) = \frac{1}{N} \sum_{\mathbf{R}_{\parallel}, \mathbf{R}'_{\parallel}} e^{i\mathbf{k}_{\parallel}(\mathbf{R}'_{\parallel} - \mathbf{R}_{\parallel})} \langle \alpha, L, \mathbf{R}_{\parallel} | \mathbf{p}^{\parallel} | \alpha', L', \mathbf{R}'_{\parallel} \rangle \quad (\text{C.88})$$

$$= \frac{1}{N} \sum_{\mathbf{R}_{\parallel}, \mathbf{R}'_{\parallel}} e^{i\mathbf{k}_{\parallel}(\mathbf{R}'_{\parallel} - \mathbf{R}_{\parallel})} \frac{m_0}{i\hbar} (\mathbf{R}'_{\parallel} - \mathbf{R}_{\parallel}) \langle \alpha, L, \mathbf{R}_{\parallel} | H_0 | \alpha', L', \mathbf{R}'_{\parallel} \rangle \quad (\text{C.89})$$

$$= \frac{1}{N} \sum_{k=1}^N \frac{m_0}{i\hbar} \frac{a_L}{4} \left[e^{ik_{\parallel} \frac{a_L}{4}} \langle \alpha, L, \mathbf{R}_{\parallel}^k | H_0 | \alpha', L', \mathbf{R}_{\parallel}^k + \frac{a_L}{4} \rangle \right. \quad (\text{C.90})$$

$$\left. - e^{-ik_{\parallel} \frac{a_L}{4}} \langle \alpha, L, \mathbf{R}_{\parallel}^k | H_0 | \alpha', L', \mathbf{R}_{\parallel}^k - \frac{a_L}{4} \rangle \right], \quad (\text{C.91})$$

Since only nearest-neighbor elements of the TB-Hamiltonian are nonzero, the $(\mathbf{R}'_{\parallel} - \mathbf{R}_{\parallel})$ -factor confines the elements to a single layer; for the POB TB-elements of the 2-band model, although only one orbital per atom is assumed, the diagonal element will be an effective one including the contributions of the only nonzero elements V_{sp} . With

$$\langle \alpha, L, \mathbf{R}_{\parallel}^k | H_0 | \alpha', L', \mathbf{R}_{\parallel}^k + \frac{a_L}{4} \rangle = \langle \alpha, L, \mathbf{R}_{\parallel}^k | H_0 | \alpha', L', \mathbf{R}_{\parallel}^k - \frac{a_L}{4} \rangle \quad (\text{C.92})$$

and

$$\langle \alpha, L, \mathbf{R}_{\parallel}^k | H_0 | \alpha', L', \mathbf{R}_{\parallel}^k + \frac{a_L}{4} \rangle = -\langle \alpha, L, \mathbf{R}_{\parallel}^k + \frac{a_L}{4} | H_0 | \alpha', L', \mathbf{R}_{\parallel}^k \rangle, \quad (\text{C.93})$$

which yields the momentum matrix elements

$$\mathbf{p}_{\alpha,L;\alpha',L'}^{\parallel}(k_{\parallel}) = \delta_{L,L'} (-1)^{\delta_{\alpha,\alpha'}} \frac{im_0}{2\hbar} a_L V_{sp} \cos\left(k_{\parallel} \frac{a_L}{4}\right). \quad (\text{C.94})$$

C.7 Spinless sp^3s^* model

To reproduce the band structure of semiconductors like GaAs or Si with reasonable accuracy, *Vogl et al.* [236] introduced the sp^3s^* empirical tight-binding model, which in addition to the sp^3 basis required for the valence bands uses an excited s^* orbital to improve the fit of the conduction bands. The basis functions are the corresponding Löwdin orbitals, i.e. the symmetrically orthogonalized atomic orbitals

$$|\alpha, b, \mathbf{k}\rangle = \frac{1}{\sqrt{N}} \sum_{j,b} e^{i\mathbf{k}\cdot(\mathbf{R}_j + \mathbf{v}_b)} |\alpha, b, \mathbf{R}_j\rangle, \quad (\text{C.95})$$

where $\alpha \in \{s, p_x, p_y, p_z, s^*\}$ labels the atomic like orbitals on the anion ($b = a$) or the cation ($b = c$) at position $\mathbf{R}_j + \mathbf{v}_b$, with $\mathbf{v}_b = \delta_{b,c} \frac{a_L}{4} (1, 1, 1)$, and the N wave vectors $\mathbf{k} = \frac{2\pi}{a_L} (u_1, u_2, u_3)$ with $u_1 + u_2 + u_3 \leq \frac{3}{2}$ lie in the first Brillouin zone (fcc -lattice in real space, bcc -lattice in reciprocal space).

In this basis, the Schrödinger equation for the Bloch functions $|n, \mathbf{k}\rangle$

$$(\hat{H} - \epsilon_n(\mathbf{k}))|n, \mathbf{k}\rangle = 0, \quad (\text{C.96})$$

where n is the band index, is written

$$\sum_{\beta} \left\{ \langle \alpha, b, \mathbf{k} | \hat{H} | \beta, b', \mathbf{k} \rangle - \epsilon_n(\mathbf{k}) \delta_{\alpha, \beta} \delta_{b, b'} \right\} \langle \beta, b', \mathbf{k} | n, \mathbf{k} \rangle = 0. \quad (\text{C.97})$$

Expanding the Bloch functions in the tight-binding basis (C.95)

$$|n, \mathbf{k}\rangle = \sum_{\alpha, b} |\alpha, b, \mathbf{k}\rangle \langle \alpha, b, \mathbf{k} | n, \mathbf{k} \rangle \equiv \sum_{\alpha, b} C_{\alpha, b}^n(\mathbf{k}) |\alpha, b, \mathbf{k}\rangle, \quad (\text{C.98})$$

the eigenequation (C.96) becomes

$$\sum_{\beta} [H_{\alpha, b; \beta, b'}(\mathbf{k}) - \epsilon_n(\mathbf{k}) \delta_{\alpha, \beta} \delta_{b, b'}] C_{\alpha, b'}^n(\mathbf{k}) = 0, \quad (\text{C.99})$$

with $C_{\alpha, b'}^n(\mathbf{k})$ the elements of the eigenvectors corresponding to the eigenvalues $\epsilon_n(\mathbf{k})$ containing the dispersion. The bulk band structure is thus obtained by diagonalizing $H_{\alpha, b; \beta, b'}(\mathbf{k})$, which is given in Tab. C.2.

The geometrical phase factors are given by

$$g_0(\mathbf{k}) = \cos(k_x a_L/4) \cos(k_y a_L/4) \cos(k_z a_L/4) - i \sin(k_x a_L/4) \sin(k_y a_L/4) \sin(k_z a_L/4) \quad (\text{C.100})$$

$$g_1(\mathbf{k}) = -\cos(k_x a_L/4) \sin(k_y a_L/4) \sin(k_z a_L/4) + i \sin(k_x a_L/4) \cos(k_y a_L/4) \cos(k_z a_L/4), \quad (\text{C.101})$$

$$g_2(\mathbf{k}) = -\sin(k_x a_L/4) \cos(k_y a_L/4) \sin(k_z a_L/4) + i \cos(k_x a_L/4) \sin(k_y a_L/4) \cos(k_z a_L/4), \quad (\text{C.102})$$

$$g_3(\mathbf{k}) = -\sin(k_x a_L/4) \sin(k_y a_L/4) \cos(k_z a_L/4) + i \cos(k_x a_L/4) \cos(k_y a_L/4) \sin(k_z a_L/4). \quad (\text{C.103})$$

Fig. C.5 shows the complex band structure, the transmission coefficient and the density of states for flat-band bulk GaAs and $\text{Al}_{0.3}\text{Ga}_{0.7}\text{As}$ using the parameters of *Vogl et al.*, given in Tab. C.3 and the virtual crystal approximation.

$ sa\rangle$	$ sc\rangle$	$ p_xa\rangle$	$ p_ya\rangle$	$ p_za\rangle$	$ p_xc\rangle$	$ p_yc\rangle$	$ p_zc\rangle$	$ s^*a\rangle$	$ s^*c\rangle$
$ sa\rangle$	E_{sa}	$V_{ss}g_0$	0	0	$V_{sapc}g_1$	$V_{sapc}g_2$	$V_{sapc}g_3$	0	0
$ sc\rangle$	$V_{ss}g_0^*$	E_{sc}	$-V_{pasc}g_1^*$	$-V_{pasc}g_2^*$	$-V_{pasc}g_3^*$	0	0	0	0
$ p_xa\rangle$	0	$-V_{pasc}g_1$	E_{pa}	0	$V_{xx}g_0$	$V_{xy}g_3$	$V_{xy}g_2$	0	$-V_{pas^*c}g_1$
$ p_ya\rangle$	0	$-V_{pasc}g_2$	0	E_{pa}	$V_{xy}g_3$	$V_{xx}g_0$	$V_{xy}g_1$	0	$-V_{pas^*c}g_2$
$ p_za\rangle$	0	$-V_{pasc}g_3$	0	E_{pa}	$V_{xy}g_2$	$V_{xy}g_1$	$V_{xx}g_0$	0	$-V_{pas^*c}g_3$
$ p_xc\rangle$	$V_{sapc}g_1^*$	0	$V_{xy}g_3^*$	$V_{xy}g_2^*$	E_{pc}	0	0	$V_{s^*apc}g_1^*$	0
$ p_yc\rangle$	$V_{sapc}g_2^*$	0	$V_{xy}g_3^*$	$V_{xx}g_0^*$	E_{pc}	E_{pc}	0	$V_{s^*apc}g_2^*$	0
$ p_zc\rangle$	$V_{sapc}g_3^*$	0	$V_{xy}g_2^*$	$V_{xx}g_0^*$	0	0	E_{pc}	$V_{s^*apc}g_3^*$	0
$ s^*a\rangle$	0	0	0	0	$V_{s^*apc}g_1$	$V_{s^*apc}g_2$	$V_{s^*apc}g_3$	E_{s^*a}	$V_{s^*s^*g_0}$
$ s^*c\rangle$	0	0	$-V_{pas^*c}g_1^*$	$-V_{pas^*c}g_2^*$	$-V_{pas^*c}g_3^*$	0	0	$V_{s^*s^*g_0}$	E_{s^*c}

 Table C.2: Orbital elements of the sp^3s^* Hamiltonian for bulk.

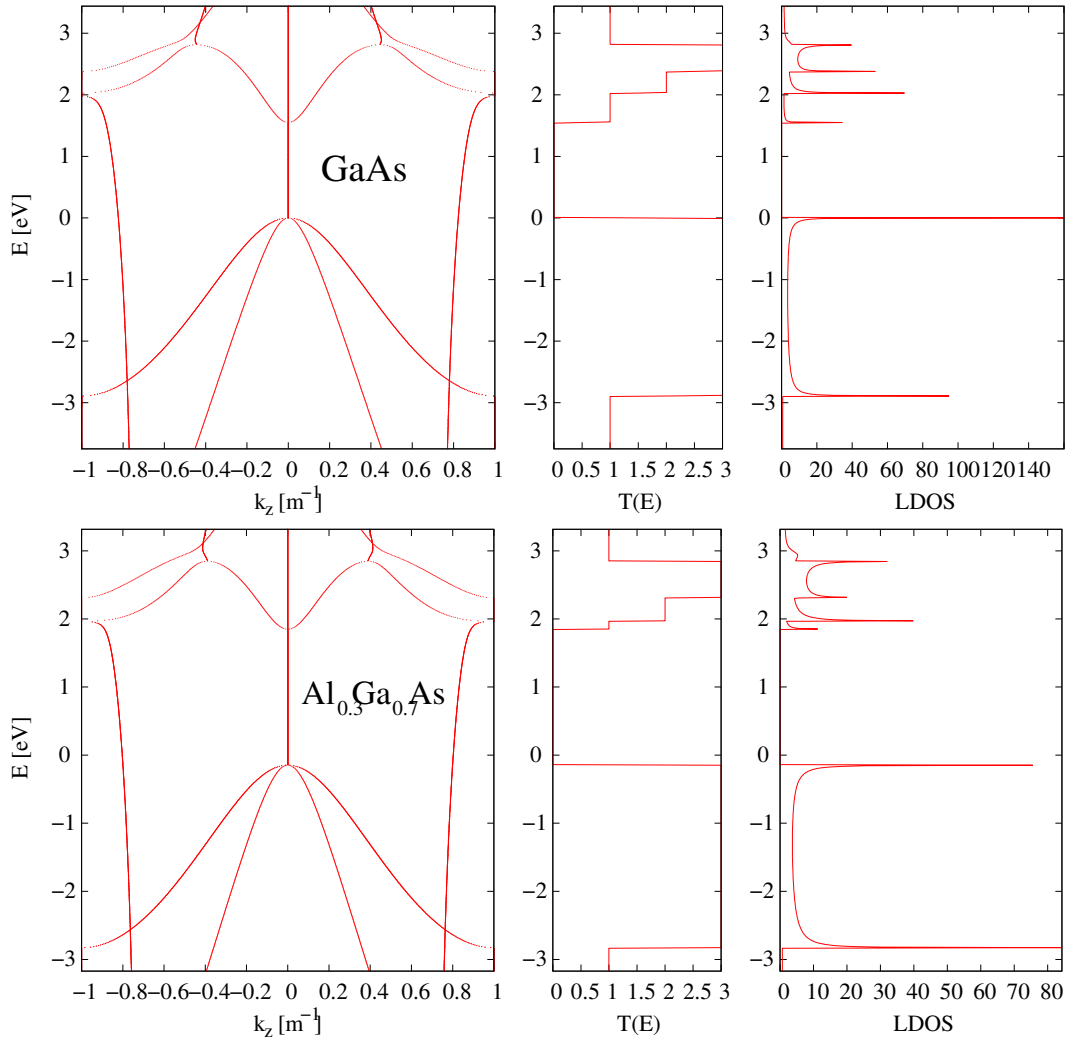


Figure C.5: Band structure, transmission and density of states for flat-band bulk GaAs and $\text{Al}_{0.3}\text{Ga}_{0.7}\text{As}$ as obtained from the sp^3s^* model using the parameters in Tab. C.3.

Table C.3: Orbital matrix elements of the sp^3s^* Hamiltonian for GaAs and AlAs.

Compound	E_{sa}	E_{pa}	E_{sc}	E_{s^*a}	E_{s^*c}	V_{ss}
GaAs	-8.3431	1.0414	-2.6569	3.6686	8.5914	6.7386
AlAs	-7.5273	0.9833	-1.1627	3.5867	7.4833	6.7267
Compound	V_{xx}	V_{xy}	V_{sapc}	V_{s^*apc}	V_{pas^*c}	$V_{s^*s^*}$
GaAs	1.9546	5.0779	4.4800	5.7839	4.8422	4.8077
AlAs	1.8780	4.2919	5.1106	5.4965	4.5216	4.9950

Planar orbital Hamiltonian for sp^3s^* basis

Labelling the atomic planes by j , the elements of the POB Hamiltonian given in Eq. (C.15) can be written as

$$\langle \alpha b j \mathbf{k}_{\parallel} | \hat{H} | \alpha' b' j' \mathbf{k}_{\parallel} \rangle = \frac{1}{L_{BZ}} \int dk_z e^{ik_z(j-j')\frac{a_L}{4}} \langle \alpha b \mathbf{k} | \hat{H} | \alpha' b' \mathbf{k} \rangle, \quad (\text{C.104})$$

where the \mathbf{k} -dependence of the bulk Hamiltonian is contained in the phase-factors (C.103). Longitudinal integration of these phase factors,

$$\tilde{g}_{n,jj'}(\mathbf{k}_{\parallel}) \equiv \frac{1}{L_{BZ}} \int dk_z e^{ik_z(j-j')\frac{a_L}{4}} g_n(\mathbf{k}), \quad n = 0, 1, 2, 3, \quad (\text{C.105})$$

yields the new expressions

$$\tilde{g}_{0,jj'}(\mathbf{k}_{\parallel}) = \delta_{j+1,j'}c_+ + \delta_{j-1,j'}c_-, \quad (\text{C.106})$$

$$\tilde{g}_{1,jj'}(\mathbf{k}_{\parallel}) = \delta_{j+1,j'}is_+ + \delta_{j-1,j'}is_-, \quad (\text{C.107})$$

$$\tilde{g}_{2,jj'}(\mathbf{k}_{\parallel}) = \delta_{j+1,j'}is_+ - \delta_{j-1,j'}is_-, \quad (\text{C.108})$$

$$\tilde{g}_{3,jj'}(\mathbf{k}_{\parallel}) = \delta_{j+1,j'}c_+ - \delta_{j-1,j'}c_-, \quad (\text{C.109})$$

where

$$c_{\pm} \equiv \frac{1}{2} \cos \mathbf{k}_{\parallel} \cdot \mathbf{d}_{\pm}, \quad s_{\pm} \equiv \frac{1}{2} \sin \mathbf{k}_{\parallel} \cdot \mathbf{d}_{\pm}, \quad \mathbf{d}_{\pm} = (1, \pm 1) \frac{a_L}{4}. \quad (\text{C.110})$$

For instance, if j labels the anion layer, one finds the matrix element

$$\langle saj \mathbf{k}_{\parallel} | \hat{H} | pzcj' \mathbf{k}_{\parallel} \rangle = V_{sabc} \tilde{g}_{3,ij'}(\mathbf{k}_{\parallel}) = V_{sabc} (\delta_{j+1,j'}c_+ - \delta_{j-1,j'}c_-). \quad (\text{C.111})$$

The elements of the block-diagonal POB-Hamiltonian (C.57) follow as

$$E_b = \begin{pmatrix} E_{sb} & & & & \\ & E_{pb} & & & \\ & & E_{pb} & & \\ & & & E_{pb} & \\ & & & & E_{s^*b} \end{pmatrix}, \quad b = c, a, \quad (\text{C.112})$$

$$U_{ac} = \begin{pmatrix} V_{ss}c_- & iV_{sabc}s_- & -iV_{sabc}s_- & -V_{sabc}c_- & 0 \\ -iV_{pasc}s_- & V_{xx}c_- & -V_{xy}c_- & -iV_{xy}s_- & -iV_{pas^*c}s_- \\ iV_{pasc}s_- & -V_{xy}c_- & V_{xx}c_- & iV_{xy}s_- & iV_{pas^*c}s_- \\ V_{pasc}c_- & -iV_{xy}s_- & iV_{xy}s_- & V_{xx}c_- & V_{pas^*c}c_- \\ 0 & iV_{s^*apc}s_- & -iV_{s^*apc}s_- & -V_{s^*apc}c_- & V_{s^*s^*c_-} \end{pmatrix}, \quad (\text{C.113})$$

$$V_{ac} = \begin{pmatrix} V_{ss}c_+ & iV_{sabc}s_+ & iV_{sabc}s_+ & V_{sabc}c_+ & 0 \\ -iV_{pasc}s_+ & V_{xx}c_+ & V_{xy}c_+ & iV_{xy}s_+ & -iV_{pas^*c}s_+ \\ -iV_{pasc}s_+ & V_{xy}c_+ & V_{xx}c_+ & iV_{xy}s_+ & -iV_{pas^*c}s_+ \\ -V_{pasc}c_+ & iV_{xy}s_+ & iV_{xy}s_+ & V_{xx}c_+ & -V_{pas^*c}c_+ \\ 0 & iV_{s^*apc}s_+ & iV_{s^*apc}s_+ & V_{s^*apc}c_+ & V_{s^*s^*c_+} \end{pmatrix}, \quad (\text{C.114})$$

and $U_{ca} = U_{ac}^\dagger$, $V_{ca} = V_{ac}^\dagger$.

Optical transitions

Fig. C.6 shows the squared optical matrix elements $|\mathbf{p}_{nm}(\mathbf{k})|^2$ for bulk GaAs and x -polarization. For the POB-representation of the optical elements, the objects in (C.24) are required. Since the whole \mathbf{k} -dependence is contained in the phase-factors, both derivative and longitudinal momentum integration affect only those.

For transverse polarization (\rightarrow interband transitions), the derivative is only with respect to \mathbf{k}_\parallel , such that the integration is not modified. The derivative can thus be considered by replacing

$$c_\pm \rightarrow -s_\pm \mathbf{d}_\pm, \quad s_\pm \rightarrow c_\pm \mathbf{d}_\pm \quad (\text{C.115})$$

in the expressions for U_{ac} and V_{ac} .

In the case of z -polarized light, the derivative with respect to k_z leads to the replacement

$$\tilde{g}_0 \rightarrow i \frac{a_L}{4} \tilde{g}_3, \quad \tilde{g}_1 \rightarrow i \frac{a_L}{4} \tilde{g}_2, \quad \tilde{g}_2 \rightarrow i \frac{a_L}{4} \tilde{g}_1, \quad \tilde{g}_3 \rightarrow i \frac{a_L}{4} \tilde{g}_0 \quad (\text{C.116})$$

in the POB-Hamiltonian. In this case the result may be obtained via partial integration, which yields

$$\mathbf{p}_{\alpha,L;\alpha',L'}(\mathbf{k}_\parallel) = \frac{m_0}{i\hbar} [(L' - L)\Delta + v_z^{\alpha'} - v_z^\alpha] H_{\alpha,L;\alpha',L'}(\mathbf{k}_\parallel). \quad (\text{C.117})$$

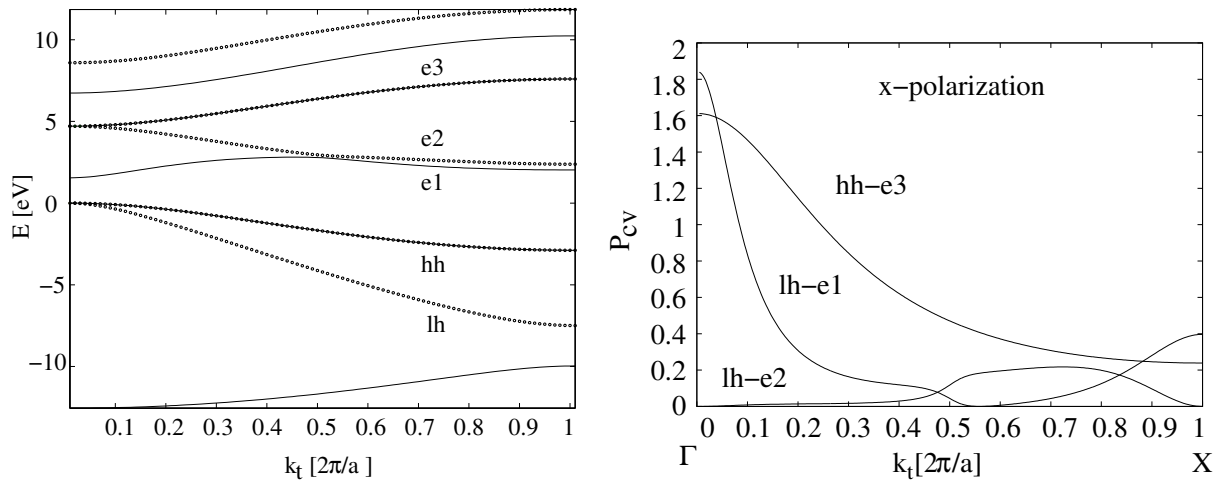


Figure C.6: Bulk band structure for the sp^3s^* model (left). Corresponding optical transition matrix elements.

Appendix D

Boundary self-energies for multiband models

To properly model the effect of semi-infinite bulk at the lead-device interface, the interface Green's function has to be linked to the propagating and evanescent states in the leads. The total electron wave function can be expressed in terms of the Bloch sum of the anion (a) and cation (c) states as a linear combination of planar orbitals $|\alpha, L, \mathbf{k}\rangle$ defined in (3.165) [238, 213],

$$|\Psi(\mathbf{k}, k_z)\rangle = \sum_{\alpha, L} C_{\alpha, L}(\mathbf{k}, k_z) |\alpha, L, \mathbf{k}\rangle \quad (\text{D.1})$$

$$= \sum_{\alpha} C_{\alpha}(\mathbf{k}, k_z) |\alpha, k_z\rangle, \quad (\text{D.2})$$

$$|\alpha, k_z\rangle = \frac{1}{\sqrt{N}} \sum_L e^{ik_z L} |\alpha, L, \mathbf{k}\rangle. \quad (\text{D.3})$$

In the planar orbital equation, projecting onto the atomic orbitals α' located at layer L , the Schrödinger equation for the Bloch function becomes

$$\sum_{\alpha} \langle \alpha', L, \mathbf{k} | \hat{H} | \alpha, k_z \rangle = 0, \quad (\text{D.4})$$

$$\langle \alpha', L, \mathbf{k} | \hat{H} | \alpha, k_z \rangle \equiv \langle \alpha', L, \mathbf{k} | \hat{H} | \alpha, k_z \rangle - E \langle \alpha', L, \mathbf{k} | \alpha, k_z \rangle. \quad (\text{D.5})$$

For a tight-binding Hamiltonian coupling m neighboring layers, which is of the form

$$\bar{H}(\mathbf{k}, k_z) = \sum_{\sigma=-m}^m \bar{H}^{\sigma}(\mathbf{k}) e^{i\sigma k_z \Delta}, \quad (\text{D.6})$$

where $\bar{H}^{\sigma}(\mathbf{k})$ represents a matrix which couples a given layer to the σ th neighboring layer and Δ is the layer spacing, and defining

$$C_{\alpha}^{\sigma} \equiv e^{i\sigma k_z \Delta} C_{\alpha}, \quad \sigma = -m, \dots, m, \quad (\text{D.7})$$

Eq. (D.5) can be written as

$$\sum_{\sigma=-m}^{m-1} \bar{H}^\sigma C^\sigma + \bar{H}^m e^{ik_z \Delta} C^{m-1} = 0, \quad (\text{D.8})$$

where it was used that $C^m = e^{ik_z \Delta} C^{m-1}$.

For a nearest neighbor Hamiltonian ($m = 1$), the projected Schrödinger equation is recast into

$$\bar{H}^{\sigma-1} C^{\sigma-1} + \bar{H}^\sigma C^\sigma + \bar{H}^{\sigma+1} C^{\sigma+1} = 0, \quad (\text{D.9})$$

which, using $C^{\sigma\pm 1} = e^{\pm ik_z \Delta} C^\sigma$, can be written as

$$\bar{H}^{\sigma-1} e^{-ik_z \Delta} C^\sigma + \bar{H}^\sigma C^\sigma + \bar{H}^{\sigma+1} e^{ik_z \Delta} C^\sigma = 0. \quad (\text{D.10})$$

This equation can then be transformed into an eigenequation for the propagation factors $\lambda = e^{ik_z \Delta}$ and the lead Bloch states in local orbital basis:

$$TC_L = \lambda C_L \equiv C_{L+1} \quad (\text{D.11})$$

where $C_L = \begin{pmatrix} C_a \\ C_c \end{pmatrix}$ and $T = T_c T_a$, where T_a and T_c are the atomic layer transfer matrices defined as

$$T_b = \begin{pmatrix} -[H_{l,l-1}^{(b)}]^{-1} [H_{l,l}^{(b)}] & -[H_{l,l-1}^{(b)}]^{-1} [H_{l,l+1}^{(b)}] \\ \mathbf{1} & \mathbf{0} \end{pmatrix}, \quad (b = a, c) \quad (\text{D.12})$$

with the matrix elements given by (l denotes the *atomic* layer)

$$H_{l,l-1,\alpha,\alpha'}^{(b)} = \langle \alpha, l, \mathbf{k} | H | \alpha', l-1, \mathbf{k} \rangle, \quad (\text{D.13})$$

$$H_{l,l,\alpha,\alpha'}^{(b)} = \langle \alpha, l, \mathbf{k} | H | \alpha', l, \mathbf{k} \rangle - E \delta_{\alpha,\alpha'}, \quad (\text{D.14})$$

$$H_{l,l+1,\alpha,\alpha'}^{(b)} = \langle \alpha, l, \mathbf{k} | H | \alpha', l+1, \mathbf{k} \rangle. \quad (\text{D.15})$$

The eigenstates χ and eigenvalues $\lambda = e^{ik_z \Delta}$ of Eq. (D.11) correspond to the bulk modes propagating (real k_z) or decaying (complex k_z) to the left ($\Im\{k_z\} < 0$) and to the right ($\Im\{k_z\} > 0$), respectively. For an N_b -band model with a two atom basis, there are $N_b/2$ states χ_ν propagating or decaying to the right ($\nu = +$) and to the left ($\nu = -$), respectively. At a given layer L , the components for left- and right travelling waves can be written as [248]

$$\mathbf{C}_{L\pm} = U_\pm \mathbf{C}_\pm, \quad (\text{D.16})$$

where \mathbf{C}_ν is a vector containing the expansion coefficients, and

$$U_+ = \left(\begin{array}{ccc|ccc} \chi_+^{(a)1} & \cdots & \chi_+^{(a)N_b/2} & & & \mathbf{0} \\ & & & \chi_+^{(c)1} & \cdots & \chi_+^{(c)N_b/2} \\ \hline & & \mathbf{0} & & & \end{array} \right). \quad (\text{D.17})$$

The corresponding expression for the adjacent layer $L + 1$ is

$$\mathbf{C}_{L+1\pm} = U_{\pm}\Lambda_z^{\pm 1}\mathbf{C}_{\pm}, \quad (\text{D.18})$$

with the propagation matrix

$$\Lambda_z = \left(\begin{array}{ccc|ccc} e^{k_z^1\Delta} & & 0 & & & \\ & \ddots & & & & \\ 0 & & e^{ik_z^{N_b/2}\Delta} & & \mathbf{0} & \\ \hline & & & e^{k_z^1\Delta} & & 0 \\ & \mathbf{0} & & & \ddots & \\ & & & 0 & & e^{ik_z^{N_b/2}\Delta} \end{array} \right) \quad (\text{D.19})$$

The relation between the two layers follows as

$$\mathbf{C}_{(L+1)\pm} = F_{\pm}\mathbf{C}_{L\pm} \quad (\text{D.20})$$

with

$$F_{\pm} = U_{\pm}\Lambda_z^{\pm 1}U_{\pm}^{-1}. \quad (\text{D.21})$$

Relation (D.20) can be used to derive the left-coupling retarded Green's function g^{lR} at the right boundary $l_z = 1$ of the uncoupled semi infinite left lead, i.e. for the case where all the couplings to the right are set to zero. The equation

$$[(E + i\eta)\mathbb{1} - H_0]g^{lR} = \mathbb{1} \quad (\text{D.22})$$

yields for the boundary element

$$[(E + i\eta)\mathbb{1} - D_1]g_{1;-1}^{lR} - t_{1;1}g_{0;1}^{lR} = 0. \quad (\text{D.23})$$

Eq. (D.20) provides the relation

$$g_{0;1}^{lR} = F_-^{-1}g_{1;1}^{lR}, \quad (\text{D.24})$$

which determines the left boundary lead Green's function in terms of the bulk modes as

$$g_{1;1}^{lR} = [E\mathbb{1} - D_1 - t_{1;0}F_-^{-1}]^{-1} \quad (\text{D.25})$$

$$\equiv [E\mathbb{1} - D_1 - \Sigma_{1;1}^{RB}]^{-1}, \quad (\text{D.26})$$

and providing thus an expression for the (left) retarded boundary self energy,

$$\Sigma_{1;1}^{RB} = -t_{1;0}(U_- \Lambda_z^{-1} U_-^{-1})^{-1}. \quad (\text{D.27})$$

The corresponding expression at the right boundary is

$$\Sigma_{N;N}^{RB} = -t_{N;N+1}U_+\Lambda_zU_+^{-1}. \quad (\text{D.28})$$

To evaluate the Keldysh equation (3.178) for the correlation functions G^{\lessgtr} , the boundary terms $\Sigma^{\lessgtr B}$ have to be determined. Under the assumption that the carriers in the contacts have an equilibrium Fermi distribution characterized by a chemical potential $\mu_{L,R}$, the fluctuation-dissipation theorem for the scattering functions yields

$$\Sigma_{i;i}^{<B} = if_{\mu_i}\Gamma_i^B, \quad \Sigma_{i;i}^{>B} = -i[1 - f_{\mu_i}]\Gamma_i^B, \quad (\text{D.29})$$

$$\Gamma_i^B = i[\Sigma_{i,i}^{RB} - (\Sigma^{RB})_{i,i}^\dagger], \quad (\text{D.30})$$

$$i = 1, N, \quad \mu_1 \equiv \mu_L, \mu_N \equiv \mu_R, \quad (\text{D.31})$$

where Γ^B denotes the broadening function of the contact, i.e. it quantifies the level broadening in the open system due to the connection to the reservoir.

Appendix E

Interaction self-energies

E.1 Introduction

In this appendix, the perturbative derivation of the interaction self-energies entering the Dyson's equations for the Green's functions is illustrated on the example of the generic interaction between fermionic and bosonic degree's of freedom applying to both carrier-photon and carrier-phonon interaction, with restriction to single particle operators for both types of particles and equilibrium averages in the case of the bosons.

E.2 Diagrammatic perturbation expansion

The interaction self-energies as defined by the Dyson equation (3.51) can be evaluated from the perturbation expansion of the nonequilibrium statistical average defining the interacting NEGF using either Wick's theorem or Feynman diagrams. In the first case, the (contour ordered) self energy Σ is derived from a perturbation expansion of the exponential in the definition of the contour ordered Green's function as the nonequilibrium expectation value of single-carrier operators,

$$G_{\alpha,L;\alpha',L'}(\mathbf{k}; t, t') \equiv -\frac{i}{\hbar} \langle \hat{T}_C \left\{ e^{-\frac{i}{\hbar} \int_C ds H'(s)} c_{\alpha,L,\mathbf{k}}(t) c_{\alpha',L',\mathbf{k}}^\dagger(t') \right\} \rangle \quad (\text{E.1})$$

which has the form of a Dyson equation. The diagrammatic version of the Dysons equation is shown in Fig. E.2.

In order to obtain the self-energies in the planar orbital basis, the Dyson equation is

rewritten as¹

$$G_{L;L'}(\mathbf{k}; t, t') = G_{L;L'}^0(\mathbf{k}; t, t') + \int_C ds \int_C ds' \sum_{L_1} \sum_{L_2} [G_{L;L_1}^0(\mathbf{k}; t, s) \Sigma_{L_1;L_2}(\mathbf{k}; s, s') G_{L_2;L'}^0(\mathbf{k}; s', t')], \quad (\text{E.2})$$

where G , G^0 and Σ correspond to the contour-ordered full and bare electron Green's functions and self-energy, respectively, with G^0 describing the unperturbed, solvable system. The real time self-energies $\Sigma^{\lessgtr, R, A}$ are then obtained by the Langreth relations.



Figure E.1: Diagrammatic Dyson equation for carrier Green's function.

E.3 Interactions of carriers with phonons and photons

The Hamiltonian for the interaction of carriers with bosons, e.g. phonons or photons, is of the form (in planar orbital basis)

$$\hat{H}_{cb}(t) = \sum_{L,L'} \sum_{\alpha,\alpha'} \sum_{\mathbf{k},\mathbf{q}} M_{\alpha,L;\alpha',L'}(\mathbf{k}, \mathbf{q}) \hat{c}_{\alpha,L,\mathbf{k}}^\dagger(t) \hat{c}_{\alpha',L',\mathbf{k}-\mathbf{q}}(t) [\hat{b}_{\mathbf{q}}(t) + \hat{b}_{-\mathbf{q}}^\dagger(t)], \quad (\text{E.3})$$

where $\hat{b}_{-\mathbf{q}}^\dagger$, $\hat{b}_{\mathbf{q}}$ are bosonic creation and annihilation operators, and the coupling element between fermions and bosons is contained in $M(\mathbf{k}, \mathbf{q})^2$. The contour ordered self energy is derived inserting the above Hamiltonian into the perturbation expansion (E.1), i.e. $\hat{H}'(s) = \hat{H}_{cb}(s)$. The first order contribution vanishes as it is proportional to $\langle \hat{b} \rangle = 0$ or $\langle \hat{b}^\dagger \rangle = 0$. For the second order contribution, one finds

$$\begin{aligned} G_{\alpha,L;\alpha',L'}^{(2)}(\mathbf{k}, t, t') &= \left(\frac{-i}{\hbar} \right)^3 \langle \hat{T}_C \int_C ds \int_C ds' \hat{H}_{cb}(s) \hat{H}_{cb}(s') \hat{c}_{\alpha,L,\mathbf{k}}(t) \hat{c}_{\alpha',L',\mathbf{k}}^\dagger(t') \rangle \\ &= \langle \hat{T}_C \int_C ds \int_C ds' \sum_{L_1, \dots, L_4} \sum_{\alpha_1, \dots, \alpha_4} \sum_{\mathbf{k}', \mathbf{k}''} \sum_{\mathbf{q}, \mathbf{q}'} M_{\alpha_1, L_1; \alpha_2, L_2}(\mathbf{k}', \mathbf{q}) \left\{ \hat{b}_{\mathbf{q}}(s) + \hat{b}_{-\mathbf{q}}^\dagger(s) \right\} \\ &\quad \times \hat{c}_{\alpha_1, L_1, \mathbf{k}'}^\dagger(s) \hat{c}_{\alpha_2, L_2, \mathbf{k}' - \mathbf{q}}(s) M_{\alpha_3, L_3; \alpha_4, L_4}(\mathbf{k}'', \mathbf{q}') \left\{ \hat{b}_{\mathbf{q}'}(s') + \hat{b}_{-\mathbf{q}'}^\dagger(s') \right\} \\ &\quad \times c_{\alpha_3, L_3, \mathbf{k}''}^\dagger(s') \hat{c}_{\alpha_4, L_4, \mathbf{k}'' - \mathbf{q}'}(s') \hat{c}_{\alpha, L, \mathbf{k}}(t) \hat{c}_{\alpha', L', \mathbf{k}}^\dagger(t') \rangle. \end{aligned} \quad (\text{E.4})$$

¹The orbital indices are suppressed, assuming the usual block matrix notation

²Note that \mathbf{k} is a 2D vector, while \mathbf{q} is a 3D-vector.

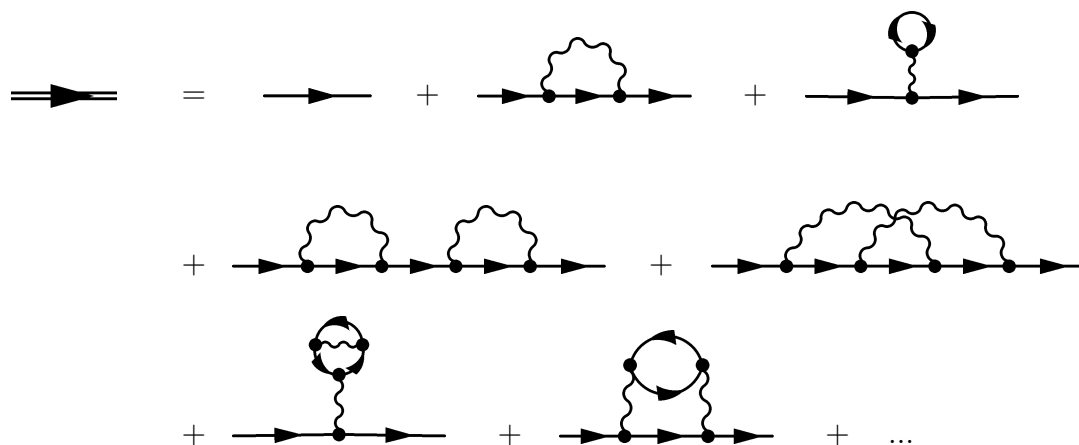


Figure E.3: Diagrammatic perturbation expansion of the full carrier Green's function

Diagrammatically, the self-energy is obtained as the sum of irreducible diagrams without external lines, as shown in Fig. E.4. For practical applications, the infinite sum has

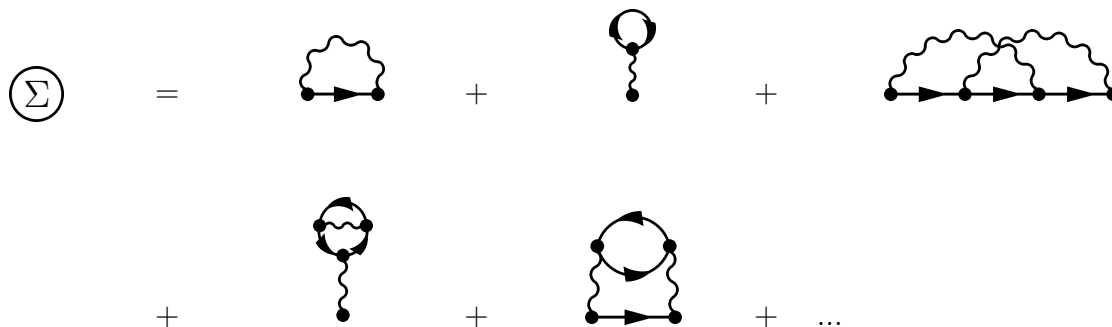


Figure E.4: Irreducible self energy diagrams

to be approximated. The first Born approximation to the perturbation expansion just neglects all higher order contributions. Including higher order terms into dressed first order diagrams corresponds to replacing the bare with the full Green's function, as shown in Fig. E.3, therefore leading to a self-consistent solution, as the Green's function both follows

$$\Sigma_{\text{SCBA}}^H = \text{[Hartree diagram]} , \quad \Sigma_{\text{SCBA}}^F = \text{[Fock diagram]}$$

Figure E.5: Hartree- and Fock diagrams of the self-consistent Born approximation to the interaction self-energy.

from and determines the self-energy. This approximation is called the self-consistent Born approximation (SCBA). The self-energy diagrams to lowest order in the interaction vertex are the Hartree- and Fock diagrams. The corresponding SCBA-diagrams are shown in Fig. E.3. Using Wick's theorem, the two nonvanishing contributions of lowest order are obtained by comparison, recalling the formal definition of the self energy in the Dyson equation,

$$\begin{aligned} G_{\alpha,L;\alpha',L'}^{(2)}(\mathbf{k}; t, t') &= \int_C ds \int_C ds' \sum_{L_1, \dots, L_4} \sum_{\alpha_1, \dots, \alpha_4} \left[- \sum_{\mathbf{k}, q_z} G_{\alpha,L;\alpha_1,L_1}^0(\mathbf{k}; t, s) M_{\alpha_1,L_1;\alpha_2,L_2}(\mathbf{k}, q_z) \right. \\ &\quad \times i\hbar D^0(q_z; s, s') G_{\alpha_4,L_4;\alpha_3,L_3}^{<0}(\mathbf{k}; s', s') M_{\alpha_3,L_3;\alpha_4,L_4}(\mathbf{k}, -q_z) G_{\alpha_2,L_2;\alpha',L'}^0(\mathbf{k}; s, t') \\ &\quad + \sum_{\mathbf{q}} G_{\alpha,L;\alpha_1,L_1}^0(\mathbf{k}; t, s) M_{\alpha_1,L_1;\alpha_2,L_2}(\mathbf{k}, \mathbf{q}) G_{\alpha_2,L_2;\alpha_3,L_3}^0(\mathbf{k} - \mathbf{q}_{\parallel}; s, s') \\ &\quad \left. \times i\hbar D^0(q; s, s') M_{\alpha_3,L_3;\alpha_4,L_4}(\mathbf{k} - \mathbf{q}_{\parallel}, -\mathbf{q}) G_{\alpha_4,L_4;\alpha',L'}^0(\mathbf{k}; s', t') \right] \quad (\text{E.6}) \end{aligned}$$

$$\begin{aligned} &\equiv \int_C ds \sum_{L_1} \sum_{L_2} \sum_{\alpha_1, \alpha_2} G_{\alpha,L;\alpha_1,L_1}^0(\mathbf{k}; t, s) \Sigma_{\alpha_1,L_1;\alpha_2,L_2}^H(s, s) G_{\alpha_2,L_2;\alpha',L'}^0(\mathbf{k}; s, t') \\ &\quad + \int_C ds \int_C ds' \sum_{L_1} \sum_{L_2} \sum_{\alpha_1, \alpha_2} G_{\alpha,L;\alpha_1,L_1}^0(\mathbf{k}; t, s) \\ &\quad \times \Sigma_{\alpha_1,L_1;\alpha_2,L_2}^F(\mathbf{k}; s, s') G_{\alpha_2,L_2;\alpha',L'}^0(\mathbf{k}; s', t') \quad (\text{E.7}) \end{aligned}$$

$$\begin{aligned} \Rightarrow \Sigma_{\alpha,L;\alpha',L'}^H(t, t) &= -i\hbar \sum_{\mathbf{k}, q_z} M_{\alpha,L;\alpha',L'}(\mathbf{k}, q_z) \sum_{L_1, L_2} \sum_{\alpha_1, \alpha_2} \int_C ds' D^0(q_z; t, s') \\ &\quad \times G_{\alpha_1,L_1;\alpha_2,L_2}^{<0}(\mathbf{k}; s', s') M_{\alpha_2,L_2;\alpha_1,L_1}(\mathbf{k}, -q_z), \quad (\text{E.8}) \end{aligned}$$

$$\begin{aligned} \Sigma_{\alpha,L;\alpha',L'}^F(\mathbf{k}; t, t') &= i\hbar \sum_{L_1, L_2} \sum_{\alpha_1, \alpha_2} \sum_{\mathbf{q}} M_{\alpha,L;\alpha_1,L_1}(\mathbf{k}, \mathbf{q}) D^0(\mathbf{q}; t, t') \\ &\quad \times G_{\alpha_1,L_1;\alpha_2,L_2}^0(\mathbf{k} - \mathbf{q}_{\parallel}; t, t') M_{\alpha_2,L_2;\alpha',L'}(\mathbf{k} - \mathbf{q}_{\parallel}, -\mathbf{q}). \quad (\text{E.9}) \end{aligned}$$

Again, in the SCBA, the bare carrier Green's functions are replaced by the full ones,

$$\Sigma_{L;L'}^H(t, t) = -i\hbar \sum_{\mathbf{k}, q_z} M_{L;L'}(\mathbf{k}, q_z) \int_C ds' D^0(q_z; t, s') \text{Tr} \{G^<(\mathbf{k}; s', s') M(\mathbf{k}, -q_z)\}, \quad (\text{E.10})$$

$$\Sigma_{L;L'}^F(\mathbf{k}; t, t') = i\hbar \sum_{L_1, L_2} \sum_{\mathbf{q}} M_{L;L_1}(\mathbf{k}, \mathbf{q}) D^0(\mathbf{q}; t, t') G_{L_1;L_2}(\mathbf{k} - \mathbf{q}_{\parallel}; t, t') M_{L_2;L'}(\mathbf{k} - \mathbf{q}_{\parallel}, -\mathbf{q}), \quad (\text{E.11})$$

where we have used block-matrix notation. Application of the Langreth theorem yields the real time Keldysh components

$$\Sigma_{L;L'}^{H, \lesseqgtr}(t, t) = -i\hbar \sum_{\mathbf{k}, q_z} M_{L;L'}(\mathbf{k}, q_z) \int_{-\infty}^{\infty} dt' D^{0\lesseqgtr}(0; t, t') \text{Tr} \{G^<(\mathbf{k}; t', t') M(\mathbf{k}, -q_z)\}, \quad (\text{E.12})$$

$$\Sigma_{L;L'}^{H, R}(t, t) = -i\hbar \sum_{\mathbf{k}, q_z} M_{L;L'}(\mathbf{k}, q_z) \int_{-\infty}^{\infty} dt' D^{0R}(0; t, t') \text{Tr} \{G^<(\mathbf{k}; t', t') M(\mathbf{k}, -q_z)\}, \quad (\text{E.13})$$

$$\Sigma_{L;L'}^{F, \lesseqgtr}(\mathbf{k}; t, t') = i\hbar \sum_{L_1, L_2} \sum_{\mathbf{q}} M_{L;L_1}(\mathbf{k}, \mathbf{q}) D^{0\lesseqgtr}(\mathbf{q}; t, t') G_{L_1;L_2}^{\lesseqgtr}(\mathbf{k} - \mathbf{q}_{\parallel}; t, t') M_{L_2;L'}(\mathbf{k} - \mathbf{q}, -\mathbf{q}), \quad (\text{E.14})$$

$$\begin{aligned} \Sigma_{L;L'}^{F, R}(\mathbf{k}; t, t') &= i\hbar \sum_{L_1, L_2} \sum_{\mathbf{q}} M_{L;L_1}(\mathbf{k}, \mathbf{q}) [D^{0R}(\mathbf{q}; t, t') G_{L;L'}^R(\mathbf{k} - \mathbf{q}_{\parallel}; t, t') \\ &\quad + D^{0R}(\mathbf{q}; t, t') G_{L;L'}^<(\mathbf{k} - \mathbf{q}_{\parallel}; t, t') + D^{0<}(\mathbf{q}; t, t') G_{L;L'}^R(\mathbf{k} - \mathbf{q}_{\parallel}; t, t')] \\ &\quad \times M_{L_2;L'}(\mathbf{k} - \mathbf{q}, -\mathbf{q}), \end{aligned} \quad (\text{E.15})$$

The Hartree term is time-independent. For steady state, where only time differences appear, it can be written as

$$\Sigma_{L;L'}^{H, R\lesseqgtr} = -i\hbar \sum_{\mathbf{k}, q_z} M_{L;L'}(\mathbf{k}, q_z) \int_{-\infty}^{\infty} dt' D^{0R, \lesseqgtr}(q_z; t') \text{Tr} \left\{ \int \frac{dE'}{2\pi\hbar} G^<(\mathbf{k}; E') M(\mathbf{k}, -q_z) \right\} \quad (\text{E.16})$$

$$= -i\hbar \sum_{\mathbf{k}, q_z} M_{L;L'}(\mathbf{k}, q_z) D^{0R, \lesseqgtr}(q_z; E = 0) \text{Tr} \left\{ \int \frac{dE'}{2\pi\hbar} G^<(\mathbf{k}; E') M(\mathbf{k}, -q_z) \right\}. \quad (\text{E.17})$$

The steady state Fourier transformation for the Fock term yields

$$\begin{aligned} \Sigma_{L;L'}^{F<}(\mathbf{k}; E) &= i\hbar \sum_{\mathbf{q}} \sum_{L_1, L_2} \int \frac{dE'}{2\pi\hbar} M_{L, L_1}(\mathbf{k}, \mathbf{q}) D^{0<}(\mathbf{q}; E') G_{L_1; L_2}^{<}(\mathbf{k} - \mathbf{q}_{\parallel}; E - E') \\ &\quad \times M_{L_2, L'}^{\dagger}(\mathbf{k} - \mathbf{q}, -\mathbf{q}), \end{aligned} \quad (\text{E.18})$$

$$\begin{aligned} \Sigma_{L;L'}^{FR}(\mathbf{k}; E) &= i\hbar \sum_{\mathbf{q}} \sum_{L_1, L_2} \int \frac{dE'}{2\pi\hbar} M_{L, L_1}(\mathbf{k}, \mathbf{q}) [D^{0R}(\mathbf{q}; E') G_{L_1; L_2}^R(\mathbf{k} - \mathbf{q}_{\parallel}; E - E') \\ &\quad + D^{0R}(\mathbf{q}; E') G_{L_1; L_2}^{<}(\mathbf{k} - \mathbf{q}_{\parallel}; E - E') + D^{0<}(\mathbf{q}; E') G_{L_1; L_2}^R(\mathbf{k} - \mathbf{q}_{\parallel}; E - E')] \\ &\quad \times M_{L_2, L'}(\mathbf{k} - \mathbf{q}, -\mathbf{q}), \end{aligned} \quad (\text{E.19})$$

The equilibrium expressions for the boson propagators are

$$D^{0\leq}(\mathbf{q}, t) = -\frac{i}{\hbar} [(N_{\mathbf{q}} + 1)e^{\pm i\omega_{\mathbf{q}}t} + N_{\mathbf{q}}e^{\mp i\omega_{\mathbf{q}}t}], \quad (\text{E.20})$$

$$D^{0R,A}(\mathbf{q}, t) = \mp \frac{2}{\hbar} \theta(\pm t) \sin(\omega_{\mathbf{q}}t). \quad (\text{E.21})$$

Fourier-transforming to energy-dependent quantities yields

$$D^{0\leq}(\mathbf{q}, E) = -2\pi i [N_{\mathbf{q}}\delta(E \mp \hbar\omega_{\mathbf{q}}) + (N_{\mathbf{q}} + 1)\delta(E \pm \hbar\omega_{\mathbf{q}})], \quad (\text{E.22})$$

$$D^{0R,A}(\mathbf{q}, E) = \frac{1}{E - \hbar\omega_{\mathbf{q}} \pm i\eta} - \frac{1}{E + \hbar\omega_{\mathbf{q}} \pm i\eta}, \quad (\text{E.23})$$

and, especially,

$$D^{0\leq}(\mathbf{q}, E = 0) = 0, \quad D^{0R,A}(\mathbf{q}, E = 0) = -\frac{2}{\hbar\omega_{\mathbf{q}}}. \quad (\text{E.24})$$

Inserting Eq. (E.23) for the free boson propagator, and applying the Cauchy principal value theorem (Eq. (3.102)) for the energy integration, the self-energies become (in full

matrix form)

$$\Sigma^{H\lessgtr} = 0, \quad \Sigma^{HR} = i\hbar \sum_{\mathbf{k}, q_z} \frac{2}{\hbar\omega_{\mathbf{q}=(0, q_z)}} M_{L;L'}(\mathbf{k}, q_z) \text{Tr} \left\{ \int \frac{dE'}{2\pi} G^<(\mathbf{k}; E') M(\mathbf{k}, -q_z) \right\}. \quad (\text{E.25})$$

$$\begin{aligned} \Sigma^{F\lessgtr}(\mathbf{k}; E) &= \sum_{\mathbf{q}} M(\mathbf{k}, \mathbf{q}) \left[N_{\mathbf{q}} G^{\lessgtr}(\mathbf{k} - \mathbf{q}_{\parallel}; E \mp \hbar\omega_{\mathbf{q}}) + (N_{\mathbf{q}} + 1) G^{\lessgtr}(\mathbf{k} - \mathbf{q}_{\parallel}; E \pm \hbar\omega_{\mathbf{q}}) \right] \\ &\quad \times M(\mathbf{k} - \mathbf{q}, -\mathbf{q}), \end{aligned} \quad (\text{E.26})$$

$$\begin{aligned} \Sigma^{FR}(\mathbf{k}; E) &= \sum_{\mathbf{q}} M(\mathbf{k}, \mathbf{q}) \left[(N_{\mathbf{q}} + 1) G^R(\mathbf{k} - \mathbf{q}_{\parallel}; E - \hbar\omega_{\mathbf{q}}) + N_{\mathbf{q}} G^R(\mathbf{k} - \mathbf{q}_{\parallel}; E + \hbar\omega_{\mathbf{q}}) \right. \\ &\quad + \frac{1}{2} (G^<(\mathbf{k} - \mathbf{q}_{\parallel}; E - \hbar\omega_{\mathbf{q}}) - G^<(\mathbf{k} - \mathbf{q}_{\parallel}; E + \hbar\omega_{\mathbf{q}})) \\ &\quad \left. + i\mathcal{P} \left\{ \int \frac{dE'}{2\pi} \left(\frac{G^<(\mathbf{k} - \mathbf{q}_{\parallel}; E - E')}{E' - \hbar\omega_{\mathbf{q}}} - \frac{G^<(\mathbf{k} - \mathbf{q}_{\parallel}; E - E')}{E' + \hbar\omega_{\mathbf{q}}} \right) \right\} \right] M(\mathbf{k} - \mathbf{q}, -\mathbf{q}) \end{aligned} \quad (\text{E.27})$$

$$\begin{aligned} &= \sum_{\mathbf{q}} M(\mathbf{k}, \mathbf{q}) \left[N_{\mathbf{q}} G^R(\mathbf{k} - \mathbf{q}_{\parallel}; E - \hbar\omega_{\mathbf{q}}) + (N_{\mathbf{q}} + 1) G^R(\mathbf{k} - \mathbf{q}_{\parallel}; E + \hbar\omega_{\mathbf{q}}) \right. \\ &\quad + \frac{1}{2} (G^>(\mathbf{k} - \mathbf{q}_{\parallel}; E - \hbar\omega_{\mathbf{q}}) - G^>(\mathbf{k} - \mathbf{q}_{\parallel}; E + \hbar\omega_{\mathbf{q}})) \\ &\quad \left. + i\mathcal{P} \left\{ \int \frac{dE'}{2\pi} \left(\frac{G^>(\mathbf{k} - \mathbf{q}_{\parallel}; E - E')}{E' - \hbar\omega_{\mathbf{q}}} - \frac{G^>(\mathbf{k} - \mathbf{q}_{\parallel}; E - E')}{E' + \hbar\omega_{\mathbf{q}}} \right) \right\} \right] M(\mathbf{k} - \mathbf{q}, -\mathbf{q}), \end{aligned} \quad (\text{E.28})$$

$$\begin{aligned} \Sigma^{FA}(\mathbf{k}; E) &= \sum_{\mathbf{q}} M(\mathbf{k}, \mathbf{q}) \left[(N_{\mathbf{q}} + 1) G^A(\mathbf{k} - \mathbf{q}_{\parallel}; E - \hbar\omega_{\mathbf{q}}) + N_{\mathbf{q}} G^A(\mathbf{k} - \mathbf{q}_{\parallel}; E + \hbar\omega_{\mathbf{q}}) \right. \\ &\quad + \frac{1}{2} (G^<(\mathbf{k} - \mathbf{q}_{\parallel}; E + \hbar\omega_{\mathbf{q}}) - G^<(\mathbf{k} - \mathbf{q}_{\parallel}; E - \hbar\omega_{\mathbf{q}})) \\ &\quad \left. + i\mathcal{P} \left\{ \int \frac{dE'}{2\pi} \left(\frac{G^<(\mathbf{k} - \mathbf{q}_{\parallel}; E - E')}{E' - \hbar\omega_{\mathbf{q}}} - \frac{G^<(\mathbf{k} - \mathbf{q}_{\parallel}; E - E')}{E' + \hbar\omega_{\mathbf{q}}} \right) \right\} \right] M(\mathbf{k} - \mathbf{q}, -\mathbf{q}). \end{aligned} \quad (\text{E.29})$$

Eq. (E.28) was written to obtain a form of the retarded self energy containing only the retarded Green's G^R function and the hole correlation function $G^<$, which is used to treat the processes in the valence band, while (E.27) is used for the conduction band.

Appendix F

The electrostatic problem

F.1 Introduction

QWSC are based on bipolar *p-i-n*-structures, where the doping difference between the contacts produces a built-in electric field that is used to separate the different species of photogenerated carriers. Near equilibrium, the resulting potential profile is well described by the depletion approximation. At larger bias, this is no longer true due to significant charge accumulation in the quantum wells located in the intrinsic region. To consider the resulting modification of the built-in potential and electric field, which significantly affects the shape of the local density of states and the location and width of the confinement levels, the Poisson equation has to be solved selfconsistently together with the equations that provide the carrier densities.

F.2 Poisson's equation for bipolar structures

At finite lattice temperature T , the density of ionized donors and acceptors is given by

$$N_T(z) = N_D^+(z) - N_A^-(z), \tag{F.1}$$

$$N_D^+(z) = N_D(z) \left\{ 1 - \left[\exp\left(\frac{\epsilon_A - \epsilon_F}{k_B T}\right) + 1 \right] \right\}, \quad N_A^-(z) = N_A(z) \left[\exp\left(\frac{\epsilon_A - \epsilon_F}{k_B T}\right) + 1 \right], \tag{F.2}$$

where $\epsilon_{D,A}$ are the donor and acceptor binding energies, respectively, and the Fermi energy is given by $\epsilon_F = \mu - U(1)$ where $U(1)$ is a correction shift due to the adjustment of the built-in potential to ensure local charge neutrality $n - p + N_A - N_D = 0$ in the bulk contact. The one dimensional Poisson equation for a dispersive medium with dielectric constant $\epsilon(z)$,

carrier densities $n(z)$, $p(z)$, doping profile $N_T(z)$ and one dimensional Hartree potential $U(z)$ is given by

$$\epsilon_0 \frac{\partial}{\partial z} \left[\epsilon(z) \frac{\partial}{\partial z} U(z) \right] = n(z) - p(z) - N(z). \quad (\text{F.3})$$

As the discretization of the system is determined by the atomic positions, a finite difference scheme is applied. The resulting linear system is converted into a nonlinear equation containing only the Hartree potential by writing the densities in terms of this potential and an additional quasi-Fermi-level E_{F_p} , $\rho = n, p$, which is found via equating the carrier densities from the NEGF to the expression for the equilibrium bulk density ρ_b ,

$$n[G^<] = n_b[F_n] = \mathcal{N}_C \mathcal{F}_{\frac{1}{2}} \left(\frac{E_{F_n} - E_C - U}{k_B T} \right), \quad (\text{F.4})$$

$$p[G^>] = p_b[F_p] = \mathcal{N}_V \mathcal{F}_{\frac{1}{2}} \left(\frac{E_V + U - E_{F_p}}{k_B T} \right), \quad (\text{F.5})$$

where

$$\mathcal{N}_C = 2 \left(\frac{m_C^* e k_B T}{2\pi \hbar^2} \right)^{\frac{3}{2}}, \quad \mathcal{N}_V = 2 \left(\frac{m_V^* e k_B T}{2\pi \hbar^2} \right)^{\frac{3}{2}}, \quad (\text{F.6})$$

are the effective densities of states for the conduction band and the valence band, respectively, and

$$\mathcal{F}_j(x) = \frac{1}{\Gamma(j+1)} \int_0^\infty \frac{t^j}{\exp(t-x) + 1} dt \quad (\text{F.7})$$

is the Fermi-Dirac integral of order j . The nonlinear equations for the quasi-Fermi potentials are solved with a Newton algorithm.

The nonlinear problem resulting for the Poisson equation is discretized using a first order finite difference scheme with the atomic spacing Δ as spatial resolution:

$$[U_{i+1}\epsilon_i^+ - U_i(\epsilon_i^+ + \epsilon_i^-) + U_{i-1}\epsilon_i^-] \frac{1}{\Delta^2} - e^2(N_i - n_i + p_i) = 0, \quad (\text{F.8})$$

where $\epsilon_i^+ = \epsilon_0(\epsilon_{i+1} + \epsilon_i)/2$ and $\epsilon_i^- = \epsilon_0(\epsilon_i + \epsilon_{i-1})/2$. The global charge neutrality condition corresponds to a vanishing derivative of the potential at the boundaries,

$$\frac{\partial U}{\partial z} \Big|_{i_z=0} = \frac{\partial U}{\partial z} \Big|_{i_z=N_p} \equiv 0, \quad (\text{F.9})$$

which is equivalent to a vanishing field or open boundary condition. In finite difference form, the boundary conditions read

$$\epsilon_1^+(U_2 - U_1), \quad \epsilon_{N_p}^-(U_{N_p-1} - U_{N_p}). \quad (\text{F.10})$$

The discrete version of Eq.(F.3) can thus be written as

$$P \cdot U + N - n + p = 0, \quad (\text{F.11})$$

whith

$$P = \begin{pmatrix} -\epsilon_1^+ & \epsilon_1^+ & 0 & \dots & 0 \\ \epsilon_2^- & -(\epsilon_2^+ + \epsilon_2^-) & \epsilon_2^+ & \ddots & \vdots \\ 0 & \ddots & \ddots & \ddots & 0 \\ \vdots & \ddots & \epsilon_{N_p-1}^- & -(\epsilon_{N_p-1}^+ + \epsilon_{N_p-1}^-) & \epsilon_{N_p-1}^+ \\ 0 & \dots & 0 & \epsilon_{N_p}^- & -\epsilon_{N_p}^+ \end{pmatrix} \quad (\text{F.12})$$

Eq. (F.11) is then solved using a *Newton-Raphson* method, providing the update to U . If the nonlinear system is written as $\mathbf{f}(\mathbf{U}) = \mathbf{0}$, the linearized equation to solve in the iterative Newton procedure is

$$\mathbf{J}(\mathbf{U}^m) \cdot \delta \mathbf{U}^{m+1} = -\mathbf{f}(\mathbf{U}^m) \quad \Rightarrow \quad \mathbf{U}^{m+1} = \mathbf{U}^m + \delta \mathbf{U}^{m+1}, \quad (\text{F.13})$$

where

$$J_{ij}(U^m) = \frac{\partial f_i(U^m)}{\partial U_j^m} \quad (\text{F.14})$$

are the elements of the Jacobian matrix. In the calculation of these elements, the derivatives of the densities are determined within the semiclassical bulk approximation,

$$\frac{\partial n_i(U)}{\partial U_j} \approx \frac{\partial n_{b,i}(U)}{\partial U_j} = \delta_{i,j} \frac{\mathcal{N}_C}{k_B T} \mathcal{F}_{-\frac{1}{2}} \left(\frac{E_{F_n,i} - E_{C,i} - U_i}{k_B T} \right), \quad (\text{F.15})$$

$$\frac{\partial p_i(U)}{\partial U_j} \approx \frac{\partial p_{b,i}(U)}{\partial U_j} = -\delta_{i,j} \frac{\mathcal{N}_V}{k_B T} \mathcal{F}_{-\frac{1}{2}} \left(\frac{E_{V,i} + U_i - E_{F_p,i}}{k_B T} \right). \quad (\text{F.16})$$

This approximation is crucial, since for the exact derivative, the system becomes singular under the imposition of open boundary conditions (F.9).

After each step of the iteration, the density is recalculated solving the steady state equations for the NEGF with the new Hartree potential. This procedure is very efficient, converging in less then ten steps at arbitrary bias voltage.

The discretized field \mathcal{E} corresponding to the potential calculated above is defined on the intercalated sites defined by

$$z_{i'} = \frac{1}{2}(z_{i+1} + z_i) \equiv z_i^+. \quad (\text{F.17})$$

The macroscopic quantity that is continuous across the dielectric multilayer formed by the multi-quantum-well system is not the electric field \mathcal{E} , but the electric *displacement* [254] $\mathcal{D} = \epsilon \mathcal{E}$, which has the discrete values

$$\mathcal{D}_{i'} \equiv \mathcal{D}_i^+ = \frac{\epsilon_i^+}{\Delta}(U_{i+1} - U_i), \mathcal{D}_{i'-1} \equiv \mathcal{D}_i^-, \quad \mathcal{D}_i = \frac{1}{2}(\mathcal{D}_i^+ + \mathcal{D}_i^-). \quad (\text{F.18})$$

Bibliography

- [1] P. Würfel, *Physics of Solar Cells*, Wiley-VCH, 2005.
- [2] M. A. Green, *Prog. Photovolt: Res. Appl.* **9**, 123 (2001).
- [3] W. Shockley and W. T. Read, *Phys. Rev.* **87**, 835 (1952).
- [4] R. Hall, *Phys. Rev.* **87**, 387 (1952).
- [5] A. Beattie and P. Landsberg, *Proc. R. Soc. London, Ser. A* **249**, 16 (1959).
- [6] J. Nelson, *The physics of solar cells*, Imperial College Press, 2003.
- [7] F. Herrmann and P. Würfel, *Am. J. Phys.* **74**, 591 (2006).
- [8] M. Green, *IEEE Trans. Electron Devices* **31**, 671 (1984).
- [9] T. Tiedje, E. Yablonovitch, G. Cody, and B. Brooks, *IEEE Trans. Electron Devices* **31**, 711 (1984).
- [10] W. Shockley and H. J. Queisser, *J. Appl. Phys.* **32**, 510 (1961).
- [11] K. Barnham and G. Duggan, *J. Appl. Phys.* **67**, 3490 (1990).
- [12] F. Bosgraaf, <http://www.vicphysics.org/documents/events/stav2005/spectrum.jpg>.
- [13] P. R. Griffin et al., *J. Appl. Phys.* **80**, 5815 (1996).
- [14] N. J. Ekins-Daukes, *An investigation into the efficiency of strained and strain-balanced quantum well solar cells*, PhD thesis, Imperial College, 1999.
- [15] N. J. Ekins-Daukes et al., *Appl. Phys. Lett.* **75**, 4195 (1999).
- [16] N. J. Ekins-Daukes et al., *Sol. Energy Mater. Sol. Cells* **68**, 71 (2001).
- [17] N. J. Ekins-Daukes et al., *Physica E* **14**, 132 (2002).

- [18] N. J. Ekins-Daukes, K. Kawaguchi, and J. Zhang, *Cryst. Growth Des.* **2**, 287 (2002).
- [19] B. G. Kluftinger, *An experimental study of the quasi-Fermi level separations in quantum well solar cells*, PhD thesis, Imperial College, London, 2000.
- [20] A. Larsson, P. Andrekson, S. Eng, and A. Yariv, *IEEE J. Quantum Electron.* **24**, 787 (1988).
- [21] S. Schmitt-Rink, D. S. Chemla, and D. A. B. Miller, *Adv. Phys.* **38**, 89 (1989).
- [22] M. Whitehead et al., *Appl. Phys. Lett.* **53**, 956 (1988).
- [23] K. W. J. Barnham et al., *Appl. Phys. Lett.* **59**, 135 (1991).
- [24] D. Bushnell et al., Light-trapping structures for multi-quantum well solar cells, in *Conference Record of the Twenty-Ninth IEEE Photovoltaic Specialists Conference*, pages 1035–1038, 2002.
- [25] D. Johnson et al., Optimisation of photon recycling effects in strain-balanced quantum well solar cells, in *Proc. 4th World Conference on Photovoltaic Energy Conversion, Hawaii*, 2006.
- [26] D. C. Johnson et al., *Appl. Phys. Lett.* **90**, 213505 (2007).
- [27] M. Islam et al., *Appl. Phys. Lett.* **50**, 1098 (1987).
- [28] G. Bastard, E. E. Mendez, L. L. Chang, and L. Esaki, *Phys. Rev. B* **28**, 3241 (1983).
- [29] I. Serdiukova, C. Monier, M. F. Vilela, and A. Freundlich, *Appl. Phys. Lett.* **74**, 2812 (1999).
- [30] C. Monier et al., *J. Vac. Sci. Technol. B* **17**, 1158 (1999).
- [31] S. C. McFarlane et al., *J. Appl. Phys.* **86**, 5109 (1999).
- [32] A. Fox, D. Miller, G. Livescu, J. Cunningham, and W. Jan, *IEEE J. Quantum Electron.* **27**, 2281 (1991).
- [33] H. Schneider and K. v. Klitzing, *Phys. Rev. B* **38**, 6160 (1988).
- [34] J. Nelson, M. Paxman, K. W. J. Barnham, J. Roberts, and C. Button, *IEEE J. Quantum Electron.* **29**, 1460 (1993).
- [35] G. Thucydides et al., *Semicond. Sci. Technol.* **11**, 331 (1996).

- [36] J. Barnes et al., J. Appl. Phys. **81**, 892 (1997).
- [37] A. Zachariou et al., J. Appl. Phys. **83**, 881 (1998).
- [38] G. Thucydides et al., Semicond. Sci. Technol. **12**, 35 (1997).
- [39] O. Y. Raisky, W. B. Wang, R. R. Alfano, C. L. Reynolds Jr., and V. Swaminathan, J. Appl. Phys **81**, 339 (1997).
- [40] O. Y. Raisky et al., J. Appl. Phys. **84**, 5790 (1998).
- [41] O. Y. Raisky et al., Appl. Phys. Lett. **74**, 129 (1999).
- [42] O. Y. Raisky, W. B. Wang, R. R. Alfano, and C. L. Reynolds Jr., Appl. Phys. Lett. **79**, 430 (2001).
- [43] A. Alemu, J. A. H. Coaquira, and A. Freundlich, J. Appl. Phys. **99**, 084506 (2006).
- [44] Y. Yazawa, T. Kitatani, J. Minemura, K. Tamura, and T. Warabisako, Carrier generation and transport in InGaAs/GaAs multiple quantum well solar cells, in *Conference Record of the Twenty Fourth. IEEE Photovoltaic Specialists Conference*, volume 2, pages 1878–1881, 1994.
- [45] J. M. Mohaidat, K. Shum, W. B. Wang, and R. R. Alfano, J. Appl. Phys. **76**, 5533 (1994).
- [46] C. Rohr, *InGaAsP Quantum Well Cells for Thermophotovoltaic Applications*, PhD thesis, Imperial College, 2000.
- [47] J. P. Connolly and C. Rohr, Semicond. Sci. Technol. **18**, S216 (2003).
- [48] J. A. Brum and G. Bastard, Phys. Rev. B **33**, 1420 (1986).
- [49] S. Morin, B. Deveaud, F. Clerot, K. Fujiwara, and K. Mitsunaga, IEEE J. Quantum Electron. **27**, 1669 (1991).
- [50] P. W. M. Blom, C. Smit, J. E. M. Haverkort, and J. H. Wolter, Phys. Rev. B **47**, 2072 (1993).
- [51] M. Abou-Khalil, M. Goano, A. Champagne, and R. Maciejko, IEEE Photonics Technol. Lett. **8**, 19 (1996).
- [52] M. Gurioli et al., Phys. Rev. B **44**, 3115 (1991).
- [53] E. O. Göbel, H. Jung, J. Kuhl, and K. Ploog, Phys. Rev. Lett. **51**, 1588 (1983).

- [54] J. Feldmann et al., Phys. Rev. Lett. **59**, 2337 (1987).
- [55] T. Matsusue and H. Sakaki, Appl. Phys. Lett. **50**, 1429 (1987).
- [56] E. E. Mendez et al., Phys. Rev. B **26**, 7101 (1982).
- [57] H. J. Polland, L. Schultheis, J. Kuhl, E. O. Göbel, and C. W. Tu, Phys. Rev. Lett. **55**, 2610 (1985).
- [58] M. G. Shorthose et al., Appl. Phys. Lett. **51**, 493 (1987).
- [59] J. Nelson et al., J. Appl. Phys **86**, 5898 (1999).
- [60] E. Yablonovitch and E. Kane, J. Lightwave Technol. **4**, 504 (1986).
- [61] J. Nelson et al., J. Appl. Phys. **82**, 6240 (1997).
- [62] K. Barnham et al., J. Appl. Phys. **80**, 1201 (1996).
- [63] K. Barnham, Recent results on quantum well solar cells, in *Proc. 3rd World Conference on Photovoltaic Energy Conversion*, page 606, 2003.
- [64] K. Barnham et al., Observation of ideal dark-current behaviour in strain-balanced quantum well solar cells, in *Proc. 19th European Photovoltaic Solar Energy Conference, Paris, France, 2004*.
- [65] J. Connolly et al., Efficiency limits of quantum well solar cells, in *Proc. 9th European Photovoltaic Solar Energy Conference, Paris, France, 2004*.
- [66] D. B. Bushnell et al., Effect of barrier composition and well number on the dark current of quantum well solar cells, in *Proc. 3rd World Conference on Photovoltaic Energy Conversion*, page 2709, 2003.
- [67] D. B. Bushnell et al., J. Appl. Phys. **97**, 124908 (2005).
- [68] M. Lynch et al., J. Mater. Sci. **40**, 1445 (2005).
- [69] G. Haarpaintner et al., Voltage performance of quantum well solar cells in the $\text{Al}_x\text{Ga}_{1-x}\text{As}/\text{GaAs}$ and the $\text{InAs}/\text{In}_y\text{Ga}_{1-y}\text{As}$ Material Systems, in *Proc. 1st World Conference on Photovoltaic Solar Energy Conversion*, page 1783, 1994.
- [70] N. G. Anderson and S. J. Wojtczuk, J. Appl. Phys. **79**, 1978 (1996).
- [71] N. Anderson, Physica E **14**, 126 (2002).

- [72] G. Araújo, A. Martí, F. Ragay, and J. Wolter, Efficiency of multiple quantum well solar cells, in *Proc. 12th European Photovoltaic Solar Energy Conference*, page 1481, 1994.
- [73] G. L. Araújo and A. Martí, *Sol. Energy Mater. Sol. Cells* **33**, 213 (1994).
- [74] G. L. Araújo and A. Martí, *Appl. Phys. Lett.* **66**, 894 (1995).
- [75] E. Tsui, J. Nelson, K. Barnham, C. Button, and J. S. Roberts, *J. Appl. Phys.* **80**, 4599 (1996).
- [76] K. W. J. Barnham et al., *J. Mater. Sci.: Mater. Electron.* **11**, 531 (2000).
- [77] B. Klüftinger, K. Barnham, J. Nelson, T. Foxon, and T. Cheng, *Microelectron. Eng.* **51-52**, 265 (2000).
- [78] B. Klüftinger, K. Barnham, J. Nelson, T. Foxon, and T. Cheng, *Sol. Energy Mater. Sol. Cells* **66**, 501 (2001).
- [79] S. Kettemann and J. Guillemoles, in *Proceedings of the 13th European Photovoltaic Solar Energy Conference*, 1995.
- [80] S. Bremner, R. Corkish, and C. Honsberg, *IEEE Trans. Electron Devices* **46**, 1932 (1999).
- [81] C. Honsberg, S. Bremner, and R. Corkish, *Physica E* **14**, 136 (2002).
- [82] A. Luque, A. Martí, and L. Cuadra, *IEEE Trans. Electron Devices* **48**, 2118 (2001).
- [83] N. J. Ekins-Daukes, Quantum well and bulk quasi Fermi level behaviour under illuminated conditions, in *Proc. 3rd World Conference on Photovoltaic Energy Conversion*, page 2702, 2003.
- [84] M. Mazzer et al., The use of III-V quantum heterostructures in PV: thermodynamic issues, in *Proc. 3rd World Conference on Photovoltaic Energy Conversion*, page 2661, 2003.
- [85] M. Mazzer et al., *Thin Solid Films* **511**, 76 (2006).
- [86] M. F. Führer et al., Quasi Fermi Level Splitting and Evidence for Hot Carrier Effects in Strain-Balanced Quantum Well Concentrator Solar Cells at High Bias, in *Proc. 21st European Photovoltaic Specialists Conference, Dresden*, 2006.

- [87] M. F. Führer et al., Quantitative study of hot carrier effects observed in strain-balanced quantum well solar cells, in *Proc. 22nd European Photovoltaic Solar Energy Conference, Milan, Italy, 2007*.
- [88] A. M. Fox, R. G. Ispasoiu, C. T. Foxon, J. E. Cunningham, and W. Y. Jan, *Appl. Phys. Lett.* **63**, 2917 (1993).
- [89] C. Henry, *J. Appl. Phys.* **51**, 4494 (1980).
- [90] R. Corkish and M. Green, Recombination of carriers in quantum well solar cells, in *Conference Record of the Twenty Third IEEE Photovoltaic Specialists Conference*, page 675, 1993.
- [91] N. Anderson, *J. Appl. Phys.* **78**, 1861 (1995).
- [92] M. Paxman et al., *J. Appl. Phys.* **74**, 614 (1993).
- [93] J. Nelson et al., Quantum well solar cell dark currents, in *Proc. 12th EU PVSEC*, 1994.
- [94] J. Connolly, *Modelling and Optimising GaAs/Al_xGa_{1-x}As Multiple Quantum Well Solar Cells*, PhD thesis, Imperial College, London, 1997.
- [95] J. P. Connolly et al., Simulating multiple quantum well solar cells, in *Proc. 28th IEEE Photovoltaic Specialists Conference*, page 1304, 2000.
- [96] G. Bastard and J. Brum, *IEEE J. Quantum Electron.* **22**, 1625 (1986).
- [97] R. Ramey and R. Khoie, *IEEE Trans. Electron Devices* **50**, 1179 (2003).
- [98] G. Lengyel, K. Jelley, and R. Engelmann, *IEEE J. Quantum Electron.* **26**, 296 (1990).
- [99] A. C. Varonides, *Physica E* **14**, 142 (2002).
- [100] R. Stratton, *Phys. Rev.* **126**, 2002 (1962).
- [101] K. Blotekjaer, *IEEE Trans. Electron Devices* **17**, 38 (1970).
- [102] T. Grasser, T.-W. Tang, H. Kosina, and S. Selberherr, *Proceedings of the IEEE* **91**, 251 (2003).
- [103] C. Gardner, *SIAM J. Appl. Math.* **54**, 409 (1994).
- [104] R. Pinnau, *Transport Theory and Statistical Physics*, 2002 (2001).

-
- [105] C. Gardner, G. Klimeck, and C. Ringhofer, *J. Comp. Electron.* **3**, 95 (2004).
- [106] T. Höhr, A. Schenk, A. Wettstein, and W. Fichtner, On density-gradient modeling of tunneling through insulators, in *Proc. of SISPAD 2002*, pages 275–278, 2002.
- [107] G. Bastard, *Phys. Rev. B* **24**, 5693 (1981).
- [108] G. Bastard, *Phys. Rev. B* **25**, 7584 (1982).
- [109] M. F. H. Schuurmans and G. W. t' Hooft, *Phys. Rev. B* **31**, 8041 (1985).
- [110] R. Eppenga, M. F. H. Schuurmans, and S. Colak, *Phys. Rev. B* **36**, 1554 (1987).
- [111] N. F. Johnson, H. Ehrenreich, P. M. Hui, and P. M. Young, *Phys. Rev. B* **41**, 3655 (1990).
- [112] C. Y.-P. Chao and S. L. Chuang, *Phys. Rev. B* **43**, 7027 (1991).
- [113] J. N. Schulman and Y.-C. Chang, *Phys. Rev. B* **27**, 2346 (1983).
- [114] Y.-C. Chang and J. N. Schulman, *Appl. Phys. Lett.* **43**, 536 (1983).
- [115] J. N. Schulman and Y.-C. Chang, *Phys. Rev. B* **31**, 2056 (1985).
- [116] J. Schulman, *J. Appl. Phys.* **60**, 3954 (1986).
- [117] Y.-C. Chang, *Phys. Rev. B* **37**, 8215 (1988).
- [118] B. Chen, M. Lazzouni, and L. R. Ram-Mohan, *Phys. Rev. B* **45**, 1204 (1992).
- [119] E. Anemogiannis, E. Glytsis, and T. Gaylord, *IEEE J. Quantum Electron.* **29**, 2731 (1993).
- [120] E. Anemogiannis, E. Glytsis, and T. Gaylord, *Microelectron. J.* **30**, 935 (1999).
- [121] C. Lent and D. Kirkner, *J. Appl. Phys.* **67**, 6353 (1990).
- [122] W. R. Frensley, *Rev. Mod. Phys.* **62**, 745 (1990).
- [123] D. Z. Y. Ting, E. T. Yu, and T. C. McGill, *Phys. Rev. B* **45**, 3583 (1992).
- [124] Y. X. Liu, D. Z. Y. Ting, and T. C. McGill, *Phys. Rev. B* **54**, 5675 (1996).
- [125] T. B. Boykin, *Phys. Rev. B* **54**, 7670 (1996).
- [126] T. B. Boykin, *Phys. Rev. B* **54**, 8107 (1996).

- [127] A. Ahland, D. Schulz, and E. Voges, *Phys. Rev. B* **60**, R5109 (1999).
- [128] S. Odermatt, M. Luisier, and B. Witzigmann, *J. Appl. Phys.* **97**, 046104 (2005).
- [129] C. Zheng, *J. Comput. Phys.* **227**, 527 (2007).
- [130] C. Cheng, J.-H. Lee, K. H. Lim, H. Z. Massoud, and Q. H. Liu, *J. Comput. Phys.* **227**, 455 (2007).
- [131] D. Mamaluy, M. Sabathil, and P. Vogl, *J. Appl. Phys.* **93**, 4628 (2003).
- [132] D. Mamaluy, D. Vasileska, M. Sabathil, T. Zibold, and P. Vogl, *Phys. Rev. B* **71**, 245321 (2005).
- [133] L. Lew Yan Voon and L. Ram-Mohan, *Phys. Rev. B* **47**, 15500 (1993).
- [134] M. Graf and P. Vogl, *Phys. Rev. B* **51**, 4940 (1995).
- [135] A. Di Carlo, S. Pescetelli, M. Paciotti, P. Lugli, and M. Graf, *Solid State Commun.* **98**, 803 (1996).
- [136] T. Boykin, *Phys. Rev. B* **60**, 15810 (1999).
- [137] T. B. Boykin, R. C. Bowen, and G. Klimeck, *Phys. Rev. B* **63**, 245314 (2001).
- [138] T. Sandu, *Phys. Rev. B* **72**, 125105 (2005).
- [139] W. Pötz, *J. Appl. Phys.* **66**, 2458 (1989).
- [140] L. R. Ram-Mohan, K. H. Yoo, and J. Moussa, *J. Appl. Phys.* **95**, 3081 (2004).
- [141] M. V. Fischetti, *J. Appl. Phys.* **83**, 270 (1998).
- [142] M. V. Fischetti, *Phys. Rev. B* **59**, 4901 (1999).
- [143] R. Landauer, *IBM J. Res. Develop.* **1**, 223 (1957).
- [144] M. Büttiker, *Phys. Rev. Lett.* **14**, 1761 (1986).
- [145] R. Landauer, *J. Phys.: Condens. Matter* **1**, 8099 (1989).
- [146] E. Wigner, *Phys. Rev.* **40**, 749 (1932).
- [147] P. Carruthers and F. Zachariasen, *Rev. Mod. Phys.* **55**, 245 (1983).
- [148] Mains and Haddad, *J. Comput. Phys.* **112**, 149 (1992).

- [149] P. Bordone et al., Phys. Rev. B **59**, 3060 (1999).
- [150] C. Jacoboni and P. Bordone, Rep. Prog. Phys. **67**, 1033 (2004).
- [151] M. Nedjalkov, H. Kosina, S. Selberherr, C. Ringhofer, and D. K. Ferry, Phys. Rev. B **70**, 115319 (2004).
- [152] N. C. Kluksdahl, A. M. Krizan, D. K. Ferry, and C. Ringhofer, Phys. Rev. B **39**, 7720 (1989).
- [153] L. Demeio, L. Barletti, A. Bertoni, P. Bordone, and C. Jacoboni, Physica B **314**, 104 (2002).
- [154] L. Demeio, P. Bordone, and C. Jacoboni, Semicond. Sci. Technol. **19**, S244 (2004).
- [155] D. Ferry and H. Grubin, Solid State Physics **49**, 283 (1995).
- [156] R. C. Iotti, E. Ciancio, and F. Rossi, Phys. Rev. B **72**, 125347 (2005).
- [157] W. R. Frensley, Phys. Rev. Lett. **57**, 2853 (1986).
- [158] W. R. Frensley, Phys. Rev. B **36**, 1570 (1987).
- [159] R. K. Mains and G. I. Haddad, J. Appl. Phys. **64**, 3564 (1988).
- [160] K. L. Jensen and F. A. Buot, J. Appl. Phys. **67**, 7602 (1990).
- [161] F. Rossi and T. Kuhn, Rev. Mod. Phys. **74**, 895 (2002).
- [162] R. C. Iotti and F. Rossi, Semicond. Sci. Technol. **19**, 323 (2004).
- [163] P. Weetman and M. S. Wartak, Phys. Rev. B **76**, 035332 (2007).
- [164] P. Weetman and M. S. Wartak, Phys. Status Solidi C **5**, 370 (2008).
- [165] P. C. Martin and J. Schwinger, Phys. Rev. **115**, 1342 (1959).
- [166] J. Schwinger, J. Math. Phys. **2**, 407 (1961).
- [167] L. P. Kadanoff and G. Baym, *Quantum Statistical Mechanics*, Benjamin-Cummings, 1995.
- [168] L. Keldysh, Sov. Phys.-JETP. **20**, 1018 (1965).
- [169] D. Langreth, in *Linear and Non-linear Electron Transport in solids* **17**, 3 (1976).

- [170] A. L. Fetter and J. D. Walecka, *Quantum theory of many-particle systems*, McGraw-Hill, San Francisco, 1971.
- [171] S. Datta, *Electronic Transport in Mesoscopic Systems*, Cambridge University Press, 1995.
- [172] R. Lake, G. Klimeck, R. Bowen, and D. Jovanovic, *J. Appl. Phys.* **81**, 7845 (1997).
- [173] M. Luisier, A. Schenk, W. Fichtner, and G. Klimeck, *Phys. Rev. B* **74**, 205323 (2006).
- [174] S. Jin, Y. J. Park, and H. S. Min, *J. Appl. Phys.* **99**, 123719 (2006).
- [175] L. E. Henrickson, A. J. Glick, G. W. Bryant, and D. F. Barbe, *Phys. Rev. B* **50**, 4482 (1994).
- [176] W. Tian et al., *J. Chem. Phys.* **109**, 2874 (1998).
- [177] Y. Xue, S. Datta, and M. A. Ratner, *J. Chem. Phys.* **115**, 4292 (2001).
- [178] M. Brandbyge, J.-L. Mozos, P. Ordejón, J. Taylor, and K. Stokbro, *Phys. Rev. B* **65**, 165401 (2002).
- [179] Y. Xue, S. Datta, and M. A. Ratner, *Chem. Phys.* **281**, 151 (2002).
- [180] A. D. Carlo, A. Pecchia, L. Latessa, T. Frauenheim, and G. Seifert, Tight-Binding DFT for Molecular Electronics (gDFTB), in *Lecture Notes in Physics*, volume 680, page 153, Springer, 2005.
- [181] K. Stokbro, J. Taylor, M. Brandbyge, and H. Guo, Ab-initio Non-Equilibrium Green's Function formalism for calculating electron transport in molecular devices, in *Lecture Notes in Physics*, Springer, 2005.
- [182] A. R. Rocha et al., *Phys. Rev. B* **73**, 085414 (2006).
- [183] K. S. Thygesen and A. Rubio, *Phys. Rev. B* **77**, 115333 (2008).
- [184] R. Lake and S. Datta, *Phys. Rev. B* **46**, 4757 (1992).
- [185] T. Frederiksen, Inelastic electron transport in nanosystems, Master's thesis, Technical University of Denmark, 2004.
- [186] A. Pecchia, G. Romano, and A. D. Carlo, *Phys. Rev. B* **75**, 035401 (2007).
- [187] J. T. Lü and J.-S. Wang, *Phys. Rev. B* **76**, 165418 (2007).

- [188] J.-S. Wang, N. Zeng, J. Wang, and C. K. Gan, *Phys. Rev. E* **75**, 061128 (2007).
- [189] A. Groshev, T. Ivanov, and V. Valtchinov, *Phys. Rev. Lett.* **66**, 1082 (1991).
- [190] L. Y. Chen and C. S. Ting, *Phys. Rev. B* **44**, 5916 (1991).
- [191] S. Hershfield, J. H. Davies, and J. W. Wilkins, *Phys. Rev. Lett.* **67**, 3720 (1991).
- [192] S. Hershfield, J. H. Davies, and J. W. Wilkins, *Phys. Rev. B* **46**, 7046 (1992).
- [193] Y. Meir, N. S. Wingreen, and P. A. Lee, *Phys. Rev. Lett.* **70**, 2601 (1993).
- [194] R. Binder and S. W. Koch, *Prog. Quantum Electron.* **19**, 307 (1995).
- [195] H. Haug and A. P. Jauho, *Quantum kinetics in transport and optics of semiconductors*, Springer, Berlin, 1996.
- [196] K. Hannewald, *Femtosecond Dynamics of Absorption and Luminescence in optically excited semiconductors: theory and simulation*, PhD thesis, Jena, 2001.
- [197] W. Schäfer and M. Wegener, *Semiconductor Optics and Transport Phenomena*, Springer, 2002.
- [198] H. Haug and S. W. Koch, *Quantum Theory of the Optical and Electronic Properties of Semiconductors*, World Scientific, 2004.
- [199] C. Caroli, R. Combescot, P. Nozières, and D. Saint-James, *J. Phys. C: Solid State Phys.* **4**, 916 (1971).
- [200] C. Caroli, R. Combescot, D. Lederer, P. Nozières, and D. Saint-James, *J. Phys. C: Solid State Phys.* **4**, 2598 (1971).
- [201] R. Combescot, *J. Phys. C: Solid State Phys.* **4**, 2611 (1971).
- [202] C. Caroli, R. Combescot, P. Nozières, and D. Saint-James, *J. Phys. C: Solid State Phys.* **5**, 21 (1972).
- [203] A. Svizhenko, M. P. Anantram, T. R. Govindan, B. Biegel, and R. Venugopal, *J. Appl. Phys.* **91**, 2343 (2002).
- [204] J. Guo and M. S. Lundstrom, *IEEE Trans. Electron Devices* **49**, 1897 (2002).
- [205] Z. Ren et al., *IEEE Trans. Electron Devices* **50**, 1914 (2003).

- [206] S. Jin, *Modeling of Quantum Transport in Nano-Scale MOSFET Devices*, PhD thesis, School of Electrical Engineering and Computer Science College of Engineering Seoul National University, 2006.
- [207] A. Martinez et al., *IEEE Trans. Electron Devices* **54**, 2213 (2007).
- [208] J. Guo, *J. Appl. Phys.* **98**, 063519 (2005).
- [209] M. Pourfath, H. Kosina, and S. Selberherr, *J. Phys: Conf. Ser.* **38**, 29 (2006).
- [210] G. Kim and G. B. Arnold, *Phys. Rev. B* **38**, 3252 (1988).
- [211] E. V. Anda and F. Flores, *J. Phys.: Condens. Matter.* **3**, 9087 (1991).
- [212] G. Kim, H.-H. Suh, and E.-H. Lee, *Phys. Rev. B* **52**, 2632 (1995).
- [213] M. Ogawa, T. Sugano, R. Tominaga, and T. Miyoshi, *Physica B* **272**, 167 (1999).
- [214] M. Ogawa and a. T. M. T. Sugano, *Solid-State Electron.* **44**, 1939 (2000).
- [215] C. Rivas et al., *Appl. Phys. Lett.* **78**, 814 (2001).
- [216] C. Rivas et al., *J. Appl. Phys.* **94**, 5005 (2003).
- [217] M. Pereira and K. Henneberger, *Phys. Rev. B* **53**, 16485 (1996).
- [218] S.-C. Lee and A. Wacker, *Phys. Rev. B* **66**, 245314 (2002).
- [219] L. E. Henrickson, *J. Appl. Phys* **91**, 6273 (2002).
- [220] D. A. Stewart and F. Leonard, *Phys. Rev. Lett.* **93**, 107401 (2004).
- [221] D. A. Stewart and F. Leonard, *Nano Lett.* **5**, 219 (2005).
- [222] J. Guo, M. A. Alam, and Y. Yoon, *Appl. Phys. Lett.* **88**, 133111 (2006).
- [223] F. Evers, F. Weigend, and M. Koentopp, *Phys. Rev. B* **69**, 235411 (2004).
- [224] A. Abrikosov, L. Gorkov, and I. Dzyaloshinski, *Methods of quantum field theory in statistical physics*, Dover Publ., New York, 1975.
- [225] G. D. Mahan, *Many-Particle Physics, 2nd ed.*, (Plenum, New York), 1990.
- [226] P. Danielewicz, *Ann. Phys.* **152**, 239 (1984).
- [227] J. Rammer and H. Smith, *Rev. Mod. Phys.* **58**, 323 (1986).

- [228] J. W. Wilkins, Phys. Rev. B **36**, 2578 (1987).
- [229] G. Mahan, Phys. Rep. **145**, 251 (1987).
- [230] M. Wagner, Phys. Rev. B **44**, 6104 (1991).
- [231] V. G. Morozov and G. Roepke, Ann. Phys. **278**, 127 (1999).
- [232] J. H. Davies, S. Hershfield, P. Hyldgaard, and J. W. Wilkins, Phys. Rev. B **47**, 4603 (1993).
- [233] S. Datta, J. Phys.: Condens. Matter **2**, 8023 (1990).
- [234] S. Datta, Superlattices Microstruct. **28**, 253 (2000).
- [235] R. Landauer, Phil. Mag. **21**, 863 (1970).
- [236] P. Vogl, H. Hjalmarsen, and J. Dow, J. Phys. Chem. Solids **44**, 365 (1983).
- [237] D. H. Lee and J. D. Joannopoulos, Phys. Rev. B **23**, 4988 (1981).
- [238] Y.-C. Chang and J. Schulman, Phys. Rev. B **25**, 3975 (1982).
- [239] J. A. Stovneng and P. Lipavsky, Phys. Rev. B **49**, 16 494 (1994).
- [240] A. Wacker, Phys. Rep. **357**, 1 (2002).
- [241] F. Guinea, C. Tejedor, F. Flores, and E. Louis, Phys. Rev. B **28**, 4397 (1983).
- [242] M. P. L. Sancho, J. M. L. Sancho, and J. Rubio, J. Phys. F: Met. Phys. **14**, 1205 (1984).
- [243] M. P. L. Sancho, J. M. L. Sancho, and J. Rubio, J. Phys. F: Met. Phys. **15**, 851 (1985).
- [244] A. Umerski, Phys. Rev. B **55**, 5266 (1997).
- [245] D. H. Lee and J. D. Joannopoulos, Phys. Rev. B **23**, 4997 (1981).
- [246] R. Bouwen, W. Frensley, G. Klimeck, and R. Lake, Phys. Rev. B **52**, 2754 (1995).
- [247] A. MacKinnon, Z. Phys. B - Condensed Matter **59**, 385 (1985).
- [248] T. Ando, Phys. Rev. B **44**, 8017 (1991).
- [249] C. Hamaguchi, *Basic Semiconductor Physics*, Springer, 2001.

-
- [250] R. K. Lake and R. R. Pandey, Non-Equilibrium Green Functions in Electronic Device Modeling, in *Handbook of Semiconductor Nanostructures*, edited by A. A. Balandin and K. L. Wang, American Scientific Publishers, 2006.
- [251] Y. Meir and N. Wingreen, Phys. Rev. Lett. **68**, 2512 (1992).
- [252] S. Datta, *Quantum Transport*, Cambridge University Press, 2005.
- [253] P. Loewdin, J. Chem. Phys. **19**, 1396 (1951).
- [254] J. Jackson, *Classical Electrodynamics*, John Wiley & Sons, 1998.

List of publications

Journal papers (peer reviewed)

- U. Aeberhard and R.H. Morf,
Microscopic non-equilibrium theory of quantum well solar cells,
Phys. Rev. B **77**, 125343 (2008)
- U. Aeberhard, K. Wakabayashi and M. Sigrist,
Effect of spin-orbit coupling on zero-conductance resonances in asymmetrically coupled one-dimensional rings,
Phys. Rev. B **72**, 075328 (2005)

Conference proceedings (peer reviewed)

- U. Aeberhard and R.H. Morf,
Microscopic Theory of Coupled Quantum Well Structures in Photovoltaics,
in 'Proc. of the 2008 MRS Spring Meeting, Symposium KK', 1101-KK07-02 (2008)
- U. Aeberhard and R.H. Morf,
Microscopic Modelling of Quantum Well Solar Cells,
in 'Simulation of Semiconductor Processes and Devices 2007', p.237-240, Springer Vienna (2007)
- U. Aeberhard and R.H. Morf,
Microscopic Modelling of Quantum Well Solar Cells,
in 'Proc. of the 22nd EU PVSEC, Milano', WIP publishing (2007)

Curriculum Vitae

Personal Data

Name: Urs Aeberhard
Date of Birth: July 7, 1978
Nationality: Swiss citizen

Education

1985-1991 Primary school in Fläsch
1991-1994 Secondary school in Madrid (Spain)
1994-1998 High school in Chur
1998 Matura Typus C (mathematics and natural sciences)
1999-2004 Undergraduate studies in physics at ETH Zürich
2004 Diploma in Theoretical Physics, thesis about the effect of Rashba spin-orbit coupling on the transmission of open ring systems, under the supervision of Prof. Dr. M. Sigrist
2004-2008 Graduate studies in the Condensed Matter Theory group at Paul Scherrer Institute under the supervision of Dr. R.H. Morf

Acknowledgements

First of all, I would like to express my deep gratitude to Dr. Rudolf H. Morf, my thesis adviser, for proposing this most fascinating project, but also for the great freedom he gave me with it. He was always ready to discuss my work and to share his tremendous knowledge in almost any area of physics and numerics. I further profited enormously from his generosity as head of our group at PSI, which allowed me to attend many stimulating workshops and conferences. Personally I also appreciated his genuine interest in my musical activities and the resulting presence at nearly all of my concerts.

Special thanks go to my Doktorvater Prof. Dr. Manfred Sigrist from the Institute of Theoretical Physics at ETH Honggerberg, for referring me to PSI and accepting the formal supervision of my thesis, but also for his continuous interest in my work and for including me in the activities of his group, in spite of my rare presence at the institute. He also kindly provided the funding of my position for the last few months of the thesis.

In this place I wish to thank Jerome Faist for agreeing to co-referee this thesis and for his valuable comments.

I am grateful to the members of the Condensed Matter Theory group at PSI, including Dr. Christopher Mudry, Dr. Bernard Delley, my present and former PhD colleagues Maurizio Storni, Sebastian Guerrero and Dr. Andreas Schnyder, our postdocs Dr. Antoine Praz, Dr. Teodora Todorova and Dr. Franois Vernay, as well as the members of the condensed matter theory groups at the ITP, for a pleasant working atmosphere and stimulating lunchtime discussions.

I am indebted to Dr. Mathieu Luisier, formerly at the institute for Integrated Systems Engineering of D-ITET ETHZ, for his advice on the numerical implementation of the NEGF formalism.

Last but not least I would like to thank the secretaries at PSI and the ITP, Renate Bercher, Denise Pin, Irene Urbanetti and Etusch Szabo, for very competent and friendly assistance in the administrative work.